NOTTINGHAM TRENT UNIVERSITY

TOWARDS AN UNDERSTANDING OF PEPTIDE - INORGANIC INTERACTIONS

MARION JEBET LIMO

A thesis submitted in partial fulfilment of the requirements of Nottingham Trent University for the degree of Doctor of Philosophy

December 2013

Abstract

This study has contributed to the developing understanding of fundamental principles through which interactions at peptide-inorganic interfaces occur. The inorganic materials; crystalline zinc oxide (ZnO) and platinum (Pt) together with specific binding peptides identified using the phage display technique and alanine scanning for mutant sequences selected on the basis of peptide stability calculated *in silico* were synthesized, extensively characterized and the mechanisms of their interaction and the effects thereof studied. Firstly ZnO growth was monitored during solution synthesis from precursors using two different ZnO methods in the absence and presence of ZnO binding peptides (ZnO-BPs); G-12 (GLHVMHKVAPPR), its mutants (G-12A6, G-12A11, G-12A12) and GT-16 (GLHVMHKVAPPR-GGGC). Secondly, adsorption characteristics and thermodynamics of interaction of ZnO with ZnO-BPs and Pt with platinum binding peptides (Pt-BPs) were studied using biophysical tools; quartz crystal microbalance with dissipation monitoring (QCM-D) and isothermal titration calorimetry (ITC).

The outcomes of the ZnO synthesis studies demonstrated that peptides are smart, versatile tools possessing different mechanisms through which material formation processes and resultant morphologies can be modulated. Biphasic isotherms were observed in the adsorption of the ZnO-BPs on ZnO consisting of an endothermic and an exothermic event with ΔG values between -6 and -8.5 kcal/mol and high adsorption affinity values indicating the occurrence of favourable interactions. Among the examined ZnO-BPs, G-12 had the highest affinity for ZnO. QCM-D studies of Pt and Pt-BPs revealed that peptides TLHVSSY and SSFPQPN adsorbed strongly to the predominantly Pt (111) surface whereas TLTTLTN had a weak reversible interaction with the surface. Information from QCM-D studies was instrumental for experimental design and data interpretation of ITC experiments for the same counterparts. Differences in isothermal profiles of the Pt-BPs with Pt nanoparticles show their unique adsorption behaviours. The adsorption of peptides on inorganic surfaces is driven by kinetic and thermodynamic factors and varies depending on inherent properties of the peptide, physico-chemical properties of the inorganic surface and reaction conditions. ITC has shown great potential for use as a standard technique to monitor peptide-inorganic interactions and for possible application in peptide design.

Dedication

To my family, Prof. and Mrs Limo, Miss Rose Limo, Mr Charles Limo, Mr Rui Feitoria and friends for their love, support and encouragement through all my ups and downs and to our Heavenly Father (Jehova-jireh) without whom the completion of this work would not be possible.

Leonardo da Vinci (Artist-scientist, 15th April 1452 – 2nd May 1519)

"Where Nature finishes producing its own species, man begins, using natural things and with the help of this nature, to create an infinity of species."

Isaac Newton (physicist/ mathematician, 4th January 1643 – 31st March 1727)

"If I have seen further it is by standing on the shoulders of Giants."

Acknowledgements

Firstly, I would like to thank my supervisor, Professor Carole C. Perry for the opportunity to carry out this research project and for her continued guidance and support. I would also like to especially thank Dr. David J. Belton and Dr. Valeria Puddu who were part of my supervisory team and whose knowledge and expertise contributed greatly to the development of my study. Special thanks go to all past and current members of the Biomolecular and Materials Interface Research Group at Nottingham Trent University who have been a great team to work with, learn from and emulate. I acknowledge the advice and expertise of Dr. Mei Keat Liang, Dr. Marco Demurtas, Dr. Olivier Deschaume, Dr. Siddharth V. Parwardhan, Dr. Akilesh Rai and Dr. Laetitia. L. S. Canabady-Rochelle. I appreciate the support and advice of fellow PhD students in my research group; Mr Rajesh Ramasamy (for the computational modelling work), Miss Estefania Boix-Lopez (for her friendship and shared ever-needed brainstorming moments), Dr. Graham Hickman (especially for mass spectrometry analysis), Dr. Muhammad S. Zafar, Mr Mithun Parambath, Mrs Anna S. R. Gimeno-Fabra, Mr Matthew Nicklin and Mr. Veeranjaneyulu Thota. I also appreciate PhD students from other research groups like Miss Halema Abudalla, Mr Wesam Alwarfaly and others who I have constantly interacted with and shared experiences over the last few years as we have been working towards the same goal. I equally thank the team of support staff at NTU especially Mr Gordon Arnott for his assistance in carrying out TEM analysis and Mrs Mary Smith for her kindness and support whenever I needed to work in the analytical laboratory. I extend my gratitude to my collaborators from US Air Force Office of Scientific Research (AFOSR) for funding this research (FA9550-10-1-0024 and FA9550-13-1-0040) and for advice from Dr. Rajesh R. Naik and Dr. Joseph M. Slocik. To each one, for all your contributions, I cannot thank you enough.

Table of Contents

Chapter 1

Introduction

1.1. Biomimetic Materials Chemistry: An Overview

A delve into history reveals that the development of human civilization is strongly intertwined with the discovery and applications of materials. Historical epochs have been named according to the principal material being explored and dominating the society at the time from the Stone Age to the discovery of metals such as copper, tin and the conception of their stronger alloys in the Bronze Age, the Iron Age and through to the on-going age of silicon (Olson, 2001; Smith, 1965; Vaia and Wagner, 2004). The uses of materials evolved and shortages drove the need for new discoveries and innovation (Sass, 1998). The steel industry spearheaded economic development with its extensive use to date in buildings, infrastructure and other items such as vehicles and appliances. Presently, the economic power of steel has been replaced by new materials with broader applications being developed in industrial and academic laboratories such as plastic and more significantly by silicon (Sass, 1998; Siffert and Krimmel, 2004; Zhang, 2002).

Technological advances continue to add quality to our lifestyles. However, now attention is not just on the discovery of new materials with desired properties but also in having a deeper understanding of their composition down to the atomic and molecular scales and how this affects their overall bulk physical and chemical properties coining a discipline known as Materials chemistry (Fahlman, 2011). This interest was initiated earlier on when properties of materials such as malleability, thermal conductivity and aging of metals were realized accidentally and experimentation began from the philosophies of alchemists such as transmutation of base metals into gold through to the first concepts of crystallinity established through development of analytical experimental techniques (Olson, 2001; Smith, 1965). The role of science to explain and to better control matter had emerged. Investigations were further spurred after early designers used materials without fully understanding them leading to disasters such as

the tragic crash of the first passenger aircrafts, British Comets made in the early 1950's and possibly the mysterious collapse of Scotland's Tay rail bridge in 1879 (Biezma and Schanack, 2007; Sass, 1998).

Materials chemistry involves the characterization of materials found in nature and artificially synthesized novel materials as well as the prediction of structure and general properties of materials that are yet to be realized using advanced computational tools (Fahlman, 2011). Two rationales are applied for the synthesis of materials, the conventional top-down method and the more prevalent bottom-up approach. The top-down approach involves the conversion of a starting material into more sought after materials *i.e.* the transformation of wood into charcoal or paper (Fahlman, 2011; Thakkar *et al*., 2010; Zhang, 2003). Top-down miniaturization processes use physical or chemical means and improvements have led to the development of techniques that allow printing and patterning to be conducted at a micro and nanoscale (microlithography and nanolithography). Examples of techniques used are plasma etching, electron-beam lithography, focused-ion beam lithography and photolithography which are limited to molecular level precision and unable to mass produce identical nanostructures especially below 100 nm (Chiu *et al*., 2013; Gogolides *et al*., 2011; Mijatovic *et al*., 2005; Shimomura and Sawadaishi, 2001). A conceptual change to the bottom-up synthesis method may be the more competent route to achieving coveted advanced materials like those found in nature.

Bottom-up processes began with combining bulk compounds to create functional devices but was revolutionized by the discovery and formation of smaller building blocks in the development of nanochemistry which lies at the same or even lower length scales than biomolecules, nature's molecular tools capable of performing functions with greatly achieved complexity (Niemeyer, 2001). The bottom-up approach however requires a thorough understanding of the characteristics of individual building blocks. Inorganic nanoparticles serve as building blocks and possess desirable optical, magnetic, catalytic, electronic, mechanical and solution properties distinctively different from those of their bulk materials (Chiu *et al.*, 2013; Niemeyer, 2001). Traditional nanoparticle synthesis methods require stringent reaction conditions such as high temperature, pressure and use of harmful pollutant reagents (Briggs and Knecht, 2012; Patwardhan *et al*., 2007; Whyburn *et al*., 2008). Desirable materials with controlled

structures have been attained although the sustainability of such methods is questionable and a great challenge still remains to engineer nanomaterials with integrated properties, programmable structures and superior functionality (Briggs and Knecht, 2012; Chiu *et al.*, 2013).

In contrast, nature through eons of evolution has mastered material design commanding intrinsic control over the hierarchical assembly of building blocks forming detailed and organized structures of different functional soft through to hard materials (Briggs and Knecht, 2012; Davis *et al*., 2003; Van Hest and Tirrell, 2001; Lehn, 2002; Sarikaya *et al.*, 2003). The light weight and strength of bamboos, the adherence properties of gecko's feet, the superhydrophobic and cleaning properties of lotus leaves, the structural colour of butterfly wings, roses, nacre, peacock feathers and the robustness of spider silk are just a few examples of natural materials possessing remarkable engineering properties (Barthelat, 2007; Feng *et al*., 2002; Kinoshita *et al*., 2002; Liu and Jiang, 2011). Materials scientists started to use the term biomimetics in the 1980's to refer to the study of systems found in nature to attain knowledge that can be used as principles and ideas to enhance modern technology (Bensaude-Vincent *et al*., 2002; Dujardin and Mann, 2002). This approach allows for synthesis to be conducted under ambient or "green" reaction conditions and greater control over nanomorphology to be achieved which in turn determines the physical and chemical properties of a material and hence their possible applications (Chiu *et al.*, 2013; Huang and Yang, 2004; Raveendran *et al*., 2003; Whyburn *et al*., 2008).

Close to the heart of biomimetic studies is the study of biomineralization which is the process through which minerals are produced by living organisms which has for a long time captivated materials scientists (Lowenstam, 1962; Mann *et al*., 1986; Webb *et al*., 1991; Weiner *et al*., 1984). The fascination has been to uncover how intricate, reproducible and highly functional inorganic structures have been produced for generations in certain species such as the magnetosome crystals consisting of the magnetic iron sulphide, greigite or the magnetic iron oxide, magnetite found in magnetotactic bacteria, calcite and aragonite (calcium carbonate) found in shells of molluscs and detailed silica structures produced by diatoms, marine sponges and higher plants (Addadi *et al*., 2006; Bazylinski *et al*., 1995; Kroger and Sandhage, 2010; Mann *et al*., 1983; Perry and Keeling-Tucker, 2000; Webb *et al*., 1991). Specialized

biomacromolecules have been identified and are believed to play significant roles in controlling and directing the processes of mineral formation (Baeuerlein, 2007; Kroger *et al.*, 1999; Kroger and Sandhage, 2010; Perry *et al*., 1987; Shimizu *et al*., 1998). These biomacromolecules mainly include carbohydrates, lipids and proteins. Proteins in particular have been found to significantly influence biosynthesis and templating of numerous natural composites and have captivated the interest of scientists because of their unique properties of recognition, specificity, self-assembly and biofabrication (Addadi *et al*., 2006; Chiu *et al*., 2013; Dickerson *et al*., 2008 b; Perry *et al*., 2009; Sanford and Kumar, 2005; Veis and Perry, 1967). It is enthralling how proteins have the ability to control the assembly of biomaterials by directing the process of nucleation, the orientation of crystallization, structural formation and can also act as couplers, binders and scaffolds for biomaterials (Naik *et al*., 2002 a; Sanford and Kumar, 2005). As proteins are vital in the formation of biological structures, they should equally be important in biomimetic systems and should therefore be included in synthesis, function and/or assembly of inorganic materials (Naik *et al*., 2002 a; Sanford and Kumar, 2005; Sarikaya *et al*., 2003; Shimizu *et al*., 1998). Studying interactions between proteins and the surfaces of materials can mutually benefit other areas of research including biomedical engineering and biotechnology which may lead to development of advanced biomedical devices, biocompatible implantable materials with superior mechanical properties, regenerative medicine and tissue engineering, enzyme-based technologies, biosensors, imaging devices and drug delivery systems (Blankschien *et al.*, 2012; Niemeyer, 2001; Sanchez *et al*., 2005, Sun *et al*., 2011; Tamerler and Sarikaya, 2007; Xia and Jiang, 2008).

1.2. Identification and Design of Inorganic Binding Peptides

1.2.1. Inorganic-Binding Peptides Identified Using Phage Display Technique

Hitherto, the direct link between functional properties of materials with their nanoscale morphological features and the potential of proteins as tools for controlled synthesis of inorganic materials have been pointed out. Proteins are biological molecules made up from variable compositions of amino acids covalently linked through peptide bonds forming subunits known as polypeptide chains of diverse size and sequence order. The linear polypeptide chains constitute the primary structure of a protein which can further fold to form secondary, tertiary or more complex quaternary structures. The structure of a protein determines its biological function which includes deoxyribonucleic acid (DNA) replication, biotransport, storage, formation of cytoskeletal structures, cell signalling, biosensing, biocatalysis, the formation of biominerals and many other functions including those that have not yet been realised (Branden and Tooze, 1991; Marine and Luquet, 2007; Whitford, 2005).

Of interest in this study are the role of proteins in the formation of biominerals. Veis and Perry (1967) were among the first to successfully identify a protein involved in biomineralization, phosphophorin which was extracted from vertebrate teeth and is believed to play a role in the nucleation and mineralization of dentine matrix. Studies to extract, isolate, fully characterize and understand the role of proteins involved in biomineralization processes continue to be conducted to date (Gotliv *et al*., 2005; Kaplan, 1998; Kröger *et al.*, 1999; Marin and Luquet, 2007; Sarashina and Endo, 1998). In fact there is evidence of successful *in vitro* mineralization activity utilizing these proteins and their shorter sequences (peptides) not just in the synthesis of biominerals produced by the organism from which they were obtained but also in controlling the synthesis of other materials of interest (Baeuerlein, 2007; Sumerel *et al*., 2003). However, this approach has been met by challenges; mainly difficulties in obtaining and growing biomineralizing species and limited composition and number of identified biomineralizing proteins that can, in effect, control synthesis of a broader spectrum of commercially relevant inorganic materials such as semiconductors and metals (Dickerson *et al*., 2008 b; Weiner, 2008). Improvements have been made in extraction

techniques and protein quantities can be amplified using bacterial based recombinant DNA protocols for the expression and purification of proteins (Dickerson *et al*., 2008 b; Patwardhan *et al*., 2007; Perry *et al*., 2009). Even so, few biomineralizing proteins have been sequenced (Baeuerlein, 2007; Grünberg *et al*., 2004; Müller *et al*, 2003; Weiner, 2008). Instead, this approach has been overtaken by combinatorial biology techniques that enable faster rational design of protein sequences that can bind specifically to any target material; biominerals and any material formed from elements in the whole of the periodic table (Naik *et al*., 2002 a; Patwardhan *et al*., 2007; Sarikaya *et al*., 2003).

Combinatorial biological protocols *i.e.* cell-surface display (CSD), ribosome display (RD) and phage display (PD) are versatile techniques that have been used to identify a myriad of sequences that bind to selected target materials without the requirement for knowledge about the system being investigated. These display techniques simply enable one to identify the genotype of the protein that binds to the selected substrate/target material (Chiu *et al*., 2013; Sarikaya *et al*., 2003; Whaley *et al*., 2000; Whyburn *et al*., 2008). Among them, PD is the most popular technique in which huge peptide libraries are generated and displayed fused to the coat protein of a bacteriophage (*i.e.* M13, T7 and λ) which is a virus that is able to infect bacteria and replicate within it (Kriplani and Kay, 2005; Smith and Petrenko, 1997). The unique feature of a display host such as bacteriophages is that there is a direct link between its genotype and its phenotype. Filamentous phage M13 was the first and is the most studied and widely used bacteriophage for drug discovery in biomedical research and has been adopted in materials science to identify materials-specific binding peptides (Figure 1.1). Randomized DNA sequences possessing billions of variable sequences encoding peptides of fixed lengths are inserted into one among the five capsid genomes (mainly in capsid proteins III and VIII) of the virus and the chimeric protein is expressed usually on the surface of the coat protein pIII which is at one end of the bacteriophage or on protein VIII which are found along the length of the bacteriophage. The minor pIII coat protein has only 5 copies but is crucial for viral infectivity while the major pVIII capsid protein has about 2700 copies (Bermudez and Hathorne, 2008; Kriplani and Kay, 2005; Marvin, 1998).

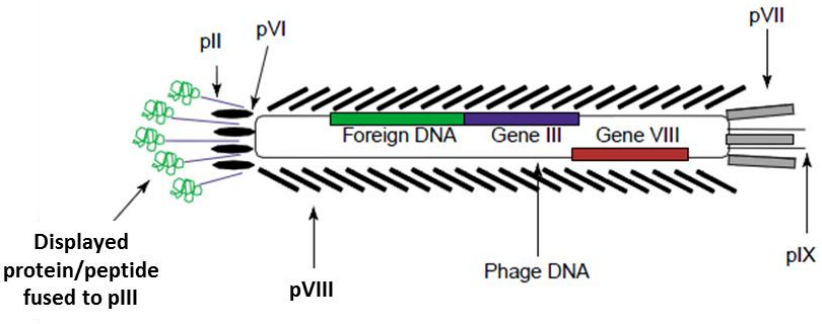

Figure 1.1. Schematic illustration of Filamentouse M13 phage highlighting gene III and VII which are mainly used in phage display technique to select peptides that specifically bind to inorganic target materials. Randomized DNA sequences are inserted into the genome and are consequently expressed in the phenotype of the bacteriophage as fused peptides/proteins. In the above illustration foreign DNA is inserted into gene III (green section) and the expressed peptide/protein fused to coat protein pIII. Illustration was adapted from Kriplani and Kay, 2005.

The phage library and target material are incubated in a suitable buffer allowing the bacteriophages displaying peptides with affinity for the substrate to bind to it after which unbound phage or weakly bound phage are washed off using an appropriate detergent-containing solution. The unwashed phage that is bound to the target material with high affinity is then eluted usually by disrupting ionic interactions by subjecting it to an acidic buffer which may also partially denature peptides (Dickerson *et al*., 2008 b; Kriplani and Kay, 2005; Naik *et al*., 2002 a; Sarikaya *et al*., 2003). Recovered phages are then amplified by infecting bacterium *Escherichia coli* (*E. coli*) in which they replicate carrying desired peptide sequences. The entire process is known as biopanning and is repeated at least 3 times with increased washing stringency to enrich for bacteriophages containing the peptides with the highest affinity for the target material. After the last round, isolation of individual phage clones is carried out for gene sequencing to identify the peptides that specifically and strongly bind to the inorganic material. More of the selected phage free peptide can be synthesized using techniques such as microwave assisted solid phase peptide synthesis and used in solution synthesis of inorganic materials from precursors with the expectation that it can potentially influence nucleation or promote the assembly of intricate structures like those found in nature.

CSD and RD techniques are carried out similarly to PD but instead of phages, CSD uses cells (*i.e.* yeast cells) that have surface expressed proteins while RD uses a synthetic DNA library with a mutated gene of interest. CSD does not require a host for amplification and RD can produce larger libraries than CSD and PD. However, both CSD and RD are more complex than PD and are more suited for biological applications. RD is not commercially available therefore CSD and PD techniques have been used more to identify inorganic binding peptides (Figure 1.2). Amino acid sequences that selectively and specifically bind to inorganic materials are by some popularly known as genetically engineered polypeptides for inorganics (GEPI) (Sarikaya *et al.*, 2003). Since the adaptation of phage display to identify inorganic material specific binding peptides, a plethora of sequences have been identified. Some sequences that bind to some metals and metal oxides are listed in Table 1.1.

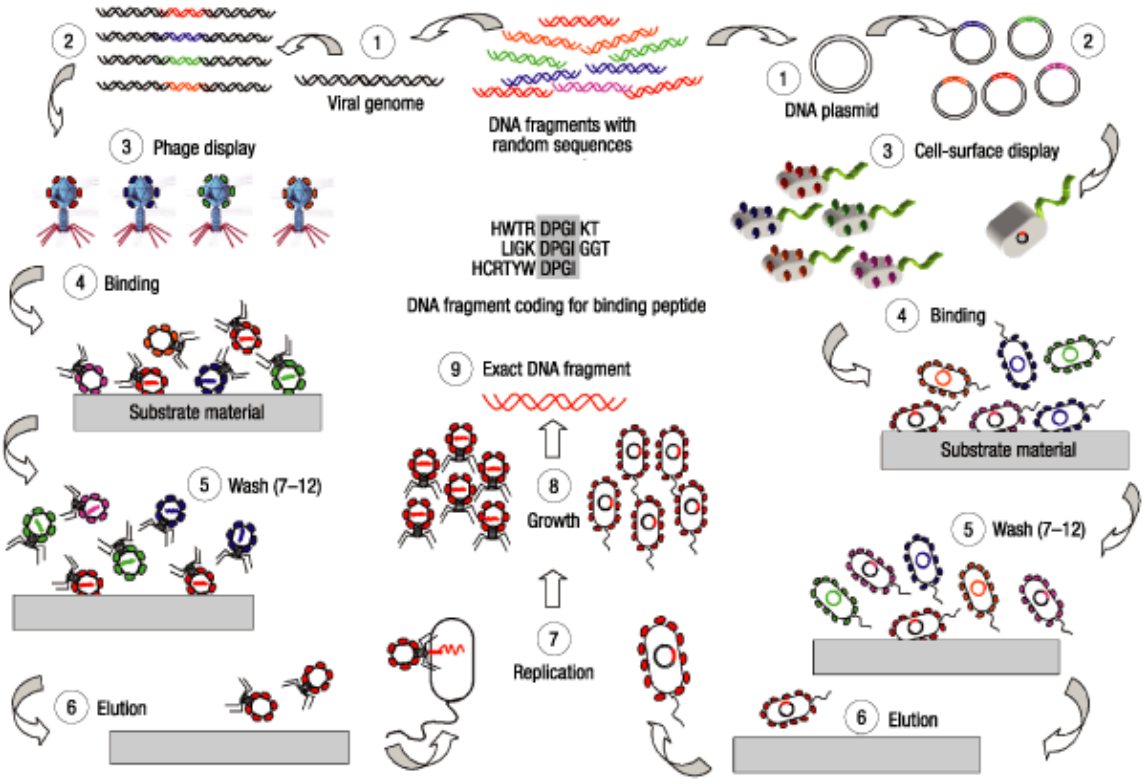

Figure 1.2. Schematic representation of phage display and cell surface display protocols used to identify peptide sequences that bind strongly and specifically to target inorganic materials. Image was reproduced from Sarikaya *et al.*, 2003.

Table 1.1. Examples of peptide sequences exhibiting affinity for various metals/metal oxides identified using PD technique

Target Material	Peptide Sequence	Source
Metals		
Gold (Au)	SWDPYSHLLQHPQ, VSGSSPDS	Huang *et al.*, 2005
	LKAHLPPSRLPS	Nam *et al*., 2006
	TGTSVLIATPYV	Kim *et al*., 2010
Silver (Ag)	AYSSGAPPMPPF, NPSSLFRYLPSD,	Naik *et al*., 2002 b
	SLATQPPRTVPP	Naik *et al*., 2004
	IRPAIHIIPISH, WSWRSPTPHVVT	
Platinum (Pt)	SSSHLNK, DRTSTWR, QSVTSTK	Sarikaya *et al*., 2003
	PTSTGQA, QSVTSTK	Oren *et al*., 2005
	TLHVSSY	Li *et al.*, 2009
	TLTTLTN, SSFPQPN	Chiu *et al*., 2011
Palladium (Pd)	HAPTPML, SPHPGPY, SVTQNKY	Sarikaya *et al*., 2003
	NFMSLPRLGHMH, TSNAVHPTLRHL	Heinz *et al.*, 2009
	QQSWPIS	Chiu *et al*., 2010
Titanium (Ti)	RKLPDAPGMHTW	Sano *et al*., 2005
	SCSDCLKSVDFIPSSLASS	Meyers *et al*., 2007
Metal oxides		
Zinc oxide (ZnO)	EAHVMHKVAPRP, EAHVMHKVAPRP -GGGSC	Umetsu *et al*., 2005
	GLHVMHLVAPPR, **GLHVMHLVAPPR-GGGC**	Tomczak *et al*., 2009
	HSSHHQPKGTNP, HHGHSPTSPQVR	Rothenstein *et al*., 2012
Silica (SiO_2)	MSPHPHPRHHHT, RGRRRRLSCRLL	Naik *et al*., 2002a
	HPPMNASHPHMH, TVVQTYSMVTRA	Eteshola *et al*., 2005
	RLNPPSQMDPPF, QTWPPPLWFSTS	Tamerler *et al*., 2007
	LDHSLHS, KSLSRHDHIHHH	Patwardhan *et al*., 2012
	KLPGWS, AFILPTG	Puddu and Perry, 2012
Titania (TiO_2)	TQHLSHPRYATKGGGW, RKKRTKNPTHKLGGGW	Dickerson *et al*., 2008 a
	YPSAPPQWLTNT, STPLVTGTNNLM,	Fang *et al*., 2008
	QSGSHVTGDLRL, ATTLHPPRTSLP	
	LNAAVPFTMAGS	Vreuls *et al*., 2010
Germania (GeO_2)	TGHQSPGAYAAH, SLKMPHWPHLLP	Dickerson *et al*., 2004

Nevertheless, combinatorial biology protocols have some disadvantages and biases associated with their use. Some of these biases arise because the methods rely on using biological systems (bacteriophages and cells) that have preferences in which DNA they choose to take up and which amino acids and proteins they express. Bacteriophages that may possess better binders for the inorganic material but fail to infect the host bacterium are also eliminated (Sarikaya *et al.*, 2003; Whyburn *et al*., 2008). A recent review by Vodnik and co-workers highlighted strategies to identify false positives which may be selected as a result of propagation advantages or target unrelated interaction of bacteriophages with other components used in the screening procedure *i.e.* plastic binders. A useful list of already acknowledged target unrelated peptides was also given (Vodnik *et al*., 2011). Additionally, the elution approach originally developed in biological protocols whereby pH is lowered to disrupt ionic bonds is suitable for disrupting interactions of peptides to proteins but may not be optimal for disrupting peptide interactions with inorganic surfaces (Naik *et al.*, 2004; Puddu and Perry, 2012). Stringent elution conditions may in effect destabilize the materials modifying the surface features leading to the isolation of peptides that bind to a material with different properties from the original material (Amstutz *et al*., 2001; Sarikaya *et al.*, 2003). These biases make it necessary to use multiple parallel screening techniques to identify inorganic binding peptides in combination with newer rational and random approaches such as bioinformatics and computational modelling tools (Oren *et al*., 2005; Sarikaya *et al.*, 2003; Slocik and Naik, 2010; Whyburn *et al*., 2008). These newer approaches have further been elaborated on in the section below.

1.2.2. Bioinformatics and Computational Modelling

Technological advances in computers have heightened the development bioinformatics (*in silico*) methods and computational modelling tools which are being applied to improve and accelerate the rational used to identify inorganic binding peptides and to progress the understanding of peptide conformation and peptide-surface interactions (Feng *et al*., 2011; Hansson *et al*., 2002; Nakajima *et al.*, 1997; Slocik and Naik, 2010). Molecular simulation techniques allow for theoretical investigation of the behaviour of complex systems at a molecular level beyond what can presently be achieved experimentally (Di Felice and Corni, 2011; Leach and Schomburg, 1996; Pandey *et al*.,

2009; Raut *et al*., 2005; Sagui and Darden, 1999). Molecular modelling methods like molecular dynamics (MD) and Monte Carlo (MC) are based on the theories that employ a force field which is a potential energy function used to calculate the total potential energy of a system by summing individual atom-atom pair interactions (Leach and Schomburg, 1996; Sagui and Darden, 1999; Raut *et al*., 2005).

MD simulations compute the dynamics of a bimolecular structure on different timescales while determining its thermodynamic and conformational properties (Hansson *et al*., 2002; Karplus and McCammon, 2002). The first report of protein simulation using MD was by McCammon and colleagues in 1977 documenting the conformational analysis of bovine pancreatic trypsin inhibitor (BPTI) which was among the first studies to disregard the perception of proteins to be relatively rigid structures. Proteins are now regarded as dynamic systems whose internal motions and resulting structural changes/conformations determine their function such as the ability of peptides to possess molecular recognition of materials (Karplus and McCammon, 2002; Oren *et al*., 2005; Slocik and Naik, 2010). Numerous force fields for protein simulation in aqueous solutions have been developed including CHARMM GROMACS, GROMOS, OPLS and AMBER. Simulations studies have focused on structural and energetic data to elucidate the mechanisms of peptide-inorganic interactions. In principle, the peptide conformation with the lowest energy minima is thought to correspond to the inorganic binding configuration (Evans *et al*., 2008, Oren *et al*., 2005).

Computational tools are continuously being developed. More recently, Oren and colleagues (2005) carried out a simulation study using MD and the CHARMM 22 force field parameters to study platinum binding peptide sequences identified using PD. The sequences that were chosen had different affinities for Platinum; strong (PTSTGQA and QSVTSTK), moderate (LGPSGPK) and weak (APPLGQA and LNDGHNY) binders. Adding cysteine residues at the *C* and *N*-termini of the peptides forming a disulphide bridge also created conformationally constrained sequences. Energy minimization was carried out in vacuum for all the sequences to identify their low energy conformations. The binding energies of the low energy conformation peptides to three crystallographic surfaces of Pt were studied and the conformational analysis compared to experimentally quantified binding affinities of the peptides determined

using fluorescence microscopy. The architecture of peptide moieties closest to the Pt crystallographic surface appeared to form protruding structures that seemed to match the features (atomic pits and grooves) of the Pt surface suggesting the occurrence of physical recognition. The strength of the interactions was attributed to the reactive groups on the protruding structures of the peptide. The need for studies of interactions in water was underlined (Oren *et al*., 2005). Solvents may significantly affect the recognition process between peptides and inorganic materials (Evans *et al*., 2008; Feng *et al*., 2011). Ghiringhelli and co-workers (2008) demonstrated the important mediating effects of water molecules near the surface of Pt (111) on the adsorption of oligopeptides by comparing their findings from MD with experimental studies in wet conditions.

The quality of the results from simulation studies can be improved by having few adjustable parameters and validating the force field used. Optimization of force fields to appropriately describe the behaviour of peptides adsorbing onto the surface of synthetic materials while describing the material's surface features is needed for accurate representation (Evans *et al*., 2008; Oren et al., 2005; Raut *et al*., 2005; Slocik and Naik, 2010). Unfortunately, many of the parameters that need to be considered that affect interactions between peptides and inorganic materials are not yet understood some of which include the length of the peptide, amino acid sequence order, peptide secondary structure as well as the surface chemistry and size of the material (Patwardhan *et al*., 2007; Slocik and Naik, 2010). The complexity of peptide inorganic interactions is even further increased by the fact that for a given set of peptides and inorganic materials, interaction occurs in a unique manner necessitating analysis to be carried out on an individual basis (Slocik and Naik, 2010). In an actual scenario where a peptide and inorganic particle interact, the intermolecular interactions may be mediated by multiple weak interactions such as electrostatic and hydrogen bonds which collectively may be as strong as a covalent interaction (Oren *et al*., 2005). A representative force field should describe the chemical and physical interactions between all components in the system and accurately balance all these interactions (Di Felice and Corni, 2011; Evans *et al*., 2008; Ponder *et al*., 2010; Raut *et al*., 2005; Walsh and Tomasio, 2010). More sophisticated force fields are being developed to describe interactions that are not accounted for in other common force fields but are

important in describing certain interactions *i.e.* AMOEBA which has been developed to describe electrostatic/polarization interactions, CHARMM-METAL and INTERFACE FF have been developed to study biomolecule interactions with noble metal surfaces and PCFF-SILICA which has been developed to specifically study silica-aqueous interfaces (Coppage *et al*., 2013; Grossfield *et al.*, 2003; Heinz *et al*., 2008; Patwardhan *et al*., 2012; Ponder *et al*, 2010; Ruan *et al*., 2013; Tang *et al*., 2013; Walsh and Tomasio, 2010).

For a force field to be used confidently, parallel experiments to probe fundamental characteristics of the interaction of a peptide with a given surface should be developed to validate the simulation (Raut *et al*., 2005). Iori and co-workers (2008) utilized experimental data and theories/calculations to derive an atomistic force field that is compatible with already developed codes such as NAMD and GROMACS and can specifically describe interfacial interactions between gold (111) surfaces and proteins in water. Their procedure to parameterize gold was investigated and proven to be reliable and can be used in studies of other molecules adsorbing onto gold or the same amino acids on different metal surfaces. The authors concluded that the strategy applied is also transferable to studies using other peptides interacting with metallic and semiconducting surfaces provided the force fields are parameterized for the specific interaction (Di Felice and Corni, 2011; Iori *et al*., 2009). Much progress is needed to design better force fields and develop more accurate simulation strategies to be able to refine molecular and atomic level details on peptide inorganic interfacial interactions (Di Felice and Corni, 2011; Wright and Walsh, 2013).

Bioinformatics methods have also proven to be an attractive general approach for the design of novel peptides and to understand the mechanisms of biomineralization proteins (Evans *et al*., 2008; Oren *et al*., 2007). One example of an *in silico* approach is a study that was conducted by Oren and co-workers (2007) to design new inorganic binding peptide sequences by comparing newly generated computational sequences to peptides that were identified experimentally through *in vivo* techniques such as PD and classified as either strong or weak binders. This rational is commonly applied in biological analysis to identify protein sequences that perform similar functions as they usually possess sequence similarities due to biochemical, biophysical and evolutionary constraints (Attwood, 2000; Shiba, 2010). They developed scoring matrices based on

sequence similarity by focusing on the similarities between strong binders and the dissimilarity between the weak and strong binders. Their accuracy was validated by computationally predicting specific binders for quartz using scoring matrices from experimentally identified sequences having strong, moderate and weak affinities to quartz. The computationally predicted sequences were then synthesized and their binding affinity to quartz compared with that of the experimentally determined strong binders using surface plasmon resonance spectroscopy. Some computationally developed peptides had higher affinity for quartz compared to the strongest binder identified *in vivo*. Further experimentation using gold quantum-dot immobilization and immunofluorescence supported their findings. They demonstrated the power of simple and general bioinformatics approach to predict new and second generation material specific binding peptides and highlighted the importance of amino acid sequence order which controls the structure of the peptide over amino acid composition in peptide-inorganic interactions (Oren *et al*., 2007).

1.3. Peptide Use in the Synthesis of Metal/Metal Oxide Materials

Metals and metal oxide materials are attractive for their many technological applications. Metal/metal oxide nanoparticles in particular have unique properties, for example, their surface chemistry that is uniquely different from the properties of their bulk material counterparts. Nanoparticles exhibit size, shape, composition and interparticle distance dependent quantum effects and their large surface area to volume ratio increases the number of surface active atoms that can be functionalized with different ligands for several applications (Daniel and Astruc, 2004; Galloway and Staniland, 2012; Ghosh *et al*., 2008; Thakkar *et al*., 2010; Tan *et al*., 2010). Gold (Au) nanoparticles for example possess enhanced scattering and adsorption of light which allows them to be used in imaging and optical devices and can be functionalized for drug targeted delivery (Bhandari *et al*., 2012; Gourishankar *et al*., 2004; Guo and Wang, 2007; Paciotti *et al*., 2004; Long *et al*., 2010). As the physical/chemical properties and functions of a material are dictated by its structure and/or morphology, controlled synthesis of materials at the micro- and nanoscale has been a research interest of many scientists for decades but is still met by challenges with a rising need for more facile, reproducible, efficient, economic and environmentally friendly

methods (Anastas and Warner, 2000; Guo and Wang, 2007; Matlack, 2001; Raveendran *et al*., 2003). Several bottom-up methodologies have been developed to synthesize metals and metal oxides including hydrothermal synthesis, template directed approach, sol-gel process, electrospinning, electrochemical deposition, chemical vapour deposition, sputtering, thermal deposition, microwave plasma method, surfactant-assisted chemical etching process, molecular beam epitaxy, vapour phase transport process and pyrolysis (Ahmad and Zhu, 2011; Djurišić and Chen, 2010; Song *et al*., 2005; Xu and Wang, 2011).

Solution synthesis methods (aqueous and non-aqueous) using precursors are prevalent for their low cost, facile and greener reaction conditions. In solution synthesis, the morphology of particles can be tuned using growth directed synthesis common in precipitation processes and using templates upon which nucleation and growth occurs (Adair and Suvaci, 2000). During the synthesis of colloidal or particles in suspension, precise control over nucleation and growth of particles is required to achieve desirable structures. In solution synthesis, the driving force for chemical reactions leading to nucleation and crystal growth is the need to minimize the free energy of the whole system and the direction of crystal growth is dictated by the surface activities of the facets under specific growth conditions (Govender *et al*., 2004; Huang and Caro, 2010; Xu and Wang, 2011). Factors such as solution composition, chemistry, temperature, reactant concentration, reaction rate and solubility are intricately linked and together influence the parameters of crystal growth and hence crystal morphology (Dove *et al*., 2003; Govender *et al*., 2004; Tao *et al*., 2008). This interplay of factors makes it difficult to determine the exact mechanism for morphology controlled particles. Molecular capping agents are able to control the structures of crystals by selectively adsorbing to specific crystal planes altering their surface energies and stabilizing them (Garcia and Semancik, 2007; Govender *et al*., 2004). The growth of the crystal planes with strongly bound capping agent is hindered and growth of the planes with no or weakly bound capping agent is promoted. Examples of shape directing agents used include surfactants (toluene, tetradecyltrimethylammonium bromide (TTAB), sodium dodecylsulfate (SDS), cetyltrimethylammonium bromide (CTAB)), polymers (poly(vinyl pyrrolidone) (PVP), poly(N-ethylacrylamide) (PNEA), small molecules and inorganic ions (metal ions, amines) and biomolecules (proteins and nucleic acids)

(Song *et al*., 2005; Tao *et al*., 2008; Peng and Yang, 2009).

Combinatorially selected material binding peptides and post selection tailored peptides designed using knowledge obtained from computational modelling and bioinformatics are proving to have great potential in improving material synthesis and in advancing device fabrication (Chen *et al*., 2008; Chiu *et al*., 2010; De la Rica and Matsui, 2010; Dickerson *et al*., 2004; Graf *et al*., 2009; Seker and Demir, 2011, Tamerler and Sarikaya, 2007; Tomczak *et al*., 2009). Brown and colleagues (2000) were among the first to realize that combinatorially selected inorganic binding peptides not only bound to the target material but could in some cases also control their formation during solution synthesis using an appropriate precursor. Several other studies have equally demonstrated controlled synthesis of materials using peptides. The AYSSGAPPMPPF (A3) peptide has been used to precipitate silver nanoparticles of different shapes and control the monodispersity, size, shape and stability of gold in aqueous solution (Naik *et al*., 2002 b; Slocik *et al*., 2005). Impressively through self-assembly properties, the A3 peptide has also been manipulated to form a complex double helical structure of gold nanoparticles (Chen *et al*., 2008). Kim and co-workers (2010) demonstrated the controlled synthesis of gold nanostructures of different morphologies; nanometer thick platelets, nanowires and nanoribbons using TSTSVLIATPYV (Midas-2) peptide and altering reaction conditions such as pH and precursor concentration. Palladium nanoparticles synthesized in the presence of Palladium binding peptide QQSWPIS (Q7) were well dispersed and size controlled compared to synthesis without peptide (Chiu *et al*., 2010).

Apart from morphology control, peptides can also act as stabilizers, reducing agents, catalysts or inhibitors during solution synthesis. Metal nanoparticles have high surface energy causing them to be highly reactive during synthesis leading to aggregation (Guo and Wang, 2007; Raveendran *et al*., 2003). To avoid aggregation during synthesis, their surfaces need to be protected to increase their stability and solubility properties. Conventional surface passivation methods include the use of stabilizers such as citrate, organics functionalized with thiols, polymeric matrixes and encapsulation of nanoparticles (Daniel and Astruc, 2004; Guo and Wang, 2007; Raveendran *et al*., 2003). The alternative use of peptides as stabilizing agents in nanoparticle syntheses is of interest for its greener application and is a step towards possible biomedical

applications (Gourishankar *et al*., 2004; Guo and Wang, 2007; Slocik *et al*., 2005; Tan *et al*., 2010). Residues of amino acids in peptides *i.e.* tyrosine and tryptophan have been shown to act as reducing agents of gold, silver and Palladium ions in solution synthesis of nanoparticles which also helps to control particle size (Chiu *et al*., 2010; Slocik *et al*., 2005; Xie *et al.*, 2007). Incorporation of titania binding peptide Ti-1 with sequence RKKRTKNPTHKLGGGW in synthesis of titania from a precursor resulted in increased yield attributed to the presence of a great amount of basic residues especially histidine demonstrated by designing and synthesizing mutants of the parent peptide (Dickerson *et al*., 2008 a). Elsewhere, peptides RGRRRRLSCRLL (Si4-10) and KSLSRHDHIHHH (pep1) have been shown to significantly inhibit the condensation rate of silicic acid from precursor solutions slowing down the precipitation of Silica (Patwardhan *et al*., 2012). Galloway and Staniland (2012) have highlighted some more examples of studies where peptides and proteins have been used to synthesize metals and metal oxides nanoparticles.

Inhouse, evidence of peptide directed morphology modification of zinc oxide *via* an adsorption-growth inhibition mechanism has been demonstrated (Liang *et al*., 2011). The specificity between inorganic crystal planes and peptides/biomolecules and the mechanisms of interaction is however not clearly understood (Dove *et al*., 2003; Liang *et al*., 2011; Naik *et al.*, 2004; Patwardhan *et al*., 2007; Sarikaya *et al.*, 2003). This study seeks to bring new insight towards the understanding of peptide-inorganic interfacial interactions at a molecular level and focuses on two materials, zinc oxide and platinum.

1.3.1. Overview of Zinc Oxide (ZnO)

The use of ZnO dates as far back as about 2000 B.C. where it was used in medicinal ointments and was later used as a source of zinc in the making of brass (Biswas, 1987; Halioua, 2005). Naturally occurring ZnO, known as zincite is found with impurities containing some manganese and other elements giving it a yellow or red appearance (Klingshirn, 2007). From as early as 1935, studies on ZnO had begun and its applications continued to be developed (Bunn, 1935). With improvements in synthetic ZnO growth technology, the last decade has seen a significant rise in research interests in developing the uses of ZnO especially for its potential electrical and optoelectronic applications (Bunn, 1935; Klingshirn *et al.*, 2005; Ozgur *et al*., 2010). The properties of ZnO continue to be studied intensively and it can be described as a II to VI compound semiconductor material with a direct wide band gap that is around 3.4 eV which is in the near ultraviolet (UV) and its exciton binding energy is comparatively large, about 60 meV at room temperature (300 K) (Norton *et al*., 2004; Pearton *et al*., 2005; Xu *et al*., 2004). There are three known crystal structures of ZnO; rocksalt which requires relatively high pressure for its formation, zinc blende which can only be synthesized using cubic substrates and the wurtzite structure which is the thermodynamically stable phase and can therefore be synthesized at ambient reaction conditions (Amrani *et al*., 2006; Govender *et al*., 2004; Ozgur *et al*., 2010).

In its polycrystalline form ZnO has been widely used as an additive for applications including facial powders, sunscreen, paint pigmentation, lubricants and in the manufacture of rubber (Bunn, 1935; Jagadish and Pearton, 2011; Moezzi *et al*., 2012). The wide band gap of ZnO makes it suitable for optoelectronic applications and its high exciton binding energy at room temperature gives it its efficient excitonic emission and luminescent properties (Hirai *et al*., 2005; Wang, 2004). Other developing technological and industrial applications include the making of field emitters, varistors, acoustic wave devices, piezoelectric devices, solar cells, photocatalysts, transparent conducting materials and possibly even chemical/biosensors (Ahmad and Zhu, 2011; Fan and Lu, 2005; Ozgur *et al.*, 2010). Its biocompatible, biodegradable and antimicrobial nature also encourages further developments for biomedical applications (Yi *et al*., 2005; Zhang *et al.*, 2012; Zhou *et al*., 2006).

The applications of ZnO highly rely on control over its properties including purity, size, morphology and chemical composition (Xu *et al.*, 2004; Huang and Caro, 2010). The wurtzite structure (Figure 1.3), is hexagonal with a unit cell having a space group *C*6*mc* and lattice parameters a = 0.325 and c = 0.521 nm giving it a c/a ratio of 1.60 which is close to the elementary translation vectors of an ideal hexagonal unit cell (c/a = 1.633) (Norton *et al.*, 2004; Pearton *et al.*, 2005). The wurtzite structure consists of tetrahedrally coordinated ions where one O^{2-} ion is surrounded tetrahedrally by four Zn^{2+} ions and vice versa forming alternating planes that are stacked along the *c*-axis resulting in a structure with no central symmetry (Li *et al.*, 2012; Wang, 2004).

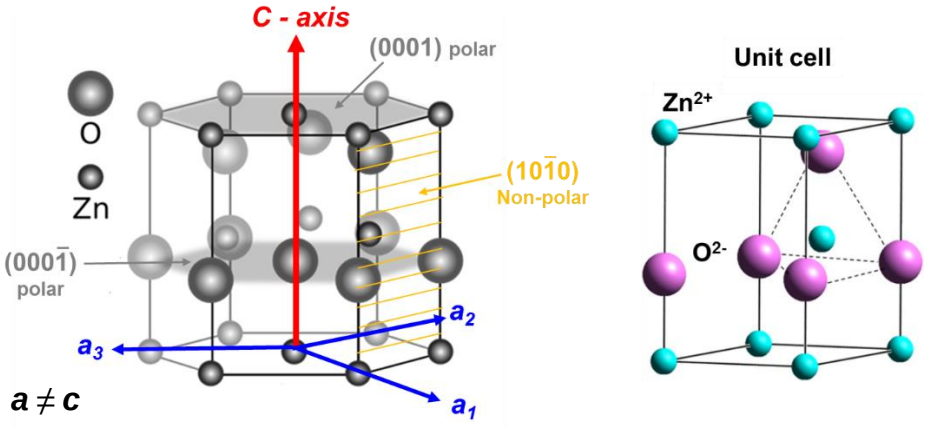

Figure 1.3. Models of ZnO crystals showing the arrangement of oxygen and zinc atoms forming the wurtzite structure and the preferential direction of crystal growth along the *c*-axis. Adapted from online research group website of Behler J., 2010 and Li *et al.*, 2012.

In aqueous solution synthesis without growth modifiers, rod-like elongated ZnO hexagonal crystals are formed which have both polar and non-polar surfaces. The most common basal planes are the positively charged (0001) Zn-terminated and the negatively charged (000$\bar{1}$) O-terminated planes which are polar (Garcia and Semancik, 2007; Govender *et al.*, 2004; Weintraub *et al.*, 2010). ZnO (0001) and (000$\bar{1}$) planes are uniquely flat which is unusual for polar surfaces which normaly undergo massive rearrangements and form facets to maintain stable structures (Baruah and Dutta, 2009). The oppositely charged polar planes result in a dipole moment and have higher surface energy than the non-polar surfaces therefore incoming precusor molecules favoroubly adsord to the polar planes resulting in anisotropic crystal growth along the *c*-axis

(Baruah and Dutta, 2009; Peng *et al*., 2006; Xu and Wang, 2011). The more thermodynamically stable non-polar planes such as the $(10\bar{1}0)$ and $(11\bar{2}0)$ planes are both Zn and O-terminated (Govender *et al*., 2004; Li *et al.*, 2012).

Using solution synthesis methods, a wide range of 1D nanometer to micrometer ZnO structures have been formed such as rods, plates, tubes, rings, tetrapods, prisms, pyramids, spheres, hollow structures, flowerlike and multi-needle shaped crystals (Masuda *et al*., 2007; Togashi *et al.*, 2011; Tomczak *et al*., 2009). These variable structures have been obtained by controlling the growth conditions thereby tuning the relative surface energy of the different growth facets, manipulating the rate and direction of crystal growth (Baruah and Dutta, 2009; Wang, 2004). Stucture directing agents (SDAs) like citrate ions, amines and polymers are commonly used in solution synthesis to attain variable morphologies. There are however not so many studies that have employed biomolecules including peptides to control the stucture of ZnO mainly because of their sensitivity to reaction conditions, complexity and high costs (Liang *et al*., 2011). Nevertheless, peptides have been shown to be smart and versatile tools with great potential in tailoring the morphology of crystals (Brown *et al*., 2000; Liang *et al*., 2011; Slocik *et al*., 2005; Tomczak *et al*., 2009).

1.3.2. Studies on Interactions between Zinc Oxide and Zinc Oxide Binding Peptides

EM-12 (EAHVMHKVAPRP) was among the first five artificial ZnO binding peptides to be identified using PD (Umetsu *et al*., 2005). EM-12 was selected for further studies as it exhibited the highest affinity for ZnO compared to the other four peptides (VSNHKALDYPTR, DSGRYSMTNHYS, ATHTNQTHALYR, QNTATAVSRLSP) identified. EM-12 was tagged with the sequence GGGSC as a linker for immobilization to a gold coated polypropylene plate for adsorption studies using fluorescent ZnO particles which confirmed the specificity of the peptide. When used in solution synthesis of ZnO from precursors, EM-12 with the GGGSC tag produced flower-like ZnO microparticles (Figure 1.4 d) (Umetsu *et al*., 2005) and fused to a collagen triple helix structure, it was able to template the growth of monodisperse single crystalline ZnO nanowires (Bai *et al*., 2009).

To understand the interactions taking place between the ZnO surface and ZnO binding peptides, Umetsu and co-workers embarked on a study where they fused a fluorescent protein (Green fluorescent protein; GFP) to the *N*-terminal of EM-12 and analysed its binding to a ZnO surface in an appropriate phosphate solution (Yokoo *et al*., 2010). The adsorption of GFP on ZnO particles was used to estimate thermodynamic parameters of binding using the Van't Hoff's equation (Yokoo *et al*., 2010). Their results showed that the electrostatic interaction between the ZnO particles and ZnO binding peptide was enthalpy-driven and involved hydrogen bonding (Yokoo *et al*., 2010). They studied the binding function of the EM-12 fused to GFP with the systematic addition of each amino acid from the *N*-terminal to the entire peptide. The studies with the short segments of the peptide suggested that the binding of the peptide to ZnO is critically affected by conformational changes and charged amino acids together with the amino acid residues next to them were the plausible hot-spots for selective affinity (Yokoo *et al*., 2010). Umetsu and group later carried out a study to specifically identify the binding sites of their ZnO binding peptide to ZnO. They used the spot method to synthesize random rotations of the amino acids in EM-12 on a cellulose membrane. In total, 125 variations of the peptide were assayed for binding against ZnO nanoparticles (Okochi *et al*., 2010). They concluded that the overall binding activity of the peptide against ZnO did not depend on physical parameters or hydrophobicity but recognition of the specific alignment of amino acids in the peptide. Shortly after, the same research group published on the effect of EM-12 on solution growth of ZnO crystals using $Zn(NO_3)_2$ and KOH to form zinc hydroxide ($Zn(OH)_2$). They found that the presence of EM-12 during solution synthesis, suppressed crystal growth of ZnO in the (0001) direction (Figure 1.4 e and f). The addition of dipeptides from the EM-12 sequence *i.e.* M_5 H_6 and H_6 K_7 was also examined and were found to suppress growth of ZnO along the (0001) direction even more than EM-12 (Togashi *et al*., 2011).

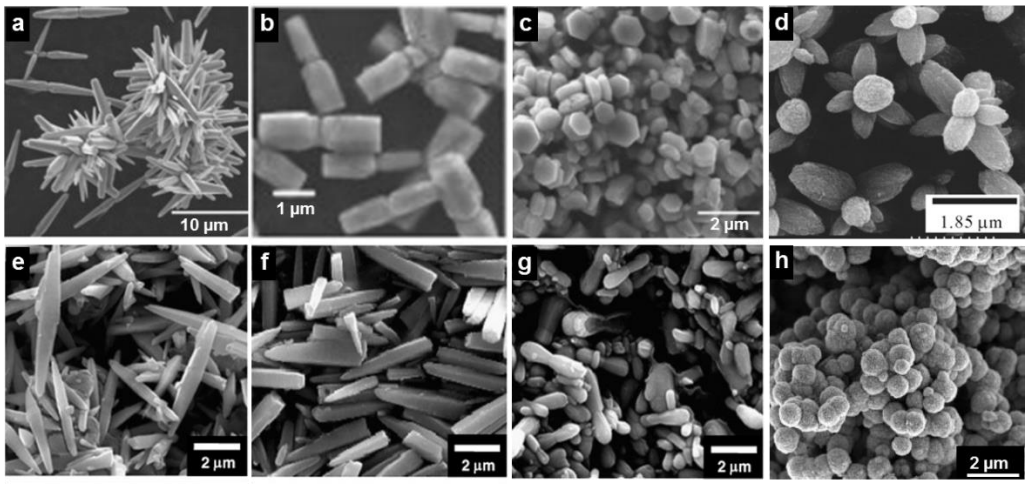

Figure 1.4. ZnO structures produced using hydrothermal synthesis methods in the absence and presence of ZnO binding peptides; (a-c) Method described by Tomczack *et al*., 2009 using precursor zinc nitrate hexahydrate ($Zn(NO_3)_2 \cdot 6H_2O$) and hexamethylenetetramine (HMTA), (a) synthesis without peptide forming ZnO twinned hexagonal rods, some of which were aggregated, (b) ZnO twinned rods with lower aspect ratio synthesized in the presence of 0.1 mg/ml GT-16 (GLHVMHKVAPPR-GGGC), (c) ZnO twinned platelets synthesized using 0.5 mg/ml GT-16. (d) ZnO flowers synthesized using $Zn(NO_3)_2$, potassium hydrate (KOH) and EM-12 (EAHVMHKVAPRP) with a GGGSC tag in a method described by Umetsu *et al*., 2005. (e-g) ZnO crystals synthesized using $Zn(NO_3)_2$ and KOH in methods described by Togashi *et al*., 2011; (e) Needle-like crystals synthesized without peptide, (f) synthesis in the presence of EM-12 forming ZnO needles with flattened edges, (g) peanut-like structures synthesis in the presence of EM-12 using a drying method. (h) Globular aggregates of ZnO synthesized using $Zn(NO_3)_2 \cdot 6H_2O$ in an aqueous buffer solution containing HHGHSPTSPQVR peptide using a method described by Baier *et al*., 2012.

Another ZnO binding peptide hereafter known as G-12 (GLHVMHKVAPPR) was isolated using phage display (Tomczak *et al*., 2009). G-12 has 67% homology to EM-12. A modification of the peptide was made by adding a GGGC tag to the *C*-terminal hereafter called GT-16 (GLHVMHKVAPPR-GGGC) (Tomczak *et al*., 2009). Synthesis of ZnO from precursor $Zn(NO_3)_2 \cdot 6H_2O$ was carried out in the absence and presence of G-12 and GT-16. Without peptide, ZnO crystals grew anisotropically along the *c*-axis forming twinned hexagonal rods, some of which were aggretated (Figure 1.4a). In the presence of GT-16, crystal growth was hindered along the *c*-axis and with increased peptide concentration, the crystals were modified to low aspect ratio hexagonal platelets (Figure 1.4 b and c) (Tomczak *et al*., 2009). Further studies on morphology modification of ZnO using G-12 and GT-16 were conducted within our research group. Peptides G-12 and GT-16 were found to use an adsorption-growth inhibition

mechanism to modify ZnO morphology (Liang *et al.*, 2011). G-12 was thought to inhibit the anisotropic growth of ZnO crystals by adsorbing non-specifically to both the (0001) and (10$\bar{1}$0) plane reducing the growth of the crystals along both the *a* and *c*-axis. GT-16 also bound to both (0001) and (10$\bar{1}$0) planes of ZnO but adsorbed preferentially to the (0001) planes causing it to have a greater effect on the growth along the *c*-axis leading to the formation of low aspect ratio ZnO twinned platelets (Liang *et al.*, 2011).

Molecular dynamics was also used to study the interaction of the peptides with surfaces of ZnO and the information obtained was compared to experimental findings (Liang *et al.*, 2011). Computational data suggested that amino acid with side chain residues that were neutral and cationic *i.e.* H_3 and K_7 of G-12 and G_1, H_6 and K_7 of GT-16 were capable of interacting with polar Zn^{2+} terminated (0001) plane. However, from FTIR studies and the pK_a values of the side chains of peptides G-12 and GT-16, NO_3^- was found to possibly complex with the cationic moieties of the peptide *i.e.* G_1, H_3 and K_7. If there were no cationic residues to interact with the ZnO planes other possible interactions include carboxylate coordination of the *C*-terminus of the peptides with the polar (0001) Zn^{2+} terminated plane. Alternatively, M_5 sulphur atoms and C_{16} thiol (in the case of GT-16) coordination with the Zn^{2+} terminated (0001) plane of ZnO could occur. In addition, Zn^{2+} and O^{2-} ions on the low index (10$\bar{1}$0) plane of ZnO could also interact with the peptides differently. G-12 was predicted to possibly interact with O^{2-} at the (10$\bar{1}$0) plane *via* electrostatic interactions with polar cationic H_3 and K_7 side chain moieties while neutral H_3 could interact with O^{2-} ions *via* hydrogen bonding or coordinate with Zn^{2+} ions. GT-16 was found to interact more possibly using non-polar side chain moieties of M_5, R_{12} and COO^- at the *C*-terminus of the GGGC-tag. Another suggested possibility involves interactions between the peptide residues and the O^{2-} present in the (10$\bar{1}$0) and (000$\bar{1}$) planes of ZnO by hydrophobic interactions, hydrogen bonding and Van der Waals forces (Liang *et al.*, 2011).

Elsewhere, 29 other different 12-mer peptides that bind to single crystalline (0001) and (000$\bar{1}$) surfaces of ZnO were identified using phage display (Rothenstein *et al.*, 2012). The target surfaces had negative zeta potential values above pH 4 which is different from the isoelectric point of ZnO powder which is about pH 9.5 (Rothenstein *et al.*, 2012; Xu and Wang, 2011). This was attributed to the structuring of water molecules on

the surface. Many of the peptide sequences identified as ZnO binders using PD pH 7.5 have a high isoelectric point and are therefore positively charged (Table 1.2). It is therefore expected that ionic interactions play an important role in the binding of these sequences to ZnO surfaces. The first indication of which amino acids may be important for the interaction can be deduced by noting which amino acids are enriched and which are depleted in the peptide pool. In the study by Rothenstein and group (2012), histidine (H) amino acid was enriched in peptides that bound to both the O and Zn-terminated substrates, arginine (R) was enriched in peptides that bound more specifically to the O-terminated substrate and lysine (K) for the peptides that bound more specifically to the Zn-terminated substrate. The enriched amino acids for the Zn-terminated substrate (K, D, L, and A) and negatively charged amino acids were depleted in peptide sequences specific for the O-terminated substrate. In the peptide sequences that bound to the Zn-terminated substrate negatively charges glutamic acid (E) was depleted while negatively charged aspartic acid (D) was enriched which indicated that ionic interaction with the positively charged surface was plausibly not the only driving force for the interaction (Rothenstein *et al*., 2012).

The two most abundant peptides (HSSHHQPKGTNP and HHGHSPTSPQVR) able to bind to both the Zn and O-terminated surfaces were selected for further studies to identify the binding epitopes using nuclear magnetic resonance (NMR) (Rothenstein *et al*., 2012). This was carried out by monitoring line broadening effects and chemical shift perturbations during interaction with ZnO. The spectrum of peptides only was compared to that of peptides plus ZnO. Possible peptide-peptide interactions were also observed in the NMR experiments. A pH dependent interaction of histidine and serine residues to ZnO nanoparticles was identified. In zinc dependent proteins such as structural zinc finger proteins, residues of histidine and cysteine are known to complex with divalent zinc ions and aspartic acid, glutamic acid, serine and threonine are also able to interact with or stabilize interactions of zinc ions with proteins (Berg and Godwin, 1997; Dudev and Lim, 2003; Maret and Li, 2009). Basic amino acids particularly histidine amino acid are prevalent in most of the peptide sequences that interact with ZnO identified using PD (Table 1.2). Nevertheless, as some of the sequences identified to bind to ZnO by Rothenstein's group (*i.e*. QWGWNMPLVEAQ and MKPDKAIRLDLL) and one (QNTATAVSRLSP) from the study by Umetsu and

group (2005) did not have histidine residues, other amino acids may also play significant roles in the interaction. Cysteine residues may be absent in these artificial peptides as they are not preferentially expressed by bacteriophages but can be substituted into a peptide sequence to increase the affinity for ZnO surfaces. Sequence alignment was seen to influence the binding efficiency of individual amino acids and uncharged residues of histidine and serine were still able to interact with ZnO nanoparticles using non-ionic interactions such as hydrogen bonding, polar interactions or van der Waals interactions. A high binding affinity, nanomolar range K_D values were determined for both peptides (HSSHHQPKGTNP and HHGHSPTSPQVR) to the ZnO nanoparticles (Rothenstein *et al*., 2012).

Table 1.2. Properties of PD identified ZnO binding peptides used in ZnO synthesis and adsorption experiments.

[a] **ZnO Binding Peptides**	**Reference**	[b] **pI (pH unit)**	**Non-polar no charge**	**Polar no charge**	**Polar +ve charge**	**Polar –ve charge**
EAHVMHKVAPRP	Umetsu *et al*.,	10.09	AVMVAPP	-	**HH**KR	E
[c] **EAHVMHKVAPRP-GGGSC**	2005	8.97	AVMVAPPGGG	SC	**HH**KR	E
GLHVMHKVAPPR	Tomczak *et*	11.49	GLVMVAPP	-	**HH**KR	-
[c] **GLHVMHKVAPPR-GGGC**	*al*., 2009	10.11	GLVMVAPPGGG	C	**HH**KR	-
HSSHHQPKGTNP	Rothenstein	10.10	PGP	SSQTN	**HHH**K	-
HHGHSPTSPQVR	*et al*., 2012	11.04	GPPV	STSQ	**HHH**R	-

[a] Different ZnO targets were used (Umetsu and Tomczak and coworkers used ZnO nanopowder and Rothenstein and colleagues used single crystalline ZnO (0001) and $(10\bar{1}0)$ substrates but the two most abundant peptides shown here were able to bind to both surfaces). [b] Isoelectric point (pI) was calculated using peptide property calculator Innovagen. [c] Peptide sequence has an additional tag to the original sequence identified using PD.

From the same peptide pool, three ZnO binding peptides were selected for use in ZnO synthesis to determine their precipitation mechanisms; HHGHSPTSPQVR (basic pH), LLADTTHHRPWT (near-neutral pH) and ERSWTLDSALSM (acidic pH) (Baier *et al*., 2012). MD using GROMACS 4.5.3 simulation package and AMBER force field was also used to compute the interaction of the three peptides with polar (0001) and non-polar $(10\bar{1}0)$ surfaces. Growth of ZnO from precursor $Zn(NO_3)_2 \cdot 6H_2O$ was seen to take place *via* a metastable intermediate layered basic zinc salt (LBZs). After 6 weeks incubation variable globular and hexagonal ZnO aggregates smaller than the crystals

synthesized without peptide were observed, formed though peptide growth inhibition mechanism (Figure 1.4h). From computational studies the amino termini and positively charged arginine residues were found to be the interaction sites for the (0001) surface whereas uncharged residues of serine, threonine and glutamine as well as positively charged histidine residues were seen to interact with the non-polar $(10\bar{1}0)$ plane of ZnO. The interactions were mainly attributed to electrostatic binding. The binding energies of the interactions were also determined computationally and were found to be in agreement with previous experimental findings identifying HHGHSPTSPQVR as the strongest ZnO binding peptide of the three (Baier *et al*., 2012).

1.3.3. Overview of Platinum (Pt)

The inevitable depletion of fossil fuel reserves and rising energy demands coupled to environmental pollution have driven the need to develop alternative energy sources. Pt is a precious transition metal that has excellent electrical properties, outstanding catalytic activity and stability plus superior corrosion resistant characteristics (Chen and Holt-Hindle, 2010; Huang *et al*., 2011). The catalytic properties of Pt make it suitable for making energy conversion devices like fuel cells which have the potential to meet the rising energy demands. Pt is also used in the making of sensors and in automotive, petroleum, and pharmaceutical industries. The new and improving applications of Pt demand for an increase in its production which its natural reserves cannot support. In an effort to decrease costs, there has been a resurgent research interests to synthesize Pt crystals with controlled size and shape which can in turn improve its properties and efficiency in its applications (Long *et al*., 2010).

Diverse fabrication methods have been developed but here we focus on solution synthesis routs that involve the reduction or decomposition of metal precursors, the manipulation of reaction conditions and the use of organic capping agents to tailor morphology (Chen and Holt-Hindle, 2010; Song *et al*., 2004). Ultimately, nucleation and growth of crystals is governed by kinetic and thermodynamic parameters. Pt crystals have a face-centered cubic (*fcc*) symmetry and their crystal planes possess different surface energies (Tao *et al*., 2008). To minimize the surface energy of the crystals and the total excess free energy of the system, Pt nanocrystals are commonly

bound by low-index crystal planes; three common ones are {111}, {100} and {110} planes (written in order from the plane with the lowest to the plane with the highest surface energy among the three) (Peng and Yang, 2009; Tao *et al*., 2008). Morphologies of single crystalline Pt include cubic, tetrahedron, octahedron and their truncated forms (Figure 1.5), however, the crystal symmetry can be broken down by defects resulting in other shapes with reduced symmetry for example hexagonal plates, triangular plates, nanorods, planer tripods and multipods (Peng and Yang, 2009; Song *et al*., 2004; Tao *et al*., 2008).

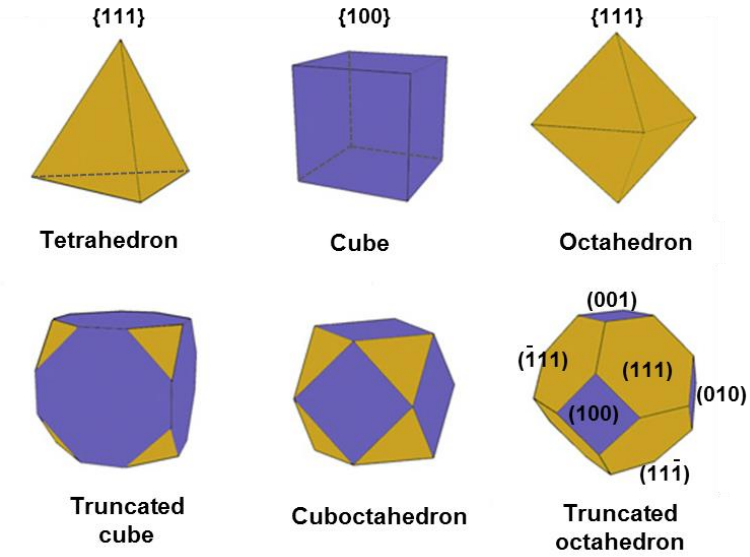

Figure 1.5. Models of Pt nanoparticles showing common single crystalline polyhedral morphologies formed without defects. Illustration was adapted from Peng and Yang, 2009.

1.3.4. Studies on Interactions between Platinum and Platinum Binding Peptides

In Pt synthesis, greener synthesis routes that avoid rigorous reaction conditions have also been explored using biomolecules including proteins, DNA and RNA (Li *et al*., 2009). For example, the organized protein structure of recombinant tobacco mosaic virus (TMV) has been used to seed the growth of size controlled Pt nanocrystals and peptide sequences identified using the phage display technique are being explored as stabilizing agents in Pt synthesis reactions (Bassindale *et al*., 2007; Dujardin *et al*., 2002; Li *et al*., 2009; Chiu *et al*., 2011). More quantitative data is being pursued to understand the molecular mechanisms of the interactions between specific crystallographic planes of Pt and peptides. As previously mentioned, Sarikaya and co-

workers published on experimental studies and preliminary computational approaches to understand the nature of Pt nanocrystal interaction with Pt-binding peptides (Oren *et al*., 2005). They concluded that interaction took place *via* physical recognition of surface features of Pt by the peptide and that the strength of the interaction was determined by the reactive groups of the peptide (Oren *et al*., 2005). The same research group later selected one of the strong Pt-binding peptide sequences (PTSTGQA) and its originally phage isolated cyclic form (CPTSTGQAC) form for further analysis (Seker *et al*., 2007). Both peptides were synthesized using solid phase peptide synthesis and the cyclic form was constrained using Cyc-Cys disulphide link. Circular dichroism (CD) and surface plasmon resonance (SPR) spectroscopy was used to study conformational properties and adsorption behaviour of the linear and cyclic peptides on Pt thin films. MD simulation was also used to study the conformations of the peptides and identify the structures with the lowest energy minima under vacuum conditions (Seker *et al*., 2007).

From SPR analysis of the adsorption and desorption of different concentrations of the peptides on the Pt thin films, the cyclic peptide exhibited a simple 1:1 (single) Langmuir absorption behaviour while the linear peptide displayed biexponential Langmuir isotherm behaviour. The constrained sequence was found to have higher binding affinity for the Pt substrate than the linearized form (Seker *et al*., 2007). Apart from well-known molecular (hydrogen bonding, electrostatic, hydrophobic, van der Waal) interactions, other more complex interactions that may be involved in the adsorption of a peptide onto a solid surface include surface diffusion and peptide-peptide interactions which can lead to peptide conformational changes and reorganization forming supramolecular self-assembled structures on the solid surface (Sarikaya *et al*., 2004; Seker *et al*., 2007). CD analysis showed that in aqueous conditions, PTSTGQA peptide mainly existed in unstable random coil conformation and polyproline type II secondary structure while cyclic CPTSTGQAC peptide formed random coiled conformation and other non-random secondary structures. In combination with computational analysis, the significance of spatial constraints on the adsorption behaviour of peptides was highlighted. The molecular architecture of a peptide may affect the availability of reactive groups for interaction with the surface and subsequently affects the degree of binding. With further experimentation and understanding, the possibility of using spatial

constraints to control structural features and adsorption strengths of peptides to inorganic materials can be developed as a tailoring strategy in molecular engineering (Seker *et al*., 2007).

In a follow up study, SPR was used to study the adsorption and desorption of linear and constrained forms of 1(single sequence, no repeat) and 3 tandem repeat sequences of CPTSTGQAC peptide and another phage display identified strong Pt binding peptide, CQSVTSTKC onto Pt thin films (Seker *et al*., 2008). The linear tandem repeat did not affect the adsorption behaviour of PTSTGQA peptide but increased the adsorption behaviour of QSVTSTK peptide. The binding affinity of constrained CPTSTGQAC peptide increased compared to its linear form whereas the binding affinity of constrained CQSVTSTKC peptide did not improve compared to its linear form. The authors concluded that the effect of structural constraints and tandem repeats is not universal and not only the amino acids sequence but also its secondary structure, influences the adsorption of the peptides on a surface (Seker *et al*., 2008). In the same study, interactions of gold binding peptides and gold surface thin films were also carried out and in general, high adsorption and low desorption was observed for GEPIs (Seker *et al*., 2008).

Pt-binding peptides have also been used to synthesize Pt nanocrystals with controlled morphology. Li and co-workers (2009) describe a facile method to synthesize size controlled monodisperse Pt nanocrystals with nearly spherical shapes using a Pt-binding peptide; TLHVSSY identified using the phage display technique. The specificity of TLHVSSY peptide interaction to Pt surface was attributed to possible interactions using hydroxyl residues from tyrosine, threonine and serine, polar residues from histidine amino acid and physical recognition of peptide functional groups by the atomic arrangement of Pt on specific crystallographic facets (Li *et al.*, 2009). Whether all the above possible mechanisms are equally important or only one or some are the most important driving factor could not be ascertained. Li and colleagues (2009) also demonstrated that TLHVSSY peptide could be unbound from the Pt surface by lowering the solution pH or by photolysis thereby recovering pure nanocrystals (Li *et al*., 2009). TLHVSSY peptide was later shown to preferentially bind to the {110} plane of platinum but could also adsorb to the {111} and {100} planes. When used in synthesis of Pt at low peptide concentration, tripod structures were formed but at higher

concentrations, spherical structures were attained (Li *et al*., 2010). In another study, a consensus sequence that binds to Pt {100} planes (PWxxQRELSV) where xx can be any random amino acid) was identified using phage display (Forbes *et al*., 2010). Forbes and colleagues (2010) demonstrated the potential of a single peptide, YQPWKTQRELSV to mediate the controlled growth of Pt crystals with variable sizes and shapes (polyhedra, cubes) by altering the precursor used and the metal reduction rate. In all the above studies, Pt nanocrystals synthesized without the material specific binding peptide were aggregated and had a wide size distribution (Forbes *et al*., 2010; Li *et al.*, 2009; Li *et al*., 2010).

Soon after, a study in which the phage display technique was used to identify facet-specific Pt-binding peptide sequences that could be used to selectively shape Pt nanocrystals was reported by the same research group (Chiu *et al*., 2011). Two peptides were identified; TLTTLTN that is a specific binder to the {100} plane of Pt and SSFPQPN that binds specifically to the {111} plane of Pt. The peptides were used in the synthesis of platinum nanocrystals. Pt nanocrystals were also synthesized without any peptide as the control reaction and using TLHVSSY peptide identified by Li and co-workers (2009) to bind to bulk polycrystalline Pt surface. In each synthesis, different morphologies were formed; without peptide aggregated crystals of different size and shapes were formed, with TLTTLTN peptide nanocrystals were predominantly cubic, with SSFPQPN peptide, mainly tetrahedral nanocrystals were formed and with TLHVSSY peptide twinned structures including tripods were present (Figure 1.6). Similar results were obtained even when different Pt precursors and synthetic conditions were used (Chiu *et al*., 2011; Li *et al*., 2010).

The growth process of Pt nanocrystals in the presence of TLTTLTN and SSFPQPN peptides was monitored individually following their Pt synthesis method. Early stage nanocrystals began to grow as truncated octahedrons consisting of eight {111} and six {100} facets. TLTTLTN peptide was reported to recognize and adsorb specifically to Pt {100} planes. The surface energy of Pt {100} planes was therefore lowered limiting crystal growth along ‹100› directions. As a consequence, growth continued on the {111} facet resulting in truncated cubes and finally into cubes with the enlargement of the {100} facet over time (Chiu *et al*., 2011). Conversely, SSFPQPN peptide specifically bound to Pt {111} planes forming tetrahedrons. For both peptides an

optimal concentration was required to achieve more complete cubes and tetrahedrons. A maximum yield of ~ 70% was achieved for the synthesis of cubes with TLTTLTN peptide and the synthesis of tetrahedrons with SSFPQPN peptide. Additionally, post-growth modification of the material morphology was demonstrated by switching between the two peptides in aqueous solution (Chiu *et al*., 2011).

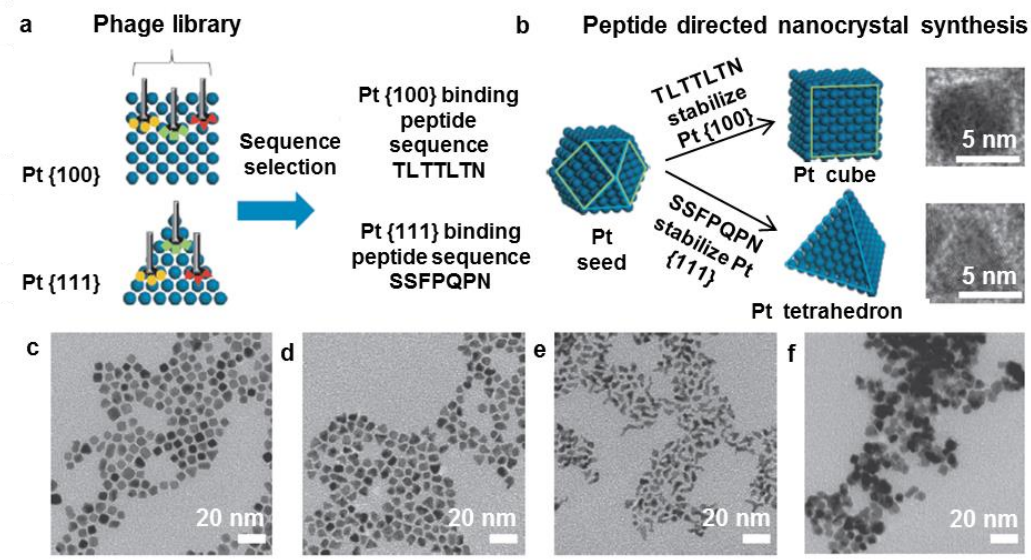

Figure 1.6. Predicted synthesis of Pt nancrystals using a bio-inspired approach; (a) Identification of Pt {100} and {111} facet specific binding peptides using phage display technique, (b) schematic illustration of directed Pt nanocrystal synthesis using facet specific peptides forming cubes using TLTTLTN peptide and tetrahedrons using SSFPQPN peptide. TEM image of the respective Pt structures are also shown, scale bars 5 nm. TEM image of; (c) predominantly Pt nanocubes synthesized using TLTTLTN peptide, (d) predominantly Pt nanotetrahedrons synthesized using SSFPQPN peptide, (e) Pt nanostructures including tripods synthesized using TLHVSSY peptide, (f) TEM image of variable and aggregated Pt nanostructures synthesized without peptide. (c-f) Scale bars, 20 nm. Samples were prepared using the same synthesis protocol and collected after 10 min of reaction. Illustration was adapted from Chiu *et al.*, 2011.

Both TLTTLTN and SSFPQPN peptide are hydroxyl rich peptides similar to other peptides identified to interact with Pt surfaces. The authors suggested that the facet selectivity of the two peptides may be as a result of their unique conformational structures and recognition of surface features of Pt at atomic scales. There was however no clear explanation of their biomolecular specificity (Chiu *et al*., 2011). Ruan and group (2011) further reported on rational design and synthesis of unconventional

twinned Pt nanostructures using TLHVSSY, TLTTLTN and SSFPQPN peptides. Single twinned seeds are generated when synthesis is carried out in the presence of TLHVSSY peptide. Further growth in the presence of TLHVSSY peptide leads to the formation of tripod structures but if the peptide is switched after nucleation, the shapes can be modulated to form right bipyramids in the presence of TLTTLTN peptide and {111} bipyramids with SSFPQPN (Figure 1.7). The concentrations of peptides used and the time of switching from one peptide to another were found to be crucial to attain the highest yield of the desired morphologies (Ruan *et al*., 2011).

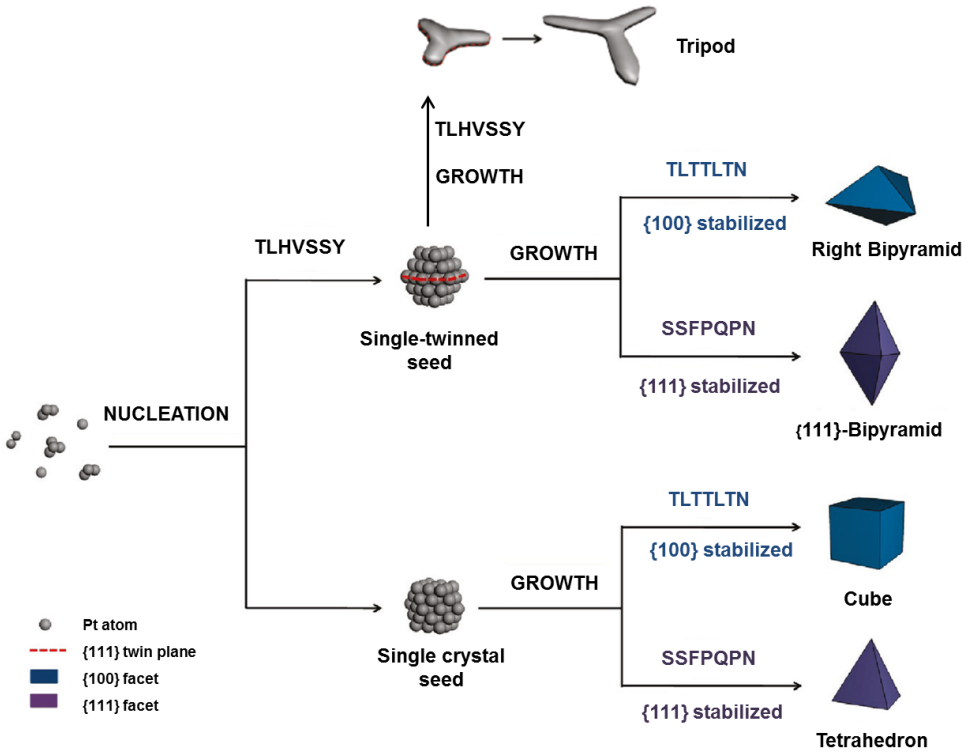

Figure 1.7. Schematic illustrations of designed Pt nanocrsytals shaped by controlling the nucleation and growth of crystals in the presence of Pt-binding peptides. TLHVSSY peptide can be used to synthesize twinned structures by promoting the formation of single-twinned seeds during nucleation. Illustration has been adapted from Ruan *et al.*, 2011.

More recently, Ruan and colleagues (2013) carried out a mechanistic study in an effort to elucidate on the mechanism through which SSFPQPN peptide attains specificity for {111} facets of Pt. Mutants of the peptide designed to individually target factors that may contribute to the peptide's binding specificity (chemical functional groups from

residues *i.e.* hydroxyl, amide and phenyl groups as well as peptide conformational changes) were synthesized and used in the synthesis of Pt nanocrstals. The yield of Pt tetrahedrons normally attained using the original sequence was used as an indicator of loss or retention of the binding specificity. Phenylalanine (F) was identified as the most significant amino acid contributing to the specificity of the peptides for the {111} facet. Growth in the presence of SSFPQPN peptide was compared to growth in the presence of mutant SSGPQPN which was found to be non-specific to Pt {111} plane. In both syntheses, cuboctahedral seeds were present during nucleation but only in later growth stages, tetrahedrons were formed with SSFPQPN peptide which has F residue (Ruan *et al*., 2013). Pt tetrahedrons were attained even when F was placed at different positions in the sequence next to different amino acids. CD analysis showed that in solution all the peptides, original and mutants existed as random coils. The authors suggest that the presence of F is most important for the specificity for Pt {111} facet, more significantly than any conformation/secondary structural changes or modifications of the binding constants or adsorption energies of the original sequence and mutants (Ruan *et al*., 2013).

MD simulations was also carried out to compare the adsorption energies of SSFPQPN peptide and mutants to {100} and {111} planes of Pt using CHARMM-METAL force field. The findings showed that the peptides that form Pt tetrahedrons in synthesis had a disaffinity for the {100} facet through steric hinderance which lead to their preferred adsorption to the {111} facets (Ruan *et al*., 2013). Table 1.3 shows a summary of the properties of the peptide sequences we have so far highlighted that have been identified using PD and have been used in synthesis of Pt crystals and/or adsorption studies with Pt surfaces. All the peptides have at least three amino acids with hydroxyl (-OH) residues from tyrosine (Y), serine (S) and threonine (T) which may impart the affinity of these peptides to Pt surfaces which can interact with oxygen atoms (Li *et al.*, 2009; Ruan *et al*., 2013). SSFPQPN is however the only sequence with an F residue. Ruan and colleagues (2013) demonstrated that replacing F in SSFPQPN peptide with Y forming mutant SSYPQPN, disrupted the perfect hexagonal symmetry of the phenyl ring with the addition of -OH group interfering with the disaffinity of the peptide for the {100} surface. The affinity towards the Pt {111} facet was therefore lost. The significant role of the phenyl ring in F amino acid was further verified by mutating Pt-

binding peptides that are not specific to Pt {111} facets by incorporating F in the sequence *i.e.* PTSPGQA peptide was mutated to PTSTFQA tuning it to become facet specific. When PTSTFQA was used in Pt synthesis, the yield of tetrahedral shaped crystals was increased significantly. These studies and findings are significant progressions in the programmable and predictable design of materials using biomolecules.

Table 1.3. Properties of some PD identified Pt binding peptides used in Pt synthesis and adsorption experiments.

Pt Binding Peptides	Pt Targets	[a] pI (pH unit)	Non-polar no charge	Polar no charge	Polar +ve charge	Polar –ve charge
[b] **CPTSTGQAC**	Nanocrystals	5.18	PGA	C**TST**QC	-	-
[b] **PTSTGQA**		6.01	PGA	**TST**Q	-	-
[b] **CQSVTSTKC**		8.29	V	CQ**STST**C	K	-
[b] **QSVTSTK**		10.1	V	Q**STST**	K	-
[c] **TLHVSSY**	Nanowires	7.76	LV	**TSSY**	H	-
[d] **YQPWKTQRELSV**	Nanocubes	9.72	PWLV	**Y**Q**T**Q**S**	KR	E
[e] **TLTTLTN**	cube {100}	6.01	LL	**TTTT**N	-	-
[e] **SSFPQPN**	tetrahedons {111}	6.01	FPP	SSQN	-	-

[a] Isoelectric point (pI) was calculated using peptide property calculator Innovagen. References; [b] (Oren *et al*., 2005), [c] (Li *et al*., 2009), [d] (Forbes *et al*., 2010), [e] (Chiu *et al*., 2011).

1.4. Peptide-Inorganic Interfaces: Thermodynamics and Kinetics

Studying interfacial interactions between proteins/peptides and surfaces is not only relevant in materials science but is also important in biotechnology and biomedical research especially for implantable devices and in the design of drug delivery carriers like gold nanoparticles (Gray, 2004; Mahmoudi *et al*., 2011; Lindman *et al*., 2007; Paciotti *et al*., 2004). The exact nature of the interactions between inorganic materials and proteins/peptides remains largely elusive and there is a need to qualitatively measure, understand and predict the interaction mechanisms.

While it may be easy to conceptualize general trends of interaction like charge-charge interactions, in reality the interaction is complex in nature, driven by the occurrence of numerous simultaneous contributions (Raut *et al.*, 2005; Sigal *et al.*, 1998). Overall, peptide adsorption on inorganic surfaces is influenced by three main factors: (i) the

intrinsic properties of the peptide, (ii) the physico-chemical properties of the inorganic surface and (iii) the media/environment where the interaction takes place. Interaction may occur through specific counterparts (reactive groups) that allow only certain peptide sequences to interact specifically with certain inorganic surfaces and not others as demonstrated using the phage display technique. The inherent characteristics of the peptide sequence that may play a role in determining whether an interaction takes place with a substrate are mainly its charge, hydropathy and conformation. The overall net charge of the peptide mainly influences the occurrence of electrostatic interactions or repulsion with a surface that may also be charged. Many studies have attributed electrostatic interactions as the principle driving force behind peptide-inorganic interactions (Lynch and Dawson, 2008; Chen *et al*., 2011). However, other non-covalent interactions such as hydrophilic or hydrophobic interactions, van der Waals forces and hydrogen bonding between peptides and a surface are equally significant and may singlehandedly drive interactions in conditions where peptides have no net charge or even under repulsive charge conditions (Lynch and Dawson, 2008; Rezwan *et al*., 2005; Puddu and Perry, 2012). The question of whether peptides adsorb as an ensemble or as individual molecules also needs to be investigated (Rabe *et al*., 2011; Sarikaya *et al*., 2004; Seker *et al*., 2007). The conditions in which the interaction takes place greatly impact on the kinetics and the thermodynamics of the interaction. Factors like the reaction temperature, pH and concentration of other species present in the media besides the peptide and the target and their possible non-specific interactions with the target surface and the peptide need to be considered (Yokoo *et al*., 2010; Rabe *et al*., 2011). The media influences the conformation and stability of the peptide which may structure itself depending on its properties, mainly the hydropathy of individual amino acids and/or the specific alignment of amino acids in the sequence relative to the polarity of the media. The overall binding activity of the peptide against a surface may therefore depend on a contribution from various chemical and physical parameters (Sarikaya *et al*., 2004; Seker *et al*., 2008). Ultimately, the interaction may be reversible or irreversible attained through a contribution from many weak interactions. Hence, some questions that need to be explored in a study of peptide-inorganic interactions include;

(i) What are the intrinsic properties of the peptide sequence and what are the differences between the free and bound states of the peptide?

(ii) What are the surface properties of the inorganic material in solution (media) and what changes take place on the surface before a peptide molecule adsorbs onto it?

(iii) Which forces drive the interaction between a specific peptide and an inorganic material, what is the strength and reversibility of the interaction and how do these interactions modify the energy barriers at the peptide-inorganic interface eventually leading to morphology modification of inorganic materials?

In the process of biomineralization, it is believed that biomolecules control mineral formation by modification of the energy barriers at the interface (Chiu *et al*., 2013; Whyburn *et al*., 2008). We have discussed the role of artificial peptides as additives in the synthesis of inorganic materials and their ability to modify crystal morphology plausibly by altering the materials surface energy and direction of crystal growth. Understanding the energetic/thermodynamic changes that occur at the interface during peptide-inorganic interactions and correlating these to structural modifications of the inorganic materials could be the key to advancing material synthesis and design and may reveal key principles through which material structure is controlled in nature (Cedervall *et al*., 2007; Perry *et al*., 2009; Whyburn *et al.*, 2008).

Conventional techniques that have been used to study peptide adsorption onto inorganic surfaces and their interfacial interaction include: surface plasmon resonance spectroscopy (SPR), quartz crystal microbalance with dissipation monitoring (QCM-D), ellipsometry, X-ray photoelectron spectroscopy (XPS), circular dichroism spectroscopy (CD), nuclear magnetic resonance (NMR), fourier transform infrared spectroscopy (FTIR), surface enhanced Raman spectroscopy (SERS), atomic force microscopy (AFM), Ultraviolet-visible (UV-Vis) spectroscopy, analytical ultracentrifugation (AUC), optical waveguide lightmode spectroscopy (OWLS), sum-frequency generation (SFG), stopped-flow and radioligand binding assays, fluorescence microscopy. Some of these techniques can be used to measure binding constants but require a series of experiments at different concentrations and temperatures before thermodynamic parameters can be determined using van't Hoff equations (Ababou and Ladbury, 2006; Chiad *et al*., 2009; Chiu *et al*., 2013; Seker *et al*., 2008; Thyparambil *et al*., 2012). More recently, isothermal titration calorimetry (ITC) has been applied to probe peptide-

surface interactions (Cho *et al*., 2011; Goobes *et al*. 2007). All of the above mentioned techniques have their unique advantages and drawbacks but isothermal titration calorimetry (ITC) stands out as it does not require labelling or immobilization of the interacting components but more significantly, it is able to determine all thermodynamic parameters (enthalpy change (ΔH), entropy change (ΔS), adsorption constant (K_A) and change in Gibbs free energy (ΔG)) of interaction from one experiment and is the only direct measure of molar enthalpy, (Ababou and Ladbury, 2006; Chiad *et al*., 2009; Cliff *et al*., 2004). These features make it superior to the other techniques. However, the use of ITC to study peptide inorganic interactions is in its infancy. To date, there are very few reported studies on peptide-inorganic interaction using ITC and this approach has its challenges which will be elaborated on.

1.5. Project Aims and Objectives

This study seeked to attain a fundamental, detailed understanding of how nature's molecular tools work by probing interactions between inorganic materials, ZnO and Pt and their specific binding peptides identified using phage display technique. ZnO was synthesized in the absence and presence of peptides and the growth process was monitored over time to understand the mechanisms through which peptides are able to interact with and in some instances control the morphology of inorganic materials. Computational tools were used to study the peptides *i.e.* alanine mutants of a ZnO binding peptide were studied from which a selection was made for experimental studies with an aim of comparing and correlating the findings. Inorganic materials and peptides were extensively characterized and their interactions monitored using biophysical tools ITC and QCM-D to determine the energetics of interaction and to characterize their adsorption behaviour. By probing the interfacial energy changes that take place during peptide-inorganic interactions we undertook not only to identify the forces driving interfacial interactions but also to understand why and how these interactions occur and their effect on material structural formation to a level where control/manipulation can be achieved, mastered and exploited.

The end goal is to understand the interactions that take place between inorganic materials and peptides at a molecular level and to use the knowledge to identify guiding principles that can be used to predict interactions between peptides and a vast number of inorganic materials including synthetic nanoscale constructs/hybrid functional materials without the need for extensive laborious experimentation of each system. Ultimately, full exploitation of all known elements and the control of materials structure for novel applications may be achieved.

1.6. References

1. Ababou, A., and Ladbury, J.E., 2006. Survey of the year 2004: literature on applications of isothermal titration calorimetry. *Journal of Molecular Recognition: JMR,* 19 (1), 79-89.
2. Adair, J.H., and Suvaci, E., 2000. Morphological control of particles. *Current Opinion in Colloid and Interface Science,* 5 (1–2), 160-167.
3. Addadi, L., Joester, D., Nudelman, F. and Weiner, S., 2006. Mollusk shell formation: a source of new concepts for understanding biomineralization processes. *Chemistry-A European Journal,* 12 (4), 980-987.
4. Ahmad, M., and Zhu, J., 2011. ZnO based advanced functional nanostructures: synthesis, properties and applications. *Journal of Materials Chemistry,* 21 (3), 599-614.
5. Amrani, B., Chiboub, I., Hiadsi, S., Benmessabih, T. and Hamdadou, N., 2006. Structural and electronic properties of ZnO under high pressures. *Solid State Communications,* 137 (7), 395-399.
6. Amstutz, P., Forrer, P., Zahnd, C. and Plückthun, A., 2001. In vitro display technologies: novel developments and applications. *Current Opinion in Biotechnology,* 12 (4), 400-405.
7. Anastas, P.T., and Warner, J.C., 2000. *Green chemistry: theory and practice.* Oxford University Press.
8. Attwood, T.K., 2000. The Babel of bioinformatics. *Science,* 290 (5491), 471-473.
9. Baeuerlein, E., Behrens, P., Epple, M., Pickett-Heaps, J., Mann, S. and Pompe, W., 2007. *Handbook of Biomineralization: Biomimetic and bioinspired chemistry.* Wiley-VCH Verlag.
10. Bai, H., Xu, F., Anjia, L. and Matsui, H., 2009. Low temperature synthesis of ZnO nanowires by using a genetically-modified collagen-like triple helix as a catalytic template. *Soft Matter,* 5 (5), 966-969.
11. Baier, J., Naumburg, T., Blumenstein, N.J., Jeurgens, L.P., Welzel, U., Do, T.A., Pleiss, J. and Bill, J., 2012. Bio-inspired mineralization of zinc oxide in presence of ZnO-binding peptides. *Biointerface Research in Applied Chemistry*, 2 (4), 380 - 391.
12. Barthelat, F., 2007. Biomimetics for next generation materials. *Philosophical Transactions of the Royal Society A: Mathematical, Physical and Engineering Sciences,* 365 (1861), 2907-2919.
13. Baruah, S., and Dutta, J., 2009. Hydrothermal growth of ZnO nanostructures. *Science and Technology of Advanced Materials,* 10 (1), 013001.
14. Bassindale, A.R., Codina-Barrios, A., Frascione, N. and Taylor, P.G., 2007. An improved phage display methodology for inorganic nanoparticle fabrication. *Chemical Communications,* (28), 2956-2958.
15. Bazylinski, D.A., Frankel, R.B., Heywood, B.R., Mann, S., King, J.W., Donaghay, P.L. and Hanson, A.K., 1995. Controlled Biomineralization of Magnetite (Fe (inf3) O (inf4)) and Greigite (Fe (inf3) S (inf4)) in a Magnetotactic Bacterium. *Applied and Environmental Microbiology,* 61 (9), 3232-3239.
16. Behler J. Group website, 2010. *A Neural Network Potential for Zinc Oxide*. Theoretische Chemie, Ruhr-Universität Bochum, Germany. Accessed online at http://www.theochem.ruhr-uni-bochum.de/~joerg.behler/zno.htm [10/10 2014].
17. Bensaude-Vincent, B., Arribart, H., Bouligand, Y. and Sanchez, C., 2002. Chemists and the school of nature. *New Journal of Chemistry,* 26 (1), 1-5.
18. Berg, J.M., and Godwin, H.A., 1997. Lessons from zinc-binding peptides. *Annual Review of Biophysics and Biomolecular Structure,* 26 (1), 357-371.
19. Bermudez, H., and Hathorne, A.P., 2008. Incorporating stimulus-responsive character into filamentous virus assemblies. *Faraday Discussions,* 139, 327-335.
20. Bhandari, R., Coppage, R. and Knecht, M.R., 2012. Mimicking nature's strategies for the design of nanocatalysts. *Catalysis Science & Technology,* 2 (2), 256-266.

21. Biezma, M.V., and Schanack, F., 2007. Collapse of steel bridges. *Journal of Performance of Constructed Facilities*, 21 (5), 398-405.

22. Biswas, A.K., 1987. Rasa-Ratna-Samuccaya and mineral processing state-of-art in the 13th Century AD India. *Indian Journal of History of Science*, 22 (1), 29-46.

23. Blankschien, M.D., Pretzer, L.A., Huschka, R., Halas, N.J., Gonzalez, R. and Wong, M.S., 2012. Light-Triggered Biocatalysis Using Thermophilic Enzyme–Gold Nanoparticle Complexes. *ACS Nano*, 7 (1), 654-663.

24. Branden, C., and Tooze, J., 1991. *Introduction to protein structure*. Garland New York.

25. Briggs, B.D., and Knecht, M.R., 2012. Nanotechnology meets biology: Peptide-based methods for the fabrication of functional materials. *J.Phys.Chem.Lett*, 3 (3), 405-418.

26. Brown, S., Sarikaya, M. and Johnson, E., 2000. A genetic analysis of crystal growth. *Journal of Molecular Biology*, 299 (3), 725-735.

27. Bunn, C., 1935. The lattice-dimensions of zinc oxide. *Proceedings of the Physical Society*, 47 (5), 835.

28. Cedervall, T., Lynch, I., Lindman, S., Berggard, T., Thulin, E., Nilsson, H., Dawson, K.A. and Linse, S., 2007. Understanding the nanoparticle-protein corona using methods to quantify exchange rates and affinities of proteins for nanoparticles. *Proceedings of the National Academy of Sciences of the United States of America*, 104 (7), 2050-2055.

29. Chen, A., and Holt-Hindle, P., 2010. Platinum-based nanostructured materials: synthesis, properties, and applications. *Chem.Rev*, 110 (6), 3767-3804.

30. Chen, H., Su, X., Neoh, K. and Choe, W., 2008. Probing the interaction between peptides and metal oxides using point mutants of a TiO2-binding peptide. *Langmuir*, 24 (13), 6852-6857.

31. Chen, K., Xu, Y., Rana, S., Miranda, O.R., Dubin, P.L., Rotello, V.M., Sun, L. and Guo, X., 2011. Electrostatic selectivity in protein–nanoparticle interactions. *Biomacromolecules*, 12 (7), 2552-2561.

32. Chiad, K., Stelzig, S.H., Gropeanu, R., Weil, T., Klapper, M. and Muİˆllen, K., 2009. Isothermal Titration Calorimetry: A Powerful Technique to Quantify Interactions in Polymer Hybrid Systems. *Macromolecules*, 42 (19), 7545-7552.

33. Chiu, C.Y., Li, Y., Ruan, L., Ye, X., Murray, C.B. and Huang, Y., 2011. Platinum nanocrystals selectively shaped using facet-specific peptide sequences. *Nature Chemistry*, 3 (5), 393-399.

34. Chiu, C., Li, Y. and Huang, Y., 2010. Size-controlled synthesis of Pd nanocrystals using a specific multifunctional peptide. *Nanoscale*, 2 (6), 927-930.

35. Chiu, C., Ruan, L. and Huang, Y., 2013. Biomolecular specificity controlled nanomaterial synthesis. *Chemical Society Reviews*, 42, 2512 - 2527.

36. Cho, N., Cheong, T., Min, J.H., Wu, J.H., Lee, S.J., Kim, D., Yang, J., Kim, S., Kim, Y.K. and Seong, S., 2011. A multifunctional core-shell nanoparticle for dendritic cell-based cancer immunotherapy. *Nature Nanotechnology*, 6 (10), 675-682.

37. Cliff, M.J., Gutierrez, A. and Ladbury, J.E., 2004. A survey of the year 2003 literature on applications of isothermal titration calorimetry. *Journal of Molecular Recognition: JMR*, 17 (6), 513-523.

38. Coppage, R., Slocik, J.M., Ramezani-Dakhel, H., Bedford, N.M., Heinz, H., Naik, R.R. and Knecht, M.R., 2013. Exploiting Localized Surface Binding Effects to Enhance the Catalytic Reactivity of Peptide-Capped Nanoparticles. *Journal of the American Chemical Society*, 135 (30), 11048-11054.

39. Daniel, M.C., and Astruc, D., 2004. Gold nanoparticles: Assembly, supramolecular chemistry, quantum-size-related properties, and applications toward biology, catalysis, and nanotechnology. *Chemical Reviews*, 104 (1), 293-346.

40. Davis, S.A., Dujardin, E. and Mann, S., 2003. Biomolecular inorganic materials chemistry. *Current Opinion in Solid State and Materials Science*, 7 (4), 273-281.

41. De la Rica, R., and Matsui, H., 2010. Applications of peptide and protein-based materials in bionanotechnology. *Chemical Society Reviews,* 39 (9), 3499-3509.

42. Di Felice, R., and Corni, S., 2011. Simulation of peptide–surface recognition. *The Journal of Physical Chemistry Letters,* 2 (13), 1510-1519.

43. Dickerson, M.B., Jones, S.E., Cai, Y., Ahmad, G., Naik, R.R., Kröger, N. and Sandhage, K.H., 2008. Identification and design of peptides for the rapid, high-yield formation of nanoparticulate TiO2 from aqueous solutions at room temperature. *Chemistry of Materials,* 20 (4), 1578-1584.

44. Dickerson, M.B., Naik, R.R., Stone, M.O., Cai, Y. and Sandhage, K.H., 2004. Identification of peptides that promote the rapid precipitation of germania nanoparticle networks *via* use of a peptide display library. *Chem. Commun.,* (15), 1776-1777.

45. Dickerson, M.B., Sandhage, K.H. and Naik, R.R., 2008. Protein-and peptide-directed syntheses of inorganic materials. *Chemical Reviews,* 108 (11), 4935-4978.

46. Djurišić, A.B., Ng, A.M.C. and Chen, X.Y., 2010. ZnO nanostructures for optoelectronics: Material properties and device applications. *Progress in Quantum Electronics,* 34 (4), 191-259.

47. Dove, P., M, De Yereo, J., J. and Weiner, S., 2003. 54th ed. Washington DC 20036 U.S.A.: Minerology Scociety of America geochemical Society.

48. Dudev, T., and Lim, C., 2003. Principles governing Mg, Ca, and Zn binding and selectivity in proteins. *Chemical Reviews,* 103 (3), 773-788.

49. Dujardin, E., and Mann, S., 2002. Bio-inspired materials chemistry. *Advanced Materials,* 14 (11), 775.

50. Eteshola, E., Brillson, L.J. and Lee, S.C., 2005. Selection and characteristics of peptides that bind thermally grown silicon dioxide films. *Biomolecular Engineering,* 22 (5), 201-204.

51. Evans, J.S., Samudrala, R., Walsh, T.R., Oren, E.E. and Tamerler, C., 2008. Molecular design of inorganic-binding polypeptides. *MRS Bulletin,* 33 (05), 514-518.

52. Fahlman, B.D., 2011. *What is Materials Chemistry?* Springer.

53. Fan, Z., and Lu, J.G., 2005. Zinc oxide nanostructures: synthesis and properties. *Journal of Nanoscience and Nanotechnology,* 5 (10), 1561-1573.

54. Fang, Y., Poulsen, N., Dickerson, M.B., Cai, Y., Jones, S.E., Naik, R.R., Kröger, N. and Sandhage, K.H., 2008. Identification of peptides capable of inducing the formation of titania but not silica *via* a subtractive bacteriophage display approach. *Journal of Materials Chemistry,* 18 (32), 3871-3875.

55. Feng, J., Pandey, R.B., Berry, R.J., Farmer, B.L., Naik, R.R. and Heinz, H., 2011. Adsorption mechanism of single amino acid and surfactant molecules to Au {111} surfaces in aqueous solution: design rules for metal-binding molecules. *Soft Matter,* 7 (5), 2113-2120.

56. Feng, L., Li, S., Li, Y., Li, H., Zhang, L., Zhai, J., Song, Y., Liu, B., Jiang, L. and Zhu, D., 2002. Super-Hydrophobic Surfaces: From Natural to Artificial. *Advanced Materials,* 14 (24), 1857-1860.

57. Forbes, L.M., Goodwin, A.P. and Cha, J.N., 2010. Tunable size and shape control of platinum nanocrystals from a single peptide sequence. *Chemistry of Materials,* 22 (24), 6524-6528.

58. Galloway, J.M., and Staniland, S.S., 2012. Protein and peptide biotemplated metal and metal oxide nanoparticles and their patterning onto surfaces. *Journal of Materials Chemistry,* 22 (25), 12423-12434.

59. Garcia, S.P., and Semancik, S., 2007. Controlling the morphology of zinc oxide nanorods crystallized from aqueous solutions: The effect of crystal growth modifiers on aspect ratio. *Chemistry of Materials,* 19 (16), 4016-4022.

60. Ghiringhelli, L.M., Hess, B., van der Vegt, Nico FA and Delle Site, L., 2008. Competing adsorption between hydrated peptides and water onto metal surfaces: from electronic to conformational properties. *Journal of the American Chemical Society,* 130 (40), 13460-13464.

61. Ghosh, P., Han, G., De, M., Kim, C.K. and Rotello, V.M., 2008. Gold nanoparticles in delivery applications. *Advanced Drug Delivery Reviews,* 60 (11), 1307-1315.

62. Gogolides, E., Constantoudis, V., Kokkoris, G., Kontziampasis, D., Tsougeni, K., Boulousis, G., Vlachopoulou, M. and Tserepi, A., 2011. Controlling roughness: from etching to nanotexturing and plasma-directed organization on organic and inorganic materials. *Journal of Physics D: Applied Physics,* 44 (17), 174021.

63. Goobes, R., Goobes, G., Shaw, W.J., Drobny, G.P., Campbell, C.T. and Stayton, P.S., 2007. Thermodynamic roles of basic amino acids in statherin recognition of hydroxyapatite. *Biochemistry,* 46 (16), 4725-4733.

64. Gotliv, B., Kessler, N., Sumerel, J.L., Morse, D.E., Tuross, N., Addadi, L. and Weiner, S., 2005. Asprich: A novel aspartic acid-rich protein family from the prismatic shell matrix of the bivalve Atrina rigida. *Chembiochem,* 6 (2), 304-314.

65. Gourishankar, A., Shukla, S., Ganesh, K.N. and Sastry, M., 2004. Isothermal titration calorimetry studies on the binding of DNA bases and PNA base monomers to gold nanoparticles. *Journal of the American Chemical Society,* 126 (41), 13186-13187.

66. Govender, K., Boyle, D., S., Kenway, P., B. and O'Brien, P., 2004. Understanding the factors that govern the deposition and morphology of thin films of ZnO from aqueous solution. *Journal of Materials Chemistry,* 14, 2575-2591.

67. Graf, P., Mantion, A., Foelske, A., Shkilnyy, A., Mašić, A., Thünemann, A.F. and Taubert, A., 2009. Peptide-Coated Silver Nanoparticles: Synthesis, Surface Chemistry, and pH-Triggered, Reversible Assembly into Particle Assemblies. *Chemistry-A European Journal,* 15 (23), 5831-5844.

68. Gray, J.J., 2004. The interaction of proteins with solid surfaces. *Current Opinion in Structural Biology,* 14 (1), 110-115.

69. Grossfield, A., Ren, P. and Ponder, J.W., 2003. Ion solvation thermodynamics from simulation with a polarizable force field. *Journal of the American Chemical Society,* 125 (50), 15671-15682.

70. Grünberg, K., Müller, E., Otto, A., Reszka, R., Linder, D., Kube, M., Reinhardt, R. and Schüler, D., 2004. Biochemical and proteomic analysis of the magnetosome membrane in Magnetospirillum gryphiswaldense. *Applied and Environmental Microbiology,* 70 (2), 1040-1050.

71. Guo, S., and Wang, E., 2007. Synthesis and electrochemical applications of gold nanoparticles. *Analytica Chimica Acta,* 598 (2), 181-192.

72. Halioua, B., 2005. *Medicine in the Days of the Pharaohs.* Harvard University Press.

73. Hansson, T., Oostenbrink, C. and van Gunsteren, W., 2002. Molecular dynamics simulations. *Current Opinion in Structural Biology,* 12 (2), 190-196.

74. Heinz, H., Farmer, B.L., Pandey, R.B., Slocik, J.M., Patnaik, S.S., Pachter, R. and Naik, R.R., 2009. Nature of Molecular Interactions of Peptides with Gold, Palladium, and Pd− Au Bimetal Surfaces in Aqueous Solution. *Journal of the American Chemical Society,* 131 (28), 9704-9714.

75. Hirai, T., Harada, Y., Hashimoto, S., Itoh, T. and Ohno, N., 2005. Luminescence of excitons in mesoscopic ZnO particles. *Journal of Luminescence,* 112 (1–4), 196-199.

76. Huang, R., Wen, Y., Zhu, Z. and Sun, S., 2011. Structure and stability of platinum nanocrystals: from low-index to high-index facets. *Journal of Materials Chemistry,* 21 (31), 11578-11584.

77. Huang, Y., Chiang, C., Lee, S.K., Gao, Y., Hu, E.L., Yoreo, J.D. and Belcher, A.M., 2005. Programmable assembly of nanoarchitectures using genetically engineered viruses. *Nano Letters,* 5 (7), 1429-1434.

78. Huang, A., and Caro, J., 2010. Controlled growth of zinc oxide crystals with tunable shape. *Journal of Crystal Growth,* 312 (7), 947-952.

79. Huang, H.Z., and Yang, X.R., 2004. Synthesis of polysaccharide-stabilized gold and silver nanoparticles: a green method. *Carbohydrate Research,* 339 (15), 2627-2631.

80. Iori, F., Di Felice, R., Molinari, E. and Corni, S., 2009. GolP: An atomistic force-field to describe the interaction of proteins with Au (111) surfaces in water. *Journal of Computational Chemistry,* 30 (9), 1465-1476.

81. Jagadish, C., and Pearton, S.J., 2011. *Zinc oxide bulk, thin films and nanostructures: processing, properties, and applications.* Elsevier.

82. Kaplan, D.L., 1998. Mollusc shell structures: novel design strategies for synthetic materials. *Current Opinion in Solid State and Materials Science,* 3 (3), 232-236.

83. Karplus, M., and McCammon, J.A., 2002. Molecular dynamics simulations of biomolecules. *Nature Structural & Molecular Biology,* 9 (9), 646-652.

84. Kim, J., Rheem, Y., Yoo, B., Chong, Y., Bozhilov, K.N., Kim, D., Sadowsky, M.J., Hur, H. and Myung, N.V., 2010. Peptide-mediated shape-and size-tunable synthesis of gold nanostructures. *Acta Biomaterialia,* 6 (7), 2681-2689.

85. Kinoshita, S., Yoshioka, S. and Kawagoe, K., 2002. Mechanisms of structural colour in the Morpho butterfly: cooperation of regularity and irregularity in an iridescent scale. *Proceedings of the Royal Society of London.Series B: Biological Sciences,* 269 (1499), 1417-1421.

86. Klingshirn, C., Hauschild, R., Priller, H., Decker, M., Zeller, J. and Kalt, H., 2005. ZnO rediscovered—once again!? *Superlattices and Microstructures,* 38 (4), 209-222.

87. Klingshirn, C., 2007. ZnO: material, physics and applications. *Chemphyschem,* 8 (6), 782-803.

88. Kriplani, U., and Kay, B.K., 2005. Selecting peptides for use in nanoscale materials using phage-displayed combinatorial peptide libraries. *Current Opinion in Biotechnology,* 16 (4), 470-475.

89. Kröger, N., Deutzmann, R. and Sumper, M., 1999. Polycationic Peptides from Diatom Biosilica That Direct Silica Nanosphere Formation. *Science,* 286 (5442), 1129-1132.

90. Kröger, N., and Sandhage, K.H., 2010. From diatom biomolecules to bioinspired syntheses of silica-and titania-based materials. *MRS Bulletin,* 35 (02), 122-126.

91. Leach, A.R., and Schomburg, D., 1996. *Molecular modelling: principles and applications.* Longman London.

92. Lehn, J.M., 2002. Toward complex matter: supramolecular chemistry and self-organization. *Proceedings of the National Academy of Sciences of the United States of America,* 99 (8), 4763-4768.

93. Li, Y., and Huang, Y., 2010. Morphology-Controlled Synthesis of Platinum Nanocrystals with Specific Peptides. *Advanced Materials,* 22 (17), 1921-1925.

94. Li, L., Zhai, T., Bando, Y. and Golberg, D., 2012. Recent progress of one-dimensional ZnO nanostructured solar cells. *Nano Energy,* 1 (1), 91-106.

95. Li, Y., Whyburn, G.P. and Huang, Y., 2009. Specific Peptide Regulated Synthesis of Ultrasmall Platinum Nanocrystals. *Journal of the American Chemical Society,* 131 (44), 15998- 15999.

96. Liang, M., Deschaume, O., Patwardhan, S.V. and Perry, C.C., 2011. Direct evidence of ZnO morphology modification *via* the selective adsorption of ZnO-binding peptides. *Journal of Materials Chemistry,* 21 (1), 80-89.

97. Lindman, S., Lynch, I., Thulin, E., Nilsson, H., Dawson, K.A. and Linse, S., 2007. Systematic investigation of the thermodynamics of HSA adsorption to N-iso-propylacrylamide/N-tert-butylacrylamide copolymer nanoparticles. Effects of particle size and hydrophobicity. *Nano Letters,* 7 (4), 914-920.

98. Liu, K., and Jiang, L., 2011. Bio-inspired design of multiscale structures for function integration. *Nano Today,* 6 (2), 155-175.

99. Long N.V., Hayakawa T., Lakshminarayana G., Nogami M., Chien N.D. and Hirata H., 2010. The synthesis and characterization of platinum nanoparticles: A method of controlling the size and morphology. *Nanotechnology Nanotechnology,* 21 (3), 305605.

100. Lowenstam, H., 1962. Goethite in radular teeth of recent marine gastropods. *Science,* 137 (3526), 279-280.

101. Lynch, I., and Dawson, K.A., 2008. Protein-nanoparticle interactions. *Nano Today,* 3 (1), 40-47.

102. Mahmoudi, M., Lynch, I., Ejtehadi, M.R., Monopoli, M.P., Bombelli, F.B. and Laurent, S., 2011. Protein− nanoparticle interactions: opportunities and challenges. *Chemical Reviews,* 111 (9), 5610-5637.

103. Mann, S., Perry, C., Webb, J., Luke, B. and Williams, R., 1986. Structure, morphology, composition and organization of biogenic minerals in limpet teeth. *Proceedings of the Royal Society of London.Series B, Biological Sciences,* 179-190.

104. Mann, S., Perry, C.C., Williams, R.J., Fyfe, C.A., Gobbi, G.C. and Kennedy, G.J., 1983. The characterisation of the nature of silica in biological systems. *Journal of the Chemical Society, Chemical Communications,* (4), 168-170.

105. Maret, W., and Li, Y., 2009. Coordination dynamics of zinc in proteins. *Chemical Reviews,* 109 (10), 4682-4707.

106. Marin, F., and Luquet, G., 2007. Unusually acidic proteins in biomineralization. *Handbook of Biomineralization: Biological Aspects and Structure Formation,* , 273-290.

107. Marvin, D., 1998. Filamentous phage structure, infection and assembly. *Current Opinion in Structural Biology,* 8 (2), 150-158.

108. Masuda, Y., Kinoshita, N. and Koumoto, K., 2007. Morphology control of ZnO crystalline particles in aqueous solution. *Electrochimica Acta,* 53 (1), 171-174.

109. Matlack, A.S., 2001. *Introduction to green chemistry.* CRC Press.

110. McCamm0n, J.A., 1977. Dynamics of folded proteins. *Nature,* 267, 16.

111. Meyers, S.R., Hamilton, P.T., Walsh, E.B., Kenan, D.J. and Grinstaff, M.W., 2007. Endothelialization of titanium surfaces. *Advanced Materials-Deerfield Beach then Weinheim-,* 19 (18), 2492.

112. Mijatovic, D., Eijkel, J. and Van Den Berg, A., 2005. Technologies for nanofluidic systems: top-down vs. bottom-up—a review. *Lab on a Chip,* 5 (5), 492-500.

113. Moezzi, A., McDonagh, A.M. and Cortie, M.B., 2012. Zinc oxide particles: Synthesis, properties and applications. *Chemical Engineering Journal,* 185–186 (0), 1-22.

114. Müller, W.E., Krasko, A., Le Pennec, G. and Schröder, H.C., 2003. Biochemistry and cell biology of silica formation in sponges. *Microscopy Research and Technique,* 62 (4), 368-377.

115. Naik, R.R., Brott, L.L., Clarson, S.J. and Stone, M.O., 2002. Silica-precipitating peptides isolated from a combinatorial phage display peptide library. *Journal of Nanoscience and Nanotechnology,* 2 (1), 95-100.

116. Naik, R.R., Jones, S.E., Murray, C.J., McAuliffe, J.C., Vaia, R.A. and Stone, M.O., 2004. Peptide Templates for Nanoparticle Synthesis Derived from Polymerase Chain Reaction-Driven Phage Display. *Advanced Functional Materials,* 14 (1), 25-30.

117. Naik, R.R., Stringer, S.J., Agarwal, G., Jones, S.E. and Stone, M.O., 2002. Biomimetic synthesis and patterning of silver nanoparticles. *Nature Materials,* 1 (3), 169-172.

118. Nakajima, N., Nakamura, H. and Kidera, A., 1997. Multicanonical ensemble generated by molecular dynamics simulation for enhanced conformational sampling of peptides. *The Journal of Physical Chemistry B,* 101 (5), 817-824.

119. Nam, K.T., Kim, D., Yoo, P.J., Chiang, C., Meethong, N., Hammond, P.T., Chiang, Y. and Belcher, A.M., 2006. Virus-enabled synthesis and assembly of nanowires for lithium ion battery electrodes. *Science,* 312 (5775), 885-888.

120. Niemeyer, C.M., 2001. Nanoparticles, proteins, and nucleic acids: biotechnology meets materials science. *Angewandte Chemie International Edition,* 40 (22), 4128-4158.

121. Norton, D.P., Heo, Y., Ivill, M., Ip, K., Pearton, S., Chisholm, M.F. and Steiner, T., 2004. ZnO: growth, doping & processing. *Materials Today,* 7 (6), 34-40.

122. Okochi, M., Sugita, T., Furusawa, S., Umetsu, M., Adschiri, T. and Honda, H., 2010. Peptide array-based characterization and design of ZnO-high affinity peptides. *Biotechnology and Bioengineering,* 106 (6), 845-851.

123. Olson, G., 2001. Beyond discovery: design for a new material world. *Calphad,* 25 (2), 175-190.

124. Oren, E.E., Tamerler, C., Sahin, D., Hnilova, M., Seker, U.O.S., Sarikaya, M. and Samudrala, R., 2007. A novel knowledge-based approach to design inorganic-binding peptides. *Bioinformatics,* 23 (21), 2816-2822.

125. Oren, E.E., Tamerler, C. and Sarikaya, M., 2005. Metal recognition of septapeptides *via* polypod molecular architecture. *Nano Letters,* 5 (3), 415-419.

126. Ozgur, U., Hofstetter, D. and Morkoc, H., 2010. ZnO Devices and Applications: A Review of Current Status and Future Prospects. *Proceedings of the IEEE,* 98 (7), 1255-1268.

127. Paciotti, G.F., Myer, L., Weinreich, D., Goia, D., Pavel, N., McLaughlin, R.E. and Tamarkin, L., 2004. Colloidal gold: a novel nanoparticle vector for tumor directed drug delivery. *Drug Delivery,* 11 (3), 169-183.

128. Pandey, R.B., Heinz, H., Feng, J., Farmer, B.L., Slocik, J.M., Drummy, L.F. and Naik, R.R., 2009. Adsorption of peptides (A3, Flg, Pd2, Pd4) on gold and palladium surfaces by a coarse-grained Monte Carlo simulation. *Physical Chemistry Chemical Physics,* 11 (12), 1989-2001.

129. Patwardhan, S.V., Emami, F.S., Berry, R.J., Jones, S.E., Naik, R.R., Deschaume, O., Heinz, H. and Perry, C.C., 2012. Chemistry of aqueous silica nanoparticle surfaces and the mechanism of selective peptide adsorption. *Journal of the American Chemical Society,* 134 (14), 6244-6256.

130. Patwardhan, S., V., Patwardhan, G. and Perry, C., C., 2007. Interactions of biomolecules with inorganic materials: principles, applications and future prospects. *Journal of Materials Chemistry,* 17, 2875-2884.

131. Pearton, S.J., Norton, D.P., Ip, K., Heo, Y.W. and Steiner, T., 2005. Recent progress in processing and properties of ZnO. *Progress in Materials Science,* 50 (3), 293-340.

132. Peng, Y., Xu, A., Deng, B., Antonietti, M. and Cölfen, H., 2006. Polymer-Controlled Crystallization of Zinc Oxide Hexagonal Nanorings and Disks. *The Journal of Physical Chemistry B,* 110 (7), 2988-2993.

133. Peng, Z., and Yang, H., 2009. Designer platinum nanoparticles: Control of shape, composition in alloy, nanostructure and electrocatalytic property. *Nano Today,* 4 (2), 143-164.

134. Perry, C.C., and Keeling-Tucker, T., 2000. Biosilicification: the role of the organic matrix in structure control. *JBIC Journal of Biological Inorganic Chemistry,* 5 (5), 537-550.

135. Perry, C.C., Patwardhan, S.V. and Deschaume, O., 2009. From biominerals to biomaterials: the role of biomolecule-mineral interactions. *Biochemical Society Transactions,* 37, 687-691.

136. Perry, C.C., Williams, R.J.P. and Fry, S.C., 1987. Cell Wall Biosynthesis during Silicification of Grass Hairs. *Journal of Plant Physiology,* 126 (4–5), 437-448.

137. Ponder, J.W., Wu, C., Ren, P., Pande, V.S., Chodera, J.D., Schnieders, M.J., Haque, I., Mobley, D.L., Lambrecht, D.S. and DiStasio Jr, R.A., 2010. Current status of the AMOEBA polarizable force field. *The Journal of Physical Chemistry B,* 114 (8), 2549-2564.

138. Puddu, V., and Perry, C.C., 2012. Peptide Adsorption on Silica Nanoparticles: Evidence of Hydrophobic Interactions. *ACS Nano,* 6 (7), 6356-6363.

139. Rabe, M., Verdes, D. and Seeger, S., 2011. Understanding protein adsorption phenomena at solid surfaces. *Advances in Colloid and Interface Science,* 162 (1), 87-106.

140. Raut, V.P., Agashe, M.A., Stuart, S.J. and Latour, R.A., 2005. Molecular dynamics simulations of peptide-surface interactions. *Langmuir,* 21 (4), 1629-1639.

141. Raveendran, P., Fu, J. and Wallen, S.L., 2003. Completely "green" synthesis and stabilization of metal nanoparticles. *Journal of the American Chemical Society,* 125 (46), 13940-13941.

142. Rezwan, K., Studart, A., Vörös, J. and Gauckler, L., 2005. Change of ζ potential of biocompatible colloidal oxide particles upon adsorption of bovine serum albumin and lysozyme. *The Journal of Physical Chemistry B,* 109 (30), 14469-14474.

143. Rothenstein, D., Claasen, B., Omiecienski, B., Lammel, P. and Bill, J., 2012. Isolation of ZnO-binding 12-mer peptides and determination of their binding epitopes by NMR spectroscopy. *Journal of the American Chemical Society,* 134 (30), 12547-12556.

144. Ruan, L., Chiu, C., Li, Y. and Huang, Y., 2011. Synthesis of Platinum Single-Twinned Right Bipyramid and {111}-Bipyramid through Targeted Control over Both Nucleation and Growth Using Specific Peptides. *Nano Letters,* 11 (7), 3040-3046.

145. Ruan, L., Ramezani-Dakhel, H., Chiu, C., Zhu, E., Li, Y., Heinz, H. and Huang, Y., 2013. Tailoring Molecular Specificity toward a Crystal Facet: a Lesson from Biorecognition toward Pt {111}. *Nano Letters,* 13 (2), 840-846.

146. Sagui, C., and Darden, T.A., 1999. Molecular dynamics simulations of biomolecules: long-range electrostatic effects. *Annual Review of Biophysics and Biomolecular Structure,* 28 (1), 155-179.

147. Sanchez, C., Arribart, H. and Guille, M.M.G., 2005. Biomimetism and bioinspiration as tools for the design of innovative materials and systems. *Nature Materials,* 4 (4), 277-288.

148. Sanford, K., and Kumar, M., 2005. New proteins in a materials world. *Current Opinion in Biotechnology,* 16 (4), 416-421.

149. Sano, K., Sasaki, H. and Shiba, K., 2005. Specificity and biomineralization activities of Ti-binding peptide-1 (TBP-1). *Langmuir,* 21 (7), 3090-3095.

150. Sarashina, I., and Endo, K., 1998. Primary structure of a soluble matrix protein of scallop shell: implications for calcium carbonate biomineralization. *American Mineralogist,* 83, 1510-1515.

151. Sarikaya, M., Tamerler, C., Jen, A.K., Schulten, K. and Baneyx, F., 2003. Molecular biomimetics: nanotechnology through biology. *Nature Materials,* 2 (9), 577-585.

152. Sarikaya, M., Tamerler, C., Schwartz, D.T. and Baneyx, F., 2004. Materials assembly and formation using engineered polypeptides. *Annu. Rev. Mater. Res.,* 34, 373-408.

153. Sass, S.L., 1998. *The Substance of Civilization: Materials and Human History from the Stone Age to the Age of Silicon.* Arcade Publishing.

154. Seker, U.O., Wilson, B., Sahin, D., Tamerler, C. and Sarikaya, M., 2008. Quantitative affinity of genetically engineered repeating polypeptides to inorganic surfaces. *Biomacromolecules,* 10 (2), 250-257.

155. Seker, U.O.S., and Demir, H.V., 2011. Material Binding Peptides for Nanotechnology. *Molecules,* 16 (2), 1426-1451.

156. Seker, U.O.S., Wilson, B., Dincer, S., Kim, I.W., Oren, E.E., Evans, J.S., Tamerler, C. and Sarikaya, M., 2007. Adsorption behavior of linear and cyclic genetically engineered platinum binding peptides. *Langmuir,* 23 (15), 7895-7900.

157. Shiba, K., 2010. Exploitation of peptide motif sequences and their use in nanobiotechnology. *Current Opinion in Biotechnology,* 21 (4), 412-425.

158. Shimizu, K., Cha, J., Stucky, G.D. and Morse, D.E., 1998. Silicatein α: cathepsin L-like protein in sponge biosilica. *Proceedings of the National Academy of Sciences,* 95 (11), 6234-6238.

159. Shimomura, M., and Sawadaishi, T., 2001. Bottom-up strategy of materials fabrication: a new trend in nanotechnology of soft materials. *Current Opinion in Colloid & Interface Science,* 6 (1), 11-16.

160. Siffert, P., and Krimmel, E., 2004. *Silicon: Evolution and future of a technology.* Springer.

161. Sigal, G.B., Mrksich, M. and Whitesides, G.M., 1998. Effect of surface wettability on the adsorption of proteins and detergents. *Journal of the American Chemical Society,* 120 (14), 3464-3473.

162. Slocik, J.M., and Naik, R.R., 2010. Probing peptide–nanomaterial interactions. *Chemical Society Reviews,* 39 (9), 3454-3463.

163. Slocik, J.M., Stone, M.O. and Naik, R.R., 2005. Synthesis of gold nanoparticles using multifunctional peptides. *Small,* 1 (11), 1048-1052.

164. Smith, C.S., 1965. Materials and the Development of Civilization and Science Empiricism and esthetic selection led to discovery of many properties on which material science is based. *Science,* 148 (3672), 908-917.

165. Smith, G.P., and Petrenko, V.A., 1997. Phage display. *Chemical Reviews,* 97 (2), 391-410.

166. Song, H., Kim, F., Connor, S., Somorjai, G.A. and Yang, P., 2005. Pt nanocrystals: Shape control and Langmuir-Blodgett monolayer formation. *The Journal of Physical Chemistry B,* 109 (1), 188-193.

167. Song, Y., Challa, S.R., Medforth, C.J., Qiu, Y., Watt, R.K., Peña, D., Miller, J.E., van Swol, F. and Shelnutt, J.A., 2004. Synthesis of peptide-nanotube platinum-nanoparticle composites. *Chemical Communications,* (9), 1044-1045.

168. Sumerel, J.L., Yang, W., Kisailus, D., Weaver, J.C., Choi, J.H. and Morse, D.E., 2003. Biocatalytically templated synthesis of titanium dioxide. *Chemistry of Materials,* 15 (25), 4804-4809.

169. Sun, T., Qing, G., Su, B. and Jiang, L., 2011. Functional biointerface materials inspired from nature. *Chemical Society Reviews,* 40 (5), 2909-2921.

170. Tamerler, C., and Sarikaya, M., 2007. Molecular biomimetics: utilizing nature's molecular ways in practical engineering. *Acta Biomaterialia,* 3 (3), 289-299.

171. Tan, Y.N., Lee, J.Y. and Wang, D.I., 2010. Uncovering the design rules for peptide synthesis of metal nanoparticles. *Journal of the American Chemical Society,* 132 (16), 5677-5686.

172. Tao, A.R., Habas, S. and Yang, P., 2008. Shape control of colloidal metal nanocrystals. *Small,* 4 (3), 310-325.

173. Thakkar, K.N., Mhatre, S.S. and Parikh, R.Y., 2010. Biological synthesis of metallic nanoparticles. *Nanomedicine: Nanotechnology, Biology and Medicine,* 6 (2), 257-262.

174. Thyparambil, A.A., Wei, Y. and Latour, R.A., 2012. Determination of Peptide–Surface Adsorption Free Energy for Material Surfaces Not Conducive to SPR or QCM using AFM. *Langmuir,* 28 (13), 5687-5694.

175. Togashi, T., Yokoo, N., Umetsu, M., Ohara, S., Naka, T., Takami, S., Abe, H., Kumagai, I. and Adschiri, T., 2011. Material-binding peptide application—ZnO crystal structure control by means of a ZnO-binding peptide. *Journal of Bioscience and Bioengineering,* 111 (2), 140-145.

176. Tomczak, M.M., Gupta, M.K., Drummy, L.F., Rozenzhak, S.M. and Naik, R.R., 2009. Morphological control and assembly of zinc oxide using a biotemplate. *Acta Biomaterialia,* 5 (3), 876-882.

177. Umetsu, M., Mizuta, M., Tsumoto, K., Ohara, S., Takami, S., Watanabe, H., Kumagai, I. and Adschiri, T., 2005. Bioassisted Room-Temperature Immobilization and Mineralization of Zinc Oxide?The Structural Ordering of ZnO Nanoparticles into a Flower-Type Morphology. *Advanced Materials,* 17 (21), 2571-2575.

178. Vaia, R.A., and Wagner, H.D., 2004. Framework for nanocomposites. *Materials Today,* 7 (11), 32-37.

179. Van Hest, J.C., and Tirrell, D.A., 2001. Protein-based materials, toward a new level of structural control. *Chemical Communications,* (19), 1897-1904.

180. Veis, A., and Perry, A., 1967. The Phosphoprotein of the Dentin Matrix. *Biochemistry,* 6 (8), 2409-2416.

181. Vodnik, M., Zager, U., Strukelj, B. and Lunder, M., 2011. Phage display: selecting straws instead of a needle from a haystack. *Molecules,* 16 (1), 790-817.

182. Vreuls, C., Zocchi, G., Genin, A., Archambeau, C., Martial, J. and de Weerdt, C.V., 2010. Inorganic-binding peptides as tools for surface quality control. *Journal of Inorganic Biochemistry,* 104 (10), 1013-1021.

183. Walsh, T.R., and Tomasio, S.d.M., 2010. Investigation of the influence of surface defects on peptide adsorption onto carbon nanotubes. *Molecular BioSystems,* 6 (9), 1707-1718.

184. Wang, Z.L., 2004. Zinc oxide nanostructures: growth, properties and applications. *Journal of Physics: Condensed Matter,* 16 (25), R829.

185. Webb, J., Evans, L., St Pierre, T. and Macey, D., 1991. Biominerals-source and inspiration for novel advanced materials. *Search,* 22 (4), 137-139.

186. Weiner, S., Traub, W. and Parker, S., 1984. Macromolecules in mollusc shells and their functions in biomineralization [and Discussion]. *Philosophical Transactions of the Royal Society of London.B, Biological Sciences,* 304 (1121), 425-434.

187. Weiner, S., 2008. Biomineralization: A structural perspective. *Journal of Structural Biology,* 163 (3), 229-234.

188. Weintraub, B., Zhou, Z., Li, Y. and Deng, Y., 2010. Solution synthesis of one-dimensional ZnO nanomaterials and their applications. *Nanoscale,* 2 (9), 1573-1587.

189. Whaley, S.R., English, D., Hu, E.L., Barbara, P.F. and Belcher, A.M., 2000. Selection of peptides with semiconductor binding specificity for directed nanocrystal assembly. *Nature,* 405 (6787), 665-668.

190. Whitford, D., 2005. *Proteins: structure and function.* Wiley. com.

191. Whyburn, G.P., Li, Y.J. and Huang, Y., 2008. Protein and protein assembly based material structures. *Journal of Materials Chemistry,* 18 (32), 3755-3762.

192. Wright, L.B., and Walsh, T.R., 2013. Efficient conformational sampling of peptides adsorbed onto inorganic surfaces: insights from a quartz binding peptide. *Phys. Chem. Chem. Phys.,* 15 (13), 4715-4726.

193. Xia, F., and Jiang, L., 2008. Bio-Inspired, Smart, Multiscale Interfacial Materials. *Advanced Materials,* 20 (15), 2842-2858.

194. Xie, J., Lee, J.Y., Wang, D.I. and Ting, Y.P., 2007. Silver nanoplates: from biological to biomimetic synthesis. *ACS Nano,* 1 (5), 429-439.

195. Xu, H., Wang, H., Zhang, Y., He, W., Zhu, M., Wang, B. and Yan, H., 2004. Hydrothermal synthesis of zinc oxide powders with controllable morphology. *Ceramics International,* 30 (1), 93-97.

196. Xu, S., and Wang, Z.L., 2011. One-dimensional ZnO nanostructures: Solution growth and functional properties. *Nano Research,* 4 (11), 1013-1098.

197. Yi, G., Wang, C. and Park, W.I., 2005. ZnO nanorods: synthesis, characterization and applications. *Semiconductor Science and Technology,* 20 (4), S22.

198. Yokoo, N., Togashi, T., Umetsu, M., Tsumoto, K., Hattori, T., Nakanishi, T., Ohara, S., Takami, S., Naka, T., Abe, H., Kumagai, I. and Adschiri, T., 2010. Direct and Selective Immobilization of Proteins by Means of an Inorganic Material-Binding Peptide: Discussion on Functionalization in the Elongation to Material-Binding Peptide. *Journal of Physical Chemistry B,* 114 (1), 480-486.

199. Zhang, S., 2003. Building from the bottom up. *Materials Today,* 6 (5), 20-27.

200. Zhang, S., 2002. Emerging biological materials through molecular self-assembly. *Biotechnology Advances,* 20 (5), 321-339.

201. Zhang, Y., Ram, M.K., Stefanakos, E.K. and Goswami, D.Y., 2012. Synthesis, characterization, and applications of ZnO nanowires. *Journal of Nanomaterials,* 2012, 20.

202. Zhou, J., Xu, N.S. and Wang, Z.L., 2006. Dissolving behavior and stability of ZnO wires in biofluids: a study on biodegradability and biocompatibility of ZnO nanostructures. *Advanced Materials,* 18 (18), 2432-2435.

Chapter 2

Experimental Methods

This chapter briefly introduces the principles of techniques that have been used in this study to synthesize or characterize peptides, inorganic materials and their interactions. Peptide sequences selected from studies where they have been identified using phage display technique or computational tools have been synthesized using microwave-assisted solid phase peptide synthesis protocol (SPPS) and their purity and molecular weight ascertained using high performance liquid chromatography (HPLC) and matrix-assisted laser desorption ionization time-of-flight (MALDI-TOF) mass spectrometry respectively. Computational tools Tripos SYBYL 8.0 (Tripos, St. Louis, MO, USA) and molecular dynamics (MD) have been used to study the conformation and stability of peptide sequences. The net charge and isoelectric point of the peptides have been calculated using Innovegen online peptide property calculator by Innovagen AB. Wet chemical methods have been used to synthesize inorganic particles which have been characterized using a number of techniques; scanning electron microscopy (SEM), transmission electron microscopy (TEM), energy dispersive X-ray analysis (EDX), X-ray diffraction (XRD), thermogravimetric analysis (TGA), fourier transform infrared spectroscopy (FTIR) and nitrogen gas adsorption/desorption analysis. The size, dispersity and net charge of some peptides and particles in solution have been analysed using dynamic light scattering (DLS) and zeta potential measurements. Inductively coupled plasma-optical emission spectroscopy (ICP-OES) has been used to quantify some elements in solution. Quartz crystal microbalance with dissipation monitoring (QCM-D) and isothermal titration calorimetry (ITC) have been used to study the interaction of peptides with inorganic materials.

2.1. Solid Phase Peptide Synthesis (SPPS)

SPPS is carried out in solution on an insoluble polymeric support known as the resin which is used as a starting point for the sequential addition of amino acids that are side chain protected. The resin can be preloaded with the *C*-terminal amino acid of the

desired peptide sequence. The carboxyl group of the amino acid can be covalently anchored to the resin using a linker which can later be cleaved usually using acidic conditions after the step by step addition of subsequent amino acids (Chan and White, 2000; Fields *et al*., 2002). The resin linked *C*-terminal amino acid is protected at its N^{α}-amino group using a temporary protecting group while its side chain (R-group) is protected using a semi-permanent protecting group, unaffected by the synthesis conditions used when attaching/coupling amino acids to form a peptide. Common examples of temporary protecting groups are 9-flurenylmethyl carbamate (Fmoc) and tert-butoxycarbonyl (Boc) and examples of semi-permanent side chain protecting groups are 2,2,4,6,7-pentamethyl-dihydrobenzofuran-5-sulfonyl (Pbf), tertiary-butyl (*t*Bu) and trityl (Trt) (Pedersen *et al*., 2012).

The N^{α}-amino protecting group is deprotected/removed selectively using a deprotecting agent such as piperazine which is then thoroughly washed using a suitable solvent. An excess of the subsequent amino acid to be coupled is then introduced in solution to the reaction vessel containing the deprotected *C*-terminal amino acid to which it is coupled *via* an amide bond with the help of activating reagents. The subsequent amino acid can also be introduced as a preactivated species (Cudic and Fields, 2008). After coupling, excess peptide and reagents are filtered away and the dipeptide linked to the resin is washed again using a suitable solvent. Synthesis thus takes place from the *C*- to *N*-direction and the process of deprotecting the N^{α}-amino group, rinsing, coupling the next amino acid and rinsing again is repeated until all the amino acids required to make the peptide sequence are coupled. After attaching the final amino acid, its N^{α}-amino group is deprotected and the peptide attached to the resin is washed using solvent. The coupling process is carried out under basic solution conditions. To release the peptide from the resin, a cleavage step is carried out using an acidic cleavage mixture that is minimally destructive to the peptide. The side chain residues of the peptide are also deprotected using the same cleavage mixture usually containing 90-95% trifluoroacetic acid (TFA) and nucleophilic reagents (scavengers) like thioanisole (TIS), water and phenol. Nucleophilic species prevent the interaction of electron rich functional groups of amino acids (*i.e.* moieties of methionine, tryptophan, tyrosine and cysteine) with highly reactive cationic species generated during the cleavage process from the resin linker and protecting groups. The cleaved peptide can then be reprecipitated and washed

in chilled diethyl ether which can then be evaporated off and the peptide can be lyophilized (Chan and White, 2000). Figure 2.1 illustrates the principle of SPPS.

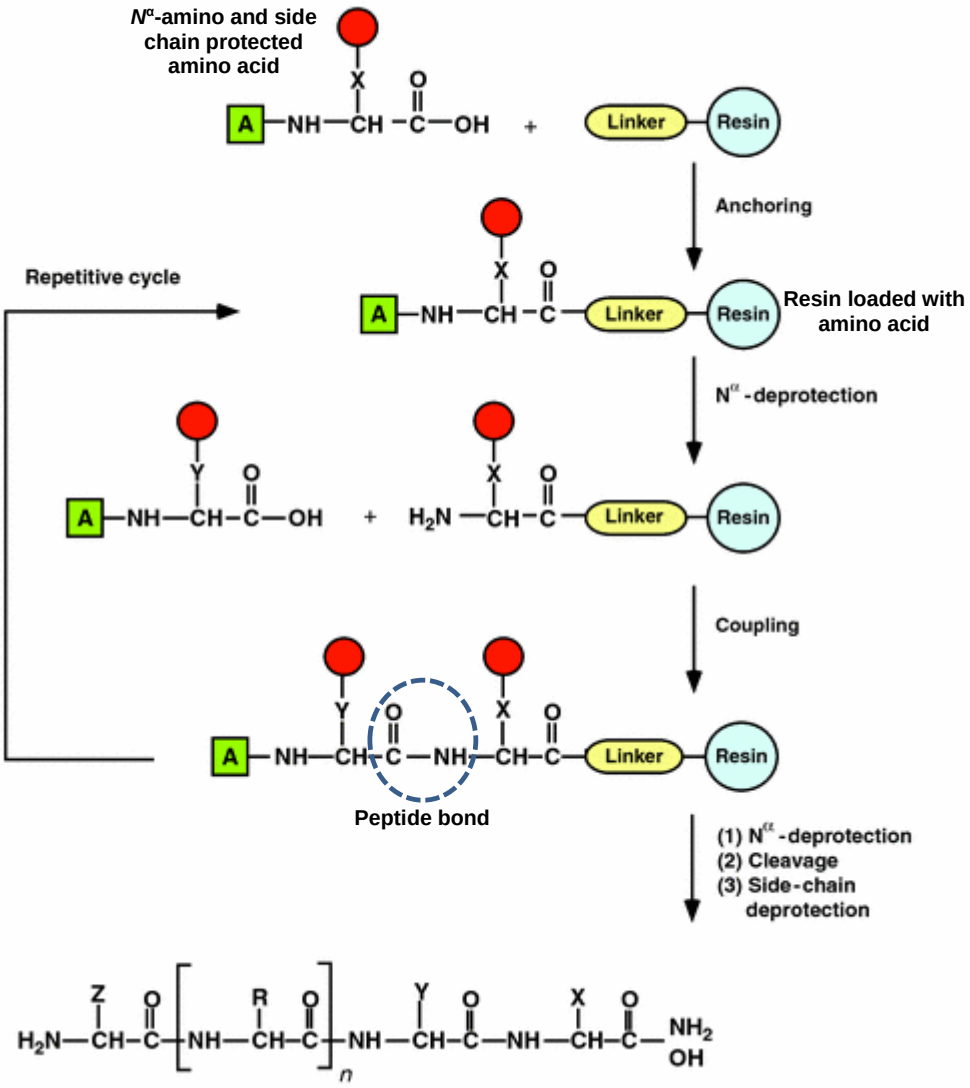

Figure 2.1. Schematic illustration of the stepwise synthesis of a linear peptide using SPPS method. The green square box designated A is the temporary N^{α}-amino acid protecting group while the smaller red circle represents the semi-permanent side-chain protecting group. Adapted from Cudic and Fields, 2008.

The synthesis process is readily amenable to automation because the synthesis steps are repetitive and all carried out in the same reaction vessel. The physical loss of the peptide is minimal as the resin acts as a solid support throughout the synthesis. There is, however, difficulty in attaining pure peptides as by-products from impure reactants, side reactions or incomplete reactions can be formed on the resin during the synthesis

process and as some of these may be very similar to the desired peptide sequence, purification of the final product can be difficult (Bacsa *et al*., 2008; Chan and White, 2000; Cudic and Fields, 2008). Microwave heating has been used to assist the coupling process which increases the reaction speed saving time and has been shown to reduce inter and intramolecular aggregation of peptides that can occur during synthesis. Additionally, microwave assisted SPPS has been shown to improve the purity and yield of peptides and longer peptide sequences up to 109 amino acids have been attained (Pedersen *et al*., 2012). There are, however, sequences that are inherently difficult to synthesize. In many cases these difficulties can be associated to premature sequence termination mainly caused by steric hindrance of side-chain protecting groups, secondary structure formation as well as intra and intermolecular aggregation which may occur through hydrophobic interactions and hydrogen bonding (Bacsa *et al*., 2008; Garcia Martin and Albericio, 2008).

2.2. High Performance Liquid Chromatography (HPLC)

HPLC is a liquid chromatography technique used to separate and quantify compounds in a mixture that have been dissolved in solution. HPLC can be described as a refinement of conventional column chromatographic techniques. In traditional column chromatography, separation of components in a mixture is achieved with a solvent (mobile phase) running down a column gravitationally, however, in HPLC, high pressure is applied using a pump which increases the pressure in the column forcing the separation to occur at much faster rates. Improvements have also included the making of new column packing materials (stationary phase) with much smaller particle sizes which increases the surface area for interaction with the molecules in the mixture passing through it. Excellent separation resolution can therefore be achieved for molecules that are very closely related. Automation of HPLC instruments make them easy to operate. The purity of a sample can therefore be determined using HPLC by separating contaminants and quantifying all the components. The use of HPLC is popular for its ease of selectivity manipulation over a wide range of elution conditions, its sensitivity, reproducibility and general high recoveries that allow for reuse of samples for other analytical procedures like mass spectrometry (Aguilar, 2004; Hennessy *et al*., 2003; Honour, 2006).

HPLC instruments, as shown in schematic in Figure 2.2 have reservoirs for the mobile phase which can contain mixtures of solvents that can be used to condition the elution process. A pump is used to control the flow of the mobile phase and the sample which is injected through a sample loop. The sample then flows through the column where the separation takes place controlled by the partitioning behaviour of the components between the mobile and stationary phase. The different components reach the detector at different times and with different quantities that can be determined. Detectors can record the presence of analytes by monitoring electrochemical responses, detecting changes in fluorescence after excitation using a suitable wavelength or detecting changes in UV-vis adsorption at a fixed wavelength (Tissue, 2000; Honour, 2006).

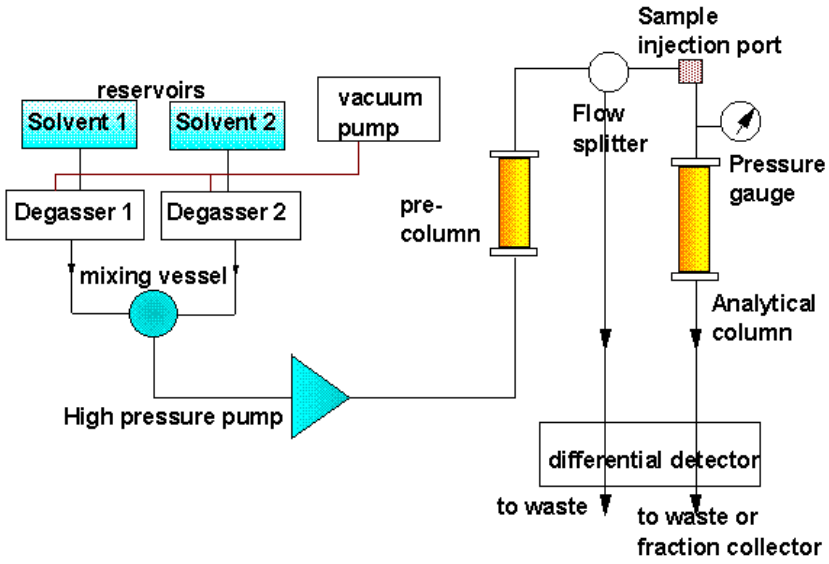

Figure 2.2. Schematic of an HPLC instrument reproduced from Tissue, 2000.

Reverse phase high-performance liquid chromatography (RP-HPLC) is used to separate molecules based on their hydrophobic properties. This employs the use of a stationary phase with immobilized hydrophobic ligands. In high aqueous phase, hydrophobic solute molecules stick to the RP-HPLC column and can only be eluted from the column by changing the eluent to a high organic mobile phase. Isocratic conditions can be applied where a constant concentration of the organic eluent is used. A gradient mobile phase can also be applied whereby the concentration of organic solvent increases over time which is an additional way to increase the resolution of the separation by elution in

the order of increasing hydrophobicity. Selection of initial and optimal separation conditions can be challenging and distinctively variable for different samples. RP-HPLC technique is commonly applied in the analysis of peptides and proteins. It may however, cause irreversible denaturation of proteins reducing the potential recovery of the biologically active form (Aguilar, 2004; Hennessy *et al*., 2003).

2.3. Matrix-Assisted Laser Desorption Ionization Time-of-Flight (MALDI -TOF) Mass Spectrometry

A mass spectrometer (MS) is an analytical instrument that is used to measure the mass to charge ratio (*m/z*) of ions. It can be used to identify and determine the molecular weight of compounds including biomolecules like proteins, peptides, oligosaccharides and oligonucleotides. The instrument consists of three main components; the ion source which produces ions from the sample, the mass analyzer which separates different ions according to their *m/z* ratio and the detector. The output is a plot of intensity (ion abundance) versus the *m/z* ratio. There are many types of MS with different ionization methods but herein, the focus is on MALDI-TOF MS which was used in this study. In MALDI-TOF MS samples which should be thermally labile and non-volatile compounds are embedded/co-crystallized in a UV-adsorbing organic matrix on a conductive sample support (probe) which can be inserted into the instrument's vacuum system. There, the samples are rapidly photo-volatized using a pulsed UV laser producing gas-phase ions which are extracted by the electric field and accelerated towards the mass analyzer (Ellis *et al*., 2013; Glish and Vachet, 2003; Jurinke *et al*., 2004). This process is illustrated in Figure 2.3.

Direct irradiation of an analyte without a matrix can cause significant fragmentation of the sample leading to low ion yields. However, limitations of using MALDI instruments include difficulties in analysing samples with low molecular weight because a large degree of noise is usually seen at *m/z* ratios below 500 Da when a matrix is used. The exact mechanism through which the electric field extracts the ions is unknown (Jurinke *et al*., 2004; Marvin *et al*., 2003). Some suggested hypothesis include ion-molecule reactions, gas-phase photoionization, excited state proton transfer, disproportionation, thermal ionization, energy pooling and desorption of preformed ions (Marvin *et al*., 2003). The

mass *m/z* ratio of ions is calculated by measuring their time of flight (TOF) which is shorter for smaller molecules and longer for larger molecules given that their initial energies are identical (Jurinke *et al*., 2004; Marvin *et al*., 2003). Single-charged, non-fragmented ions are predominantly generated which makes it easier to identify parent ion masses from the plot of intensity versus the *m/z* ratio. The masses from the plot can be accessed as numerical data for processing and analysis. MALDI-TOF MS instruments have high accuracy, sensitivity and a requirement for very little sample. They also have a wide useable mass range (500 to 300,000 Da) and a relatively high tolerance to buffers and salts. The set up and automation of the technique can allow hundreds of samples to be analysed daily (Glish and Vachet, 2003; Marvin *et al*., 2003). MS analysis in this study was carried out with the help of Hickman G., a fellow PhD student within the research group.

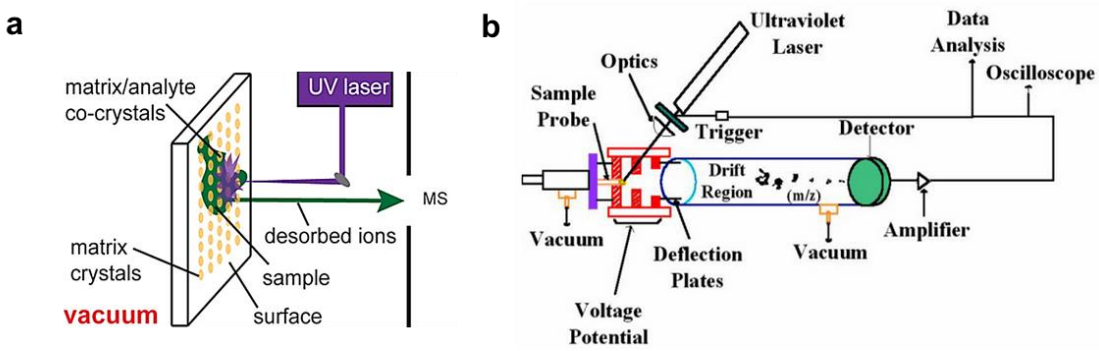

Figure 2.3. (a) Schematic representation of matrix-assisted laser desorption Ionization showing the irradiation of a sample in a matrix to produce ions, reproduced from Ellis *et al*., 2013. (b) Schematic Illustration of a MALDI-TOF MS instrument reproduced from Tansurat, 2007.

2.4. Fourier Transform Infrared Spectroscopy (FTIR)

Light can best be described as electromagnetic radiation as it is composed of magnetic and electric waves. The electromagnetic spectrum has different regions beyond the visible spectrum which can be detected *i.e.* radiowave, microwave, infrared, ultraviolet (UV), x-ray and gamma-rays. Molecules behave differently when they absorb light from different regions of the electromagnetic spectrum. Electrons in molecules that absorb visible or ultraviolet light transition from lower to higher electronic energy levels, molecules that absorb microwaves rotate and those that absorb IR light vibrate at

different energies. The infrared (IR) region can be divided into the near-IR (14,000 - 4000 cm^{-1}), mid-IR region (4000 - 400 cm^{-1}) and far-IR region (400 - 4 cm^{-1}). IR spectroscopy is commonly carried out between 4000 - 400 cm^{-1} where most organic and inorganic compounds absorb. In FTIR, radiation at a particular energy is passed through an interferometer then to a sample and the fraction of the radiation that is absorbed is determined with the aid of a detector, signal amplifier, analog to digital converter and a computer which uses a mathematical method of Fourier-transformation (Figure 2.4). Molecules must possess an electric dipole moment which must change as they vibrate and rotate depending on their degrees of freedom for absorption to be measurable using IR. Vibration modes include bending (*i.e.* rocking, scissoring, wagging and twisting) and stretching (symmetric and asymmetric). The frequencies at which the bonds in molecules vibrate vary depending on the strength of the bonds and the mass of the atoms. An absorption spectrum is attained with each energy peak corresponding to the vibration frequency of a part of the molecule being examined. FTIR can therefore be used to identify the functional groups which make up the structure of a sample (Pavia and Lampman, 1996; Stuart, 2004).

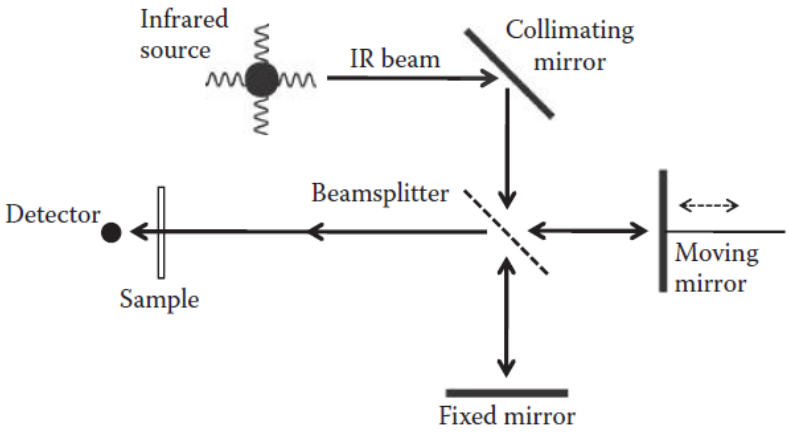

Figure 2.4. Schematic illustration of a Michelson interferometer which is an optical device commonly found in many FTIR instruments. Illustration has been reproduced from Smith, 2011.

Different infrared spectra are produced by different molecules. Similarities in absorbed frequencies may occur between different molecules but identical spectra are not generated by molecules with different structures. FTIR has different preparation and

analysis techniques that allow one to study almost any sample in any state, solid liquid or gas. FTIR analysis does not required the use of restricting devices like slits found in older dispersive IR instruments therefore higher signals are received by the detector improving the signal to noise ratio (Smith, 2011; Stuart, 2004). FTIRs are highly sensitive instruments that require minimal amounts of sample and spectra can be obtained on a millisecond timescale especially when using techniques like Attenuated Total Reflectance (ATR) spectroscopy. The intensity of the band can be measured as absorbance or percentage transmittance which is interchangeable using mathematical formulae. For quantitative data, absorbance is preferable as it can directly be related to concentration using Beer Lambert's law (Smith, 2011; Stuart, 2004). For example, the concentration of a particular molecule in a sample can be determined by comparing its absorbance to a calibration curve generated from known concentrations and the concomitant FTIR determined absorbance values of the molecule. Chemical species that do not have a dipole moment and cannot vibrate such as homonuclear diatomic molecules, single atoms of noble gases like argon and helium or monoatomic ions cannot be examined using IR. Complex mixtures with complex compositions can also be difficult to interpret but some strategies have been developed to overcome this including the use of software that enable one to subtract simple spectra form the spectrum of a mixture or that can perform library search comparisons of spectra. Interference or artefacts in spectra can be caused by atmospheric gases such as carbon dioxide and also water which should be avoided in samples because of its intense and broad peaks as well as its ability to dissolve some of the materials used in FTIR sample preparation like NaCl and KBr (Smith, 2011; Stuart, 2004).

2.5. Scanning Electron Microscopy (SEM) Coupled to Energy Dispersive X-Ray Analysis (EDX)

SEM instruments are powerful magnification tools used to examine morphological features of materials at very small scales ranging from nanometres (nm) to micrometers (μm) using a finely focused electron beam. Detailed observations of surface microstructure and cross-sectional morphological features of materials can be made and topographic images that appear to be three-dimensional can be captured. Samples are prepared and placed on the sample stage under vacuum pressure (Figure 2.5 a). Only

solid samples that can withstand high vacuum pressure can be used. The instrument's electron gun uses a heated filament (cathode) covered with a Wehnelt cap to generate a stream of electrons which are directed towards the object being examined with a positive electrical potential from the anode. The electrons are confined and finely focused into a thin monochromatic electron beam using metal apertures and electromagnetic lenses. The monochromatic beam irradiates the object causing interactions inside the object. The electron beam traces the sample in a raster pattern and the user can adjust the beam to determine the surface area to be scanned and the magnification. The acceleration rate of the incident electron beam affects the interaction of the electrons with the atoms in the sample which then releases energetic electrons including secondary electrons, x-rays and backscattered electrons which are scattered and attracted by various detectors as shown in Figure 2.5. The scatter pattern yields information on shape, size, texture and composition (Goldstein *et al.*, 2003; Voutou and Stefaniki, 2008).

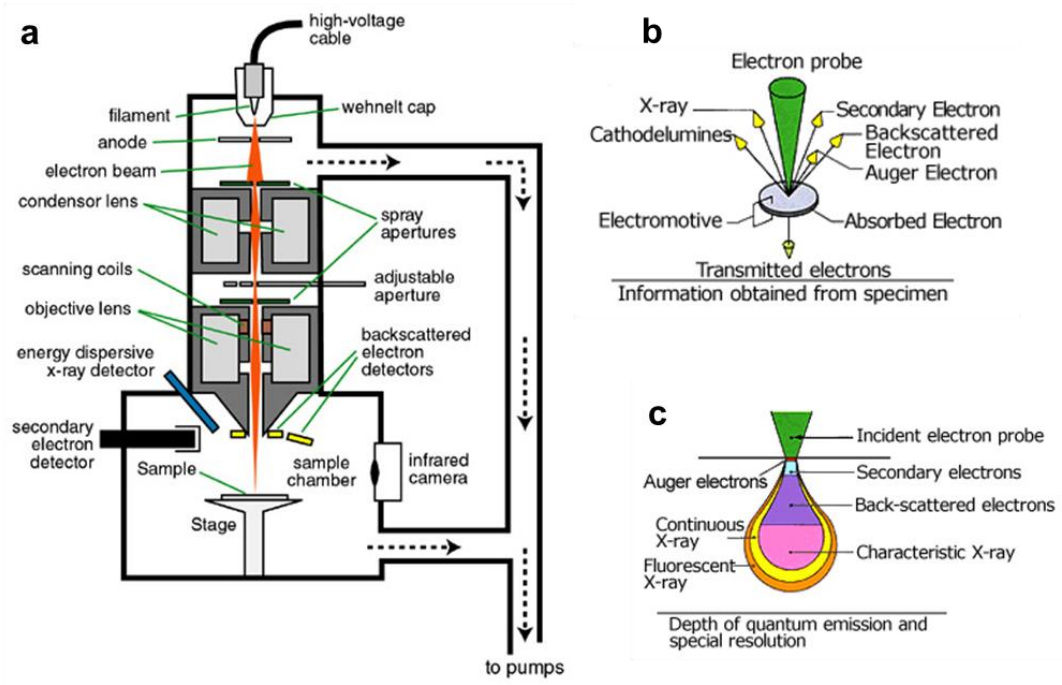

Figure 2.5. (a) Schematic illustration showing an example of an SEM instrument reproduced from Wittke, 2008, (b) electron-specimen interactions (c) Depth of penetration of the incident electron beam in the sample. (b,c) reproduced from JEOL Ltd 2013.

When an incident electron interacts with a sample, the electrons in the atoms of the sample become excited (unstable) losing most of their energy and move to the surface of the sample where they can escape as low energy secondary electrons if they still have sufficient energy. Detection of these secondary electrons yields detailed information on the topography of the sample. High-energy incident electrons that are reflected out of the sample's interaction volume generate backscattered electrons which vary depending on the samples atomic number and are therefore used to detect differences in average atomic number on sites of a specimen. With time, the unstable electrons in samples relax giving off excess energy as cathodeluminescence, Auger electrons and x-rays. X-rays are emitted when an atom becomes excited losing electrons and creating an electron vacancy which is then filled by higher shell electrons which need to give off excess energy. EDX detectors quantify the emitted X-rays (e.g. K_{α}, L_{α}) against their energy which is a fingerprint for the element from which it was emitted. Samples that are not conductive need to be prepared by coating using a material that is conductive *e.g.* gold or carbon in order to avoid the accumulation of static electric charge on the sample when exposed to electrons. SEM is an essential scientific and industrial characterization tool (Goldstein *et al.*, 2003; JEOL Ltd., 2013; Voutou and Stefaniki, 2008).

2.6. Transmission Electron Microscopy (TEM) Coupled to Energy Dispersive X-Ray Analysis (EDX)

Like SEM, TEM is an imaging technique which uses an electron beam but is more powerful with higher magnification allowing imaging of samples at atomic resolution. TEM can produce two dimensional images with high resolution enabling detailed characterisation of morphological features of a sample. Compositional and crystallographic information can also be obtained. A thin sample is prepared and placed in a vacuum chamber of a TEM. Three different interactions of the electron beam and the specimen can be exploited by TEM instruments; unscattered electrons known as the transmitted beam, electrons that are elastically scattered (without loss of energy) known as the diffracted beam and inelastically scattered electrons (with loss of energy). When the incident electron beam passes through the sample (unscattered) without any interaction, the transmitted beam is inversely proportional to the thickness of a sample.

Thicker areas of samples will have fewer transmitted electrons and thus appear darker. Conversely, thinner areas will appear lighter as they have more transmitted electrons. The image which is magnified can be focused onto a fluorescent screen, a photographic film or with the use sensors like charge-coupled devices. The differences in transmitted electrons give information on size, shape, texture and structure of the sample. Incident electrons that are scattered by the atoms of a sample without loss of energy can also be transmitted through other parts of the sample. Incident electrons scattered by atoms with the same spacing will be scattered at the same angle and the information can be collated to obtain a diffraction pattern. Incident electrons that interact with the atoms in the sample and loose energy can be exploited for EDX elemental analysis. Only small samples that are electron transparent and can withstand high vacuum pressures can be examined. TEMs have a wide range of applications in scientific research and industrial fields (Voutou and Stefaniki, 2008; Wang, 2000).

2.7. X-Ray Diffraction (XRD)

XRD is a technique that is used for structural characterization of samples able to clearly distinguish between crystalline and amorphous materials. Here we specifically refer to x-ray powder diffraction where finely ground materials are analysed. Figure 2.7a illustrates the main components of an XRD instrument. High energy x-rays with short wavelengths which are similar in magnitude to the atomic spacing in solids are generated from an electromagnetic radiation source, filtered to produce monochromatic radiation and directed towards a solid material. The angle of the X-ray can be focused on the sample from its source at increasing incident angles θ while the detector always reads the intensities of the diffracted waves at 2θ away from the path of the x-ray source. The incident beam encounters a material made up of regularly spaced atoms that can scatter the waves constructively (waves that remain in phase and mutually reinforce each other) as shown in Figure 2.7b. Diffraction conditions have to satisfy Bragg's Law ($n\lambda = 2d\sin\theta$, where n represents the order of reflection which is normally an integer value, λ is wavelength of the in phase beam of x-rays, d is the inter-planar distance and θ is the incident angle). The phase relationships between two or more scattered waves produce a diffraction pattern characteristic of the material's structure. Diffraction patterns with sharp peaks can only be attained from highly regular structures such as

crystalline solids, not from amorphous materials. Minerals have unique d-spacings therefore, reference patterns have been made that can be used to identify samples giving information on their purity. The identity of contaminants can also be determined using reference databases. XRD is a non-destructive and reproducible technique (Callister, 2007).

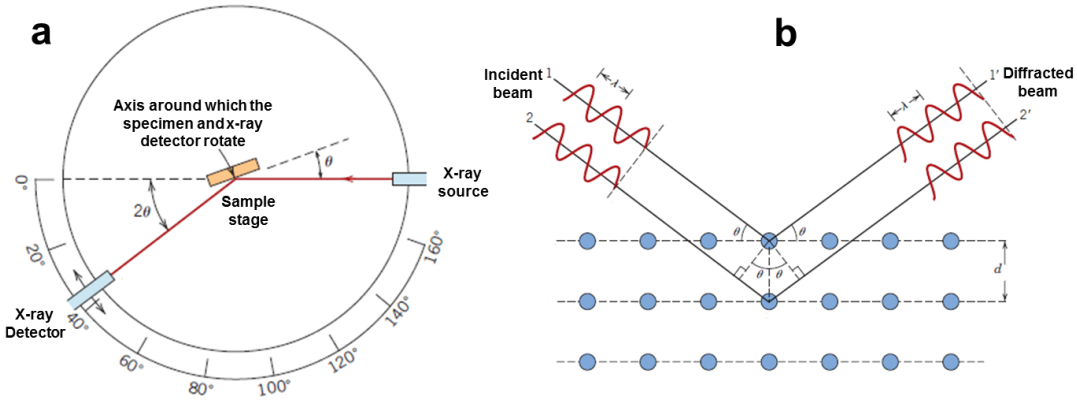

Figure 2.7. (a) Schematic illustration of an XRD instrument (b) Constructive diffraction of x-rays by planes in atoms of a solid material. Images were adapted from Callister, 2007.

2.8. Inductively Coupled Plasma-Optical Emission Spectroscopy (ICP-OES)

ICP-OES is an optical emission spectrometric method that can be used to qualitatively and quantitatively determine which elements are present in a sample. This technique was founded upon an understanding of the fundamentals of measurements of emission and absorption of electromagnetic radiation and the characteristics of atomic and ionic spectra. In an atom, when electrons occupy low energy orbitals closest to its nucleus, the atoms are in their most stable state (ground state). Atoms can take up energy by collision with other particles such as electrons, ions, atoms or molecules or by adsorption of electromagnetic radiation. The UV/visible region from (160 – 800 nm) of the electromagnetic spectrum is frequently used in analytical atomic spectrometry for its precision and low cost. The energy taken up can cause the atom to become excited or can increase the atom's kinetic energy. In excited atoms, electrons move from low energy orbitals to higher energy level orbitals making the atoms unstable. To revert

(decay) back to its ground state, the atom needs to emit energy as electromagnetic radiation (photon) or loose energy by collision with other particles. In other cases, electrons that have absorbed high energy can be completely dissociated from the atom in a process known as ionization leaving the atom with a net positive charge. The energy required is known as the ionization potential of the atom and is unique for each element. Ions like atoms can undergo excitation and decay processes (Boss and Fredeen, 1997; Hou and Jones, 2000).

In ICP-OES, liquid and gas samples can be analysed directly but solid samples need to undergo acid digestion or extraction processes to release the analytes into solution. Samples are injected into the instrument, converted into an aerosol using a nebulizer and directed towards the central channel of the plasma which is generated using argon gas. High temperatures (approximately 10,000 K) are used to dissociate/vaporize samples into free atoms in the gaseous state and also to cause collision excitation and ionization. Excited atoms/ions decay to the ground state and the concentration of the elements can be determined by measuring the intensity of the light emitted at specific wavelengths. The total number of emitted photons is directly proportional to the concentration of the element from which it originated. The high temperature used in ICP-OES can excite electrons from different energy levels of different elements (atoms/ ions) simultaneously which can simultaneously emit their characteristic radiation. This gives a possibility to measure emission from a number of different elements simultaneously or the choice to select different emission wavelengths for a specific element. However, interference and overlap in intensity measurements can occur when several different elements which emit photons that are measurable at wavelengths that are very close to each other are analysed. Over 70 elements can be identified from samples using ICP-OES at concentration below 1 µg/L (ppb) range. (Hou and Jones, 2000). Elements that cannot be determined using ICP-OES include argon which is used to generate the plasma and other trace contaminants such as nitrogen from the atmosphere, carbon from carbon dioxide which can be present in the argon gas and constituents of the solvent used to dilute or dissolve the sample. Short-lived radioactive elements and elements like halogens which require high excitation energies cannot also be analysed using ICP-OES (Boss and Fredeen, 1997; Hou and Jones, 2000).

2.9. Zeta Potential and Dynamics Light Scattering (DLS)

The surface charge of a particle in solution affects the distribution of other ions around it. At the particle-solution interface, an electrical double layer is formed which consists of two regions, an inner part called the Stern layer which has tightly bound counter ions that are attracted to and accumulate close to the particles surface and an outer diffuse layer which has ions that are more loosely bound to the particle (Figure 2.9a). The ions within the electrical double layer form a stable entity with the particle and migrate with the moving particle while other ions beyond the boundary (slipping plane) do not. The potential that exists at the slipping plane is known as zeta potential and it can be used to gauge the stability of a colloidal system. Within a suspension, particles that have a large positive zeta potential, about +30 mV and above tend to repel each other and are considered stable. The same applies for particles with a large negative zeta potential, about -30 mV and below which also repel each other and are stable. Particles with low zeta potential values, within the upper and lower limits mentioned have a tendency to flocculate (Malvern Instruments, 2004). The pH of the solution largely affects the zeta potential of particles. At low pH, the zeta potential values are more positive than at high pH. The isoelectric point is at the pH value where the zeta potential is zero and the system is most unstable (Malvern Instruments, 2004).

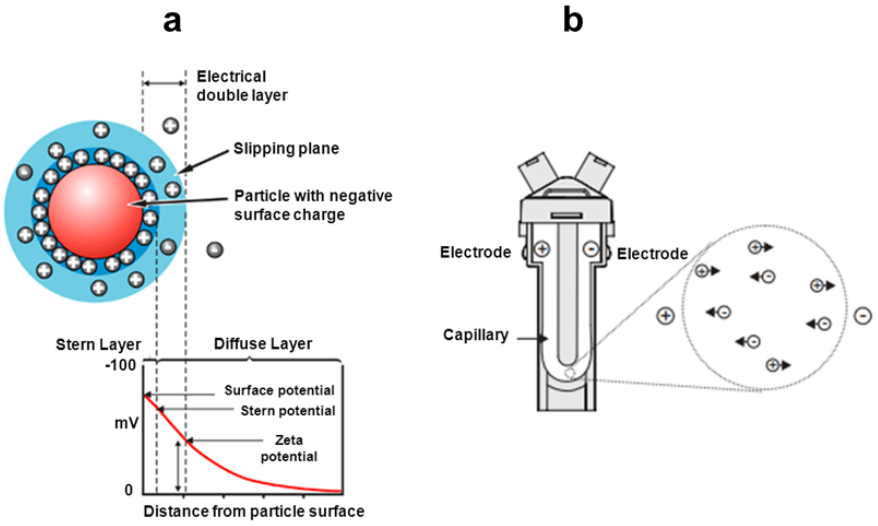

Figure 2.9. (a) Schematic diagram showing the electrical double layer (b) Illustration of a capillary cell commonly used to measure zeta potential. Illustrations reproduced from Malvern Instruments, 2004.

Practically, in a micro-electrophoresis system, it is the electrophoretic mobility which is the movement of the particles towards oppositely charged electrodes at a constant velocity that is measured and the zeta potential is determined theoretically. Charged particles suspended in an electrolyte exhibit electrokinetic effects when an electric field is applied. A special capillary cell with electrodes of opposite charge at the ends is used to measure the electrophoretic mobility of particles (Figure 2.9b). Overall, the electrophoretic mobility (U_E) of particles is influenced by the viscosity (η) of the medium, the strength of the electric field, the zeta potential (z) and the medium's dielectric constant (ε). These factors are related using the Henry equation ($U_E = 2\varepsilon z f(ka)/3\eta$) where $f(ka)$ is Henry's function. Equilibrium is reached between charge based attractive forces and solution influenced viscous forces that oppose movement of the particles. Particles then move towards the electrode with opposite charge and their velocity is measured using techniques such as Laser Doppler Velocimetry (LDV) used in Malvern instruments (Malvern Instruments, 2004).

Dynamic light scattering (DLS) or photon correlation spectroscopy (PCS) is used to measure the size of particles by relating it to the Brownian motion of the particles in solution. In solution particles move due to random collisions with the molecules of the medium in which they are suspended. Small particles move much faster than large particles. When particles are illuminated with a laser, some of the light is scattered and a detector can capture a speckle pattern with dark patches where no light is detected and light patches where light is detected. The speckle pattern appears to move because the particles are moving constantly. The intensity fluctuation rate of the scattered light can be analysed and used to calculate particle size (Malvern Instruments, 2004). The time dependent degree of similarity between signals is measured using a digital correlator that is within the instrument. Intensity signals measuresed at close time intervals are more similar than those measured at futher apart intervals. Thus there is a decay in the correlation function over time and the decay rate is related to the size of the particles being much slower for large particles and faster for small particles. Size distribution is fundamentally generated as an intensity distribution but can also be converted to volume and number distribution (Malvern Instruments, 2004).

2.10. Thermogravimetric Analysis (TGA)

TGA is a technique that can be used to monitor changes in mass of a substance as a function of time and temperature when a material is progressively heated at controlled temperatures over time in a controlled atmosphere. This gives information about the materials thermal stability and its composition by being able to distinguish between organic and inorganic fractions in a specimen. In a TGA experiment, the instrument's precision balance is used to weigh the sample pan which is put into a furnace where it is heated and cooled while monitoring changes in mass. The environment in the instrument is controlled using a gas flow which may be reactive or inert. Commonly used gases include air, oxygen, argon and nitrogen (PerkinElmer, 2010). Quantifiable physical and chemical processes include loss of water and solvent (physisorption and chemisorption), decarboxylation, oxidation, pyrolysis, decomposition and inorganic weight component. TGA instruments are able to perform accurate and reproducible measurements and the incorporation of autosampler accessories make it easy to run several samples unattended. At least 1 mg of sample is required for analysis. Thermal curves are displayed as percentage weight or weight in mg against time or temperature. Using TGA software data can be presented in a differential form which can give more information than the original thermal curve. For example peaks (inflection points) in first derivative plots indicate the temperature at which the greatest rate of change in mass occurs (PerkinElmer, 2010). Gas evolved from a TGA experiment can be analysed using other techniques (TGA-FTIR, TGA-MS, TGA-GC/MS) in an approach called evolved gas analysis (EDA) (PerkinElmer, 2010).

2.11. Nitrogen Gas Adsorption/Desorption Analysis

Nitrogen gas adsorption/desorption analysis can be used to determine the surface area and porosity of a material. The amount of gas adsorbed onto or desorbed from the surface of a solid material can be measured at an equilibrium vapour pressure. Samples are prepared by removing moisture, carbon dioxide and other contaminants that are physically adsorbed to their surface. The procedure used to clean the samples should not cause any detectable chemical or physical change in the sample. Ordinarily, samples in a sample cell are placed under vacuum and purged using a continuous flow of an inert

dry gas passed over the surface or by performing repetitive adsorption and desorption of adsorbate on the surface with each cycle removing some contaminants. This process is known as outgassing or degassing. In the degassing process, heat can also be applied at an appropriate temperature to increase the decontamination rate while desorbing volatile species and moisture without interfering with the integrity of the sample. Thereafter, the sample is cooled to cryogenic temperature, for nitrogen it is the temperature of liquid nitrogen (77 K, -196 °C). The sample is then exposed to a known quantity of nitrogen gas at low pressure which is attracted by the sample's intrinsic surface energy and begins to physically adsorb onto its surface using weak forces like van der Waals interactions. With increased pressure, more gas is adsorbed until the surface is covered and pores are filled where equilibrium is established. Instruments can measure the amount of gas adsorbed and desorbed using volumetric or continuous flow methods (Quantachrome Instruments, 2008).

The most widely used procedure to calculate the specific surface area of the sample is the Brunauer-Emmett-Teller (BET) method. A multipoint or single point BET method may be employed. In the multipoint BET method, an adsorption isotherm at constant temperature is recorded *i.e.* the volume of adsorbed gas is plotted against increasing relative pressure (sample pressure/saturation vapour pressure which is designated as P/P_0). A small change in temperature can significantly change the saturation vapour pressure thus relative pressure is used to minimize this effect. The BET equation is $1/[W(P_0/P)-1] = 1/W_mC + (C-1/W_mC)(P/P_0)$ where W is the weight of gas adsorbed at P/P_0 and W_m is the weight of adsorbate required to form a monolayer surface coverage of the sample and C is the BET constant which gives information on the energy of adsorption of the first monolayer thus is an indication of the strength of the interaction between the adsorbate and adsorbent. In the multi-point BET method, a linear plot of $1/[W(P_0/P)-1]$ against P/P_0 is required with at least three points in the P/P_0 range of 0.05 to 0.35 when nitrogen is used as the adsorbate. At higher relative pressure, condensation occurs and pores in the sample are filled. When saturation is reached, where all pores are filled with liquid nitrogen, the adsorptive gas pressure can be reduced incrementally causing the condensed gas to evaporate. The quantity of gas desorbed can be monitored and information on the surface area of adsorbent, pore size, pore volume, and adsorption-desorption behaviour can be attained by assessing the

shape of the isotherm. The shapes of isotherms have been classified into five types (I, II, III, IV and V) using the Brunauer, Demmind, Demming and Teller (BDDT). Type I, II and III isotherms are reversible but Type I isotherms from microporous materials (pore size less than 20Å) can exhibit hysteresis between the adsorption and desorption isotherms. Type IV and V isotherms which are associated with mesoporous materials (pore size between 20 - 500 Å) normally display hysteresis. Hysteresis loops have been identified and classified by Boer into five types (A, B, C, D and E) which can be correlated to pore shapes (Quantachrome Instruments, 2008).

The single point BET method can be used which employs a simplified form of the BET equation and works within the linear region in a BET plot where a single point in the adsorption isotherm can be used. When nitrogen is used as the adsorbate, the *C* value is taken as sufficiently large and intercept in the BET equation can be assumed to be zero. As in this study, single point BET can be carried out using instruments like the Monosorb from Quantachrome which can rapidly and accurately analyse small quantities of sample, less than 1 gram and quantify surface areas as low as $0.1m^2$ irrespective of the adsorbate gas used. Other adsorbates apart from nitrogen can be used provided they are non-corrosive gases like krypton, argon, carbon dioxide. The surface area is directly displayed at the end of the analysis. With Monosorb instruments a gas mixture of known volume is required to carry out surface area measurements *i.e.* nitrogen gas and a carrier gas such as helium which does not adsorb to the surface are required. Changes in the volumes of the adsorbed and desorbed gas and the carrier gas are detected by a thermal conductivity detector that is highly sensitive. Measurements are then compared to a calibration plot which should be linear, obtained by injecting different known volumes of nitrogen and measuring the counts generated (Quantachrome Instruments, 2008; Quantachrome Instruments, 2013). Surface area measurements in this study were carried out by Dr. Belton D., a research fellow within the research group.

2.12. Molecular Dynamics (MD) Computational Simulation

Computational alanine scanning mutagenesis has been used to identify the role of moieties in proteins and peptides by using alanine to replace specific functional groups

(Massova and Kollman, 1999). The significance of the replaced functional groups is determined based on the effect the substitution has on the binding mode of the peptide/protein. Generally, an assumption is made that the mutation only causes localized changes to the conformation of the peptide/protein which do not affect overall binding modes (Massova and Kollman, 1999). MD can be used to theoretically compute the conformations of the original sequence and compare them to alanine mutants while identifying the most stable conformations based on energy minima values. The original sequence and mutant sequences can be built using software such as SYBYL then several rounds of sequence minimization can be performed over time in a vacuum (non-solvated) or in a solvent such as water using MD. The interaction energy should be governed using an appropriate representative force field which can be difficult to develop (Coppage *et al*., 2012; Massova and Kollman, 1999; Pandey *et al*., 2009). The mismatch between the size of protein/peptide moieties and small inorganic ions that may be present in solution and the complexity of the structuring effect of water molecules make theoretical approaches difficult and in need of further development to be able to accurately simulate wet laboratory experimental processes at appropriate length and time scales (Muthukumara, 2009; Unwin, 2007). All computational analysis in this study was carried out by Ramasamy R., who was a fellow student within the research group.

2.13. Quartz Crystal Microbalance with Dissipation Monitoring (QCM-D)

QCM-D is a nanogram sensitive thickness shear mode device able to measure perturbations that occur when vapour is deposited on a quartz crystal surface (sensor) or when a ligand binds to the surface. A sensor which is the substrate for adsorption is made by coating a desired material on a piezoelectric quartz crystal which has a pair of electrodes. Voltage is applied to the sensor which then mechanically oscillates at a certain frequency (f) which is measured. When the power is disconnected, the time taken for this oscillation to stop is measured as dissipation (D). When water and/or a molecule adsorbs to the surface of the sensor, the added mass changes the f and D measured (Dolatshahi-Pirouz *et al.*, 2008; Rodahl *et al*., 1997; Spangler *et al*., 2001; Voinova *et al.*, 2002).

The Sauerbrey equation *(*$\Delta m = -C\Delta f/n$) can be applied to determine the mass of an adsorbed layer in the case where a rigid film is formed which is assumed to be evenly distributed and sufficiently thin (Rodahl *et al*., 1997; Sauerbrey, 1959). In this case the change in mass (Δm) can directly be correlated to the change in frequency (Δf). For a 5 MHz crystal, the mass sensitivity constant, C is 17.7 ng/cm^2. The overtone number is denoted as n of which the 3rd overtone (15 MHz) is chosen when using the Sauerbrey equation (Dolatshahi-Pirouz *et al.,* 2008; Sauerbrey, 1959). For rigid films, the molecule adsorbs flat on the sensor therefore less water is incorporated and dissipation decreases. For soft layers, the Sauerbrey equation cannot be applied as soft layers do not fully couple to crystal oscillation therefore the actual mass adsorbed would be underestimated (Rodahl *et al*., 1997). In the case of soft film formation for example in the upright adsorption of an elongated molecule on a sensor, more water is adsorbed and a soft (viscoelastic) layer is formed increasing dissipation. For soft films, frequency and dissipation measurements at multiple overtones can be applied and combined using a Voigt-based viscoelastic model (Rodahl *et al*., 1997).

2.14. Isothermal Titration Calorimetry (ITC)

The chemical or physical interaction of any two components forming a complex is accompanied by an exchange of heat with the environment, with heat either being adsorbed (endothermic) or released (exothermic). The complex may also further undergo a physical change forming a product in a process which also produces a heat change. Modern ITC instruments are powerful precision devices designed to use power compensation to monitor heat changes that occur when two components interact. An ITC consists of a reference cell and a sample cell which are enclosed in an adiabatic outer shield jacket (Figure 2.14). The cells are made using chemically inert and thermal conducting material such as Hastelloy alloy used in VP-ITC Microcal instruments. The reference cell should contain the solvent in which the component in the sample cell (*i.e.* macromolecule) is dissolved or suspended in. An important component of the instrument is its automated pipette containing a syringe which is filled with a second component (*i.e.* ligand) dissolved in the same solvent used to fill the reference cell and containing the component in the sample cell (Cliff *et al*., 2004; MicroCal, 1998).

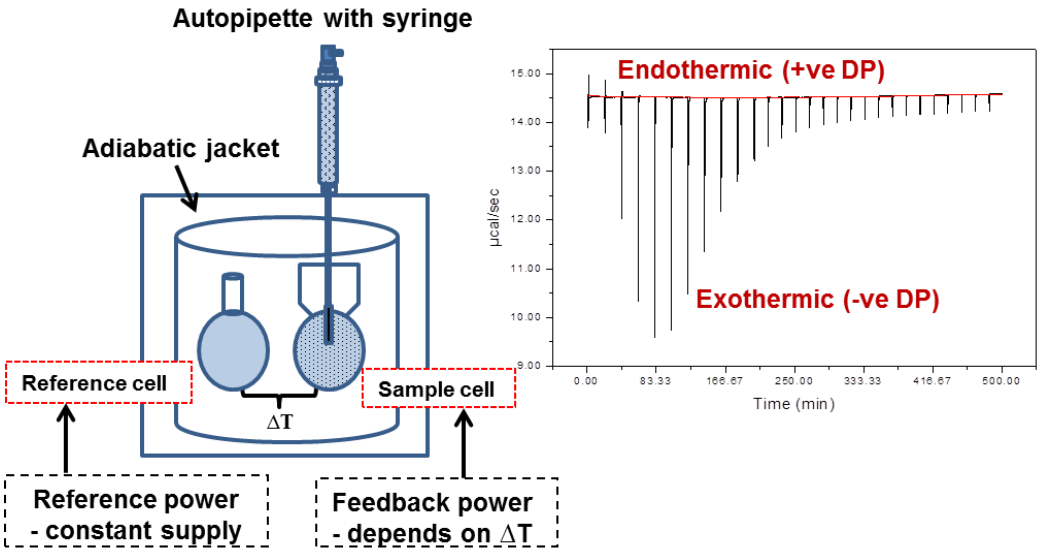

Figure 2.14. A simplified diagram of an ITC instrument showing its components and a representation of raw data

At the start of a measurement, the temperature of the reference cell and the sample cell is at equilibrium. A reference power which is defined by the user is constantly supplied to the reference cell offset heater to maintain a positive differential power (DP) feedback system also acknowledged as the baseline setting (thermal equilibrium). The positive DP can be used to supply compensating power to the sample cell whose temperature changes when a component from the syringe is titrated into the sample cell containing another component with which it is expected to interact. Differences in temperature between the sample cell and the reference cell are monitored using a sensitive thermocouple circuit throughout the experiment. The extent of heat change depends on whether an interaction occurs or not. If no interaction takes place, only heat change as a result of titrating the syringe component into the sample cell component is measured which may be similar to the dilution heat change of titrating the syringe component into the sample cell containing only the solvent. However, if an interaction occurs forming a complex, a greater heat change than dilution heat change occurs causing the sample cell to be either hotter or cooler than the reference cell. If the sample cell is hotter than the reference cell (exothermic reaction) less power will be required to maintain thermal equilibrium between the two cells thus a negative DP (µcal/sec) will

be registered. The opposite happens if the sample cell is cooler than the reference cell (endothermic reaction), more power will be required to maintain thermal equilibrium hence a positive DP will be recorded. The heat signal/power required to return to thermal equilibrium is integrated with respect to time and is directly proportional to the amount of interaction that occurs (Cliff *et al*., 2004; MicroCal, 1998).

The total volume of the component in the syringe can all be injected slowly and continuously into the sample cell component in what is known as the single injection method (SIM). However, the conventional ITC method involves the injection of the total syringe volume in several small aliquots of known volume. With continuous addition of the syringe component into the sample cell component, the cell component eventually becomes saturated at which point the heat signal decreases until only dilution heats are observed (Liang, 2008; Thomson and Ladbury, 2004). The extent of the reaction can therefore be probed per injected aliquot and this heat signal can be described as apparent ΔH (ΔH_{app}) or observed ΔH (ΔH_{obs}) heat change which is a global response, as it includes the sum total of all heat changes. Total heat change is attributed to (i) non-covalent (hydrogen bonding, electrostatic interactions, hydrophobic interactions and van der Waals forces) binding/interaction (ΔH_{bind}) which principally reflect the strength of the interaction (ii) other contributions to heat change such as protonation/ deprotonation events (ΔH_{ion}) and (iii) conformational changes as well as the incorporation or displacement of solvent both of which are reflected in the ΔS of the interaction (Ababou and Ladbury, 2006; Cliff *et al*., 2004; Leavitt and Freire, 2001).

Data analysis can be carried out with the help of software such as Origin to plot and fit data using suitable binding models made available by MicroCal that use a non-linear least-squares algorithm (MicroCal, 2004). After subtracting the baseline experiment (dilution heat change) from the ligand binding experiment, data is plotted as normalized integrated heat change in kcal/mole of injectant against the molar ratio of ligand to macromolecule to obtain the binding isotherm. The equilibrium binding constant (K_B) can then be determined from precise knowledge of the concentration of free and bound ligand. The accuracy of K_B can be evaluated based on a measurement known as the critical parameter (C) which determines the shape of the isotherm and is a product of the total concentration of the cell component, K_B and the stoichiometry (n) and should

ideally lie between 10 and 100 (Cliff *et al*., 2004). The stoichiometry value (*n*) represents the number of binding sites per particle or macromolecule for a specific ligand. *C* values lower than 10 have featureless curves to almost straight lines which imply that there is very little change in enthalpy from one injection to the next hence determining the concentration of bound and free ligand becomes erroneous. On the other extreme scenario where *C* values are higher than 100, the shape of the isotherm tend towards an angular form as saturation occurs too fast in the first few injections equally precluding accurate determination of K_B (Cliff *et al*., 2004; Leavitt and Freire, 2001; Thomson and Ladbury, 2004). From ΔH and K_B, other thermodynamic parameters of interaction; entropy (ΔS) and Gibbs free energy (ΔG) can then be determined using the equation $\Delta G = \Delta H - T\Delta S = -RTlnK_B$ where *T* is the experimental temperature and *R* is the gas constant (Cliff *et al*., 2004; Thomson and Ladbury, 2004). ITC is therefore a powerful technique able to determine all thermodynamic parameters of interaction from one experiment and is the only direct measure of molar enthalpy. It is a highly sensitive tool that can measure as little as 0.1 µcal heat change and can determine binding constants in the millimolar to picomolar range (10^2 to 10^9 M^{-1}). Additional advantages are that ITC does not require labelling or immobilization of the interacting components (Cliff *et al*., 2004).

2.15. References

1. Ababou, A., and Ladbury, J.E., 2006. Survey of the year 2004: literature on applications of isothermal titration calorimetry. *Journal of Molecular Recognition: JMR,* 19 (1), 79-89.
2. Aguilar, M., 2004. *HPLC of Peptides and Proteins.* Springer.
3. Bacsa, B., Horváti, K., Bõsze, S., Andreae, F. and Kappe, C.O., 2008. Solid-phase synthesis of difficult peptide sequences at elevated temperatures: a critical comparison of microwave and conventional heating technologies. *The Journal of Organic Chemistry,* 73 (19), 7532-7542.
4. Boss, C.B., and Fredeen, K.J., 1997. *Concepts, instrumentation and techniques in inductively coupled plasma optical emission spectrometry.* 2nd ed. U.S.A: Perkin Elmer Norwalk.
5. Callister, W.D., 2007. *Materials science and engineering: an introduction.* 7th ed. New York: John Wiley & Sons, Incorporated.
6. Chan, W.C., and White, P.D., 2000. *Fmoc solid phase peptide synthesis.* Oxford University Press.
7. Cliff, M.J., Gutierrez, A. and Ladbury, J.E., 2004. A survey of the year 2003 literature on applications of isothermal titration calorimetry. *Journal of Molecular Recognition: JMR,* 17 (6), 513-523.
8. Coppage, R., Slocik, J.M., Briggs, B.D., Frenkel, A.I., Naik, R.R. and Knecht, M.R., 2012. Determining Peptide Sequence Effects That Control the Size, Structure, and Function of Nanoparticles. *ACS Nano,* 6 (2), 1625-1636.
9. Cudic, M., and Fields, G.B., 2008. Solid-Phase Peptide Synthesis. *In:* Solid-Phase Peptide Synthesis. *Molecular Biomethods Handbook.* Springer, 2008, pp. 515-546.
10. Dixon MC, 2008. Quartz crystal microbalance with dissipation monitoring: enabling real-time characterization of biological materials and their interactions. *Journal of Biomolecular Techniques: JBT,* 19 (3), 151-8.
11. Dolatshahi-Pirouz, A., Rechendorff, K., Hovgaard, M.B., Foss, M., Chevallier, J. and Besenbacher, F., 2008. Bovine serum albumin adsorption on nano-rough platinum surfaces studied by QCM-D. *Colloids and Surfaces.B, Biointerfaces,* 66 (1), 53.
12. Ellis, S.R., Brown, S.H., in het Panhuis, M., Blanksby, S.J. and Mitchell, T.W., 2013. Surface analysis of lipids by mass spectrometry: More than just imaging. *Progress in Lipid Research,* 52 (4), 329-353.
13. Fields, G.B., Lauer-Fields, J.L., Liu, R. and Barany, G., 2002. Principles and practice of solid-phase peptide synthesis. *Synthetic Peptides: A user's Guide,* 2, 93-219.
14. Garcia Martin, F., and Albericio, F., 2008. Solid supports for the synthesis of peptides. From the first resin used to the most sophisticated in the market. *Chimica Oggi,* 26 (4).
15. Glish, G.L., and Vachet, R.W., 2003. The basics of mass spectrometry in the twenty-first century. *Nature Reviews Drug Discovery,* 2 (2), 140-150.
16. Goldstein, J., Newbury, Y, J., D., E., Joy, D., C., Echlin, P., Lyman, C., E., Lifeshin, E., and Sawyer, L., 2003. *Scanning electron microscopy and x-ray microanalysis.* 3rd ed. New York: Kluwer Academic/Plenum Publishers.
17. Hennessy, T.P., Boysen, R.I., Huber, M.I., Unger, K.K. and Hearn, M.T.W., 2003. Peptide mapping by reversed-phase high-performance liquid chromatography employing silica rod monoliths. *Journal of Chromatography A,* 1009 (1–2), 15-28.
18. Honour, J.W., 2006. High-performance liquid chromatography for hormone assay. *Methods in Molecular Biology-Clifton then Totowa-,* 324, 25.
19. Hou, X., and Jones, B.T., 2000. Inductively Coupled Plasma-Optical Emission Spectrometry. *Encyclopedia of Analytical Chemistry*.
20. JEOL, L.T.D., 2013. *Scanning Electron Microscopes (SEM)* [online]. JEOL. Available at: http://www.jeol.co.jp/en/science/sem.html [Accessed 09/20 2013].

21. Jurinke, C., Oeth, P. and van den Boom, D., 2004. MALDI-TOF mass spectrometry. *Molecular Biotechnology,* 26 (2), 147-163.

22. Leavitt, S., and Freire, E., 2001. Direct measurement of protein binding energetics by isothermal titration calorimetry. *Current Opinion in Structural Biology,* 11 (5), 560-566.

23. Liang, Y., 2008. Applications of isothermal titration calorimetry in protein science. *Acta Biochimica Et Biophysica Sinica,* 40 (7), 565-576.

24. Malvern Instruments, 2004. *Zetasizer Nano Series User Manual.* Worcestershire, United Kingdom: Malvern Instruments Ltd.

25. Marvin, L.F., Roberts, M.A. and Fay, L.B., 2003. Matrix-assisted laser desorption/ionization time-of-flight mass spectrometry in clinical chemistry. *Clinica Chimica Acta,* 337 (1), 11-21.

26. Massova, I., and Kollman, P.A., 1999. Computational alanine scanning to probe protein-protein interactions: a novel approach to evaluate binding free energies. *Journal of the American Chemical Society,* 121 (36), 8133-8143.

27. MicroCal, L., 1998. *VP-ITC Microcalorimeter User's Manual* [online]. MicroCal, LLC, Northampton, MA. Available at: http://www.uic.edu/orgs/ctrstbio/manuals/vpitc_manual.pdf [Accessed 09/20 2013].

28. Muthukumara, M., 2009. Theory of competitive adsorption-nucleation in polypeptide-mediated biomineralization. *The Journal of Chemical Physics,* 130, 161101-161105.

29. Pandey, R.B., Heinz, H., Feng, J., Farmer, B.L., Slocik, J.M., Drummy, L.F. and Naik, R.R., 2009. Adsorption of peptides (A3, Flg, Pd2, Pd4) on gold and palladium surfaces by a coarse-grained Monte Carlo simulation. *Physical Chemistry Chemical Physics,* 11 (12), 1989-2001.

30. Pavia, D.L., and Lampman, G.M., 1996. *Introduction to spectroscopy: a guide for students of organic chemistry.* 2nd ed. California: Harcourt Brace College Publishers.

31. Pedersen, S.L., Tofteng, A.P., Malik, L. and Jensen, K.J., 2012. Microwave heating in solid-phase peptide synthesis. *Chemical Society Reviews,* 41 (5), 1826-1844.

32. PerkinElmer, 2010. *Thermogravimetric Analysis (TGA): A Beginner's Guide* [online]. PerkinElmer, Inc, USA. Available at: http://www.perkinelmer.co.uk/CMSResources/Images/44-74556GDE_TGABeginnersGuide.pdf [Accessed 09/29 2013].

33. Quantachrome Instruments, 2013. *Monosorb Rapis Surface Area Analyzer* [online]. Quantachrome Corporation. Available at: http://www.quantachrome.com/pdf_brochures/07109.pdf [Accessed 29/09 2013].

34. Quantachrome Instruments, 2008. *Aurosorb AS-1 AS1Win (21CFR-Part 11 compliant) Gas Sorption System Operation Manual.* Florida, USA: Quantachrome Corporation.

35. Rodahl M, Höök F, Fredriksson C, Keller CA, Krozer A, Brzezinski P, Voinova M and Kasemo B, 1997. Simultaneous frequency and dissipation factor QCM measurements of biomolecular adsorption and cell adhesion. *Faraday Discussions,* (107), 229-46.

36. Sauerbrey, G., 1959. Use of quartz vibration for weighing thin films on a microbalance. *J.Physik,* 155, 206-212.

37. Smith, B.C., 2011. *Fundamentals of Fourier transform infrared spectroscopy.* CRC press.

38. Spangler, B.D., Wilkinson, E.A., Murphy, J.T. and Tyler, B.J., 2001. Comparison of the Spreeta® surface plasmon resonance sensor and a quartz crystal microbalance for detection of Escherichia coli heat-labile enterotoxin. *Analytica Chimica Acta,* 444 (1), 149-161.

39. Stuart, B.H., 2004. *Infrared spectroscopy: fundamentals and applications.* Wiley. com.

40. Tansurat, P., 2007. *Proteomes Proteins Expressed by a Genome* [online]. Bioinformatics world of life. Available at: http://pawatbioinformatics.exteen.com/ [Accessed 09/19 2013].

41. Thomson, J.A., and Ladbury, J.E., 2004. Isothermal titration calorimetry: a tutorial. *Biocalorimetry,* 2, 37-58.

42. Tissue, B.M., 2000. *High-Performance Liquid Chromatography (HPLC)* [online]. The Chemistry Hypermedia Project. Available at: http://www.files.chem.vt.edu/chem-ed/sep/lc/hplc.html [Accessed 09/19 2013].

43. Tripos International, *SYBYL 8.0*. 699 South Hanley Rd., St. Louis, Missouri, 63144, USA.

44. Unwin, P.R., 2007. Concluding RemarksCrystal growth and nucleation: tracking precursors to polymorphs. *Faraday Discussions,* 136, 409-416.

45. Voinova, M., Jonson, M. and Kasemo, B., 2002. 'Missing mass' effect in biosensor's QCM applications. *Biosensors and Bioelectronics,* 17 (10), 835-841.

46. Voutou, B., and Stefaniki, E., 2008. *Electron Microscopy: The Basics.* Greece: National Center for Scientific Research 'Demokritos'.

47. Wang, Z.L., 2000. Transmission Electron Microscopy of Shape-Controlled Nanocrystals and Their Assemblies. *Journal of Physical Chemistry B,* 104, 1153-1175.

48. Wittke, J.H., 2008. *Instrumentation* [online]. http://www4.nau.edu/microanalysis/Microprobe-SEM/Instrumentation.html [Accessed 09/20 2013].

Chapter 3

Peptide Directed Modification of Zinc Oxide Growth Mechanism and Morphology

3.1. Introduction

Like many other materials, the applications of ZnO are highly dependent on the crystal growth process which pervades all aspects of morphology control as discussed briefly in chapter 1. Over the last decade, complex materials with specific composition, size, shape and hierarchical organization have been synthesized from the exploration and application of bio-inspired approaches. Following biomimetic strategies, materials synthesis is usually carried out in aqueous solutions at ambient or nearly ambient reaction conditions (Cölfen and Mann, 2003; Xu *et al*., 2007). Hydrothermal synthesis methods are often used for their low cost and flexibility which allows a variety of parameters to be modulated and manipulated. For example, external factors that can be fine-tuned to achieve desirable materials include the reaction temperature and solution composition which can vary in its chemistry including pH and ionic strength (De Yoreo and Vekilove, 2003; Li *et al*., 1999). Ultimately, the main goal in solution crystallization is to produce particles with the desired morphology and purity in a reproducible manner. To achieve this, an understanding of crystal nucleation and growth processes/mechanisms becomes paramount (Erdemir *et al*., 2009; Li *et al*., 1999; Xu and Wang, 2011).

In aqueous systems, chemical reactions are normally considered to be in a reversible equilibrium and on initiation of synthesis, the free energy of the solution containing reactants is greater than the sum of the free energies of the product phase plus the remaining final solution phase (Gibbs, 1878). Therefore, the driving force of crystal growth in wet chemical methods is the need to minimize the total free energy of the system. Nucleation is the first step in the formation of a new crystalline entity from precursor solutions and is a difficult process to study. A number of theories have been proposed that explain the nucleation processes. One is classical nucleation theory, based

on the view that crystallization is controlled by thermodynamic effects (Becker and Döring, 1935; De Yoreo and Vekilove, 2003; Erdemir *et al*., 2009; Gibbs, 1878; Kashchiev, 2003). Nucleation can be defined as the process of rearrangement or phase transition of atoms or molecules of reactants in a solvated state of high free energy into lower energy clusters of the product phase which are known as nuclei (Cubillas and Anderson, 2010; De Yoreo and Vekilove, 2003; Gibbs, 1878). Although free energy per molecule forming the bulk of the nucleus is less than the free energy of the molecules in the solvated phase, the surface of the nucleus has a high interfacial/'surface' energy and is therefore unstable. This occurs because the molecules at the nucleus surface are weakly bound to neighbouring molecules compared to other molecules in the bulk of the nucleus. Irreversible growth of nuclei into larger and more stable crystals can only occur when growth exceeds the threshold value known as the critical radius (r_c) at which point its free energy decreases (Figure 3.1). This phenomenon is known as the Gibbs Thomson Effect (De Yoreo and Vekilove, 2003; Erdemir *et al*., 2009; Gibbs, 1878; Kashchiev, 2003).

Small nuclei that fail to attain the critical size dissolve back into solution (Cölfen and Mann, 2003; De Yoreo and Vekilove, 2003). The critical size therefore determines the probability of nucleation and its kinetics. The small size of the critical nuclei and the spontaneity of the nucleation process make it a challenging phenomenon to study. The critical size of the nucleus as well as its associated activation energy and the kinetics of nucleation are influenced and can be modulated by the level of supersaturation; defined as the variation in chemical potential between a molecule in solution and a molecule in the bulk of the crystal phase (Cubillas and Anderson, 2010; Gibbs, 1878). Assumptions are made in classical nucleation theory to simplify the process. Some assumptions include; the composition and structure of the nucleus and the bulk crystalline phase are the same, growth of clusters is assumed to occur through sequential addition of monomers, one at a time. The possibility of clusters being in motion, the plausible occurrence of collisions between clusters to form one or the disintegration of a cluster into smaller clusters and the possible formation of intermediate complexes are not considered (Cölfen and Mann, 2003; Erdemir *et al*., 2009).

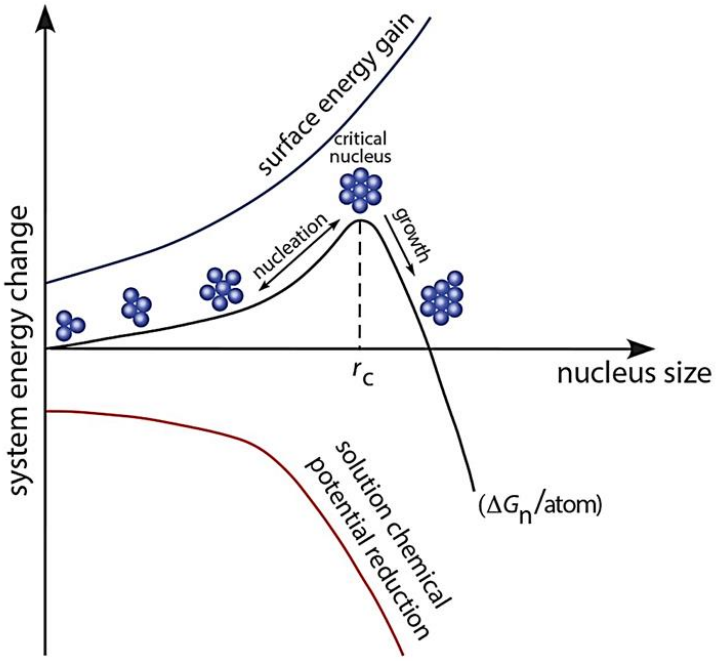

Figure 3.1. Illustration of termodynamically controlled pathway through which molecules in a supersaturated solution form clusters through sequential addition of monomers which at critical radius form a nucleus that can grow irreveribly into solid crystals as described in classical nucleation theory. The surface energy is increased by the formation of an interface and the solution chemical potential decreases with reduction in solute concentration. ΔG_n/atom is the total free energy as each monomer (ion, atom, or molecule) is added to the solid phase. Image has been reproduced from Teng, 2013.

The morphology of an inorganic structure is the amplification of its unit cell structure affected by its external growth environment (Li *et al*., 1999). From a thermodynamic perspective, the slowest growing faces have the lowest surface energy and they eventually surround the growing crystal dictating its morphology as the fast growing, high energy surfaces vanish (Govender *et al*., 2004; Li *et al*., 1999; Peng and Yang, 2009; Song *et al*., 2004; Xu *et al*., 2007). It is in this manner that additives can be used in solution synthesis to modify the morphology of crystals by adsorbing to crystal faces lowering their surface energy and inhibiting their growth (Baruah and Dutta, 2009; Liang *et al*., 2011; Tomczak *et al*., 2009; Wang, 2004).

Observations from biomineralization studies suggest that nucleation may follow more complex routes than proposed by classical nucleation theory (Cölfen and Mann, 2003; Teng, 2013). For example, formation of calcite, vaterite or aragonite occurs through an intermediate, amorphous calcium carbonate which is highly soluble and needs to be kinetically stabilized before being phase transformed into crystals (Cölfen and Mann, 2003; Rieger *et al*., 2007; Unwin, 2007; Xu *et al*., 2007). Alternative non-classical models such as prenucleation cluster aggregation (Gebauer and Cölfen, 2011) and oriented nanocrystal attachment (Penn and Banfield, 1998) have been proposed. Crystal growth is not thought to occur through ordered monomer attachment, instead, the formation of nanoclusters as basic building blocks is considered. Nanoparticles formed from solution self-organise through aggregation or following crystallographic systems to form nanoclusters. Kinetic driving forces are thought to control the process of nucleation and growth (Cölfen and Mann, 2003; Unwin, 2007; Xu *et al*., 2007). Kinetic control is achieved through change of activation energy barriers in the process of nucleation, growth and phase transformation as shown in Figure 3.2.

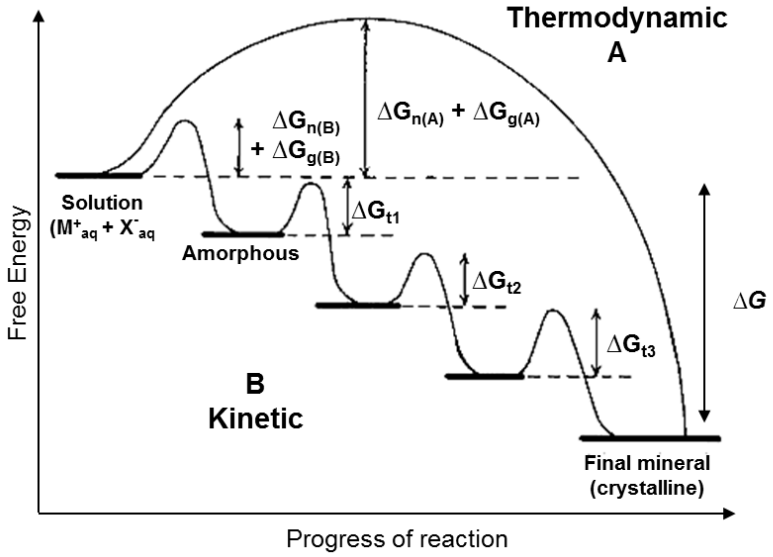

Figure 3.2. Illustration of proposed crystallization pathways; (A) one-step thermodynamic pathway (B) multistep kinetic pathway. Free energy of activation is ($\Delta G_{n\,(A)} + \Delta G_{g(A)}$) or ($\Delta G_{n\,(B)} + \Delta G_{g(B)} + \Delta G_{t1,2,3}$) where nucleation is designated as (n), growth (g) and phase transformation (t). Image has been adapted from Cölfen and Mann, 2003.

Crystallization therefore proceeds through a multi-step pathway involving structural and compositional transformation of amorphous precursors which subsequently crystallize forming intermediates which are transformed to the final crystalline structure (Söhnel and Mullin, 1982; Cölfen and Mann, 2003; Teng, 2013). The progress of phase transformation usually occurs through dissolution and reprecipitation processes depending on the free energy of activation and the solubility of the intermediates (Cölfen and Mann, 2003; De Yoreo and Vekilove, 2003; Liu and Zeng, 2004; Xie *et al*., 2012). By and large, the resulting crystal morphology is governed by contributions from thermodynamic and kinetic effects as well as the formation of defects which can alter the crystal structure (Erdemir *et al*., 2009; Peng and Yang, 2009; Song *et al*., 2004; Xu *et al*., 2007).

There is an increasing substantial body of evidence showing that peptides are able to control crystal morphology by modulating crystal nucleation and controlling the orientation of crystal growth. The anisotropic growth habit of ZnO from precursors in aqueous solution forming elongated hexagonal crystals with the wurtzite structure and the modification of ZnO morphology using ZnO binding peptides have been elaborated in detail in sections 1.3.1 and 1.3.2. Previous studies have demonstrated the formation of low aspect ratio twinned ZnO rods and platelets in the presence of GLHVMHKVAPPR (G-12) and GLHVMHKVAPPR-GGGC (GT-16) peptides respectively, compared to higher aspect ratio twinned ZnO rods formed without additive (Liang *et al*., 2011; Tomczak *et al*., 2009). In these studies, the syntheses were carried out in aqueous solution using zinc nitrate hexahydrate ($Zn(NO_3)_2 \cdot 6H_2O$) as a precursor and hexamethylenetetramine (HMTA). The mechanism of morphology modification was studied and evidence suggested that peptides adsorb to ZnO crystal planes inhibiting anisotropic growth along the *c*-axis. Further evidence for this process was generated using single crystalline (0001) and ($10\bar{1}0$) ZnO films deposited onto silicon wafers using atomic layer deposition (ALD) technique that uses deposition temperature to selectively deposit different crystal orientations. X-ray photoelectron spectroscopy (XPS) was then used to study the adsorption of G-12 and GT-16 peptides individually on specific ZnO planes. Both peptides adsorbed to both crystal planes but GT-16 peptide was found to adsorb more selectively to the (0001) plane which may be attributed to its GGGC tag (Liang *et al*., 2011).

The above findings were in agreement with a theoretical study on the modification of ZnO structure using GT-16 peptide carried out by Muthukumara (2009), who developed a theoretical model based on effective interfacial energies to understand the morphology modification of ZnO using GT-16 peptide and validated the predictions using aspect ratio measurements from experimental findings reported by Tomczak and colleagues (2009). In addition, strong binding behaviour of histidine and cysteine residues to zinc has been observed in zinc finger nucleases (Berg and Godwin, 1997; Dudev and Lim, 2003; Muthukumara, 2009). The flexible spacer in GT-16 peptide between histidine and cysteine, similar to the motif in zinc fingers may facilitate the plane selectivity of GT-16 to the (0001) plane of ZnO that has the highest density of zinc atoms compared to other planes of ZnO (Govender *et al*., 2004; Liang *et al*., 2011; Muthukumara, 2009). Peptides like TVSRPTAPYVTP which have no histidine or cysteine residues have been shown to have no effect on the growth habit and morphology of ZnO (Umetsu *et al*., 2005).

Further studies are needed to identify the nature of these complex phenomena. Specifically, elucidation of the roles of individual amino acid functionalities in ZnO binding peptide sequences, the significance of sequence order and the mechanisms through which peptides interact with ZnO surfaces leading to morphology modification. The detailed study presented in this chapter was designed to investigate the progression of ZnO formation in the absence and presence of peptides using two different hydrothermal synthesis methods with two different precursors. A clearer understanding of peptide-inorganic interactions may generate guiding principles that can be used to advance materials design.

3.2. Materials and Methods

3.2.1. Molecular Dynamics Computational Simulation

Molecular dynamics (MD) and computational alanine scanning mutagenesis have been employed in this study in an effort to understand how peptide sequences are able to specifically bind to certain inorganic materials. G-12 peptide which has been shown to bind to both the (0001) and $(10\bar{1}0)$ planes of ZnO causing aspect ratio reduction during ZnO synthesis (Liang *et al*., 2011) was selected for this study. Computational alanine scanning mutagenesis as well as experimental alanine mutations of sequences can enable one to elucidate on the roles of functional groups of amino acids in a peptide sequence (Coppage *et al*., 2012; Massova and Kollman, 1999; Pandey et al., 2009; Sano *et al*., 2003; Serizawa *et al*., 2007). Replacing amino acids in G-12 peptide sequence may cause localized changes on the peptide structure which may not affect its ability to interact with ZnO surfaces or may significantly modify the peptide's conformation and affects its affinity for the surface. Tripos SYBYL was used to build random structures of G-12 peptide and its mutant sequences after which MD was used to monitor the conformation and stability of each peptide sequence over time. The initial random structures of the original peptide and mutants were dissimilar in conformational energies and structural configurations therefore energy minimization was carried out multiple numbers of times (11 times) in vacuum and after solvation in water. The simple point charge (SPC) water model was used which has the ability to flexibly change the structure of water over time intervals in dynamic simulations (Wasserman *et al*., 1995). The force field AMBER (assisted model building with energy refinement) which can be used to describe the internal free potential energy of a system was used to simulate and minimize G-12 peptide and mutants. This work was carried out within the research group by Ramasamy R.

3.2.2. Synthesis of Peptides and Inorganic Materials

3.2.2.1. Materials for the Synthesis of Peptides

Fmoc-protected amino acids and the activator 2-(1H-benzotriazole-1-yl)-1,1,3,3-tetramethyluronium hexafluorophosphate (HBTU) were obtained from CEM Corporation. Amino acid-preloaded Wang resins used as the solid supports were purchased from Novabiochem. Piperazine, which was used as a deprotecting agent and diisopropyl ethylamine (DIPEA), an activator base were acquired from Sigma-Aldrich. Organic solvents; *N*,*N*-dimethylformamide (DMF), diethyl ether and dichloromethane (DCM) were obtained from Fisher Scientific and *N*-methyl-2-pyrrolidone (NMP) was purchased from Rathburn Chemicals. The cleavage solution was prepared using thioanisole (TIS, C_7H_8S), trifluoroacetic acid (TFA, $C_2HF_3O_2$) and 3,6-dioxa-1,8-octanedithiol (DODT, $C_6H_{14}O_2S_2$), which were all acquired from Sigma-Aldrich. All reagents were utilized in their purchased form. Where required, distilled-deionized water (ddH_2O) having conductivity measurement of less than 1 $\mu S\ cm^{-1}$ at 25 °C was used.

3.2.2.2. Materials for the Synthesis of Zinc Oxide

Precursors, zinc nitrate hexahydrate $Zn(NO_3)_2{\cdot}6H_2O$ with a M_r 297.48, zinc acetate ($Zn(CH_3COO)_2$ with a M_r 183.46 and 1,3-hexamethylenetetramine (HMTA, $C_6H_{12}N_4$) with a M_r 140.19 were purchased from Sigma Aldrich. Concentrated ammonia solution (35%) was purchased from Fisher scientific. Reagents were used without any further treatment.

3.2.2.3. Microwave Assisted Solid Phase Peptide Synthesis

Peptides were synthesized using microwave-assisted solid phase peptide synthesis technique using a CEM Liberty1 Single Channel Automated Peptide Synthesizer. Amino acid coupled resins were used as a solid support and starting point for the synthesis. The chosen preloaded resins were bound to the *C*-terminal amino acid of the peptide to be synthesized. For instance, G-12 (GLHVMHKVAPPR) required Wang resin that was preloaded with arginine that is Fmoc protected. The resin was allowed to

swell in DMF then rinsed using DMF. Thereafter, the *N*-terminal end of the peptide was deprotected using piperazine dissolved in DMF. DMF was again used to rinse the resin before coupling the next amino acid with the help of an activator (HBTU dissolved in DMF) and an activator base (DIEA mixed with NMP). The process of deprotection, rinsing, coupling and rinsing again was repeated until all the amino acids required to make the peptide were all coupled. The final deprotection of the last coupled amino acid was carried out followed by cleavage using a cleaver and scavenger made of a mixture of TFA, TIS, DODT and ddH_2O (v/v% ratio of 91.7/ 1.0/ 4.9/ 2.4 respectively). The cleaved peptide was then precipitated of chilled diethyl ether (100 ml) and washed in diethyl ether (×3) while centrifuging to re-constitute the precipitate. Diethyl ether was evaporated off and the peptide precipitate was lyophilized at -70 °C using a Virtis-110 freeze dryer before analysis using HPLC and Mass spectrometry to determine the purity and molecular weight.

3.2.2.4. Synthesis of ZnO crystals; $Zn(NO_3)_2 \cdot 6H_2O$ and HMTA Reaction

In this study ZnO crystals were grown in aqueous solution as described by Tomczak *et al*., (2009) and Liang *et al*., (2011). Stock solutions of the precursor $Zn(NO_3)_2 \cdot 6H_2O$ (104.17 mM), HMTA (100 mM) and each peptide (30 mM) were prepared. For the control reaction to synthesize ZnO hexagonal twinned rods, an equimolar concentration (50 mM) of zinc ions to base was was attained in the final reaction volume (20 ml) after mixing $Zn(NO_3)_2 \cdot 6H_2O$ (9.6 ml) with HMTA (10 ml) and ddH_2O (0.4 ml) in a glass vial while stirring using a magnetic stirrer. The pH of the reaction solutions at the start of the synthesis was 6.9 ± 0.1. Synthesis was also carried out in the presence of ZnO binding peptides (0.4 ml) in place of ddH_2O used in the control experiment. A predetermined peptide concentration (0.3 mM) was attained in the final reaction volume by adding a higher concentration of the peptide prepared from the peptide stock solution. In some reactions, synthesis was also carried out with different peptide concentrations (0.1 mM and 0.5 mM). The reactions were incubated (20 °C, 24 hrs) after which they were transferred to a water-bath (65 °C, 48 hrs). Each reaction was carried out in triplicate and samples were collected at different time points (24, 25, 48 and 72 hrs) after the start of the reaction. Samples were centrifuged at 13000 rpm for 3 min to separate the precipitate from the supernatant. The supernatants were stored in the fridge for further

analysis using ICP-OES and the precipitates were washed in ddH_2O (×3) and lyophilized before further analysis using SEM, XRD, FTIR and TGA.

3.2.2.5. Synthesis of ZnO crystals; $Zn(CH_3COO)_2$ and NH_3 Reaction

Another technique used to synthesize ZnO crystals in aqueous solution was similar to the method described by Masuda *et al*., (2007). Distilled deionised water was heated in a water-bath (50 °C) and used to prepare a stock solution of the precursor $Zn(CH_3COO)_2$ (30 mM). A solution of NH_3 (31.25 mM) was prepared from an NH_3 (5%) stock solution whose exact concentration was ascertained prior to performing the synthesis experiment by carrying out a back titration using KOH (1M) titrated against a mixture of HCl (1M, 10 ml) and the NH_3 (5%, 2 ml) stock solution with phenolphthalein indicator. For the control reaction, to synthesize twinned ZnO hexagonal rods, ddH_2O (0.4 ml) and NH_3 (31.25 mM, 9.6 ml) were poured into glass vials containing $Zn(CH_3COO)_2$ (30 mM, 10 ml) while stirring using magnetic stirrers. In each reaction, an equimolar concentration (15 mM) of the precursor and the base was obtained. Upon addition of NH_3 (31.25 mM) solution, the mixture became turbid and particles quickly precipitated. Synthesis was also carried out in the presence of peptides. The pH of the solutions in the absence and presence of peptides was 7.0 ± 0.1. Samples were collected immediately after mixing precursors and additives and as reactions progressed (24, 48 and 72 hrs). The supernatants were separated from the precipitates by centrifuging at 13000 rpm for 3 min. The supernatants were stored in the fridge for further analysis using ICP-OES and the precipitates were washed in ddH_2O (×3) and lyophilized before further analysis using SEM, XRD, FTIR and TGA.

3.2.3. Characterization of Peptides and Inorganic Materials

3.2.3.1. Reverse Phase High Performance Liquid Chromatography (RP-HPLC)

The purity of peptides synthesized using SPPS was ascertained using a Dionex RP-HPLC with gradient elution and UV detection at 214 nm, the wavelength at which peptide bonds absorb and with the help of Chromeleon® software. Other analytes apart from the desired peptide that may be detected include sequences that are incompletely

deprotected, truncations, deletions or other impurities. The column stationary phase consisted of tightly packed silica particles functionalized with hydrophobic alkyl chains (C18) that can interact with the analyte. A mobile phase gradient (50%) was created by priming the column with two solvent mixtures of different polarity; (a) mass spectrometry grade distilled water (95%), HPLC grade acetonitrile (5%) and formic acid (0.1%) and (b) mass spectrometry grade distilled water (5%), HPLC grade acetonitrile (95%) and formic acid (0.1%). Both solvent mixtures were degased and primed through the column separately for equal periods of time. The peptide analytes (1 mg/ml) were prepared in a different solvent mixture (mass spectrometry grade ddH_2O (50%), HPLC grade acetonitrile (50%) and formic acid (0.1%)) then injected into the sample loop. Pressure was then used to move the mobile phase and the analyte through the column and the analyte was eluted depending on the strength of the interaction with the stationary phase. The detector gave information on analyte retention time and UV absorption. Data was represented as peaks and the area under each peak was integrated to determine the percentage of the compound in the total analyte and hence the purity of the sample. A control/blank (consisting of the same solvent mixture used to dissolve the peptide) was also analysed for comparison.

3.2.3.2. Matrix-assisted Laser Desorption/Ionization Time-of-flight (MALDI -TOF) Mass Spectrometry

This technique was used to further characterize the peptide synthesized by determining its molecular weight. The instrument model used in this study was a Bruker Ultraflex III which is a MALDI tandem spectrometer designed for automated and high throughput identification of peptides and proteins. The instrument has a high mass resolution at every mass between 700 and 6000 Da (Bruker, 2006). Peptide samples (1 mg/ml) were prepared in a solvent mixture (mass spectrometry grade ddH_2O (50%), HPLC grade acetonitrile (50%) and TFA (0.1%)). A UV-light absorbing matrix which protects the peptide from fragmentation was co-precipitated with the peptide, dried and analysis carried out to determine the mass to charge (*m/z*) ratios of the analytes. The data was collected by a fellow PhD student within the research group, Hickman G.

3.2.3.3. Scanning Electron Microscopy (SEM) Coupled to EDX

SEM and EDX were used for morphology and elemental analysis. The SEM instrument used in this study was a JSM-840A JEOL SEM (Tokyo, Japan). Precipitates that had been collected at different time points during synthesis were washed, lyophilized and redispered in ethanol with sonication for 15 min. Aliquots of the dispersed samples were pipetted onto aluminium stubs and the ethanol allowed to evaporate. The dry samples were sputter coated with gold to make them conductive using an Edwards sputter coater S150B. The instrument was operated following manufacturer's instructions and at an acceleration voltage (A.V.) of 20 kV. The samples were scanned in raster mode and images captured at different magnifications. EDX was used to carry out elemental analysis of the precipitates collected during synthesis using an INCAx-sight Oxford Instrument (United Kingdom) that was coupled to the SEM. Sample preparation for EDX analysis was carried out similarly to that for SEM samples but coating was done using carbon fibre. Carbon is more suitable for EDX analysis because it has fewer peaks than gold which has several peaks that can overlap with peaks of interest from samples. Each spectrum was collected after allowing an elapsed time of 180 s for acquisition at a count rate that was maintained at about 3 kcounts/sec for each sample.

3.2.3.4. X-Ray Diffraction (XRD)

The crystallinity of precipitates was characterized using XRD. Lyophilized samples were closely packed into an aluminium sample holder and the surface smoothed using a glass slide. A PANalytical X'Pert PRO X-ray diffractometer having a Cu K_α radiation operating at a wavelength of 1.54056 Å was used for the analysis. The samples were scanned over a range between 3° to 90° of 2θ with a step size of 0.02° s^{-1}. The experiment was carried out at room temperature with an acceleration voltage of 45 kV and 40 mA filament current. The X'Pert-HighScore Plus (Version 2.0 a) programme was used to analyse and identify peaks in the diffraction patterns.

3.2.3.5. Fourier Transform Infrared Spectroscopy (FTIR)

FTIR KBr was used to identify functional groups present in different samples; precursors used in ZnO synthesis, peptides and precipitates collected during synthesis in the presence and absence of peptides. To prepare samples, 1 mg was mixed with 199 mg of KBr, ground to fine powder then compressed to form a transparent disk using a pellet press applying 10 tons weight. Analysis was carried out using a Nicolet Magna IR-750 FTIR. Samples were scanned 256 times at a resolution of 2 cm^{-1} and the wavenumber range between 4000 to 400 cm^{-1}. The baseline was corrected and the spectra were recorded in absorbance mode.

3.2.3.6. Thermogravimetric Analysis (TGA)

In this study, TGA was used to determine whether the precipitate obtained in ZnO synthesis contained any organic material possibly from the precursors used. The thermal analyzer used was a METTLER TOLEDO TGA/ SDTA 851e. The samples were heated at 30 °C for 10 min after which time the temperature was raised to 900 °C at a steady rate of 10 °C/min then held constantly at 900 °C for a 10 min period. The data was collected and analysis conducted using STARe software.

3.2.3.7. Inductively Coupled Plasma-optical Emission Spectroscopy (ICP-OES)

ICP-OES was used to monitor the synthesis of ZnO by studying changes in the solution. The instrument model used in this study was a Perkin Elmer Inductively Coupled Plasma Optical Emission Spectrometer Optima 2100DV. Samples from triplicate reactions were collected during the course of the synthesis for analysis to determine the concentration of Zn^{2+} ions present in the supernatant. Aliquots drawn from reaction vials were centrifuged at 13,000 rpm for 3 min to separate the supernatant from the pellet. Supernatants were then diluted in 0.9% HCl. Different concentrations of zinc standard solutions were prepared from a zinc atomic adsorption standard solution (1000 ppm) in 0.9% HCl purchased from Sigma Aldrich. A calibration curve was made using the standard solutions of known concentrations and their correlated intensity of light emitted at a wavelength of 206.2 nm. The concentration of the Zn^{2+} present in each sample was extrapolated by comparing the intensity of the light emitted at the same wavelength to the intensities of the calibration standards.

3.3. Results and Discussion

3.3.1. Hydrothermal Synthesis of ZnO; $Zn(NO_3)_2 \cdot 6H_2O$ and HMTA Reaction Method

The deposition of ZnO crystals from aqueous solution requires careful control of condensation and/or hydrolysis reactions of metal ions and/or complexes to form the thermodynamically stable wurtzite structure (Govender *et al.*, 2004). In this study, anisotropic growth of ZnO crystals was carried out in aqueous solution from precursor $Zn(NO_3)_2 \cdot 6H_2O$, the source of Zn^{2+} ions and HMTA which is a water soluble, non-ionic tertiary amine commonly used in ZnO synthesis but whose exact role is unclear (Ashfold *et al*., 2007; McPeak *et al*., 2011; Xu and Wang, 2011). The synthesis process was monitored to understand the growth habits of ZnO without additives such that the effects of incorporating peptides in synthesis could be understood. Samples were collected from the reaction vials during the course of the reaction; at the start of synthesis after mixing precursors then at 24, 25, 48 and 72 hrs (± 2 min). Supernatants and precipitates were separated using centrifugation and treated as described in section 3.2.2.4.

The microstructure of washed precipitates was analysed using SEM. Control samples collected after the incubation period (24 h = $t_{20\,°C}$), before transfer to higher temperature contained gel-like precipitates which under the microscope looked like continuous sheets with rough surfaces (Figure 3.3a). At 25 hrs (24 h, $t_{20\,°C}$ + 1 h, $t_{65\,°C}$), solutions quickly became cloudy and white particles precipitated at the bottom and stuck to the walls of glass vials. When viewed using the microscope, the samples consisted of both continuous sheets and short twinned hexagonal rods (Figure 3.3b). At 48 hrs (24 h, $t_{20\,°C}$ + 24 h, $t_{65\,°C}$), more precipitates were present which largely consisted of slightly tapered twinned hexagonal rods some of which were aggregated (Figure 3.3c, d, e). At 72 hrs (24 h, $t_{20\,°C}$ + 48 h, $t_{65\,°C}$), the precipitates contained hexagonal rods which were further aggregated and bundled together (Figure 3.3f). EDX analysis of the precipitates collected over time confirmed the presence of atomic zinc and oxygen in the samples (Appendix 3.1). These findings coincided with previous studies (Liang *et al*., 2011; Tomczak *et al*., 2009).

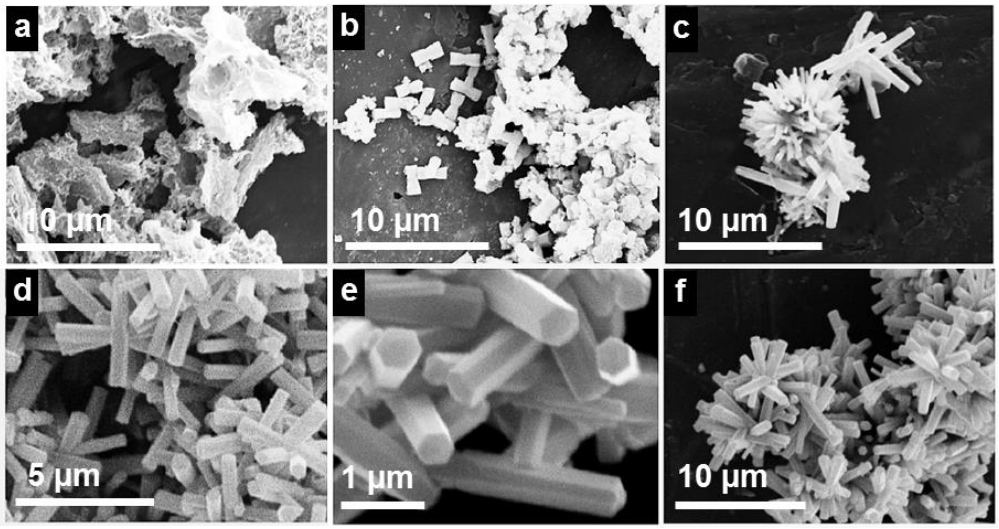

Figure 3.3. SEM micrographs of precipitates synthesized using precursor $Zn(NO_3)_2 \cdot 6H_2O$ and HMTA collected at (a) 24 hrs, (b) 25 hrs, (c-e) 48 hrs and (f) 72 hrs. Precipitates collected at 48 hrs of synthesis consisted of slightly tapered hexagonal twinned rods with an aspect ratio = L/D Avg 8.9 ± 3.3. Scale bars; (a-c) 10 µm, (d) 5 µm, (e) 1 µm, (f) 10 µm.

ICP-OES was used to quantify the percentage of Zn^{2+} ions present in the supernatant over reaction time to monitor its consumption during the formation of precipitates (Figure 3.4). A decrease in the amount of Zn^{2+} in solution from precursor $Zn(NO_3)_2 \cdot 6H_2O$ was observed and the rate at which it was consumed increased with the increase in temperature from 20 °C to 65 °C. These results are in agreement with previous findings where the consumption of Zn^{2+} in this reaction was monitored from samples collected at the same time intervals for a longer period up to 198 hrs which reported that a minimal amount of Zn^{2+} (~10%) was consumed during the first 24 hrs of synthesis at 20 °C followed by a steady increase in Zn^{2+} consumption with an increase in temperature to 65 °C until an equilibrium state was attained where about 60% of Zn^{2+} was consumed (Liang *et al*., 2011).

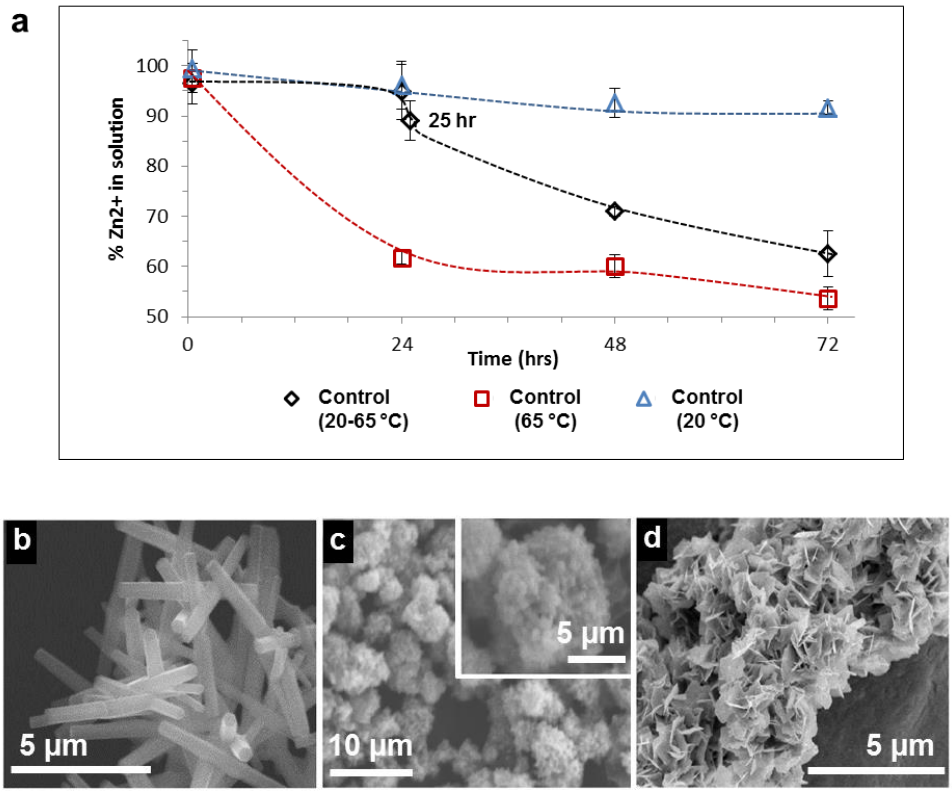

Figure 3.4. (a) Percentage concentration of Zn^{2+} ions in supernatants obtained from samples collected during the course of ZnO synthesis reactions using precursor $Zn(NO_3)_2{\cdot}6H_2O$ and HMTA quantified using inductively coupled plasma-optical emission spectroscopy (ICP-OES). (b-d) SEM micrograph of (b) 48-hr (24 h, $t_{20\ °C}$ + 24 h, $t_{65\ °C}$) precipitates consisting of twinned hexagonal rods, (c) 48-hr ($t_{65\ °C}$) precipitates consisting of aggregated crystals with unclearly defined morphologies, (d) 48-hr ($t_{20\ °C}$) precipitate consisting of layered structures. Scale bars; (a) 5 µm, (b) 10 µm, inset 5 µm and (c) 5 µm.

The incubation period (24 h = $t_{20\ °C}$) was needed for the nucleation and growth of twinned hexagonal crystal rods (Figure 3.4a, b). Where synthesis commenced at higher temperatures *i.e.* 65 °C, an immediate and fast consumption rate of Zn^{2+} ions occured as observed from ICP-OES analysis of the modified reactions (Figure 3.4a). When synthesis was started at 65 °C, the solution rapidly became cloudy and a white precipitate was formed. The precipitate consisted of aggregates which did not develop into the desired orientation of twinned hexagonal crystals (Figure 3.4c). Similarly when the reaction was maintained at 20 °C throughout, only layered structures were formed and a minimal amount of Zn^{2+} ions (~10%) was consumed (Figure 3.4d).

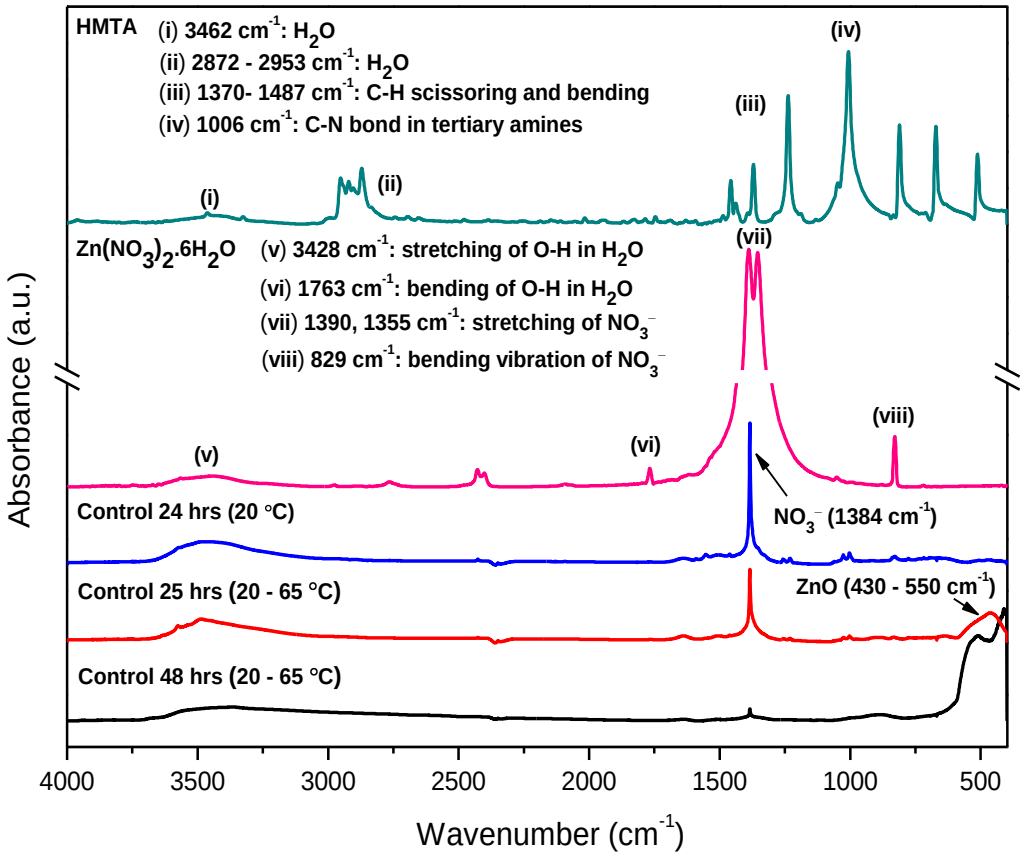

Figure 3.5. FTIR spectra of reagents used in ZnO synthesis; precursor $Zn(NO_3)_2 \cdot 6H_2O$ and HMTA and precipitates collected during the reaction at time 24, 25 and 48 hrs. ZnO began to form only after the reaction temperature was increased to 65 °C. The NO_3^- peak at 1384 cm^{-1} decreases with time as ZnO was formed.

The formation of ZnO was confirmed using FTIR (Figure 3.5) and XRD analysis (Figure 3.6). The FTIR absorption band characteristic of ZnO stretching mode was observed in the region of 430 to 550 cm^{-1}. FTIR analysis of precursor $Zn(NO_3)_2 \cdot 6H_2O$, HMTA and the precipitates collected during ZnO synthesis also gave evidence of precursor use in the process of crystal growth in solution. FTIR analysis of precursor $Zn(NO_3)_2 \cdot 6H_2O$ revealed a broad peak at 3428 cm^{-1} and a peak at 1763 cm^{-1} that can be attributed to stretching and bending vibrations of O-H bonds in water. The peaks at 1355 cm^{-1} and 1390 cm^{-1} can be indexed to asymmetric stretching of nitrate groups (NO_3^-) whereas the peak at 829 cm^{-1} characterizes the bending of NO_3^-. The spectrum of HMTA has characteristic peaks at 3462 cm^{-1} from water, 2872 - 2953 cm^{-1} which can be attributed to C-H stretching vibrations, 1370 - 1487 cm^{-1} which is characteristic of C-H scissoring and bending vibrations and 1006 cm^{-1} present because of the C-N bond in

tertiary amines. The gel-like precipitate collected at 24 hrs mainly had a sharp peak in its spectrum at 1384 cm $^{-1}$ characteristic of NO_3^- (Figure 3.5).

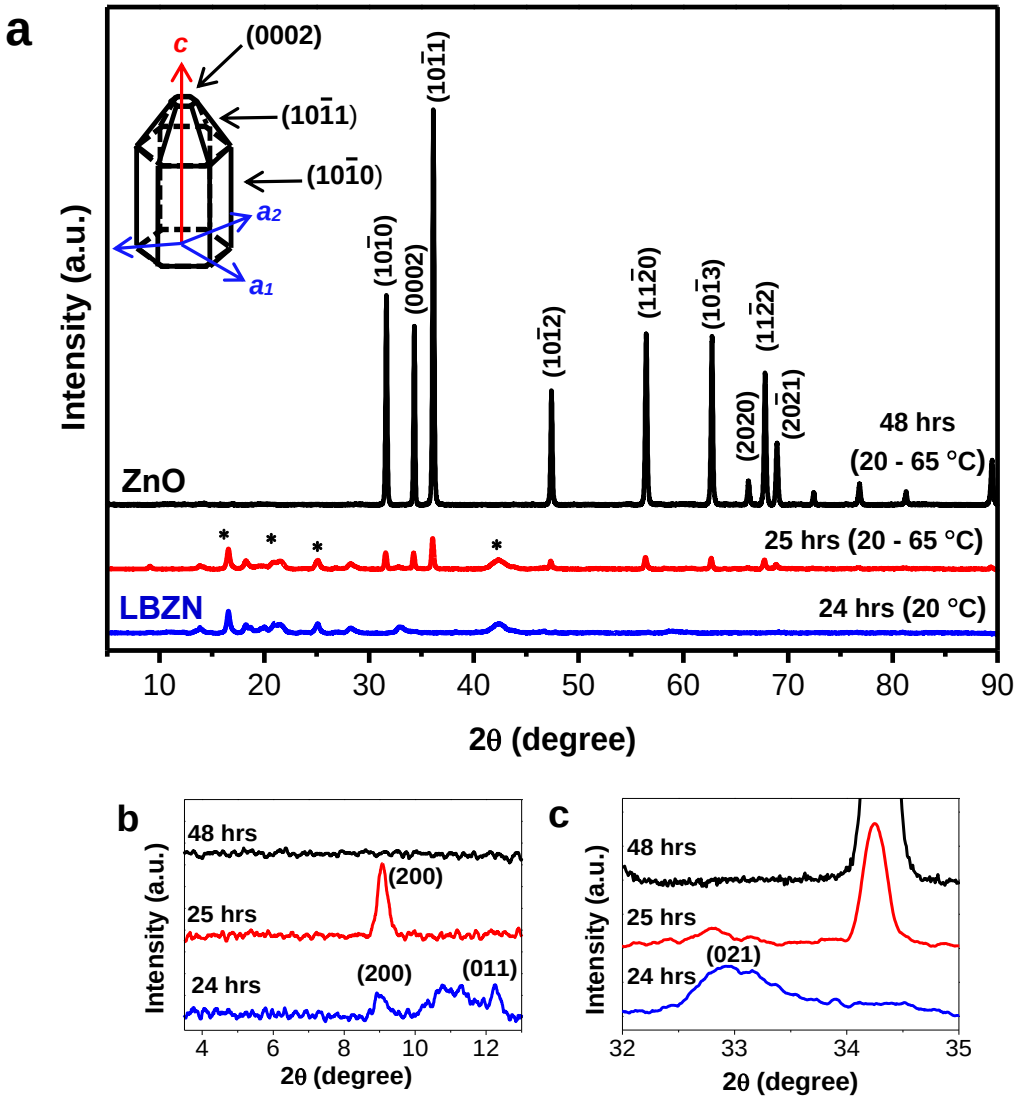

Figure 3.6. (a-c) X-ray diffractograms of 24-hr, 25-hr and 48-hr precipitates synthesized using the precursor $Zn(NO_3)_2 \cdot 6H_2O$ and HMTA. (a) Inset is a schematic representation of the crystal planes of ZnO hexagonal rods with the wurtzite structure which is the predominant phase in 48-hr precipitates. (b, c) The regions from 4° to 13° and from 32° to 35° of 2θ are highlighted where the peaks found confirm the presence of LBZN. Conventional three digit miller indices have been used to label/designate directions, point locations and planes of LBZN. Indices of hexagonal crystals are uniquely designated using a four-axis Miller-Bravis coordinate system because axes of the crystal planes are not mutually perpendicular. **(*)** denotes peaks from the polypropylene sample holder.

XRD analysis of the 24-hr gel-like precipitate confirmed the presence of an intermediate with diffractogram peaks at ~9° and at ~32.9° of 2θ (Figure 3.6) which can be attributed to the presence of a nitrate containing crystalline LBZs (Baier *et al.,* 2012; Inoue and Fujihara, 2011; Li *et al*., 2012). This LBZs could have been zinc hydroxide nitrate, $Zn_5(OH)_8(NO_3)\cdot 2H_2O$ which has a brucite like, $Mg(OH)_2$ like structure that can be described as stacked layers of positively charged metal hydroxides intercalated with hydrated anions that balance the charge of the structure, all held together using electrostatic attraction and hydrogen bonding as illustrated in Appendix 3.2 (Cavani *et al*., 1991; Newman and Jones, 1999). The peak at ~9° was attributed to the (200) plane and the peak at ~32.9° of 2θ to the (021) plane of layered basic zinc nitrate (LBZN) (Ahmadi *et al*., 2013). In the FTIR spectrum of the gel-like precipitate, a broad peak at 3359 cm^{-1} was also present indicating that water molecules may have been adsorbed on the surfaces or was present in the interlayer spaces of the LBZN. Research on the possible applications of such layered hydroxide salts that have ion exchange properties and intercalation capacity is increasing *i.e.* as matrices of functional nanocomposites with other materials like polymers and as catalysts (Li *et al*., 2012; Newman and Jones, 1999; Tronto *et al*., 2013). Phase transformation of the intermediate LBZN only occurred after the temperature of the reaction was raised from 20 °C to 65 °C. This was confirmed from XRD analysis of precipitates from reactions maintained at 20 °C up to 72 hrs where only peaks of LBZN were present (Appendix 3.3).

There have been controversial views in literature about the role of HMTA in the solution synthesis of ZnO. According to some authors, upon heating, HMTA is slowly hydrolysed in water to form ammonia (NH_3) and formaldehyde (HCHO) (Ashfold *et al*., 2007; Baruah and Dutta, 2009; Tada, 1960; Vayssieres, 2003). Ammonia is thought to have two roles in ZnO synthesis, it may coordinate with and stabilize aqueous Zn^{2+} or it may be hydrolysed to form hydroxide ions (OH^-) which are required to drive the process of ZnO precipitation. Hydroxide ions ions form a basic environment needed for the formation of zinc hydroxide ($Zn(OH)_2$). At the pH conditions buffered by HMTA, $Zn(OH)_2$ has minimum solubility and is precipitated as a solid monomer which is then dehydrated to form ZnO (Ashfold *et al*., 2007; Govender *et al*., 2004; Jang *et al*., 2012; Xu and Wang, 2011). When the critical radius of the ZnO nuclei is achieved, precursor molecules continue to adsorb to the growing crystals. The resultant morphology is

dictated by the need to minimize the surface energy of the crystals. Anisotropic growth of ZnO hexagonal rods occurs as precursor molecules adsorb to the polar planes of the crystal which have the highest surface energy (Govender *et al*., 2004; Li *et al*., 1999; Peng and Yang, 2009; Song *et al*., 2004; Xu *et al*., 2007). Slow hydrolysis of HMTA is critical because fast hydrolysis would lead to formation of a large amount of OH^- ions which would quickly raise the pH environment and cause rapid precipitation of unoriented ZnO structures (Xu and Wang, 2011). An overly simplified representation of the chemical reactions involved in the formation of ZnO using $Zn(NO_3)_2 \cdot 6H_2O$ and HMTA have been summarized in the following equations (Jang *et al*., 2012; Xu and Wang, 2011).

$$C_6H_{12}N_4 + 6H_2O \rightleftharpoons 6CH_2O + 4NH_3 \qquad (1)$$

$$NH_3 + H_2O \rightleftharpoons NH_4^+ + OH^- \qquad (2)$$

$$Zn^{2+} + 4OH^- \rightleftharpoons Zn(OH)_4^{2-} \qquad (3)$$

$$Zn(OH)_4^{2-} \rightleftharpoons Zn(OH)_2 + 2OH^- \qquad (4)$$

$$Zn(OH)_2 \rightleftharpoons ZnO + 2H_2O \qquad (5)$$

Sugunan and co-workers had a different view on the role of HMTA. They used FTIR (ATR) analysis to argue that HMTA does not decompose on heating to 65 °C and concluded that HMTA, which is a non-polar chelating agent may preferably absorb to and cap the non-polar ZnO $(10\bar{1}0)$ plane aiding in the anisotropic growth of ZnO forming nanowires (Sugunan *et al.,* 2006). Sugunan and co-workers also demonstrated that preheating the chemical bath to decompose HMTA before seeding the growth of ZnO did not affect the resultant ZnO morphology thus slow degradation of HMTA and release of OH^- was not important for morphology control (Sugunan *et al.,* 2006). Elsewhere, McPeak and colleagues (2011) demonstrated that HMTA did not complex with Zn^{2+} ions in solution by studying the species in solution during chemical bath deposition of ZnO using $Zn(NO_3)_2$ and HMTA using in situ X-ray absorption near edge structure (XANES) spectroscopy. They also demonstrated that HMTA did not adsorb to the planes of ZnO by studying the surface of ZnO using FTIR (McPeak *et al*., 2011). Furthermore they carried out ZnO synthesis without HMTA or ammonia. In its place, a

buffer which could not form a metal ion complex with the ZnO surface was used to maintain the same pH conditions. ZnO nanowires similar to those synthesized in the presence of HMTA were formed (McPeak *et al*., 2011). Their findings contradicted the results by Sugunan and co-workers (2006) but were in agreement with other studies that concluded that the role of HMTA is to control the saturation index of ZnO and to buffer the solution pH (Ashfold *et al*., 2007; Govender *et al*., 2004; Jang *et al*., 2012; McPeak *et al*., 2011). From FTIR (KBr) analysis in this study, the tertiary amine (~1006 cm^{-1}) of HMTA was not detected in the ZnO precipitate formed at 48 hrs of synthesis (Figure 3.5). We therefore concluded that HMTA does not adsorb to the surface of ZnO or precipitate with the synthesized crystals.

Here, a detailed study on the effects of incorporating peptides as additives in the synthesis of ZnO has been carried out. G-12 and GT-16 which were previously identified as ZnO binding peptides have been used in this study as control reactions whose effects on the growth and morphology of ZnO have already been studied using the $Zn(NO_3)_2 \cdot 6H_2O$ and HMTA reaction method (Liang *et al*., 2011; Tomczak *et al*., 2009). Exclusive to this study, alanine mutants of G-12 peptide selected after computational studies which were carried out by Ramasamy R. have been used in the synthesis of ZnO. Also unique to this study, the growth habit of ZnO in the presence of G-12 peptide and selected alanine mutants have been compared using two different synthesis methods; $Zn(NO_3)_2 \cdot 6H_2O$ and HMTA reaction method (Tomczak *et al*., 2009) and $Zn(CH_3COO)_2$ and NH_3 reaction method (Masuda *et al*., 2007).

3.3.2. Molecular Dynamics (MD) Simulations of G-12 Peptide and Mutants

The average conformational energy of G-12 and its mutants were computed after several rounds of energy minimization in solvated and non-solvated states using MD. Sequences with the lowest values of conformational energy are thought to be more stable than those with higher energy values and are also thought to be the most plausible inorganic binding configurations (Evans *et al*., 2008; Oren *et al*., 2005). Table 3.1 lists the conformational energy of G-12 and its alanine mutants after energy minimization in solvated and non-solvated states using MD. The data reported is an average of minimization repeated 11 times for each sequence. A stability score has been used to

order the sequences from the most stable to the least stable in the analysis carried out in the solvated as well as in the non-solvated state for comparison purposes.

Table 3.1. Conformational energy (kcals/mol) of G-12 peptide and its alanine mutants obtained after minimization in vacuum (non-solvated) and in water (solvated) using MD.

Peptide name	Sequence	Minimization in vacuum (kcals/mol)	Stability score	Minimization with water (kcals/mol)	Stability score	Total stability score	Inference
G-12	**GLHVMHKVAPPR**	**-77.395**	**6**	**-1276.716**	**7**	**13**	
G-12A1	**A**LHVMHKVAPPR	-69.376	11	-1274.426	8	19	
G-12A2	G**A**HVMHKVAPPR	-75.394	9	-1267.645	9	18	
G-12A3	GL**A**VMHKVAPPR	-86.987	3	-1294.814	4	7	
G-12A4	GLH**A**MHKVAPPR	-76.520	7	-1279.474	6	13	
G-12A5	GLHV**A**HKVAPPR	-74.035	10	-1296.611	3	13	
G-12A6	**GLHVM<u>A</u>KVAPPR**	**-91.851**	**2**	**-1317.375**	**2**	**4**	**Most Stable**
G-12A7	GLHVMH**A**VAPPR	-83.353	5	-1247.708	10	15	
G-12A8	GLHVMHK**A**APPR	-75.944	8	-1287.953	5	13	
G-12A10	GLHVMHKVA**A**PR	-92.691	1	-1228.218	11	12	
G-12A11	**GLHVMHKVAP<u>A</u>R**	**-85.248**	**4**	**-1351.661**	**1**	**5**	
G-12A12	**GLHVMHKVAPP<u>A</u>**	**-52.985**	**12**	**-1226.368**	**12**	**24**	**Least Stable**

The energy values were averaged after minimization was repeated 11 times for each sequence. The sequence with the lowest energy minima is thought to be the most stable. A stability score has been assigned for comparison purposes ordering the sequences from the most stable (1) to least stable (12) according to conformational energy values. The stability score from minimization in vacuum and with water have been added to give the total stability score to show the most stable sequence (lowest total value) and lest stable sequence (greatest total value).

In vacuum, the most stable conformations with the lowest conformational energies were G-12A10 followed by G-12A6 then G-12A3 while in water the most stable sequences were G-12A11 followed by G-12A6 then G-12A5. Scoring the total stability of the sequences in both solvated and non-solvated states indicates that G-12A6 and G-12A11 may be the most stable sequences whereas G-12A12 sequence may be the most unstable sequence. Based on these findings, G-12A6, G-12A11 and G-12A12 were selected

together with the original G-12 peptide for further investigation to compare the theoretical computational outcomes to experimental findings. Table 3.2 lists some of the properties of the selected peptide sequences. These sequences were synthesized using microwave assisted solid phase peptide synthesis technique. The peptides used in this study had purity of 80% and above determined using HPLC and their molecular weight was ascertained using mass spectrometry (Appendix 3.4).

Table 3.2. Properties of ZnO binding peptides and mutants synthesized using SPPS and used in hydrothermal synthesis of ZnO.

ZnO Binding Peptides Sequence	Sequence Name	[a]pI (pH unit)	[a]Net charge at pH 7	Non-polar no charge	Polar no charge	Polar +ve charge	Polar -ve charge
GLHVMHKVAPPR	G-12	11.49	2.2	GLVMVAPP	-	**HH**KR	-
GLHVMHKVAPPR-GGGC	GT-16	10.11	2.1	GLVMVAPPGGG	C	**HH**KR	-
GLHVMAKVAPPR	G-12A6	11.49	2.1	GLVMAVAPP	-	**H**KR	-
GLHVMHKVAPAR	G-12A11	11.49	2.2	GLVMVAAP	-	**HH**KR	-
GLHVMHKVAPPA	G-12A12	10.10	1.2	GLVMVAPPA	-	**HH**K	-

[a] Isoelectric point (pI) and the net charge of the peptides at pH 7 was calculated using peptide property calculator Innovagen.

3.3.3. Synthesis of ZnO in the Presence of G-12 Peptide and Selected Mutant Peptides

Synthesis of ZnO crystals using precursor $Zn(NO_3)_2 \cdot 6H_2O$ and HMTA was carried out in the same manner as the control reaction previously described but now in the presence of G-12 and each of the selected alanine mutants; G-12A6, G-12A11 and G-12A12 in separate reactions. In each reaction, a peptide concentration of 0.3 mM was used, which had been shown to significantly reduce the aspect ratio of ZnO crystals in previous studies with G-12 (Liang *et al*., 2011). Collected samples were characterized as before. In the synthesis reaction without peptide, after the nucleation period (24 h = $t_{20\ ^\circ C}$), reaction solutions contained a gel-like precipitate which was confirmed to be a nitrate containing LBZs using XRD, FTIR and SEM analysis. However, in the presence of all peptides, the solutions remained clear during the 24 hr nucleation period. Aliquots of the solutions were dried on aluminium stubs and observed using SEM. The solutions were found to contain layered structures similar to LBZN observed in the control gel

like precipitate with the exception of the synthesis solution with G-12A6 peptide where a distinct morphology of precipitates was observed *i.e.* microspheres with rough porous surfaces that varied in size from as large as 50 µm to as small as 5 µm, some of which appeared to be fused together and others which were broken apart (Figure 3.7). The presence of peptides appeared to have reduced the amount of intermediate product formed during the nucleation period and in the presence of G-12A6, the morphology of the product had been altered.

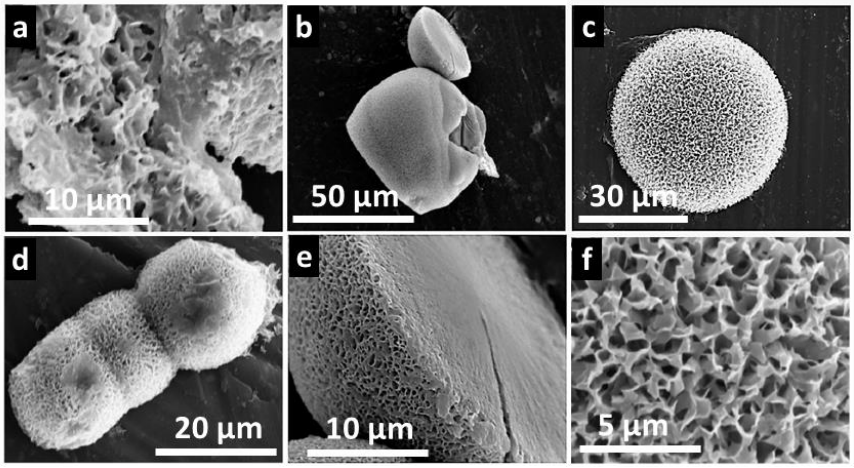

Figure 3.7. SEM micrographs showing the morphology of precipitates present in samples synthesized using precursor $Zn(NO_3)_2 \cdot 6H_2O$ and HMTA and (a) 0.3 mM G-12 (b - f) 0.3 mM G-12A6, all collected at 24 hrs of synthesis at 20 °C. Precipitates in samples synthesized with G-12, G-12A11 and G-12A12 had layered structures similar to the structure of LBZN formed in the control synthesis without peptide. Syntheses in the presence of G-12A6 lead to the formation of microspheres that appeared to have porous like surfaces and were more solid towards the centres. Some of the microspheres were fused and some were broken apart. Scale bars; (a) 10 µm, (b) 50 µm, (c) 30 µm (d) 20 µm, (e) 10 µm, (f) 5 µm.

When the temperature of the reactions was increased to 65 °C, all solutions became cloudy and solid white precipitates were formed. Samples collected at 48 hrs (24 h, $t_{20\,°C}$ + 24 h, $t_{65\,°C}$) of synthesis in the presence of G-12 consisted of low aspect ratio (L/D = 2.16 ± 0.86) short twinned hexagonal rods (Figure 3.8b). Their aspect ratio was significantly lower than those of the twinned hexagonal rods (L/D = 8.92 ± 3.26) formed without peptide (Figure 3.8 a). These findings were in agreement with previous studies where the observed aspect ratio reduction was attributed to adsorption of G-12 peptide to the (0001) and $(10\bar{1}0)$ planes of ZnO (Liang *et al.*, 2011). The crystal structures formed at 48 hrs of synthesis in the presence of mutants G-12A11 (Figure 3.4e) and G-

12A12 (Figure 3.4f) appeared to be very similar to those synthesized with G-12. However, in the presence of G-12A6 peptide, the morphology of the crystals was distinctively different having microspheres with porous rough surfaces and hexagonal rods, many of which were not twinned. In all samples, aggregation was present and some crystals did not have well defined crystal structure.

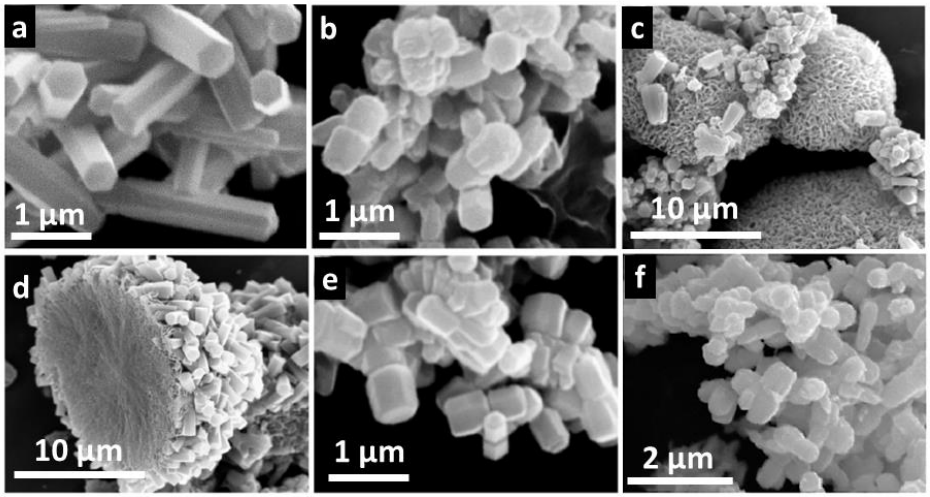

Figure 3.8. SEM micrographs ZnO crystals synthesized using $Zn(NO_3)_2 \cdot 6H_2O$ and HMTA, (a) control experiment, synthesis without peptide forming long hexagonal rods, L/D = 8.92 ± 3.26, (b) synthesis in the presence of 0.3 mM G-12 as a growth modifier forming short hexagonal twinned rods, L/D = 2.16 ± 0.86, (c-d) synthesis in the presence 0.3 mM G-12A6 forming porous microspheres and hexagonal rods some of which are attached to the surface of the microspheres. The aspect ratio (L/D) of the loose and attached rods was 2.05 ± 0.82, (e) synthesis in the presence of 0.3 mM G-12A11 peptide as a growth modifier forming short hexagonal twinned rods, L/D = 1.89 ± 0.77, (f) synthesis in the presence of 0.3 mM G-12A12 as a growth modifier forming short hexagonal twinned rods, L/D = 2.25 ± 0.72. All samples were collected at 48 hrs of synthesis and the aspect ratio was measured from 50 crystals, Scale bar; (a) 1 µm, (b) 1 µm, (c) 10 µm , (d) 10 µm, (e) 1 µm, (f) 2 µm.

XRD analysis confirmed that wurtzite structured ZnO was the principle component in all 48-hr precipitates synthesised with all the peptides (Figure 3.9). No additional peaks were detected suggesting that the microspheres present in G-12A6 synthesized samples had similar crystallography to the ZnO hexagonal rods. EDX analysis confirmed the presence of atomic zinc and oxygen in both ZnO rods and the microspheres (Appendix 3.5). ICP-OES analysis showed that the peptides did not significantly alter the kinetics of Zn^{2+} consumption in ZnO synthesis (Appendix 3.6). The observed modifications in

the growth habit and morphology of ZnO was also confirmed by repeating the synthesis using G-12A6 peptide purchased from Pepceuticals, Leicester who provided HPLC and mass spectrometric evidence for the composition and purity level of the peptide.

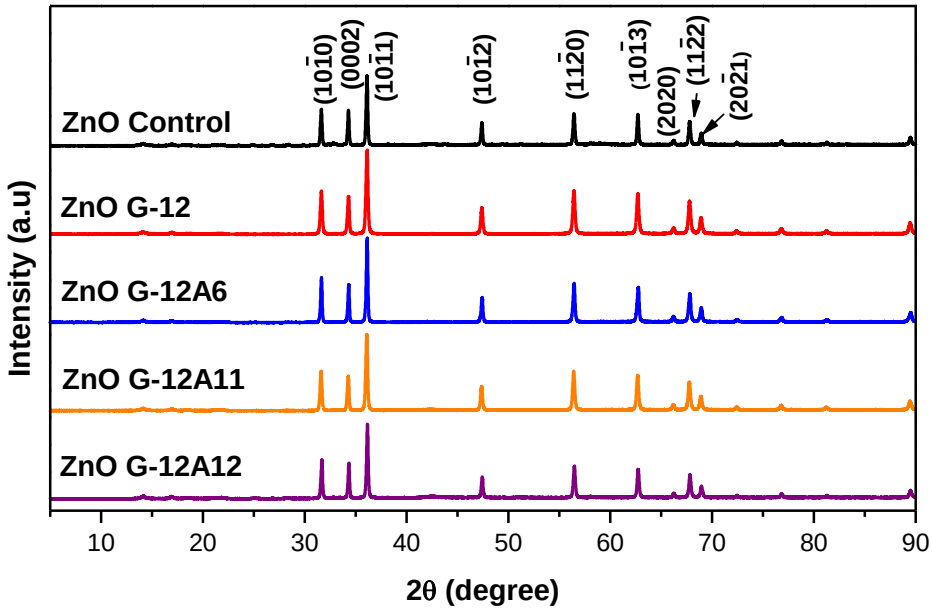

Figure 3.9. X-ray diffractograms of 48-hr precipitates synthesized using $Zn(NO_3)_2{\cdot}6H_2O$ and HMTA in the presence of 0.3 mM G-12 and alanine mutants; G-12A6, G-12A11 and G-12A12. **(*)** denotes peaks from the polypropylene sample holder.

Previous TGA studies showed that ZnO crystals synthesized with GT-16 peptide had significantly more organic matter than the crystals synthesized with G-12 peptide (Liang *et al*., 2011). The high organic content in GT-16 samples was correlated to its ability to adsorb to ZnO crystals planes modifying the growth process to form ZnO twined platelets (Liang *et al*., 2011). TGA analysis of crystals synthesized with the different peptides (G-12 peptide and selected mutant sequences) was carried out up to a temperature of 900 °C to determine if there were differences in the organic content of the samples which may give an indication as to how the observed morphology modification occurred. ZnO is known to decompose at a temperature of about 1975 °C (Oka *et al.*, 2002), therefore the inorganic weight component is not degraded at the temperatures employed. For comparison, TGA analysis was also carried out for the ZnO rods synthesized without peptide and ZnO platelets synthesized using the same reaction process but in the presence of 0.3 mM GT-16 (Appendix 3.7).

TGA weight loss data (Appendix 3.8a), plotted as 1st derivative [d(weight)/d(time)] against temperature was divided into three sections, (i) weight loss observed from 30-100 °C, attributed to loss of physisorbed water, (ii) weight loss observed from 100 -250 °C, attributed to the removal or chemisorbed water and dehydroxylation of zinc hydroxide forming ZnO (iii) weight loss observed from 250 - 700 °C, attributed to the decomposition of organic matter (Hosono *et al*., 2004; Wang *et al*., 2011). A temperature of 700 °C was needed for complete degradation of peptides releasing volatile species including carbon dioxide gas (Appendix 3.8 b). Overall, the organic weight component in all the samples was low but the amount in all the samples synthesized with the different peptides was significantly greater (p value < 0.05, 95% CI, $n = 3$) than in the ZnO crystals synthesized without peptide (Figure 3.10). This suggests that peptides were adsorbed to the precipitates. Again, ZnO precipitates synthesized with GT-16 peptide were seen to contain the highest organic weight component which may have caused the greater extent in aspect ratio reduction observed (Appendix 3.7). There was, however, no particularly distinct dissimilarity in the amount of organic matter present in ZnO precipitates synthesized using G-12A6 compared to G-12 and the other examined mutants (G-12A11 and G-12A12) that could directly be correlated to, or give an indication of the possible cause for the formation of the observed microspheres.

Nevertheless, we can deduce that the adsorption growth inhibition mechanism (Muthukumara, 2009; Liang *et al*., 2011) occurred because ZnO rods with reduced aspect ratios were present in all the samples synthesized with the different peptides. However, in the case of synthesis with G-12A6, the formation of microspheres suggests that for some nuclei, anisotropic growth of ZnO along its *c*-axis was prevented and instead isotropic growth took place. Further experiments were designed to investigate this phenomenon by carrying out ZnO synthesis using G-12A6 at different concentrations (0.1 mM, 0.3 mM and 0.5 mM) and comparing the finding with parallel experiments using the original G-12 peptide. Furthermore, synthesis was carried out using two different methods with different precursors. In addition to the $Zn(NO_3)_2{\cdot}6H_2O$ and HMTA synthesis method, ZnO was synthesized using $Zn(CH_3COO)_2$ and NH_3 solution reaction in a similar method to that previously described by Masuda *et al*., (2007).

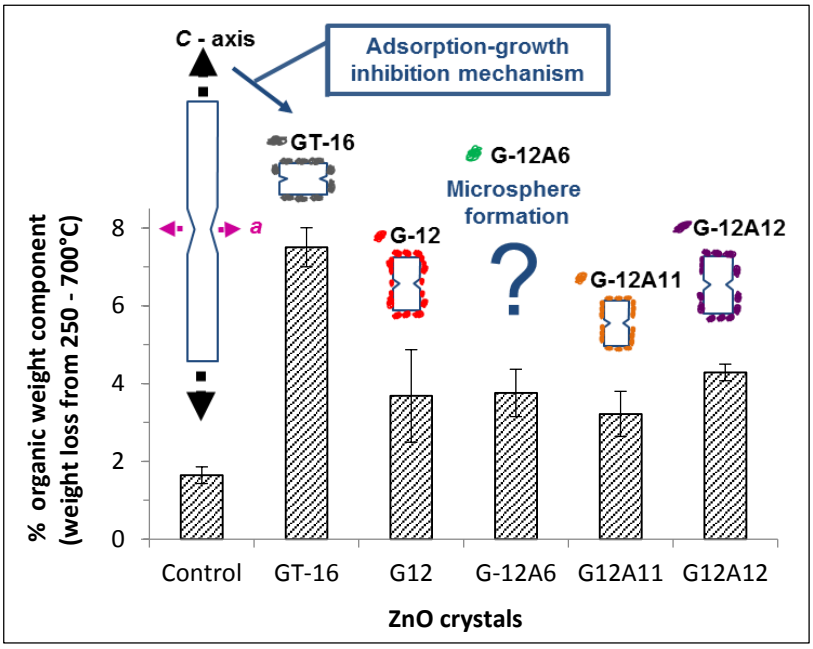

Figure 3.10. Organic weight component in ZnO precipitates collected at 48 hrs of synthesis using $Zn(NO_3)_2 \cdot 6H_2O$ and HMTA determined using TGA analysis. The organic component in ZnO precipitates synthesized with the different peptides was significantly higher (p value < 0.05, 95% CI, n = 3) than in the control which was synthesized without peptide. A schematic representation of the previously proposed adsorption growth inhibition mechanism has been illustrated to show the possible relationship between the amount of adsorbed organic material and aspect ratio reduction of GT-16 and G-12 synthesized crystals. In the control synthesis (without peptide) anisotropic growth of crystals is highlighted which is greater growth along the *c*-axis is than growth along the *a*-axis.

3.3.4. Hydrothermal Synthesis of ZnO; $Zn(CH_3COO)_2$ and NH_3 Reaction Method

In the synthesis studies using $Zn(CH_3COO)_2$ and NH_3, stock solutions of the reactants at 50 °C were mixed to attain an equimolar concentration of 15 mM to synthesize ZnO crystals as described in section 3.2.2.5. The precursor and base concentration used in this reaction (15 mM) was lower than the concentration used in the $Zn(NO_3)_2 \cdot 6H_2O$, HMTA reaction (50 mM) where a pH of 6.9 ± 0.1 was obtained. However, the goal was to use a different reaction method in which ZnO hexagonal rods could be synthesized without any additives at neutral pH so that the effect of incorporating peptides could be studied. Above 15 mM of NH_3 solution, the reaction solution would become more basic and other structures would be formed *i.e.* multi-needle and flower shaped crystals (Masuda *et al*., 2007). In this reaction, at 15 mM, the pH of the solution mixtures was

7.0 ± 0.1 in reactions without peptide and even in those with peptide that will be discussed later. In both methods, ZnO rods were obtained when synthesis was carried out in the absence of peptides at neutral pH. Details on the outcomes of the control reaction of ZnO synthesis using the $Zn(NO_3)_2 \cdot 6H_2O$, HMTA have already been described (section 3.3.1).

Upon the mixing of precursor $Zn(CH_3COO)_2$ and NH_3 solution at 50 °C, the reaction solution instantaneously became turbid and precipitation occurred. The amount of material formed was much more than that which formed in the synthesis with $Zn(NO_3)_2 \cdot 6H_2O$ and HMTA which was initiated at 20 °C. Samples were collected immediately after mixing the reagents at the start of the synthesis (± 2 min) and at 24 hrs (± 2 min) and 48 hrs (± 2 min) of synthesis. SEM was used to characterize the morphology of the precipitates (Figure 3.11). Samples collected at the start of synthesis (< 0.5 hr) consisted of layered structures similar to those collected during the nucleation period in the $Zn(NO_3)_2 \cdot 6H_2O$ and HMTA reaction method. Samples collected at 24 hrs and 48 hrs of synthesis consisted of hexagonal twinned rods. Some of the twinned rods formed were attached to each other at the centres while in others, one half of the structure appeared to have a larger diameter than the other half as highlighted in Figure 3.11e. This asymmetrical twinning forming grenade-like structures may be attributed to slower growth along one axis which later becomes symmetrical in solutions with adequate precursor growth units (Yu *et al*., 2007; Wang *et al*., 2011). Similar asymmetrical structures have also be observed during the formation of other ZnO structures *i.e.* when synthesis was carried using $Zn(CH_3COO)_2$ and NH_3 solution mixed at a molar ratio of $[NH_3]/[Zn^{2+}] = 6$, multi-needle shaped crystals are formed which have some planes which grow more slowly than others (Masuda *et al*., 2007).

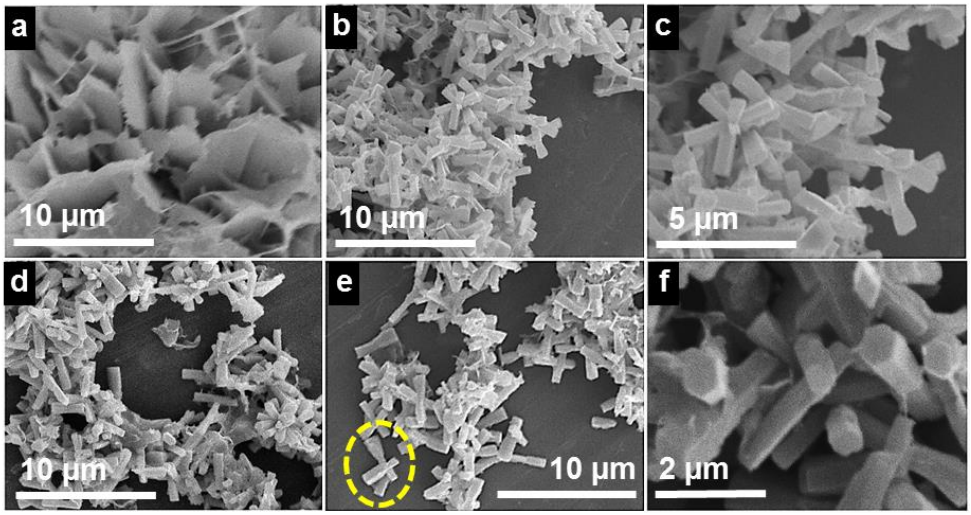

Figure 3.11. SEM micrographs of precipitates synthesized using precursor $Zn(CH_3COO)_2$ and NH_3 solution at 50 °C, (a) layered structures collected at the start (< 0.5 hr) of synthesis, (b, c) hexagonal twinned rods collected at 24 hrs of synthesis, (d - f) hexagonal twinned rods collected at 48 hrs of synthesis, aspect ratio (L/D = 4.5 ± 1.1. Scale bar; (a, b, d, e) 10 µm, (c) 5 µm, (f) 2 µm.

The crystallography of the layered structure in the precipitates formed on mixing the reagents (< 0.5 hr) was analysed using XRD and confirmed to be layered basic zinc acetate (LBZA) with the diffraction peak (001) at ~6° of 2θ having the highest intensity (Figure 3.12). As in the previous syntheses using the $Zn(NO_3)_2{\cdot}6H_2O$ and HMTA reaction method, ZnO formation appears to occur *via* an intermediate. The crystal structure of LBZA, $Zn_5(OH)_8(CH_3COO)_2.2H_2O$ is thought to consist of brucite-type layers of positively charged zinc hydroxyl $[Zn_5(OH)_8(H_2O)_2]^{2+}$ units in which cations are positioned in tetrahedral and octahedral sites and between which acetate anions are intercalated (Hosono *et al*., 2004, Wang *et al*., 2011). Acetate anions serve to control the interlayer spacing and balance the charge of the structure (Ogata *et al.*, 2000, Wang *et al*., 2011). As the reaction proceeded, phase transformation occurred and the intensity of the peaks characteristic of ZnO wurtzite structure increased. The precipitates with hexagonal twinned rods collected at 48 hrs of synthesis were predominantly ZnO (Figure 3.12).

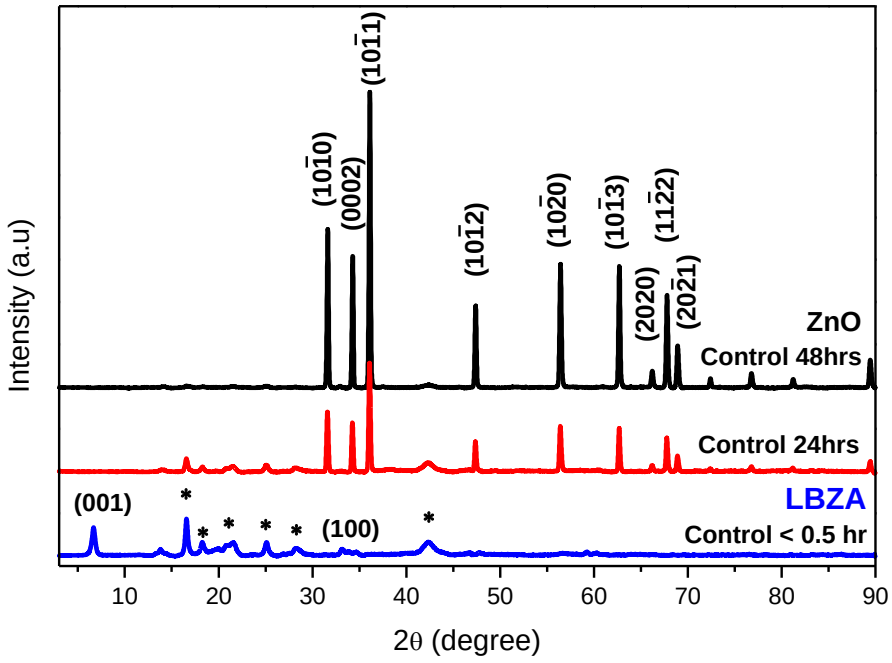

Figure 3.12. X-ray diffractograms showing growth of ZnO rods from precursor $Zn(CH_3COO)_2$ and NH_3 solution at 50 °C. Diffractograms are of samples collected immediately at the start of synthesis and at 24 hrs and 48 hrs of synthesis. **(*)** denotes peaks from the polyproplylene sample holder. Conventional three Miller indices have been used to designate directions, point locations and planes of LBZA. Indices of hexagonal crystals are designated using a four-axis Miller-Bravis coordinate system.

The formation of ZnO was also confirmed using FTIR with the ZnO stretching mode in the region of 430 to 550 cm^{-1} being prominent in 48-hr precipitates (Appendix 3.9). The fingerprint region of acetate anions lies within 1350 to 1600 cm^{-1}. The difference between the carboxyl group (COO^-) asymmetric stretching vibration (ν_{as}) and the COO^- symmetric stretching vibration (ν_s) gives an indication of the type of coordination the acetate group makes with zinc cations (Nara *et al*., 1996; Sakohara *et al*., 1998; Wang *et al*, 2011). Acetate ions can coordinate with zinc ions using either unidentate, bidentate (chelate) or bridging modes illustrated in appendix 3.10 (Nara *et al*., 1996; Sakohara *et al*., 1998). Precursor $Zn(CH_3COO)_2$ had sharp peaks at 1546 cm^{-1} and 1460 cm^{-1} which can be attributed to the presence of COO^- (ν_{as}) and (ν_s) respectively hence $\Delta\nu_{as\text{-}s}$ is 86 cm^{-1} which may be of a bidentate type whereby the zinc ion is able to interact with both oxygen atoms of COO^- equally. When precursor $Zn(CH_3COO)_2$ was mixed with NH_3 solution, a precipitate was formed and collected immediately for analysis. This layered precipitate had a broad peak in the region of 3000 to 3600 cm^{-1} which is characteristic of

O-H vibrations suggesting the presence of intercalated water in the intermediate compound identified as LBZA using XRD. The two peaks of the layered structure at 2850 cm^{-1} and 2974 cm^{-1} are due to the presence of C-H stretching vibration mode. Acetate was present in the structure of the intermediate compound evidenced by peaks of COO^- at 1555 cm^{-1} (ν_{as}) and 1392 cm^{-1} (ν_s) thus the $\Delta\nu_{as\text{-}s}$ was 163 which suggest that acetate ions acted as a bridging ligand for zinc ions. The band of ZnO stretching mode in the region of 430-550 cm^{-1} was prominent in the precipitates collected at 24 hrs and 48 hrs of synthesis (Appendix 3.9). In a previous study, where precipitates were collected at more time intervals (1 hr, 4 hrs, 7 hrs, 16 hrs, 20 hrs, 24 hrs, 48 hrs, and 72 hrs), FTIR and XRD analysis demonstrated that the absorbance of ZnO was detectable in all the precipitates but only became the dominant structure (with peaks of higher intensity than the peaks of the LBZA detected using XRD and with greater absorbance than acetate peaks detected using FTIR) at 16 hrs of synthesis (Liang, 2010). The outcome of this study were in agreement with the previous findings and ZnO was the dominant structure at 48 hrs of synthesis evidenced by XRD analysis but peaks from the acetate were still detected using FTIR suggesting that remnants of the intermediate, LBZA were still present.

ICP-OES analysis was used to determine the percentage of Zn^{2+} ions present in the supernatant over reaction time (Appendix 3.11). Upon mixing precursor $Zn(CH_3COO)_2$ and NH_3 solution, the reaction solution became supersaturated and a majority of the Zn^{2+} ions were immediately utilized to form precipitates of LBZA. The percentage of Zn^{2+} ions in solution therefore rapidly decreased to 27.2 ± 2.2%. In aqueous solution, NH_3 is readily hydrolysed forming hydroxide ions (OH^-) which may drive the process of ZnO formation (Ashfold *et al*., 2007; Govender *et al*., 2004; Jang *et al*., 2012; McPeak *et al*., 2011) *via* intermediate LBZA (Baier *et al*., 2012; Liang, 2010). As the reaction proceeds, phase transformation occurs in which acetate anions in LBZA are replaced by OH^- groups in solution forming $Zn(OH)_2$ which is dehydrated by heat to form ZnO (Wang *et al*., 2011). A rise in the amount of Zn^{2+} was detected using ICP-OES in the supernatant collected at 24 hrs of synthesis (Appendix 3.11) which suggests that dissolution of unstable precipitates could have occurred. Only stable nuclei that grow larger than the critical radius may be able to grow further into ZnO crystals (De Yoreo and Vekilove, 2003). As the reaction further proceeded to form ZnO crystals, a slight

decrease in the amount of Zn^{2+} ions in solution was again observed. The dissolution and re-precipitation of Zn^{2+} in solution during the formation ZnO occurs through a mechanism known as Ostwald ripening which commonly occurs when the amount of Zn^{2+} in solution has largely been consumed and small particles which have a higher solubility are re-dissolved and re-precipitated onto larger particles which grow at their expense (De Yoreo and Vekilove, 2003; Liu and Zeng, 2004; Xie *et al*., 2012). This again may explain why more grenade-like asymmetrically twinned ZnO rods were observed when synthesis was carried out using this method where the availability of Zn^{2+} ions was quickly depleted compared to growth using the $Zn(NO_3)_2.6H_2O$ and HMTA method in which the concentration of Zn^{2+} in solution was always in excess and therefore ZnO twinned rods were able to grow more symmetrically.

3.3.5. Peptide Sequence and Concentration Dependent Modification of ZnO Growth

Further studies using G-12A6 were carried out at three different peptide concentrations and using the two ZnO synthesis methods previously described (section 3.2.2.4 and section 3.2.2.5). Studies with G-12 were also carried out for comparison. When synthesis was conducted using the $Zn(NO_3)_2 \cdot 6H_2O$ and HMTA reaction method with G-12A6, there was an evident peptide concentration dependent influence on the resultant morphologies (Figure 3.13a-c). At a low concentration of 0.1 mM G-12A6, 25-hr precipitates consisted of continuous sheets with some aggregated microspheres ~2 µm in diameter (Appendix 3.12a, d). At 48 hrs (Figure 3.13a, Appendix 3.12g, i), ZnO rods were formed with lower aspect ratio than those synthesized without peptide. Continuous networks of porous sheets were also present throughout the sample. At a higher concentration of 0.3 mM G-12A6, at 25 hrs, porous microspheres ~5µm in diameter were present that appeared to have been distorted and broken apart by the sudden increase of reaction temperature from 20 °C to 65 °C (Appendix 3.12b, e) compared to the large microspheres we had previously observed (Figure 3.7) from samples collected during the nucleation period at 20 °C. At 48 hrs, larger microspheres with more defined structure, some of which were fused together were present (Figure 3.13b, Appendix 3.12h, k). When compared to the microspheres observed at 25 hrs they appeared to have grown in size and some had untwined ZnO rods on their surface. ZnO rods were also

present some of which were singular and others aggregated but very few were twinned. At the highest peptide concentration, 0.5 mM G-12A6, large aggregates with rough surfaces were present at 25 hrs of synthesis (Appendix 3.12 c, f) which developed into small aggregated rod-like structures at 48 hrs but the high peptide content appears to have inhibited anisotropic crystal growth (Figure 3.13c, Appendix 3.12i, l).

In all reactions using the $Zn(CH_3COO)_2$ and NH_3 there was a clear observable decrease in the turbidity of the solutions and the amount of precipitating material with an increase in peptide concentration. In synthesis using precursor $Zn(CH_3COO)_2$, NH_3 and G-12A6 peptide, with an increase in peptide concentration, from 0.1 mM to 0.3 mM, there was a decreased in the length of the crystals which also became wider (Figure 3.13g, i). Some of the crystals had grenade-like structures due to asymmetry of the twins. At the highest peptide concentration, 0.5 mM G-12A6 (Figure 3.13i), the crystals were much smaller in size compared to the control and the crystals synthesized with 0.1 and 0.3 mM peptide. The crystals synthesized with 0.5 mM G-12A6 were low aspect ratio twinned hexagonal rods that were symmetrically shaped with minimal aggregation compared to all other syntheses. Generally, in the presence of G-12A6, aggregation was less in samples synthesized using $Zn(CH_3COO)_2$ and NH_3 compared to those synthesized using $Zn(NO_3)_2 \cdot 6H_2O$ and HMTA. Appendix 3.13 shows more SEM images of crystals synthesized using the $Zn(CH_3COO)_2$ and NH_3 method at 25 hrs and 48 hrs of synthesis.

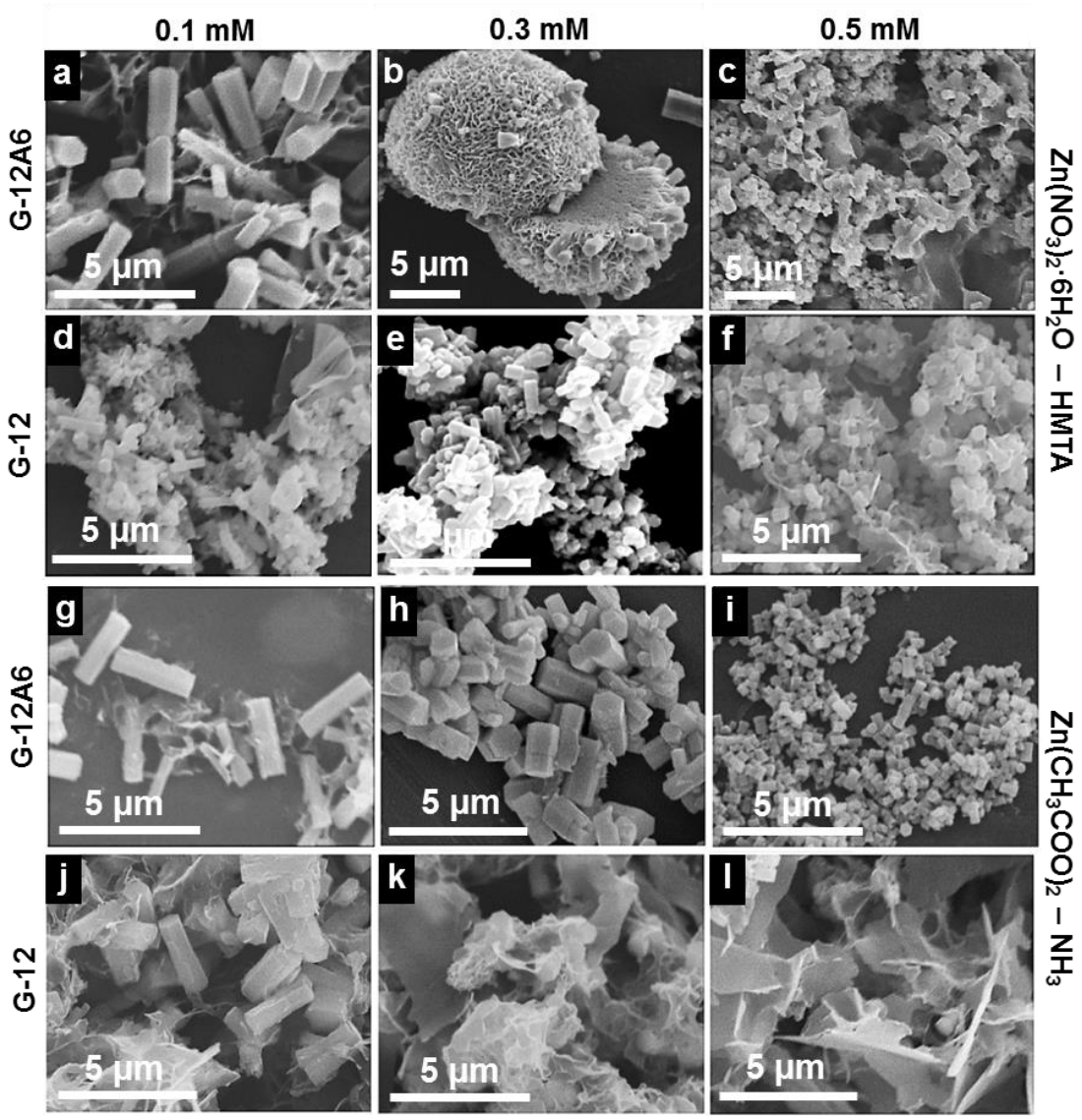

Figure 3.13. SEM micrographs of 48-hr precipitates synthesis using; (a-f) precursor $Zn(NO_3)_2 \cdot 6H_2O$, HMTA and G-12A6 or G-12 peptide at different concentrations, 0.1 mM, 0.3 mM and 0.5 mM, (g-l) precursor $Zn(CH_3COO)_2$, NH_3 and G-12A6 or G-12 peptide at different concentrations, 0.1 mM, 0.3 mM and 0.5 mM. There is a clear peptide sequence and peptide concentration dependent influence on morphology modification of precipitates. The growth conditions and precursors used also influence the resultant morphologies.

In the synthesis using $Zn(NO_3)_2 \cdot 6H_2O$, HMTA and G-12, the aspect ratio of crystals decreased with an increase in peptide concentration (Figure 3.13d-f, Appendix 3.14). This was attributed to adsorption of peptide to both (0001) and $(10\bar{1}0)$ planes (determined using XPS analysis) inhibiting growth along the *c* and *a*-axis (Liang *et al*., 2011). Interestingly, in samples collected at 25 hrs of synthesis with the highest concentration of G-12 peptide used, 0.5 mM, a few structures similar to the microspheres observed when synthesis was carried out with G-12A6 were seen (Appendix 3.14). However, these structures did not remain stable over time as there were none in the samples collected at 48 hrs of synthesis in which only aggregated short rods were present.

In synthesis using precursor $Zn(CH_3COO)_2$, NH_3 and G-12 (Figure 3.13j-l), with an increase in peptide concentration, fewer rods were present and with 0.5 mM G-12, only layered structures were found (Figure 3.13l). The layered structures were confirmed to be LBZA using XRD with the diffraction peak (001) at ~6° of 2θ having the highest intensity (Figure 3.14a). XRD analysis revealed that in fact, when synthesis was carried out using $Zn(CH_3COO)_2$ and NH_3, suppression of ZnO growth occurred in the presence of both G-12 and G-12A6 but was more prominent with G-12. Suppression/inhibition of ZnO formation was more effective with an increase in peptide concentration. For example with 0.3 mM peptide LBZA was present only in 24-hr precipitates synthesized with G-12 peptide and not in 24-hr precipitates synthesized with G-12A6 (Appendix 3.16). However, LBZA was not detected in 48-hr precipitates synthesised using 0.3 mM of both peptides, only the wurtzite ZnO structure was detected using XRD. When a higher peptide concentration was used, 0.5 mM, LBZA was present in 48-hr precipitates synthesized with both peptides. However, ZnO growth inhibition was greater with G-12 peptide as peaks of the wurtzite structure were absent in XRD analysis and only layered structures were observed using SEM. In both synthesis methods, where ZnO rods were formed, the aspect ratio of the rods decreased with an increase of peptide concentration (Figure 3.14b, c). The suppression of ZnO growth by both peptides was only prominent in the synthesis carried out using $Zn(CH_3COO)_2$ and NH_3, not in precipitates synthesized using the $Zn(NO_3)_2 \cdot 6H_2O$ and HMTA reaction method where ZnO formation at 48 hrs was confirmed using XRD analysis (Appendix 3.17).

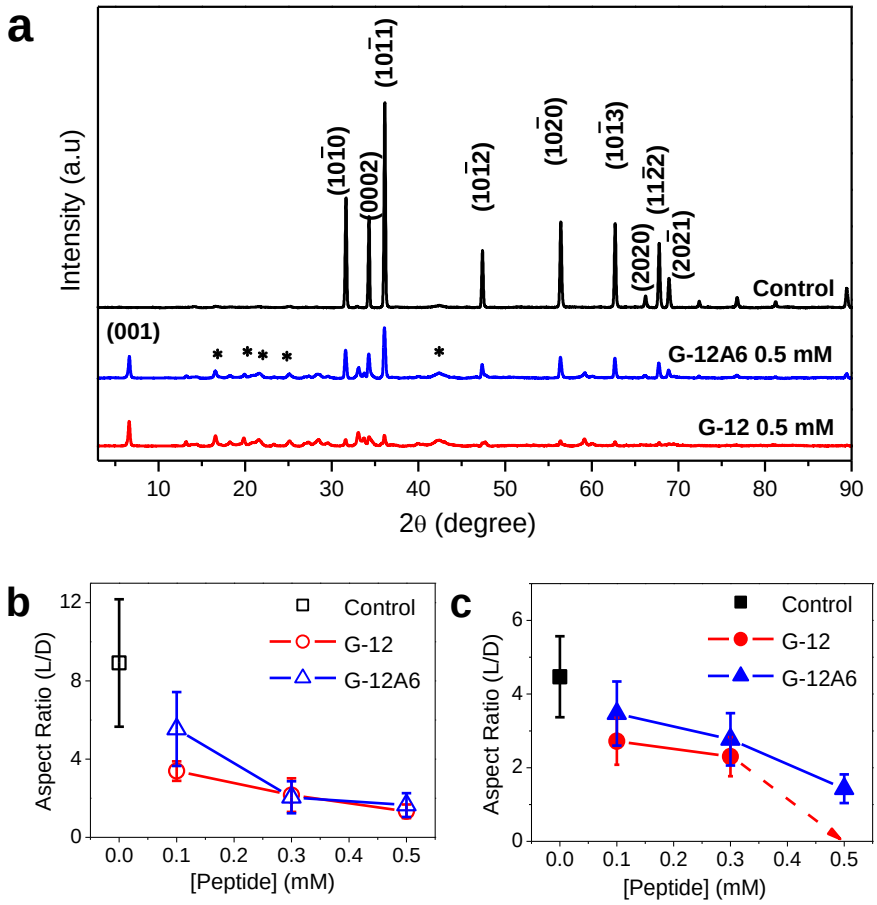

Figure 3.14. (a) XRD diffractogram of 48-hr ZnO precipitates synthesised using the $Zn(CH_3COO)_2$ and NH_3 synthesis method in the absence of peptides (control) and in the presence of 0.5 mM G-12 and G-12A6. Peptides appear to stabilize LBZA and supress the formation of ZnO wurtzite structure. Inhibition of ZnO formation was more prominent with G-12. (∗) denotes peaks from the polypropylene sample holder. (b) Aspect ratio (L/D) measurements of ZnO synthesized using the $Zn(NO_3)_2{\cdot}6H_2O$ and HMTA synthesis method without peptide (control) and in the presence of G-12 and G-12A6 at different concentrations. (c) Aspect ratio (L/D) measurements of ZnO formed using the $Zn(CH_3COO)_2$ and NH_3 synthesis method without peptide (control) and in the presence of G-12 and G-12A6 at different concentrations. For each data point, aspect ratio measurements of 50 crystals were made from SEM micrographs of 48-hr precipitates. With 0.5 mM G-12, there were hardly any rods to measure as mainly LBZA was present.

ICP-OES analysis was carried out to determine the percentage of Zn^{2+} ions present in the supernatants over reaction time (Figure 3.15). When synthesis was carried out using the $Zn(NO_3)_2{\cdot}6H_2O$ and HMTA method, in all reactions, only a small amount of Zn^{2+}

ions (~10%) was used to form LBZN during the initial 24 hr nucleation period at 20 °C. There was an excess of Zn^{2+} ions in the solution available for phase transformation of the LBZN into ZnO and at the end of the reactions, only ~60% of the available Zn^{2+} ions had been utilized to form ZnO crystals. The kinetics of the reaction was not altered by the use of different peptide concentrations nor the sequence dissimilarity between G-12 and G-12A6. In one reaction, peptide G-12A6 (0.3 mM) was added later (at 24 hrs of reaction) after the nucleation period. This modification in additive addition time did not alter the kinetics of Zn^{2+} consumption. The only observation was that there were fewer microspheres formed and more networks of porous-like material similar to what was observed with the synthesis of 0.1 mM G-12A6. Overall, the peptides did not have an effect on the kinetics of the reaction.

When the reaction was carried out using $Zn(CH_3COO)_2$ and NH_3, the consumption of Zn^{2+} ions was different from the reaction using $Zn(NO_3)_2 \cdot 6H_2O$ and HMTA method. After mixing the reagents, the concentration of Zn^{2+} ions in the solutions immediately decreased to less than 45% for all the synthesis reactions using the $Zn(CH_3COO)_2$ and NH_3 method. The ready availability of OH^- ions from the hydrolysis of NH_3 may have contributed to driving the reaction forward. The solution was supersaturated and LBZA was immediately precipitated evidenced from SEM and XRD analysis. However, low concentrations of Zn^{2+} ions in the solution may have not been favourable for further growth of crystals. The dissolution of soluble and unstable precipitates may have been induced to sustain the growth of larger and more stable crystals (De Yoreo and Vekilove, 2003; Liu and Zeng, 2004; Xie *et al*., 2012). A clear trend between the data obtained using different peptide concentrations of G-12 and G-12A6 could not be established from ICP-OES analysis. However, the dissolution of Zn^{2+} ions back into the solution and re-precipitation to form ZnO rods appears to have taken place at a faster rate in the control reaction over the first 24 hrs compared to reactions in which peptides were incorporated where the amount of Zn^{2+} in solution appeared to be more stably maintained in solution.

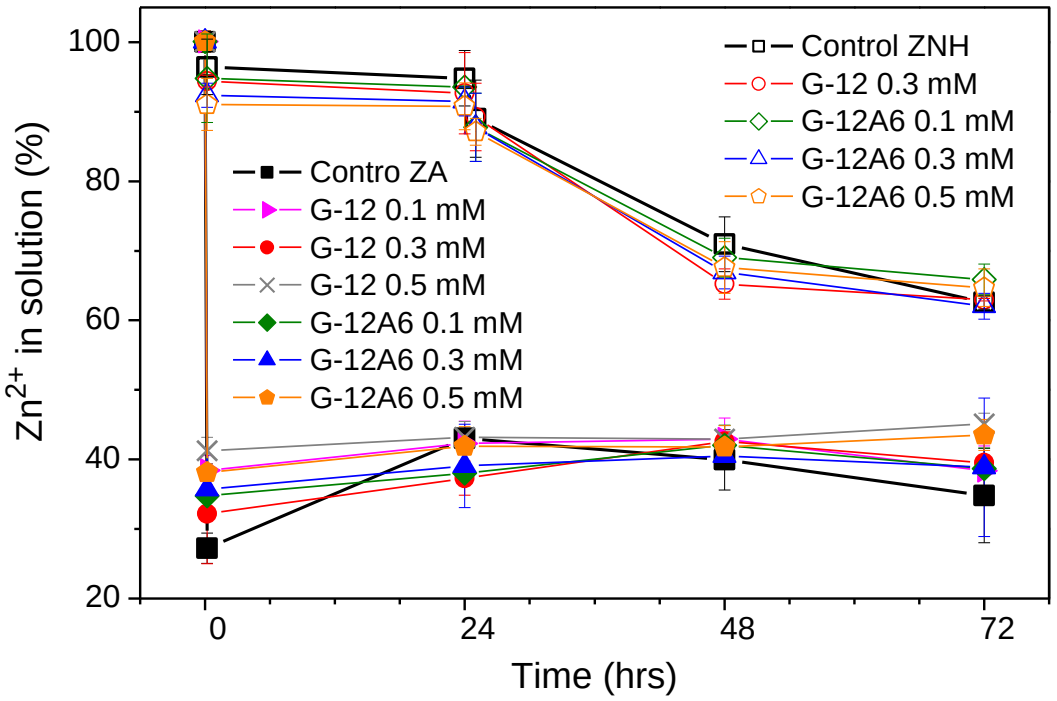

Figure 3.15. ICP-OES analysis of the percentage of Zn^{2+} ions in supernatants collected at different time points during the synthesis of ZnO using two different methods. Data points above 60% are from syntheses using the $Zn(NO_3)_2{\cdot}6H_2O$ and HMTA method in the absence (control ZNH: zinc nitrate hexahydrate) and presence of peptides. The kinetics of the consumption of Zn^{2+} ions is not significantly altered by peptides. Data points below 60% are from syntheses using the $Zn(CH_3COO)_2$ and NH_3 method in the absence (control ZA: zinc acetate) and presence of peptides. Peptides appear to have altered the kinetics of Zn^{2+} consumption. At least three samples were analysed for each data point to obtain standard deviation values represented as error bars.

3.3.5.1. Determination of the Organic Content in Precipitates

It was already established that in the control synthesis, at 48 hrs, ZnO was the predominant structure in precipitates formed. TGA and FTIR analysis of 48-hr precipitates was therefore carried out to determine how much organic material was adsorbed to the precipitates and to identify the functional groups present which may give an indication of how adsorbed peptides if present interact with ZnO. Precipitates had all been thoroughly washed before analysis such that only strongly bound material would remain adsorbed. The organic content in the precipitates was quantified using TGA (weight loss between 250 -700 °C) (Appendix 3.18).

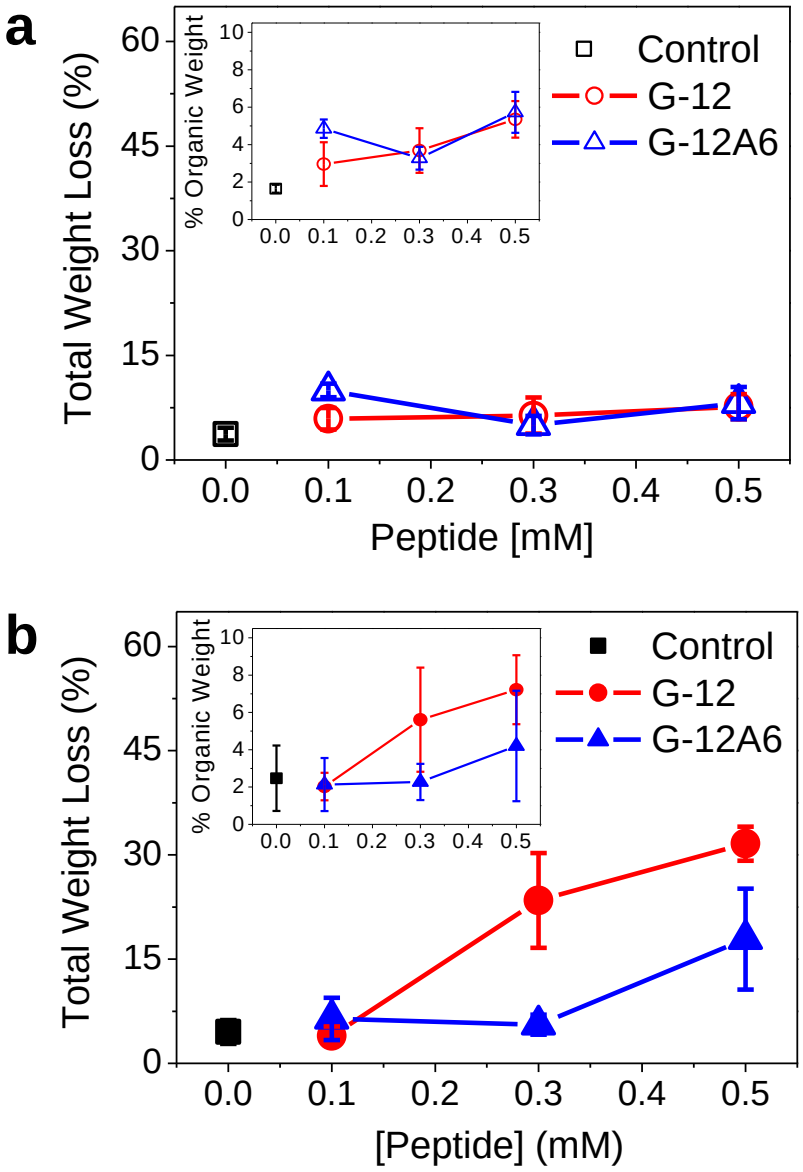

Figure 3.16. TGA determination of the total weight loss and insets, organic content in 48-hr precipitates synthesised using (a) the $Zn(NO_3)_2{\cdot}6H_2O$ and HMTA synthesis method and (b) the $Zn(CH_3COO)_2$ and NH_3 synthesis method. The difference in organic content in (a) between the control sample and the samples synthesized with peptides is attributed to peptide adsorption. The organic content in (b) is attributed to the presence of LBZA and is greatest in samples synthesized using 0.5 mM G-12 peptide.

In the precipitates synthesized using the $Zn(NO_3)_2{\cdot}6H_2O$ and HMTA method (Figure 3.16a), there was a significant difference in the organic content in the control samples and the precipitates which were synthesized with peptide. With an increase in the concentration of G-12, there was an increase in the organic content in the samples. However with G-12A6, the relationship between peptide concentration and the amount

of organic material present was not linear which may be attributed to the presence of variable morphologies in the samples (0.1 mM peptide resulted in the formation of continuous rough porous sheets and elongated ZnO rods, 0.3 mM peptide resulted in microspheres and short rods). Nevertheless, because the amount of organic matter was significantly greater than in the control precipitate, we can deduce that the peptides were adsorbed to ZnO.

When the synthesis was carried out using $Zn(CH_3COO)_2$ and NH_3, from SEM and XRD analysis, it was already established that with an increase in peptide concentration (especially with G-12), the precipitates formed had a greater content of LBZA. In agreement, the total weight loss in 48-hr precipitates synthesized using 0.5 mM G-12 was 31.62 ± 2.45% which was close to weight loss (32.66 ± 1.44%) of the LBZA in the control precipitate collected not long after mixing of reagents (< 0.5 hr) (Appendix 3.18). The organic weight loss observed between 250 °C and ~400 °C (Figure 3.16b) was therefore attributed to dehydroxylation of zinc hydroxide in LBZA and decomposition of acetates and not the presence of adsorbed peptide. Peptides appear to inhibit the formation of ZnO by stabilizing the intermediate compound LBZA. This inhibition effect was greater in the presence of G-12 than with G-12A6 of the same concentration; total weight loss in 48-hr precipitates synthesised using 0.5 mM G-12A6 was 17.88 ± 7.28% (Figure 3.16b).

FTIR analysis of the precipitates was also carried out and the results supported the findings from TGA analysis. Peptides were adsorbed to precipitates synthesized using the $Zn(NO_3)_2{\cdot}6H_2O$ and HMTA method (Appendix 3.19) and not to precipitates synthesized using the $Zn(CH_3COO)_2$ and NH_3 method (Appendix 3.20). Peptides characteristically have an FTIR amide I peak in the region of 1600 - 1700 cm^{-1} and an amide II band between 1500 and 1600 cm^{-1}. When synthesis was carried out using $Zn(NO_3)_2{\cdot}6H_2O$, HMTA and peptide (G-12 or G-12A6), a shift in amide I band (*i.e.* ~1673 cm^{-1} to ~1646 cm^{-1}) was observed in the spectra of the ZnO precipitates (O-Zn-O stretching mode in the region of 430 - 550 cm^{-1}) compared to the spectra of pure peptides (Appendix 3.19). The energy of vibration of amide I may have been altered by the adsorption of peptide to ZnO surfaces (Barth, 2000; Liang *et al.*, 2011). The NO_3^- vibration at 1384 cm^{-1} was also present in all the precipitates. With an increase in

peptide (G-12 and G-12A6) concentration, the intensity of the NO_3^- vibration peak as well as the amide I band at 1646 cm^{-1} increased in comparison to the spectra of the control precipitate.

The incorporation of G-12 peptide in ZnO precipitates had previously been analysed using FTIR by Liang and co-workers (2011) who suggested the plausible complexation of NO_3^- with some cationic moieties of peptides which then adsorb to the surface of ZnO. The presence of NO_3^- with ZnO structures has been observed in other studies and has been thought to co-precipitate with the ZnO (Weinzierl *et al.*, 2008). However the co-precipitation of NO_3^- with ZnO does not occur without the presence of peptides because in the control reaction (without peptide), there was less NO_3^- in the precipitates over reaction time and not *vice versa*. From FTIR and XRD analysis of the precipitates of the control reaction, the presence of a high amount of NO_3^- in the precipitates collected at 24 hrs was attributed to the presence of LBZN which decreased at 48 hrs where ZnO was the major component. The increased presence of NO_3^- with an increase in peptide concentration over reaction time compared to the control may plausibly imply that there may have been more LBZN present in predominantly ZnO precipitates which had been synthesized with higher peptide concentrations. Contrarily, when synthesis was carried out using $Zn(CH_3COO)_2$, NH_3 and peptide G-12 or G-12A6, adsorption of peptides to precipitates was not detected (Appendix 3.20). However, there was an increase in the amount of acetate detected in the precipitates with an increase in peptide (G-12 and G-12A6) concentration used which was attributed to the presence of LBZA. This stabilization of intermediates effect of peptide incorporation was similar in precipitates synthesized with peptides using the $Zn(NO_3)_2 \cdot 6H_2O$ and HMTA reaction method.

3.3.5.2. Summary and Proposed Mechanisms for Peptide Directed ZnO Growth

Herein demonstrated is that controlled modification of ZnO morphology can be achieved using peptides and that under favourable reaction conditions, peptides can also modify the growth kinetics of ZnO formation. MD coupled to computational alanine scanning mutagenesis was used to theoretically identify the differences in the stability of the original G-12 sequence and mutant sequences with alanine substituted into each

position in the original sequence. The stability of the sequences was determined by considering the overall stability in both solvated and non-solvated states. G-12A6 peptide was identified as the most stable sequence and the original G-12 sequence was found to have medial stability. G-12A11 was found to be the second most stable sequence and G-12A12 was identified as the least stable sequence. Further computational studies to model the interaction of ZnO binding peptides onto ZnO planes are being carried out using software such as Material Studio but there are challenges in generating force-fields that can be used to representatively simulate the ZnO surface, the peptides as well as the ions that are present in the environment where the interactions take place. Experimental studies should always be carried out alongside theoretical computational studies to validate outcomes.

Experimental analyses were carried out to determine the effects of incorporating the selected peptides in the synthesis of ZnO. G-12, G-12A11 and G-12A12 had similar effects on the growth of ZnO when synthesis was carried out using the $Zn(NO_3)_2 \cdot 6H_2O$ and HMTA method. In the presence of these peptides, aspect ratio reduction occurred which could be attributed to peptide adsorption onto ZnO crystal planes inhibiting growth. A difference was observed when ZnO was synthesized in the presence of G-12A6 beginning with the morphology of the precipitates obtained during the initial nucleation period in the synthesis. Unique microspheres were found in syntheses with G-12A6 unlike in other syntheses without peptide and in the presence of the other examined peptides (G-12, G-12A11 and G-12A12) where continuous sheets of layered structures identified as LBZN were present during the nucleation period which developed into low aspect ratio ZnO twinned rods. This intriguing difference as a consequence of a single amino acid substitution in a peptide sequence prompted further investigation into ZnO synthesis in the presence of G-12A6 peptide.

The substitution of basic, polar amino acid H_6 with non-polar acid alanine (A_6) to generate the G-12A6 peptide greatly influenced the stability of the sequence, based on theoretical computational studies and the growth mechanism of ZnO leading to differences in morphology modification in synthesis. Residues of histidine amino acid are thought to be significant for the interaction of zinc ions with proteins in zinc dependent proteins like Zinc finger nucleases (Berg and Godwin, 1997; Dudev and Lim,

2003). Similarly, histidine may be an important amino acid in the interaction of peptides with ZnO surface through complexation with divalent zinc ions. Most of the peptide sequences that have been identified to interact with ZnO using phage display technique have histidine residues (Rhothenstein *et al*., 2012). Okochi and co-workers (2010) highlighted the importance of histidine amino acid for the binding activity of EM-12 (EAHVMHKVAPRP) which has 67% homology to G-12 (GLHVMHKVAPPR). They also suggested that the binding sites on ZnO surfaces were able to recognise the specific alignment of amino acids in EM-12 peptide and that HVMHKV and HKVAPR were the 'hot spot' regions for interaction with ZnO. The same hot spot regions may lie within G-12 peptide which is very similar and could mean that substitution of H_6 may greatly affect the affinity of the peptide for ZnO surfaces.

Nevertheless, the aspect ratio reduction in crystals synthesized using the $Zn(NO_3)_2{\cdot}6H_2O$ and HMTA method and either G-12 or G-12A6 peptides was very similar and the amount of organic matter adsorbed to the crystals was also not significantly different. Both sequences are able to bind to and modify the morphology of ZnO using the adsorption growth inhibition mechanism. It is however, important to note that although TGA analysis can enable one to establish if peptides are strongly absorbed to the precipitates or not, the amount quantified may not be representative of the actual amount of peptide adsorbed to the precipitates during synthesis in solution. Previous studies have reported that in solutions, peptides may be able to interact with each other (Puddu and Perry, 2012; Rabe *et al*., 2011; Sarikaya *et al*., 2004; Seker *et al*., 2007). Therefore, in solution synthesis, plausible multilayer adsorption of peptides onto inorganic surfaces through peptide-peptide interactions needs to be considered. Peptides that are loosely bound to the surface may significantly affect the growth of the crystals in solution but may easily be perturbed and washed away when collecting and preparing the precipitates for analysis.

The formation of ZnO microspheres in the presence of G-12A6 in the $Zn(NO_3)_2{\cdot}6H_2O$ and HMTA reaction method suggests that the peptide under suitable growth conditions is able to induce isotropic growth of ZnO. Alanine is a hydrophobic amino acid and its substitution into the sixth position in the sequence forming G-12A6 may in a suitable environment (*i.e.* in the growth environment of the $Zn(NO_3)_2{\cdot}6H_2O$ and HMTA

reaction), modulate its organisation to form micelle like structures which may act as a template upon which nucleation and growth of ZnO begins. A specific peptide concentration, 0.3 mM was required for microspheres to be formed which suggests that a critical micellization concentration was needed for the formation of a stable template structure. Only microspheres were formed initially during the nucleation period with G-12A6, therefore, the peptide may be templating the structure of the intermediate LBZN. XRD powder diffraction could not be carried out to determine the crystallinity of the microspheres formed during the 20 °C nucleation period because the amount present was too little, not even visible to the naked eye. With the sudden increase of reaction temperature to 65 °C, the microspheres were broken apart but as the reaction proceeded, SEM micrographs show that the structures recovered forming well defined microspheres which grew to a maximum size of about ~10 µm in diameter at 48 hrs of synthesis. Only the wurtzite ZnO structure was detected in XRD analysis of the precipitate collected at 48 hrs of synthesis containing microspheres and rods. If the microspheres formed during the nucleation period consisted of LBZN, phase transformation may have taken place while retaining the structure of LBZN. The phase transformation of LBZs into a ZnO structure without changing the morphology has also been reported elsewhere *via* heat treatment generally in the range of 70 - 140 °C (Hosono *et al*., 2004; Inoue and Fujihara, 2011). The porous microspheres formed at 48 hrs of synthesis had stable structures able to retain their morphology even after calcination up to 900 °C. Some microspheres appeared to have twinned structures which are a common feature in ZnO structures, thought to reduce the surface energy of crystals lowering the total Gibbs free energy of the system (Yan *et al*., 2008; Yu *et al.,* 2007). It is interesting to note that with 0.5 mM G-12, few microspheres were observed at 25 hrs of synthesis but these did not develop further like in the synthesis with 0.3 mM G-12A6. This may be explained by the observations from computational analysis which showed that G-12 is structurally less stable than G-12A6 and may therefore have formed weaker template structures.

Additionally at 48 hrs of synthesis, ZnO rods were also present some of which were attached to the surface of the microspheres and most of the loose crystals were not twinned or were asymmetrically twinned (Figure 3.17). Increasing the reaction temperature from 20 °C to 65 °C in the $Zn(NO_3)_2 \cdot 6H_2O$ and HMTA reaction changed

the rates of the chemical reactions in solution which may have led to a subsequent secondary nucleation and growth of hexagonal rods. TEM analysis shows the growth of rods on the surface of microspheres which appeared to be rough with large pores but had more solid centres (Figure 3.17e). TEM images also reveal that the surfaces of the ZnO rods were not very smooth and may have been microporous (Figure 3.17f).

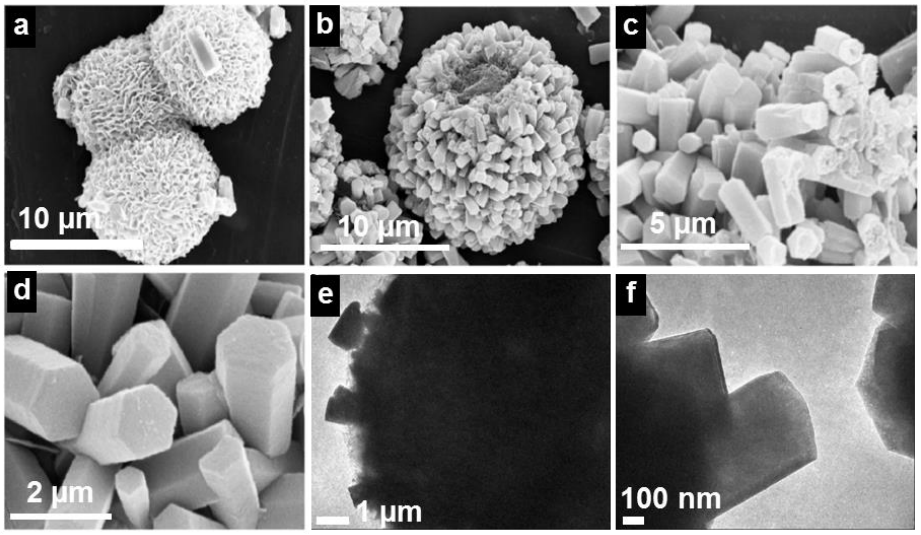

Figure 3.17. (a, d) SEM micrographs ZnO crystal samples collected at 72 hrs of synthesis using precursor $Zn(NO_3)_2{\cdot}6H_2O$ and HMTA and 0.3 mM G-12A6 as a growth modifier. Samples consisted of microspheres with porous rough surfaces and hexagonal rods some of which were attached to the surface of the microspheres. Many of the loose hexagonal rods (L/D = 2.34 ± 1.21) were not twinned or were asymmetrically twinned. (e, f) TEM image of a ZnO microsphere and hexagonal rods attached on the surface showing rough and porous surface of the microsphere which had a solid/whole centre. The surface of the rods appeared to be rough and could be microporous. Scale bars; (a-b) 10 µm, (c) 5 µm, (d) 2 µm, (e) 1 µm, (f) 100 nm.

When synthesis was carried out using $Zn(CH_3COO)_2$, NH_3 and peptide G-12 and G-12A6, the importance of histidine amino acid in the interaction of the ZnO binding peptides with ZnO was more clearly highlighted. The amount of LBZA precipitate formed in the presence of the peptides (G-12 and G-12A6) visibly decreased with an increase in peptide concentrations. Also observed is that LBZA was stabilized for longer periods in reactions where the peptides were incorporated and this effect was more prominent at higher peptide concentrations and more pronounced in the presence

of G-12 than G-12A6. These observations were not prominent when the reaction was carried out using the $Zn(NO_3)_2 \cdot 6H_2O$ and HMTA method. The only indication that peptides may stabilize or interact with the intermediate LBZN was from FTIR analysis which showed an increase in the intensity of the NO_3^- peak with increased peptide concentration. In this synthesis, the suppression of ZnO growth was not as effective because not much LBZN was formed and Zn^{2+} ions in solution were in excess throughout the reaction. This was, however, not the case in the reaction using $Zn(CH_3COO)_2$ and NH_3 where the reaction conditions were favourable for the immediate precipitation of most of the Zn^{2+} ions in the LBZA structure which the peptides were be able to stabilize, evidenced from XRD and SEM analysis. This coupled to the reduction in the Zn^{2+} concentration in the reaction condition may have resulted in the evident suppression of ZnO formation.

The exact mechanism through which peptides may be able to stabilize LBZA is not clear. However, because G-12 had a greater ability to stabilize LBZA than G-12A6, histidine amino acid must have played an important role in achieving this stabilization. At the experimental conditions used (pH 7.0 ± 0.1) based on p*Ka* values, more than 50% of the side chain group of histidine was unprotonated (Liang *et al*., 2011) therefore, imidazole nitrogen atoms could have used a lone pair of electrons to coordinate with Zn^{2+} in the LBZA structure stabilizing it. Two processes/factors are needed for phase transformation of LBZA into ZnO; (i) OH^- ions should replace acetate ions in LBZA forming $Zn(OH)_2$ which undergoes dehydration to form ZnO, (ii) an adequate supply of Zn^{2+} ions is required to form the building units of ZnO crystals. In this system there is an excess of OH^- ions in the solution and a deficit of Zn^{2+} ions. Dissolution of some of the unstable Zn^{2+} containing intermediate precipitate may have been needed to provide Zn^{2+} ions required for ZnO growth but this may have been prevented by stabilization of LBZA. Cationic residues of the peptides in solution may have also slowed down the process of acetate replacement by OH^- ions in the LBZA structure through steric hindrance thereby stabilizing LBZA for longer periods. Alternatively, as the amount of LBZA precipitated decreased with an increase in peptide concentration, histidine residues in peptides may have been able to coordinate with Zn^{2+} ions in solution like in zinc finger nucleases and metalloproteins stabilizing aqueous Zn^{2+}. These hypotheses are however difficult to prove. Supressed formation of ZnO has

also been observed using EM-12 (EAHVMHKVAPRP) peptide when incorporated in ZnO synthesis using the $Zn(CH_3COO)_2$ and NH_3 reaction method (Liang, 2010).

In the synthesis of ZnO using the $Zn(CH_3COO)_2$ and NH_3 reaction method with G-12 and G-12A6, we concluded from TGA and FTIR analysis that there was no peptide adsorbed to the precipitates. However, when looking at the morphology of the crystals formed with increasing amounts of G-12A6 peptide (Figure 3.13g-i) there was a clear peptide concentration dependent aspect ratio reduction. This may have been a consequence of a lack of ZnO growth units due to the stabilization of LBZA but may have also occurred if the peptides in solution were able to weakly and reversibly adsorb to the ZnO surface and inhibit growth. The 48-hr precipitate formed using 0.5 mM of G-12A6 consisted of twinned rods that appeared homogenous, symmetrical with minimal aggregation (Figure 3.13i, Appendix 3.13g-i). G-12A6 may have acted as a surfactant or capping agent during the synthesis of ZnO using the $Zn(CH_3COO)_2$ and NH_3 reaction which prevented aggregation of crystals. Figures 3.18 and 3.19 summarize possible mechanisms through which peptides may modify the growth and morphology of ZnO crystals.

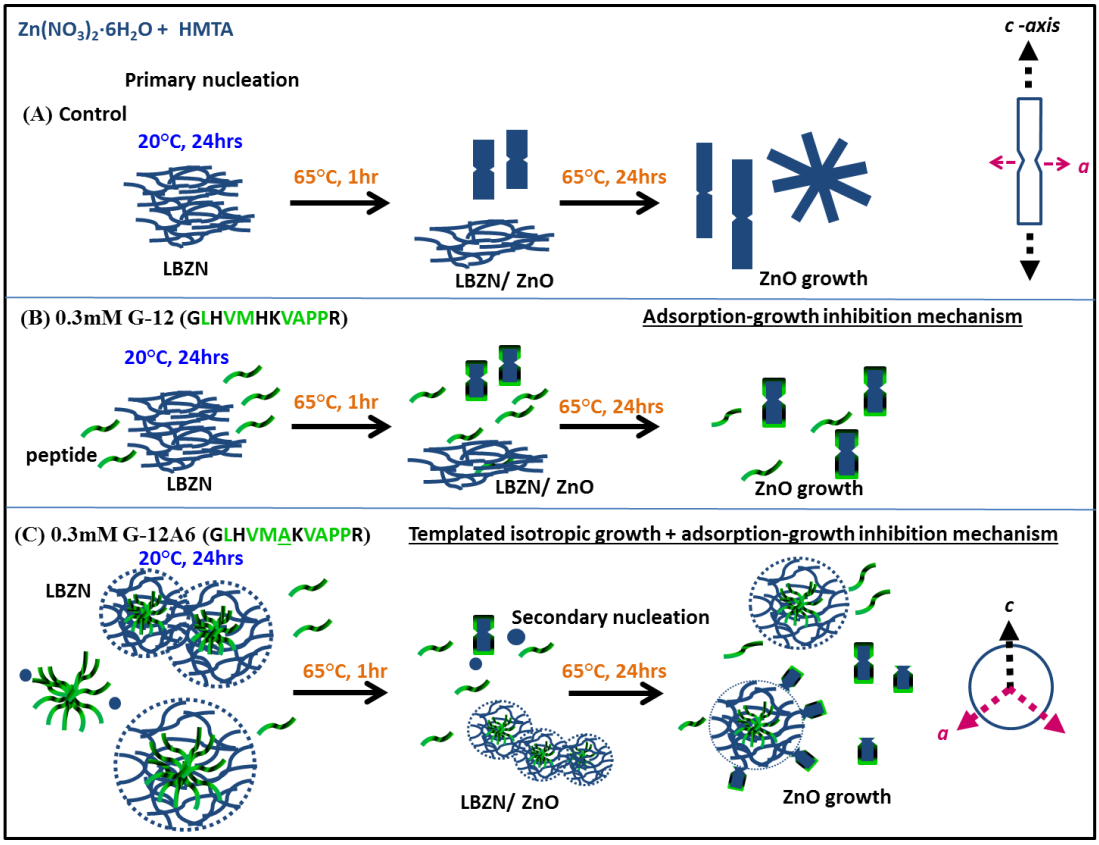

Figure 3.18. Schematic representation of ZnO growth processes in solution synthesis using the $Zn(NO_3)_2 \cdot 6H_2O$ and HMTA method without and with peptide. (A) anisotropic growth of ZnO rods (preferential growth along the *c*-axis) without peptide forming elongated ZnO twinned rods (L/D = 8.9 ± 3.3), (B) Growth in the presence of 0.3 mM G-12 peptide forming low aspect ratio ZnO twinned rods (L/D = 2.2 ± 0.9) attributed to peptide adsorption to ZnO inhibiting growth. (C) Growth in the presence of 0.3 mM G-12A6 peptide causing aspect ratio reduction (L/D = 2.1 ± 0.8) also due to peptide adsorption to growing crystals but unique formation of ZnO microspheres was also observed. The illustration depicts the possible organisation of G-12A6 peptide into micelle-like structures which may then act as templates upon which ZnO nuclei can grow isotropically (equally along the *a* and *c*-axis) forming microspheres which are phase transformed into ZnO at 65 °C. In this synthesis method, the increase in temperature to 65 °C after an initial 24 hr nucleation period at 20 °C induces the occurrence of secondary nucleation. Image is not drawn to scale.

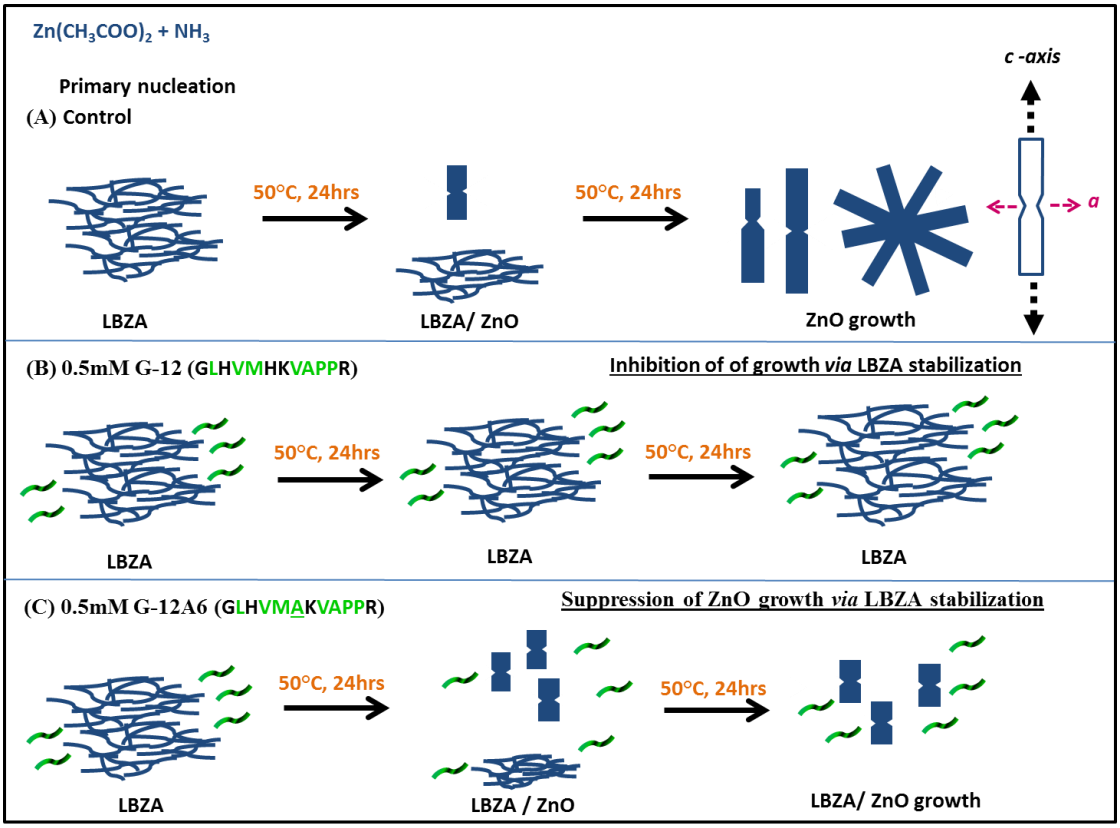

Figure 3.19. Schematic representation of ZnO growth processes in solution synthesis using the $Zn(CH_3COO)_2$ and NH_3 method without and with peptide. (A) anisotropic growth of ZnO rods (preferential growth along the *c*-axis) without peptide forming elongated ZnO twinned rods (L/D = 4.5 ± 1.1), (B) Growth in the presence of 0.5 mM G-12 peptide where formation of ZnO was inhibited, (C) Growth in the presence of 0.5 mM G-12A6 peptide forming lower aspect ratio twinned rods (L/D =1.4 ± 0.4). Supressed growth of ZnO was observed in the presence of both G-12 and G-12A6 peptide. LBZA was stabilized for longer periods when synthesis was carried out using both peptides but the effect was greater with G-12 peptide. Aspect ratio reduction may have occurred as a result of a lack of ZnO growth units due to LBZA stabilization. Alternatively, as analysis suggested that no peptide was strongly adsorbed to the precipitates, peptides may have been weakly and reversibly bound in solution synthesis causing aspect ratio reduction.

3.4. Conclusion

In this study, peptides were seen to act as multifunctional tools that can be harnessed to control material formation. Peptide directed modification of ZnO morphology was achieved using peptide adsorption growth inhibition mechanism (Muthukumara, 2009; Liang *et al*., 2011) which resulted in aspect ratio reduction of ZnO rods synthesized in the presence of ZnO-BPs. Certain peptides could act as structure directing templates that could modulate the growth habit of ZnO *i.e.* in a suitable environment, the inherent properties of G-12A6 peptide plausibly the presence of hydrophobic residues at certain positions in the sequence could have enabled it to self-assemble into stable micelle-like structures which could template the otherwise unfavourable isotropic growth of ZnO to form microspheres. Similar ZnO microspheres have been synthesized elsewhere using amino acid based surfactants with different head group functionalities; lauroyl chloride coupled to aspartic acid, glutamic acid or alanine (Kim *et al*., 2012). The synthesis of ZnO whole and hollow spherical structures have also been reported using other structure directing agents including poly (vinylpyrrolidone), polyethylene glycol and citrate (Gerstel *et al.,* 2006; Yan *et al*., 2008). Porous microspheres with high surface area can have enhanced properties needed for electrochemical and physiochemical applications such as photocatalysts and gas sensors (Inoue and Fujihara, 2011; Kuo *et al*., 2005). The synthesis method using G-12A6 peptide can be modified in pursuit of a homogenous ZnO microsphere containing precipitate for the development of potential applications.

Additionally under certain conditions, ZnO-BPs were able to supress/inhibit the formation of ZnO by stabilizing the intermediate LBZs. The influence of physical properties of the solution like temperature and pH as well as chemical properties of the solution such as precursor concentration and control over the solution's super-saturation index have also been highlighted and can be manipulated to control the resultant materials chemical and physical properties. Generally, all processes in synthesis with or without peptide are influenced by the system's need to attain thermodynamic equilibrium by lowering Gibbs free energy. Peptides have proven to be smart versatile tools having different properties that if well understood can be used to advance material synthesis and design. A direct link between peptide adsorption and morphology

modification may be obtained by measuring adsorption isotherms of different peptides on different crystallographic planes of ZnO (Muthukumara, 2009). This approach has been taken towards progressing our understanding of peptide-inorganic interactions and is discussed in the next chapter.

3.5. References

1. Ahmadi, S.J., Hosseinpour, M., Javadi, F. and Tayebee, R., 2013. Optimization Study on Formation and Decomposition of Zinc Hydroxynitrates to Pure Zinc Oxide Nanoparticles in Supercritical Water. *Industrial & Engineering Chemistry Research,* 52 (4), 1448-1454.
2. Ashfold, M.N.R., Doherty, R.P., Ndifor-Angwafor, N.G., Riley, D.J. and Sun, Y., 2007. The kinetics of the hydrothermal growth of ZnO nanostructures. *Thin Solid Films,* 515 (24), 8679-8683.
3. Baier, J., Naumburg, T., Blumenstein, N.J., Jeurgens, L.P., Welzel, U., Do, T.A., Pleiss, J. and Bill, J., 2012. Bio-inspired mineralization of zinc oxide in presence of ZnO-binding peptides. *Biointerface Research in Applied Chemistry,* 2 (4), 380 - 391.
4. Barth, A., 2000. The infrared absorption of amino acid side chains. *Progress in Biophysics and Molecular Biology,* 74 (3), 141-173.
5. Baruah, S., and Dutta, J., 2009. Hydrothermal growth of ZnO nanostructures. *Science and Technology of Advanced Materials,* 10 (1), 013001.
6. Becker, R., and Döring, W., 1935. Kinetische behandlung der keimbildung in übersättigten dämpfen. *Annalen Der Physik,* 416 (8), 719-752.
7. Berg, J.M., and Godwin, H.A., 1997. Lessons from zinc-binding peptides. *Annual Review of Biophysics and Biomolecular Structure,* 26 (1), 357-371.
8. Bruker, 2006. *Ultraflex III user manual.* Version 1.0 ed. Germany: Bruker Daltonik GmbH.
9. Cavani, F., Trifirò, F. and Vaccari, A., 1991. Hydrotalcite-type anionic clays: Preparation, properties and applications. *Catalysis Today,* 11 (2), 173-301.
10. Cölfen, H. and Mann, S., 2003. Higher-order organization by mesoscale self-assembly and transformation of hybrid nanostructures. *Angewandte Chemie International Edition,* 42 (21), 2350-2365.
11. Coppage, R., Slocik, J.M., Briggs, B.D., Frenkel, A.I., Naik, R.R. and Knecht, M.R., 2012. Determining Peptide Sequence Effects That Control the Size, Structure, and Function of Nanoparticles. *ACS Nano,* 6 (2), 1625-1636.
12. Cubillas, P., and Anderson, M.W., 2010. Synthesis mechanism: crystal growth and nucleation. *Zeolites and Catalysis: Synthesis, Reactions and Applications*, 1-55.
13. De Yoreo, J.J., and Vekilov, P.G., 2003. Principles of crystal nucleation and growth. *Reviews in Mineralogy and Geochemistry,* 54 (1), 57-93.
14. Dudev, T., and Lim, C., 2003. Principles governing Mg, Ca, and Zn binding and selectivity in proteins. *Chemical Reviews,* 103 (3), 773-788.
15. Erdemir, D., Lee, A.Y. and Myerson, A.S., 2009. Nucleation of crystals from solution: classical and two-step models. *Accounts of Chemical Research,* 42 (5), 621-629.
16. Evans, J.S., Samudrala, R., Walsh, T.R., Oren, E.E. and Tamerler, C., 2008. Molecular design of inorganic-binding polypeptides. *MRS Bulletin,* 33 (05), 514-518.
17. Gebauer, D. and Cölfen, H., 2011. Prenucleation clusters and non-classical nucleation. *Nano Today,* 6 (6), 564-584.
18. Gerstel, P., Lipowsky, P., Durupthy, O., Hoffmann, R.C., Bellina, P., Bill, J. and Aldinger, F., 2006. Deposition of zinc oxide and layered basic zinc salts from aqueous solutions containing amino acids and dipeptides. *Journal of the Ceramic Society of Japan,* 114 (1335), 911-917.
19. Gibbs, J.W., 1878. On the equilibrium of heterogeneous substances. *American Journal of Science,* (96), 441-458.

20. Govender, K., Boyle, D., S., Kenway, P., B. and O'Brien, P., 2004. Understanding the factors that govern the deposition and morphology of thin films of ZnO from aqueous solution. *Journal of Materials Chemistry,* 14, 2575-2591.

21. Hosono, E., Fujihara, S., Kimura, T. and Imai, H., 2004. Growth of layered basic zinc acetate in methanolic solutions and its pyrolytic transformation into porous zinc oxide films. *Journal of Colloid and Interface Science Journal of Colloid and Interface Science,* 272 (2), 391-398.

22. Inoue, S., and Fujihara, S., 2011. Liquid− Liquid Biphasic Synthesis of Layered Zinc Hydroxides Intercalated with Long-Chain Carboxylate Ions and Their Conversion into ZnO Nanostructures. *Inorganic Chemistry,* 50 (8), 3605-3612.

23. Jang, W.S., Lee, T.I., Oh, J.Y., Hwang, S.H., Shon, S.W., Xia, Y., Myoung, J.M. and Baik, H.K., 2012. Kinetically controlled way to create highly uniform mono-dispersed ZnO sub-microrods for electronics. *Journal of Materials Chemistry,* 22 (38), 20719-20727.

24. Kashchiev, D., 2003. Thermodynamically consistent description of the work to form a nucleus of any size. *The Journal of Chemical Physics,* 118, 1837.

25. Kim, S.H., Olson, T.Y., Satcher, J.H. and Yong-Jin Han, T., 2011. Hierarchical ZnO structures templated with amino acid based surfactants. *Microporous and Mesoporous Materials*.

26. Kuo CL, Kuo TJ and Huang MH, 2005. Hydrothermal synthesis of ZnO microspheres and hexagonal microrods with sheetlike and platelike nanostructures. *The Journal of Physical Chemistry.B,* 109 (43), 20115-21.

27. Li, P., Xu, Z.P., Hampton, M.A., Vu, D.T., Huang, L., Rudolph, V. and Nguyen, A.V., 2012. Control preparation of zinc hydroxide nitrate nanocrystals and examination of the chemical and structural stability. *The Journal of Physical Chemistry C,* 116 (18), 10325-10332.

28. Li, W., Shi, E., Zhong, W. and Yin, Z., 1999. Growth mechanism and growth habit of oxide crystals. *Journal of Crystal Growth,* 203 (1), 186-196.

29. Liang, M., 2010. *Study of peptide-mineral interactions.* PhD Thesis. Nottingham Trent University.

30. Liang, M., Deschaume, O., Patwardhan, S.V. and Perry, C.C., 2011. Direct evidence of ZnO morphology modification *via* the selective adsorption of ZnO-binding peptides. *Journal of Materials Chemistry,* 21 (1), 80-89.

31. Liu, B., and Zeng, H.C., 2004. Room temperature solution synthesis of monodispersed single-crystalline ZnO nanorods and derived hierarchical nanostructures. *Langmuir,* 20 (10), 4196-4204.

32. Massova, I., and Kollman, P.A., 1999. Computational alanine scanning to probe protein-protein interactions: a novel approach to evaluate binding free energies. *Journal of the American Chemical Society,* 121 (36), 8133-8143.

33. Masuda, Y., Kinoshita, N. and Koumoto, K., 2007. Morphology control of ZnO crystalline particles in aqueous solution. *Electrochimica Acta,* 53 (1), 171-174.

34. McPeak, K.M., Le, T.P., Britton, N.G., Nickolov, Z.S., Elabd, Y.A. and Baxter, J.B., 2011. Chemical Bath Deposition of ZnO Nanowires at Near-Neutral pH Conditions without Hexamethylenetetramine (HMTA): Understanding the Role of HMTA in ZnO Nanowire Growth. *Langmuir,* 27 (7), 3672-3677.

35. Muthukumara, M., 2009. Theory of competitive adsorption-nucleation in polypeptide-mediated biomineralization. *The Journal of Chemical Physics,* 130, 161101-161105.

36. Nara, M., Torii, H. and Tasumi, M., 1996. Correlation between the vibrational frequencies of the carboxylate group and the types of its coordination to a metal ion: an ab initio molecular orbital study. *The Journal of Physical Chemistry,* 100 (51), 19812-19817.

37. Newman, S.P., and Jones, W., 1999. Comparative Study of Some Layered Hydroxide Salts Containing Exchangeable Interlayer Anions. *Journal of Solid State Chemistry,* 148 (1), 26-40.

38. Ogata, S., Tagaya, H., Karasu, M. and Kadokawa, J., 2000. New preparation method for organic–inorganic layered compounds by organo derivatization reaction of $Zn(OH)_2$ with carboxylic acids. *Journal of Materials Chemistry,* 10 (2), 321-327.

39. Oka, K., Shibata, H. and Kashiwaya, S., 2002. Crystal growth of ZnO. *Journal of Crystal Growth*, 237-239, Part 1 (0), 509-513.

40. Oren, E.E., Tamerler, C. and Sarikaya, M., 2005. Metal recognition of septapeptides via polypod molecular architecture. *Nano Letters*, 5 (3), 415-419.

41. Pandey, R.B., Heinz, H., Feng, J., Farmer, B.L., Slocik, J.M., Drummy, L.F. and Naik, R.R., 2009. Adsorption of peptides (A3, Flg, Pd2, Pd4) on gold and palladium surfaces by a coarse-grained Monte Carlo simulation. *Physical Chemistry Chemical Physics*, 11 (12), 1989-2001.

42. Peng, Z., and Yang, H., 2009. Designer platinum nanoparticles: Control of shape, composition in alloy, nanostructure and electrocatalytic property. *Nano Today*, 4 (2), 143-164.

43. Penn, R.L., and Banfield, J.F., 1998. Imperfect oriented attachment: dislocation generation in defect-free nanocrystals. *Science*, 281 (5379), 969-971.

44. Puddu, V., and Perry, C.C., 2012. Peptide Adsorption on Silica Nanoparticles: Evidence of Hydrophobic Interactions. *ACS Nano*, 6 (7), 6356-6363.

45. Rabe, M., Verdes, D. and Seeger, S., 2011. Understanding protein adsorption phenomena at solid surfaces. *Advances in Colloid and Interface Science*, 162 (1), 87-106.

46. Rieger, J., Frechen, T., Cox, G., Heckmann, W., Schmidt, C. and Thieme, J., 2007. Precursor structures in the crystallization/precipitation processes of CaCO3 and control of particle formation by polyelectrolytes. *Faraday Discussions*, 136, 265-277.

47. Rothenstein, D., Claasen, B., Omiecienski, B., Lammel, P. and Bill, J., 2012. Isolation of ZnO-binding 12-mer peptides and determination of their binding epitopes by NMR spectroscopy. *Journal of the American Chemical Society*, 134 (30), 12547-12556.

48. Sakohara, S., Ishida, M. and Anderson, M.A., 1998. Visible luminescence and surface properties of nanosized ZnO colloids prepared by hydrolyzing zinc acetate. *The Journal of Physical Chemistry B*, 102 (50), 10169-10175.

49. Sano, K., and Shiba, K., 2003. A hexapeptide motif that electrostatically binds to the surface of titanium. *Journal of the American Chemical Society*, 125 (47), 14234-14235.

50. Sarikaya, M., Tamerler, C., Schwartz, D.T. and Baneyx, F., 2004. Materials assembly and formation using engineered polypeptides. *Annu. Rev. Mater. Res.*, 34, 373-408.

51. Seker, U.O.S., Wilson, B., Dincer, S., Kim, I.W., Oren, E.E., Evans, J.S., Tamerler, C. and Sarikaya, M., 2007. Adsorption behavior of linear and cyclic genetically engineered platinum binding peptides. *Langmuir*, 23 (15), 7895-7900.

52. Serizawa, T., Sawada, T. and Matsuno, H., 2007. Highly specific affinities of short peptides against synthetic polymers. *Langmuir*, 23 (22), 11127-11133.

53. Söhnel, O., and Mullin, J., 1982. Precipitation of calcium carbonate. *Journal of Crystal Growth*, 60 (2), 239-250.

54. Song, R., Liu, Y. and He, L., 2008. Synthesis and characterization of mercaptoacetic acid-modified ZnO nanoparticles. *Solid State Sciences*, 10 (11), 1563-1567.

55. Song, Y., Challa, S.R., Medforth, C.J., Qiu, Y., Watt, R.K., Peña, D., Miller, J.E., van Swol, F. and Shelnutt, J.A., 2004. Synthesis of peptide-nanotube platinum-nanoparticle composites. *Chemical Communications*, (9), 1044-1045.

56. Sugunan, A., Warad, H., Boman, M. and Dutta, J., 2006. Zinc oxide nanowires in chemical bath on seeded substrates: Role of hexamine. *Journal of Sol-Gel Science and Technology*, 39 (1), 49-56.

57. Tada, H., 1960. Decomposition reaction of hexamine by acid. *Journal of the American Chemical Society*, 82 (2), 255-263.

58. Teng, H.H., 2013. How Ions and Molecules Organize to Form Crystals. *Elements*, 9 (3), 189-194.

59. Tomczak, M.M., Gupta, M.K., Drummy, L.F., Rozenzhak, S.M. and Naik, R.R., 2009. Morphological control and assembly of zinc oxide using a biotemplate. *Acta Biomaterialia,* 5 (3), 876-882.

60. Tronto, J., Bordonal, A.C., Naal, Z. and Valim, J.B., 2013. Conducting Polymers/Layered Double Hydroxides Intercalated Nanocomposites. *In:* Y. Mastai, ed., *Materials Science - Advanced Topics.* InTech, 2013, pp. 3-30.

61. Umetsu, M., Mizuta, M., Tsumoto, K., Ohara, S., Takami, S., Watanabe, H., Kumagai, I. and Adschiri, T., 2005. Bioassisted Room-Temperature Immobilization and Mineralization of Zinc Oxide—The Structural Ordering of ZnO Nanoparticles into a Flower-Type Morphology. *Advanced Materials,* 17 (21), 2571-2575.

62. Unwin, P.R., 2007. Concluding RemarksCrystal growth and nucleation: tracking precursors to polymorphs. *Faraday Discussions,* 136, 409-416.

63. Vayssieres, L., 2003. Growth of Arrayed Nanorods and Nanowires of ZnO from Aqueous Solutions. *Advanced Materials,* 15 (5), 464.

64. Wang, Z.L., 2004. Zinc oxide nanostructures: growth, properties and applications. *Journal of Physics: Condensed Matter,* 16 (25), R829.

65. Wang, Y., Li, Y., Zhou, Z., Zu, X. and Deng, Y., 2011. Evolution of the zinc compound nanostructures in zinc acetate single-source solution. *Journal of Nanoparticle Research,* 13 (10), 5193-5202.

66. Wasserman, E., Wood, B. and Brodhol, J., 1995. The static dielectric constant of water at pressures up to 20 kbar and temperatures to 1273 K: Experiment, simulations, and empirical equations. *Geochimica Et Cosmochimica Acta,* 59 (1), 1-6.

67. Weinzierl, D., Touraud, D., Lecker, A., Pfitzner, A. and Kunz, W., 2008. Controlled preparation of hollow zinc oxide microspheres from aqueous solution using hexamethylenetetramine and cysteine. *Materials Research Bulletin,* 43 (1), 62-67.

68. Xie, Q., Li, J., Tian, Q. and Shi, R., 2012. Template-free synthesis of zinc citrate yolk–shell microspheres and their transformation to ZnO yolk–shell nanospheres. *Journal of Materials Chemistry,* 22 (27), 13541-13547.

69. Xu, A., Ma, Y. and Cölfen, H., 2007. Biomimetic mineralization. *Journal of Materials Chemistry,* 17 (5), 415-449.

70. Xu, S., and Wang, Z.L., 2011. One-dimensional ZnO nanostructures: Solution growth and functional properties. *Nano Research,* 4 (11), 1013-1098.

71. Yan Z., Ma Y., Wang D., Wang J., Gao Z. and Song T., 2008. Surfactant-free fabrication of ZnO spheres and pseudospherical structures. *J.Phys.Chem.C Journal of Physical Chemistry C,* 112 (25), 9219-9222.

72. Yu SY, Zhang HJ, Peng ZP, Sun LN and Shi WD, 2007. Template-free fabrication of hexagonal ZnO microprism with an interior space. *Inorganic Chemistry,* 46 (19), 8019-23.

Chapter 4

Thermodynamic Study of Interactions between Zinc Oxide and ZnO Binding Peptides Using ITC

4.1. Introduction

So far established, is that thermodynamic and kinetic factors play important roles in directing inorganic crystal growth and morphology. Also observed that peptides are able to modify the growth mechanisms and morphology of inorganic materials when incorporated in solution synthesis from precursors. However, the exact mechanism through which peptides interact with and in some instances modify the morphology of inorganic materials remains largely elusive. There may be a direct link between thermodynamic changes that occur at the peptide-inorganic interface and peptide-directed structural modification of inorganic materials. Therefore, probing thermodynamic changes during peptide-inorganic interactions may reveal principles through which material structure is controlled in nature by biomolecules for the advancement of material synthesis and design (Chiu *et al*., 2013; Muthukumara, 2009; Perry *et al*., 2009; Whyburn *et al*., 2008).

Few studies have attempted to kinetically and thermodynamically characterize the interaction of ZnO binding peptides (ZnO-PBs) with ZnO surfaces. Yokoo and colleagues (2010), fused EM-12 (EAHVMHKVAPRP) peptide to the *N*-terminus of Green fluorescent protein (GFP) using a linker sequence and studied its adsorption to ZnO particles by allowing the tagged peptide to interact with the particles and quantifying the amount of unbound peptide remaining in the supernatant after centrifugation. This process was also carried out for truncations of the peptide sequence *i.e.* GFP-EAHV and GFP-EAHVMHK. Adsorption isotherms were measured at several temperatures and thermodynamic parameters were estimated using van't Hoff equations. ΔG values of the adsorption of the tagged ZnO-BPs were estimated to lie in-between -7.17 and -8.37 kcal/mol. The interaction was enthalpy driven with the main

contribution from ΔH values (Yokoo *et al*., 2010). The interaction was mainly attributed to hydrogen bonding and electrostatic interactions through charged residues of the peptide but studying truncations of the peptide demonstrated that the specificity and affinity of the interactions was also influenced by specific recognition of the alignment of the sequence and the peptides conformation by the ZnO surfaces (Yokoo *et al*., 2010).

Further studies on the interaction of EM-12 peptide with ZnO particles were conducted by Okochi and co-workers (2010) from the same research group. EM-12 peptide was labelled using fluorescein isothiocyanate (FITC). Peptides with alanine mutations on each position of the sequence were also synthesized and FITC labelled. Additionally, 125 random rotations of EM-12 peptide were also synthesized and fluorescence labelled. Adsorption studies of FITC labelled peptides on ZnO particles showed that the imidazolium cations of histidine residues in position 3 and 6 of the sequence were important for the interaction of the peptide to ZnO. Additionally, sequences with higher affinity for ZnO were generated through randomly changing the alignment of the sequence which demonstrated that phage display had biases in translation of sequences and supported the complementary use of spot synthesis as a peptide array-based screening method (Okochi *et al*., 2010). The 'hot spot' regions for the adsorption of FITC labelled EM-12 peptide onto ZnO particles were also identified to be HVMHKV and HKVAPR. This was determined by studying ZnO adsorption and subsequent fluorescent intensity of stepwise truncations of EM-12 peptide from both *C*- and *N*-termini. The binding constant and the maximum amount of adsorbed peptide were determined for the FITC labelled EM-12 peptide and a couple of the truncated sequences. HVMHKV ($K_A = 5.6 \times 10^3$ M^{-1}) and HKVAPR ($K_A = 7.7 \times 10^3$ M^{-1}) peptides had lower binding affinity for ZnO particles than the original EM-12 sequence ($K_A = 2.7 \times 10^4$ M^{-1}). However, substitution of histidine and cysteine amino acids into certain positions in the truncated sequences (*i.e.* H<u>C</u>VA<u>H</u>R, $K_A = 9.8 \times 10^6$ M^{-1}) increased the binding affinity of the sequences for ZnO (Okochi *et al*., 2010).

A study by Rothenstein and co-workers (2012) reported the use of ^{1}H NMR to determine the binding affinity of two phage display identified ZnO binding peptides (HSSHHQPKGTNP and HHGHSPTSPQVR) for ZnO particles. The binding affinities

were obtained by determining the line broadening effects during interaction of the peptides with different concentrations of ZnO and assuming a 1:1 binding model. The affinity constant of HHGHSPTSPQVR peptide (K_D = 10 ± 3 nM) was lower than the affinity constant of HSSHHQPKGTNP peptide (K_D = 260 ± 160 nM). Therefore, the authors deduced that the HHGHSPTSPQVR peptide was the stronger binder for the ZnO substrate used (Rothenstein *et al*., 2012). From the above studies, its is evident that studying the interactions of phage display identified peptides with inorganic materials can give a clearer understanding of why these particular material specific peptide sequences were selected as stronger binders. Also underlined is that phage display technique has biases thus, the peptides identified may not be the strongest attainable binders for a particular substrate (Puddu and Perry, 2012). Using complementary approaches such as making random rotations of the original sequence, carrying out site specific mutations, introducing certain amino acids expected to improve the interaction of the sequence, studying the binding affinities and thermodynamic parameters of interaction together with computational approaches can enable one to improve the rational used to select specific sequences for a target material.

Herein, ITC was used to directly probe the thermodynamic changes that occur during the interaction of ZnO-BPs with ZnO crystals. Some of the advantages of using ITC over other more conventional techniques that can be used to study the interaction of peptides with inorganic materials (*i.e.* SPR, QCM-D, XPS, NMR and others techniques highlighted in section 1.4) include; it is a direct measure of molar enthalpy, it is able to determine all thermodynamic parameters *(*ΔH, ΔS, K_A and ΔG) from a single experiment and it does not require labelling or immobilization of the interacting components (Ababou and Ladbury, 2006; Chiad *et al*., 2009; Cliff *et al*., 2004). Applications of ITC have evolved from conventional biomolecular recognition reactions into diverse areas of interest in academic, medical and industrial laboratories. Some examples of novel research areas where interactions at biotic abiotic interfaces are being studied using ITC include; probing interactions between proteins/peptides and inorganic nanoparticles being developed for use in medical products (Cedervall *et al*., 2007; Cho *et al*., 2011; Goobes G. *et al*., 2007; Goobes R. *et al*., 2007; Gourishankar *et al*., 2004; Huang *et al*., 2013; Lindman *et al*., 2007; Lynch and Dawson, 2008; Mahmoudi *et al*., 2011; Rautaray *et al*., 2005) and probing interactions between inorganic/organic particles and

ligands for industrial advancements (Camci-Unal and Pohl, 2010; Chiad *et al*., 2009; Joshi *et al*., 2004; Karlsen *et al.*, 2010). Some of these studies and research directions mainly involving interactions with suspensions of metals and metal oxide particles have been highlighted in this chapter to provide a snapshot of the evolving applications of ITC in materials science.

4.1.1. Case studies on the Application of ITC in Materials Science

Among the pioneering studies applying ITC to investigate ligand nanoparticle interactions was a study to characterize interactions between amino acids and the surface of gold nanoparticles (Joshi *et al*., 2004). ITC was used to investigate the interactions between gold nanoparticles with a basic (lysine) and an acidic (aspartic acid) amino acid. They observed that amine groups bound more strongly with gold nanoparticles in their unprotonated state therefore at physiological pH lysine was found to interact weakly with gold nanoparticles compared to aspartic acid (Joshi *et al*., 2004). Similarly, ITC was used to characterize the energetics of interaction of deoxyribonucleic acid (DNA) and peptide nucleic acids (PNA) base monomers with gold nanoparticles. The aim was to design oligonucleotides that could complex with gold nanoparticles based on their different binding strengths without the need for thiolation (Gourishankar *et al*., 2004). In another study ITC was used to characterize interactions between gold nanoparticles capped with aspartic acid to calcium ions which can template the growth of hydroxyapatite crystals for interests in biomedical applications (Rautaray *et al*., 2005). In all the above studies, the authors did not determine the thermodynamic parameters of the interaction because they concluded that it was not possible to accurately determine the binding sites available for interaction. However, the nature of the interactions and qualitative trends in the binding behaviors of interacting components could be identified from the isotherms (Gourishankar *et al*., 2004; Joshi *et al*., 2004, Rautaray *et al*., 2005). ITC showed great potential in its use to monitor the interactions between ligands and nanoparticles and the development of its application into new fields was encouraged.

More recently, the surface modification of SiO_2 *via* interactions with amphiphilic monomers and copolymers was investigated using ITC (Chiad *et al*., 2009). The

formation of these organic-inorganic hybrid systems occurs through noncovalent adsorption of amphiphilic compounds to the surface of inorganic particles and the strength and irreversibility of the interaction was of great interest (Chiad *et al*., 2009; Hoffmann *et al*., 2006). The polymers were titrated into 10 mg/ml suspensions of SiO_2 nanoparticles (diameter ~10 nm) in a solvent mixture (1,4-dioxane/ethanol/H_2O) suitable for solubilizing the amphiphilic copolymers and preventing particle aggregation. Thermodynamic parameters of interaction were determined using one set and two sets of sites fitting models. Determination of thermodynamic parameters from ITC experiments requires accurate determination of the concentration of the syringe and sample component (Leavitt and Freire, 2001; Thomson and Ladbury, 2004). The authors plotted the normalized heat change against the molar ratio of the concentration of polymer used versus the concentration of SiO_2 which may be considered as inaccurate because the polymers interacted with the surface of the nanoparticle, not its bulk therefore only the concentration of the surface sites should have been used (Goobes G. *et al*., 2007; Goobes R. *et al*., 2007). However, the accuracy of determining the concentration of the syringe component in ITC experiments directly affects the accuracy of determining the parameters K_A, n and ΔH whereas the accuracy of determining the concentration of the sample cell component only affects the molar binding ratio (n) (Myszka *et al*., 2003). From their study, Chiad and co-workers (2009) concluded that probing thermodynamic changes occurring at interfaces could possibly allow one to directly correlate adsorption strength to the structure of inorganic particles allowing materials engineering to be conducted using more rational and optimized methods.

ITC has also been used in biomineralization studies, to determine thermodynamic parameters of biomolecule interactions with biominerals. One such study was on statherin which is an oral cavity protein that regulates the nucleation and growth of hydroxyapatite (HAP) and serves as a receptor for bacterial adhesion to enamel (Goobes G. *et al*., 2007; Goobes R. *et al*., 2007). The wild type sequence of statherin consists of 43 amino acid residues in which the first five residues are negatively charged and have been identified to directly participate in binding to hydroxyapatite (Goobes G. *et al*., 2007; Wikiel *et al*., 1994). The acidic amino acids are followed by a basic amino acid rich segment whose role was not known, thus Goobes R. and co-workers (2007)

designed a study to uncover the role by carrying out single and multiple point mutations replacing the positively charges basic residues with alanine amino acid. The interaction of the wild type and mutant proteins with HAP crystals was studied using ITC and equilibrium adsorption binding isotherms (AI). Synthesized proteins were also all labelled at specific positions for studies on the structure of the adsorbed proteins using solid-state NMR (Goobes G. *et al*., 2007). Normalized heat changes were plotted against the molar ratio of the protein concentration versus the effective concentration of sites (M_t') on the surface of HAP available for interaction with the protein using the following expression:

$$M_t' = N_{max}\left(\frac{moles}{m^2}\right) \times SA\left(\frac{m^2}{gr}\right) \times D\left(\frac{gr}{L}\right)$$

Equilibrium adsorption isotherm measurements (AI) were used to quantify the maximum number of peptide interaction sites (N_{max}) per unit surface area of the inorganic particle using a simple Langmuir adsorption model. Their data demonstrated that the sensitivity of distinguishing between free and bound protein was lowered by use of small amounts of HAP and that with increasing coverage, the method was insensitive to differences in adsorption between the mutants and the wild type. The total surface area (SA) of the inorganic particles was determined from BET measurements although there may have been discrepancies between the surface sites that were accessible to small gaseous molecules such as nitrogen used in BET experiments compared to the size of interacting molecules being studied (Goobes R. *et al*. 2007). The density (D) of the inorganic particles in the ITC cell was obtained by dividing its mass by the volume of the cell. Both protein-surface as well as protein-peptide interactions were though to take place based on differences in surface coverage determined using AI studies. The isothermal profiles obtained were sigmoid shaped, characteristic of one set of independent binding sites model which is identical to Langmuir adsorption model. The authors argued that only the initial peptide-surface interaction produced a heat change that was measurable using ITC. They concluded that the basic amino acids did not significantly contribute to the protein's enthalpy of adsorption but influenced the packing density of the protein at saturation (Goobes G. *et al*., 2007).

Studies where ITC has been successfully used to probe interactions between different ligand molecules with inorganic/organic materials continue to emerge. ITC has developed from its conventional use to study equilibrium processes to a universal tool that can be used to investigate irreversible processes of binding/adsorption of artificial molecules and biopolymers on surfaces or with each other (Chiad *et al*., 2009; Schmidtchen, 2012). This approach of using ITC to study interactions between peptides and inorganic materials has its challenges. Nevertheless, great prospects lie in using information obtained from ITC studies to advance design processes and exploration into novel systems equally drives the development and improvement of ITC experiment strategies and data analysis protocols.

4.1.2. Crystal Structure and the Surface of ZnO

The crystal structure of ZnO was briefly discussed in section 1.3.1 of chapter 1. The hexagonal wurtzite structure of ZnO (Figure 4.1) is the thermodynamically stable crystal phase that can be synthesized at ambient reaction conditions (Govender *et al*., 2004). The metastable zinc blende (sphalerite) structure (Figure 4.1) of ZnO can only be stabilized by growth using cubic substrates such as ZnS and GaAs (Almamum *et al*., 2000). The wurtzite and zinc blende structure both have ions that are tetrahedrally coordinated (*i.e.* one O^{2-} ion is surrounded tetrahedrally by four Zn^{2+} ions and vice versa forming alternating planes stacked along the *c*-axis) resulting in the same bond distance between the four nearest neighbours and the next twelve closest neighbours (Li *et al.*, 2012; Morkoc and Ozgur, 2009; Wang, 2004). The difference between the wurtzite and zinc blende structure is the stacking sequence of close-packed diatomic planes resulting from differences in the bond angel of the second closest neighbour (Figure 4.1). The wurtzite structure has triangularly arranged alternating planes stacked in a mirror image (without in-plane rotation) along the (0001) plane whereas the zinc blende structure has triangularly arranged alternating planes stacked with an in-plane rotation of 60° along the (111) plane (Morkoc and Ozgur, 2009). For interaction studies with peptides using ITC, hexagonal wurtzite structured ZnO crystals were suitable for their facile synthesis in aqueous solution obtaining particles in suspension as opposed to zinc blende structures that require a substrate for synthesis and are therefore immobilized.

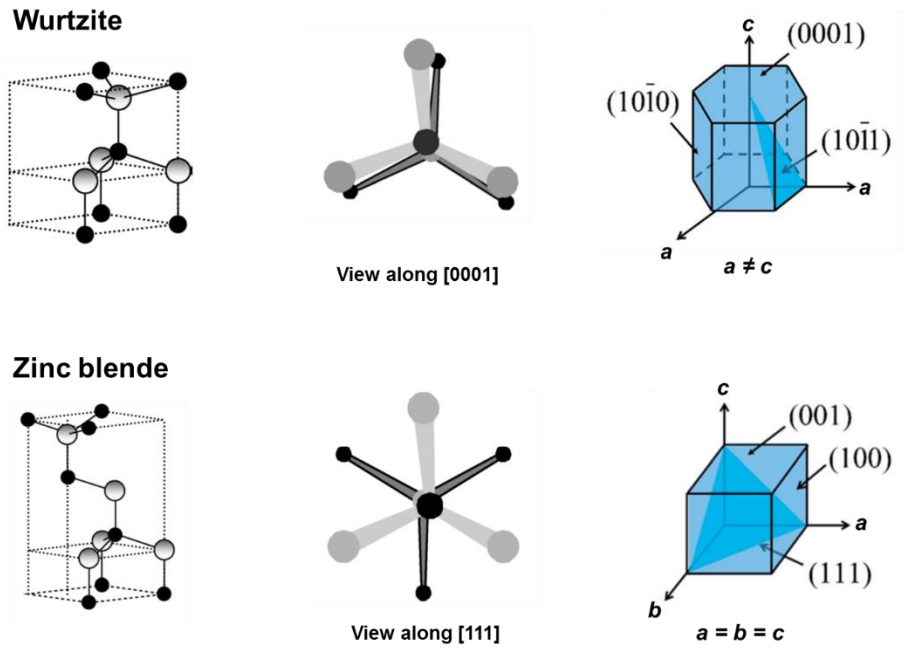

Figure 4.1. Models of the hexagonal wurtzite and cubic zinc blende structures of ZnO. Gray and black spheres represent Zn and O atoms, respectively in the ball and stick representations of unit cells and the stacking of planes viewed along the (0001) and (111) plane. Schematics of common crystal planesare also shown. Adapted from Morkoc and Ozgur, 2009 and Chang and Waclawik, 2014.

From literature, the general growth mechanism of twinned hexagonal wurtzite ZnO rods synthesized in aqueous soluton without any additive can be summerized as follows; Anisotropic crystal growth is thought to occur because oppositely charged (0001) Zn-terminated and (10$\bar{1}$0) O-terminated polar planes of ZnO result in a dipole moment and have higher surface energy than non-polar planes like the (10$\bar{1}$0) plane that is both Zn/O-terminated (Govender *et al*., 2004; Xu and Wang., 2011). Therefore, to minimize the total free energy of the system, incoming precusor molecules favoroubly adsord to the polar planes resulting in growth along the *c*-axis. The twinning mechanism, also a divice thought to reduce the surface energy of crystals, occurs through the O-terminated (10$\bar{1}$0) polar plane as the common connection plane (Wang *et al*., 1998; Xu and Wang., 2011). Thus, for elongated ZnO rods, the main planes exposed to possible interaction with peptide may be the (0001) Zn-terminated polar plane and the (10$\bar{1}$0) Zn/O-terminated non-polar plane of ZnO.

The surface of ZnO has been studied using experimental and theoretical techniques such as low energy electron diffraction (LEED), X-ray photoelectron spectroscopy (XPS), X-ray emission spectroscopy (XES), scanning tunneling microscopy (STM) and density functional theory (DFT) (Diebold *et al*., 2004; Dulub *et al*., 2002; Woll, 2007). STM has been particularly useful for structural characterization of ZnO surfaces at the atomic scale (Diebold *et al*., 2004; Dulub *et al*., 2002). For example, using STM microscopy, the surface of the polar thermodynamically unstable Zn-terminated (0001) plane has been found to be rough with triangular step edges, small terraces, holes and islands which may play an important role in the growth processes at atomic scale (Diebold *et al*., 2004; Dulub *et al*., 2002; Woll, 2007). The energetically favourable mixed Zn/O-terminated non-polar ($10\bar{1}0$) plane has been described as a surface with a well defined flat (small roughness) terrace step structure associated with ZnO dimers that are elongated and aligned along the [0001] or [$\bar{1}2\bar{1}0$] and direction (Dulub *et al*., 2002). The adsorption of molecules such as water on the surface of ZnO has also been of considerable interest in research. Molecules can be physisorbed or chemisorbed onto the surface of ZnO in single or several layers (Degen and Kosec, 2000). In water, the surface of ZnO is hydrolysed forming hydroxide layers which depending on solution pH become charged by reacting with either H^+ or OH^- ions due to the surface amphoteric nature of ZnO and $Zn(OH)_2$ (Degen and Kosec, 2000). This affects the surface charge of ZnO crystals in aqueous solution and therfore influences interaction with other molecules such as peptides.

4.2. Materials and Methods

4.2.1. Synthesis of Peptides and ZnO Crystals Used in ITC Experiments

Peptides used in this study were synthesized using microwave-assisted solid phase peptide synthesis protocol as described in section 3.2.2.4. The peptide sequences were ZnO-BPs previously identified using phage display technique by Tomczak and co-workers (2009); G-12 and GT-16 peptide and mutants of G-12 peptide (G-12A6, G-12A11 and G-12A12 peptide) selected after computational studies by Ramasamy R. (section 3.3.2). ZnO crystals used in ITC experiments were synthesized following a

hydrothermal synthesis method previously described in section 3.2.2.4 that used precursor $Zn(NO_3)_2 \cdot 6H_2O$ and HMTA. Two different morphologies of ZnO were used, ZnO twinned rods and ZnO twinned platelets (synthesized in the presence of GT-16 peptide).

4.2.2. Characterization of ZnO Crystals and Peptides for ITC Experiments

ZnO crystals and peptides were characterized using several analytical techniques described in detail in section 3.2.3. The purity and molecular weight of synthesized peptides were ascertained using HPLC and MALDI-TOF mass spectrometry. Computational tools, Tripos SYBYL and MD were used to study the conformation and stability of peptide sequences. The net charge and isoelectric point of the peptides were determined using an online peptide property calculator from Innovagen.

ZnO crystals were thoroughly characterized *i.e.* SEM and EDX was used to characterize the morphology and elementally analyze the material, XRD was used to study their crystallinity and FTIR and TGA analysis were used to determine the composition of the materials. All the above ZnO characterization methods have been described and discussed in chapter 3. The surface area of ZnO crystals was determined using the single-point Brunauer-Emmett-Teller (BET) method by Dr Belton D. using a Quantachrome Monosorb instrument. Samples were heated and gas flowed over the inorganic surface to remove surface contaminants. The samples were then cooled to cryogenic temperatures and a mixture of helium (He) and nitrogen (N_2) of known volume flowed over the samples. At low temperature, N_2 gas adsorbed on the surface of the material. He which is an inert gas was used as a carrier gas. The sample was heated to room temperature desorbing the adsorbed N_2. The volume of the adsorbed and desorbed gas was detected by a thermal conductivity detector that is highly sensitive and compared to a calibration using counts measured from different volumes of N_2.

4.2.3. ITC Study of Interactions between ZnO Microcrystals and ZnO-BPs

Thermodynamic binding experiments were carried out using VP-ITC Northampton, MA instrument. Preliminary experiments were carried out to optimize the experimental conditions to; (i) attain saturation of the ZnO particles by the peptide which is an

indicator of the endpoint of the interaction, (ii) minimize dilution heats to avoid interference in measurement of interaction heats and (iii) attain sufficient measurements and curve shape to be able to accurately distinguish between bound and unbound peptide, hence determine K_A (Cliff *et al*., 2004; Leavitt and Freire, 2001; Thomson and Ladbury 2004; Ladbury and Doyle, 2005; Liang, 2008). Some of the parameters that were altered to optimize the experiment was the amount of ZnO suspended in solution inside the sample cell, the peptide concentration in the syringe, the number of injections, the volume per injection, the spacing between injections and the stirring speed. The maximum syringe volume was 280 µl and the sample cell volume was 1.4 ml. The temperature of the reaction was kept constant at 25 °C and samples prepared were degassed for 7 min using a thermovac before loading in the ITC to ensure no air bubbles were present that could interfere with calorimetric readings.

Preliminary studies determined that a very small amount of ZnO was required to be able to reach saturation with the peptide concentration chosen. Stock suspensions of ZnO samples were prepared by suspending a known weight of particles in water (filtered distilled deionized water). From the stock suspension, further dilutions were prepared by vortexing the stock and quickly pipetting a predetermined volume containing the ZnO crystals then diluting to the volume required for ITC experiments. A dissolution study was designed to test the reproducibility of sample preparation between ITC experiments. ZnO crystals in samples prepared for ITC experiments were dissolved in dilute (0.9%) hydrochloric acid releasing Zn^{2+} ions into solution which was quantified using ICP-OES. Using ANOVA a p-value > 0.05, n = 21 was attained thus there was no significant difference in the amount of Zn^{2+} ions between samples prepared. The concentration of Zn^{2+} ions present was 0.10 ± 0.01 mM which was slightly lower than the amount that was anticipated to be present (0.15 mM) if it was directly calculated from the mass of ZnO weighed to prepare the stock suspension. This process was repeated severally during the course of the experiments to ensure that sample preparations were comparable.

The parameters chosen for the experiments were; a reference power of 15 µcal/sec, the syringe was rotated continuously throughout the experiment at a stirring speed of 394 rpm to ensure the particles remained in suspension, a peptide concentration of 3.1 mM

was chosen and 280 µl was injected periodically into the sample cell in 10 µl aliquots. At least 1000 sec was required in between injections as the interactions were slow to return to the baseline equilibrium after each injection. For the first 10 injections, a spacing of 1200 sec was used and for the remaining 18 injections, a spacing of 1000 sec was used. In some experiments with GT-16 peptide, the spacing of the first 10 injections needed to be increased to 1600 sec. Water was the solvent of choice because previous studies had shown that peptides were able to adsorb to ZnO particles in the synthesis experiments carried out in aqueous media (Liang *et al*., 2011). Ideally, all ions that were also present in the solutions during synthesis from precursor $Zn(NO_3)_2 \cdot 6H_2O$ and hydrolysed species from HMTA would also be included. However, as several different reactions would take place simultaneously and contribute to the global heat change measured by the ITC instrument, it would not be possible to determine contributions of individual events. Simplifying the experiment was therefore the best approach to confine measured heat changes to heat changes that could be attributed to interactions between the peptides and the ZnO particles.

Matching the composition of the components in the sample cell and syringe such as concentration of salts used, pH and buffers helps to minimize dilution heat changes that may plausibly override binding signals (Freyer and Lewis, 2008). The disadvantage of using water as the solvent is that there was a decrease in the pH in the sample cell with continued injection of peptide but the same effect occurred in the control experiment (titration of peptide into water) and the interaction experiment (titration of peptide into water containing ZnO particles). At a concentration of 3.1 mM, the pH of the peptides were pH 3.08 ± 0.35 and the pH of the water was pH 5.77 ± 0.23 without and with the ZnO particles. At the end of the titration of the controls and interaction experiments the pH in the sample cell had been decreased to pH 3.92 ± 0.35. There was no expected heat change contribution from peptide protonation events at the working pH range. The dilution heat change of titrating peptide into water was acceptably small regardless of the change in pH. Buffers could be used in the ITC experiments to maintain a constant pH during titration however buffer related contributions to the observed heat change would need to be considered (Leavitt and Freire 2001; Thomsaon and Ladbury, 2004). Also buffer ions that were not present in the ZnO synthesis reaction would need to be included which was not preferred.

The heat changes measured in the peptide dilution experiment were subtracted from the heat changes of interaction during the titration of peptide with the ZnO particles. Other dilution experiments that were performed were dilution of water into the cell containing the ZnO particles and the dilution of water into water which had negligible heat measurements. Each experiment was repeated three times. Data analysis was conducted using ORIGIN 7.0 software and fitting done using a non-linear least-squares algorithm with binding models made available by MicroCal.

4.3. Results and Discussion

4.3.1. Thermodynamic Study Probing Interfacial Interactions of G-12 and GT-16 Peptides with ZnO Rods and Platelets

Previous studies on the adsorption of G-12 and GT-16 peptide to single crystalline ZnO surfaces showed that both peptides adsorbed to the $(10\bar{1}0)$ and (0001) planes of ZnO but GT-16 peptide preferentially adsorbed to the (0001) plane (Liang *et al*., 2011). ITC was used to study the interaction of G-12 and GT-16 peptides with two different morphologies of ZnO crystals; ZnO twinned rods and ZnO twinned platelets (Figure 4.2). The interest in this study was to determine if ITC could be used to monitor interactions between ZnO and ZnO-BPs and if differences in adsorption characteristics between the two peptides with the same crystal morphology and the same peptide with two crystal morphologies could be detected. Also sought was to determine if there was a direct link between thermodynamic changes that occur at the peptide-inorganic interface and peptide-directed structural modifications of inorganic materials.

The ZnO rods and platelets used in ITC experiments had been collected at 48 hrs of synthesis using the $Zn(NO_3)_2{\cdot}6H_2O$ and HMTA method previously described in detail in chapter 3. After washing and lyophilisation, samples were characterized using SEM, EDX, XRD, TGA and FTIR as discussed in sections 3.3.1 and 3.3.3. Synthesized ZnO rods had adsorbed water and 1.6 ± 0.2% organic matter attributed to the presence of intermediate compound, LBZN. ZnO platelets also contained adsorbed water and 7.5 ±

0.5% organic material (LBZN and strongly adsorbed GT-16 peptide). TGA profiles showing weight loss during calcination of ZnO rods and platelets is shown in Appendix

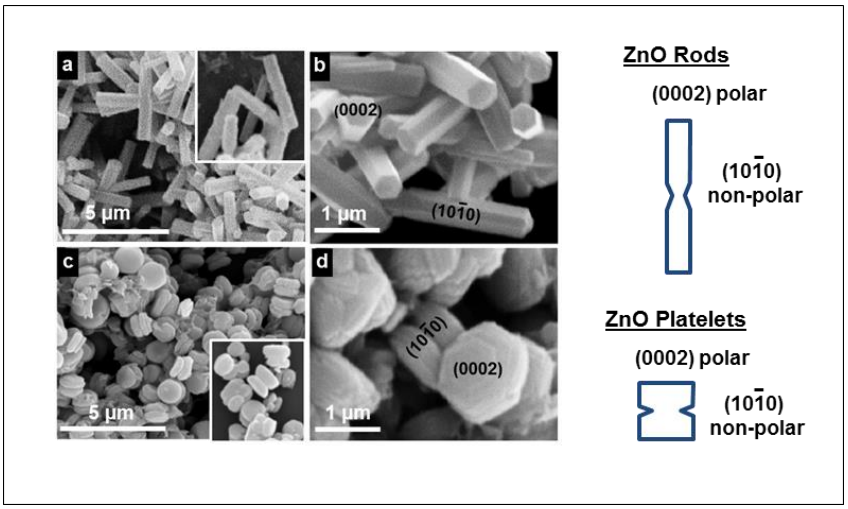

Figure 4.2. SEM micrographs (a, b) ZnO twinned rods collected at 48 hrs of synthesis using precursor $Zn(NO_3)_2 \cdot 6H_2O$ and HMTA (L/D = 8.9 ± 3.3), (c, d) ZnO twinned platelets collected at 48 hrs of synthesis using precursors $Zn(NO_3)_2 \cdot 6H_2O$, HMTA and 0.3 mM GT-16 peptide as a morphology modifier (L/D = 0.88 ± 0.5). Inset of figure (a) and (c) are calcined ZnO rods and platelets respectively. Scale bars; (a, c) 5 µm, (b, d) 1 µm. A schematic representation of the different ZnO morphologies has also been shown (not drawn to scale).

3.8. Some of the particles of both morphologies were calcined to 900 °C to decompose organic material and obtain pure surfaces for ITC interaction studies with peptides. The particles were not sintered by calcination as sintering of micron scale ZnO usually requires temperatures much higher than 950 °C (Cai and Zhang, 2008). XRD analysis of the calcined particles confirmed that phase transformation had not taken place during calcination (Appendix 4.1). There was little risk of phase transformation of the ZnO crystals as it requires temperatures above 1300 °C (Mazaheri *et al*., 2008). However, calcination could have altered some surface physical or chemical features that were not apparent but may be recognizable by peptides. We therefore decided to carry out ITC experiments using as synthesized ZnO particles (non-calcined) as well as calcined particles.

Interaction of G-12 and GT-16 peptide with ZnO rods and ZnO platelets produced heat changes that were measurable using ITC (Figure 4.3). For each interaction, the heat

change of diluting the peptide into water (baseline experiment) was subtracted from the global observed heat change (ΔH_{obs}) obtained during titration of ZnO particles with peptide. The heat change produced by diluting water into ZnO suspensions and the heat change produced by diluting water into water was insignificant. Remaining ΔH_{obs} after subtracting baseline experiments could be attributed to heat changes produced in the process of peptide interaction with the ZnO crystal surfaces. From the shapes of isothermal profiles, there were two binding events occurring, an endothermic event followed by an exothermic event evidenced by positive and negative changes in differential power (*Dp*). To measure more of the endothermic event that occurred at the beginning of the interaction, the ratio of the interacting species had to be decreased at the expense of reaching saturation of the subsequent exothermic event. An example of interaction of GT-16 peptide with ZnO rods at low molar ratios where the endothermic process was dominant has been shown in Appendix 4.2. Experiments were carried out at higher ratios of interacting species where endothermic heat changes could still be measured and the endpoint/saturation of the exothermic interaction could be reached where only dilution heat changes were measured with continued addition of peptide. For the same peptide and inorganic crystal, similar shapes of isothermal profiles were obtained showing reproducibility of interaction processes. Normalized heat changes in kcal/mole of injectant were plotted against the molar ratio of the peptide concentration and the bulk concentration of ZnO determined using ICP-OES even though the peptide would only interact with the surface of particles. The reason behind this will be explained.

Qualitative differences in binding isotherms could be identified when interactions of both peptides (G-12 and GT-16) with the same particles (either rods or platelets, calcined or non-calcined) or the same peptide with different particles was compared. Each peptide was injected into the ITC cell containing ZnO particles in 10 µl aliquots. Interestingly, longer time spacing in between injections was needed with GT-16 peptide for the heat change per injection to return to thermal equilibrium (back to the baseline) compared to G-12 peptide. This was observed with all the particles except the non-calcined ZnO rods. Higher peptide concentration was required to saturate the same mass of ZnO platelets compared to ZnO rods as ZnO platelets had a greater surface area available for interaction. The surface area of the ZnO rods was estimated to be 3.8 m^2/g

and the surface area of the platelets was estimated to be 4.2 m^2/g using single point BET. Calcination of ZnO samples caused changes in physico-chemical properties of ZnO surfaces (*i.e.* differences in the amount of chemisorbed water and organic contaminants evidenced from TGA analysis) compared to non-calcined crystals and these differences may have been recognised by the peptides in the adsorption process and reflected in the isothermal profiles produced.

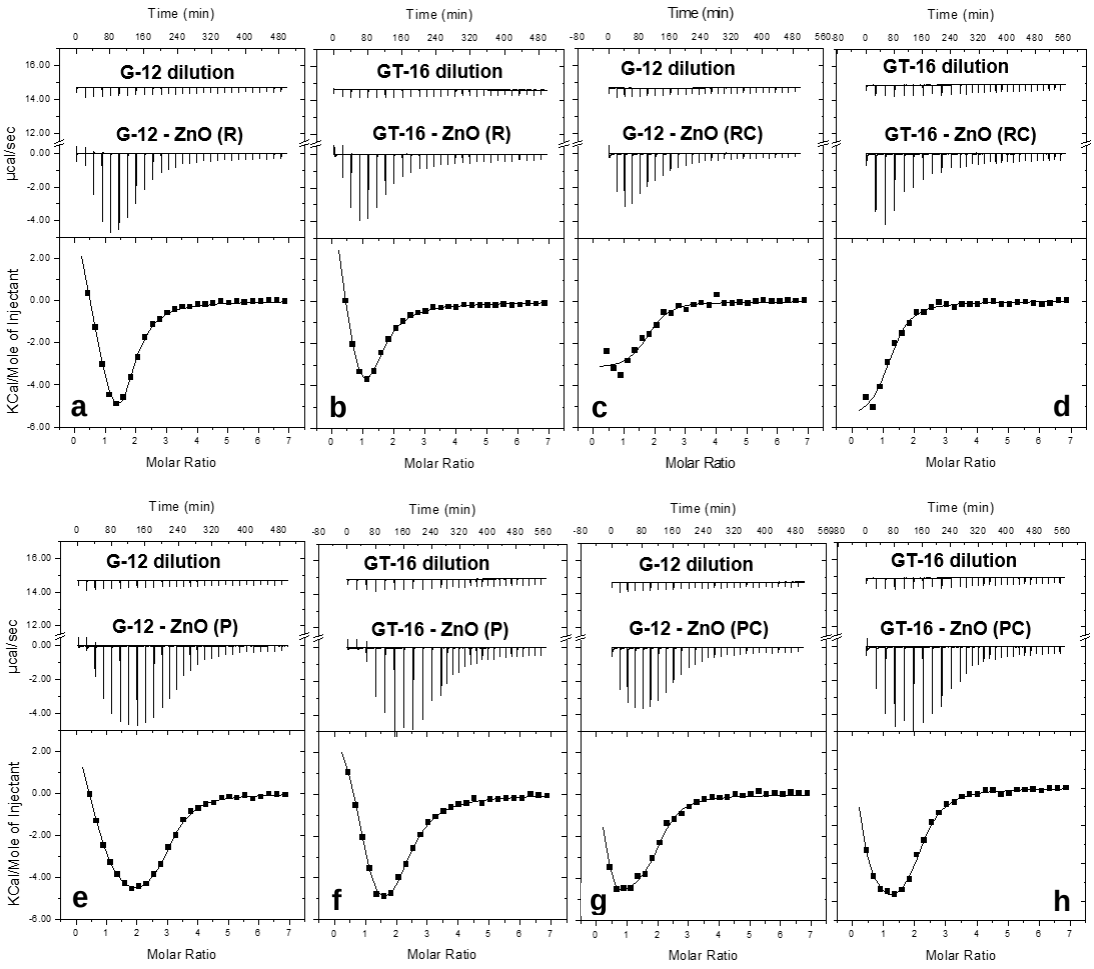

Figure 4.3. (a-d) ITC isotherms representing heat changes that occured when G-12 and GT-16 were titrated into suspensions of ZnO twinned rods in water. (e-h) ITC Isotherms representing heat changes that occured when G-12 and GT-16 were titrated into suspensions of ZnO twinned platelets in water. ZnO morphologies have been designated; (R) rods, (RC) rods calcined, (P) platelets, (PC) platelets calcined. In each experiment, a titration of 3.1 mM peptide in 28 injections each with 10 µl aliquots was made from a syringe into a sample cell containing 0.1 mM ZnO (bulk concentration). A constant cell temperature of 298 K was maintained. Titration of peptides into water to measure dilution heats is also shown and was subtracted from the heat change of peptide interaction with ZnO. The heat change of the first injection was deleted before data fitting because of its large dilution heat change. Data was fit using one or two sets of sites models.

In a typical ITC experiment to characterize the interaction of a ligand with a receptor, an interaction occurs forming a ligand-receptor complex described by E. Fisher as a lock and key mechanism (Ball and Maechline, 2009). The receptor binding site is specific as it is defined by a precise geometry/recognition motif and the interaction is achieved through chemical functions at the binding site through which it can complex to a ligand (Ball and Maechline, 2009). Quantifying the binding sites on the surface of inorganic particles can be challenging. For instance, some studies on solution synthesis of inorganic materials in the presence of peptides have demonstrated that, in some cases, peptides adsorb preferentially or solely to specific crystal planes (Chiu *et al*., 2011; Liang *et al*., 2011; Togashi *et al*., 2011). Therefore, for inorganic crystals with different crystal planes, the total surface area available for interaction in ITC experiments cannot always be equated to the surface area of actual binding sites. Also there may not be any clearly defined recognition pattern on the surface of an inorganic material similar to a lock and key mechanism (Ball and Maechline, 2009). However, there are studies that have defined recognition patters in peptide-inorganic surface interactions (Oren *et al*., 2005; Ruan *et al*., 2013). The binding site on an inorganic surface can thus be defined as the physico-chemical characteristics of the inorganic material surface that can be recognized by the reactive groups present on the peptide-sequence that form the 'hot spot' regions through which interactions can take place. The importance of thorough characterization of peptides and inorganic materials used in such studies therefore becomes paramount. Quantification of the binding site on an inorganic material can further be complicated by the possible different adsorption orientations of peptide molecules (*i.e.* end-on surface adsorption, flat-on surface adsorption, adsorption as a monolayer or multilayers and aggregates formed through possible peptide-peptide interactions) as illustrated in Figure 4.4. These parameters are challenging to determine and require a combination of several complementary techniques and methodologies to ascertain.

Determination of surface coverage is essential for quantification of binding potency and is an indicator of whether monolayers or multilayers are formed (Cohavi *et al*., 2011; Lindman *et al*., 2007). In all the measured interactions, at least 100 µl of 3.1 mM peptide was needed to reach saturation. The size of peptide molecules were estimated using MD software and the maximum number of peptide molecules needed to form

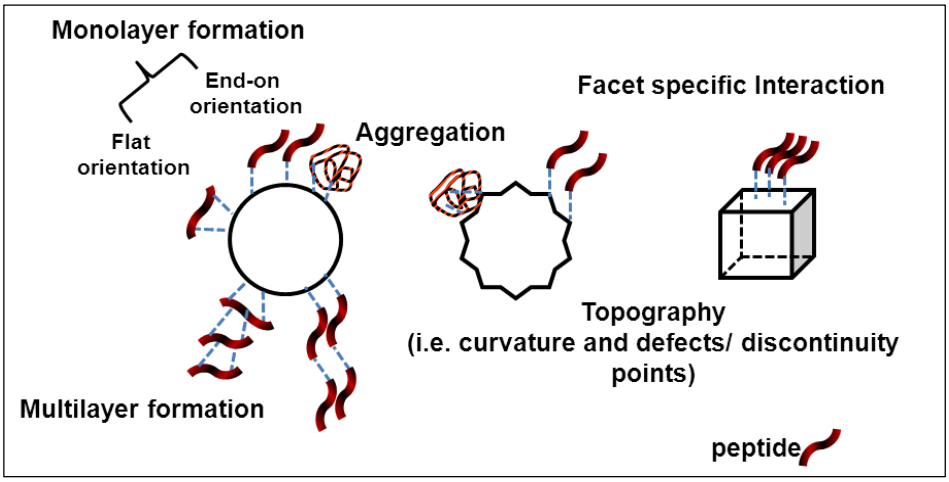

Figure 4.4. Illustration of some possible peptide-surface and peptide-peptide modes of interaction. Peptides may interact with the inorganic materials using specific functional groups of the amino acids in the sequence which may recognize chemical/physical surface features of the inorganic material. Image is not drawn to scale.

monolayer coverage of ZnO particles theoretically calculated assuming that the peptides adsorbed to the ZnO surfaces end-on/upright. For G-12 peptide for example, the number of unit molecules estimated to fill a monolayer was 8.91 x 10^{13} and the amount needed to reach saturation in ITC experiments was 2.46 x 10^{17}. The amount of peptide needed to obtain saturation in all the interactions was in great excess of the amount required to form a monolayer of peptide on the surface of ZnO available. A dense peptide multilayer may have been formed on the surface of ZnO.

The effective concentration of surface sites available for interaction (M_t') can be estimated using the method described by Goobes R. and co-workers (2007) but may only be suitable where monolayers are formed. Where multilayers form like in the adsorption of G-12 and GT-16 peptide on ZnO crystals as observed in this study, the value of M_t' obtained would represent both the surface sites available on ZnO as well as the peptide binding sites that allow intermolecular interaction. Normalized heat change in kcal/mole of injectant was therefore plotted against the molar ratio of the peptide concentration and the bulk concentration of ZnO. The concentration of peptide used was known therefore thermodynamic parameters of interaction K_A and ΔH could be estimated after data fitting. The molar binding ratio (n) was not determined because of the uncertainty of determining the concentration of surface binding sites on ZnO.

On detailed inspection of literature, one can begin to appreciate that there are uncertainties in using mathematical models when it comes to appropriate representation of an interaction being studied. When little or no information is known about the binding site of an interaction, the shape of the isothermal profile may reveal some characteristics of the interaction. However, the shapes of isothermal profiles from different interactions can vary dramatically and modelling of ITC data can become challenging especially if there are multiple binding sites involved and where there is no knowledge on whether the sites are dependent or independent.

Depending on the shape of the isotherm, data was fit using either one or two sets of binding sites model provided by MicroCal. The mathematical models obtain thermodynamic parameters using a curve fitting process that applies a non-linear regression procedure. Initial estimates of the parameters are made to generate a theoretical curve that is compared to and fit to the experiment data. This is achieved using an algorithm through an iteration process that minimizes the error function. The one set of identical sites model is normally applied where all binding sites have the same ΔH and K values as shown in the equation below:

$$K = \frac{\Theta}{(1 - \Theta)\,[X]}$$

1 represents the total number of binding sites of the macromolecule (inorganic surface) available and unoccupied (unbound macromolecule), Θ represents the fraction of sites that are occupied by ligand X (peptide) and the concentration of free/unbound ligand is represented as [X]. From this binding model the output gives one value for n, K, ΔH and ΔS (Freyer and Lewis, 2008; MicroCal, 2004).

The two sets of independent sites model is applied for interactions where macromolecules have two different binding sites with separate values of K and ΔH. Therefore, two values are obtained for each parameter n, K, ΔH *and* ΔS relating to the first and the second binding site. Each binding site being independent means that where n1 = 1 and n2 = 2, one ligand with a unique thermodynamic signature binds to the first

site and 2 ligands of equivalent thermodynamics bind to the second site (Freyer and Lewis, 2008; MicroCal, 2004). Equations for this model are shown below:

$$K_1 = \frac{\Theta_1}{(1-\Theta_1)\,[X]} \quad \text{and} \quad K_2 = \frac{\Theta_2}{(1-\Theta_2)\,[X]}$$

The two sets of independent sites binding model may be the most suitable model to meaningfully represent interactions observed in this study as there are two separate events. In some cases, very few data points for the endothermic process were obtained *i.e.* in the interactions with calcined crystals where the profile was almost sigmoid shaped thus the one set of independent sites model was used. Working at the high peptide concentration ensured that saturation of the exothermic process was reached but led to rapid saturation of the endothermic event generating errors in modelling i.e. for peptide interaction with calcined platelets, two sets of site model could still be applied but large errors were generated in fitting of the endothermic process thus the values were negated but parameters for the endothermic process were obtained. Thermodynamic data obtained after fitting isotherms from three replicates of the interaction of G-12 peptide with ZnO platelets have been shown in Appendix 4.3 to demonstrate practical difficulties in modelling. Inconsistencies in values can be obtained even where isothermal profiles have very similar shapes.

From the thermodynamic parameters obtained (Table 4.1), the interaction of both peptides with the different ZnO morphologies was deduced to be favourable based on the high affinity values obtained and negative values of ΔG (Bouchemal and Mazzaferro, 2012; Chiad *et al.*, 2009). The values of ΔH and ΔS were commonly positive in the endothermic process. The surfaces of many metal oxides like ZnO become hydroxylated in aqueous solution. The polar hydroxylated ZnO surface attracts and adsorbs water molecules which can either be chemisorbed or physisorbed (Degen and Kosec, 2000). As peptides moved towards the ZnO surface, peptide conformational changes as well as incorporation or displacement of water molecules may have occurred producing measurable endothermic heat change with the largest contribution from positive values of ΔS (Cameron *et al.*, 2002; Chiad *et al.*, 2009; Cliff *et al.*, 2004; Leavitt and Freire, 2001; Norde and Lyklema, 1979).

Table 4.1. Thermodynamic parameters obtained from ITC measurements of interactions between 3.1 mM G-12 and GT-16 with 0.1 mM ZnO twinned rods/platelets (bulk concentration). A constant cell temperature of 298 K was maintained. Entropy change and Gibbs free energy were calculated using the equation: $\Delta H - T\Delta S = -RT\ln K_A = \Delta G$.

Peptide and ZnO	Model	*Dp*	K_A (M^{-1})	ΔH (Kcal mol^{-1})	$T\Delta S$ (Kcal mol^{-1})	ΔG (Kcal mol^{-1})
G-12 Rods	2	+ve	$1.40 \times 10^6 \pm 0.33 \times 10^6$	2.36 ± 0.68	10.73 ± 0.55	-8.37 ± 0.13
		-ve	$9.01 \times 10^4 \pm 0.32 \times 10^4$	-7.55 ± 1.09	-0.79 ± 1.06	-6.76 ± 0.02
GT-16 Rods	2	+ve	$1.37 \times 10^5 \pm 2.52 \times 10^5$ *	3.01 ± 4.16*	10.01*	-7.00 *
		-ve	$3.65 \times 10^4 \pm 3.12 \times 10^3$ *	-3.06 ± 0.21 *	3.16 *	-6.22 *
G-12 Rods (C)	1	-ve	$1.77 \times 10^5 \pm 0.33 \times 10^5$	-3.07 ± 0.21	4.08 ± 0.34	-7.16 ± 0.12
GT-16 Rods (C)	1	-ve	$1.31 \times 10^5 \pm 0.36 \times 10^5$	-5.54 ± 0.27	1.44 ± 0.44	-6.97 ± 0.17
G-12 Platelets	2	+ve	$9.94 \times 10^5 \pm 2.98 \times 10^5$ *	5.82 ± 2.4 *	14.01*	-8.19 *
		-ve	$1.45 \times 10^5 \pm 0.21 \times 10^5$	-6.18 ± 0.16	0.85 ± 0.25	-7.04 ± 0.09
GT-16 Platelets	2	+ve	$7.88 \times 10^5 \pm 2.93 \times 10^5$	3.48 ± 1.13	11.49 ± 0.91	-8.01 ± 0.22
		-ve	$6.32 \times 10^4 \pm 0.97 \times 10^4$	-9.42 ± 0.16	-2.87 ± 0.24	-6.55 ± 0.08
G-12 Platelets (C)	2	+ve	-	-	-	-
		-ve	$1.14 \times 10^5 \pm 0.13 \times 10^5$	-4.76 ± 0.36	2.14 ± 0.28	-6.89 ± 0.07
GT-16 Platelets (C)	2	+ve	-	-	-	-
		-ve	$1.26 \times 10^5 \pm 0.04 \times 10^5$	-8.23 ± 0.44	-1.27 ± 0.41	-6.95 ± 0.02

(+ve) endothermic, (-ve) exothermic, (1) one set of sites model, (2) two sets of sites model. Data is an average of at least two measurements, however in some experiments designated (*), only one experiment gave reasonable values after fitting, (-) inaccurate values left out that were caused by few data points collected for the endothermic event.

The affinity of G-12 for non-calcined ZnO rods and platelets appears to be slightly greater than the affinity of GT-16, however, for the calcined crystals the peptides have similar affinity. Negative ΔH values for the exothermic process indicate the occurrence of non-covalent interactions like hydrogen bonding, van der Waals forces or electrostatic interactions (Ababou and Ladbury, 2006; Cliff *et al*., 2004; Leavitt and Freire, 2001). Determination of change in non-covalent interactions (K_A, ΔH, ΔS) may not rigorously define interactions at an atomic scale but can be a guideline towards understanding the binding/adsorption process (Cliff *et al*., 2004). At the pH used in ITC studies, (~pH 5.8 to ~3.9) the net charge of the peptides was positive with moieties of amino acids H_3, H_6, K_7 and R_{12} protonated. The calculated net charge of the peptides is

shown in appendix 4.4. Hydroxylated ZnO at pH below its pI (~9.5), may react with protons from solution due to surface amphoteric reactions to become a positively charged surface with $ZnOH_2^+$ groups (Degen and Kosec, 2000; Rasmussen *et al*., 2010; Xu and Wang, 2011). This proton accepting behaviour of the ZnO surface may have attracted the positively charged peptides to the surface. Peptide adsorption may have also occurred through complexation of histidine residues (in G-12 and GT-16) and cysteine residues (in GT-16) with divalent zinc ions like in zinc finger dependent proteins and metalloproteins (Berg and Godwin, 1997; Dudev and Lim, 2003; Maret and Li, 2009).

The amount of adsorbed peptide was greater than that needed to form monolayer coverage, therefore the observed exothermic heat change was attributed to contributions from both peptide-surface adsorption as well as peptide-peptide interactions. Two saturation events could have been taking place; peptide binding and saturation of the surface of ZnO and peptide binding to peptide until peptide-peptide binding site saturation was achieved. Multilayer formation in ITC experiments are usually identified by the formation of isotherms with steps showing the saturation of the different layers (Lee *et al*., 2005). Such sequential adsorption requires clear distinction between saturation phases which can be difficult to identify if saturation of both phases occur simultaneously (MicroCal, 1998). The size of peptide molecules in solution measured using DLS (Appendix 4.5) indicated that a majority of the peptide molecules were in aggregates, therefore, peptide-peptide interactions could have already occurred and peptides could have adsorbed to the ZnO surface as aggregated entities. Lindman and co-workers (2007) reported multilayer adsorption of human serum albumin (HSA) to copolymer nanoparticles using ITC and did not also observe step-wise saturation events in isothermal profiles. More detailed studies need to be designed to determine if there are conformational and organizational differences between free standing and bound peptides taking into consideration the occurrence of peptide-peptide interactions in both states.

ZnO platelets had a greater surface area of (0001) plane than ZnO rods. We however did not observe a clear difference in the interaction of GT-16 to the two crystal morphologies that could directly be attributed to the preferential adsorption of GT-16 to

(0001) plane as anticipated. Here, the peptides were exposed to interaction with whole crystals as opposed to single crystalline films as in the previous study by Liang and co-workers (2011), therefore the preferential adsorption behaviour of GT-16 peptide to (0001) plane of ZnO may have been more difficult to detect as GT-16 peptide is also able to adsorb to the $(10\bar{1}0)$ plane of ZnO. If there was a clear difference, it could have also been masked in ITC experiments by simultaneous occurrence of peptide-surface and peptide-peptide interactions forming multilayers.

4.3.2. Thermodynamic Study to Compare Interfacial Interactions between G-12 Peptide and Alanine Mutants with ZnO Rods

The adsorption of alanine mutants G-12A6, G-12A11 and G-12A12 on ZnO twinned hexagonal rods was probed using ITC and compared to the adsorption of G-12. The influences of incorporating the mutants and original peptide have been discussed in chapter 3. All the above peptides were found to tightly adsorb to the surface of ZnO during solution synthesis, altering the resultant morphologies of the crystals. The aim was to determine if the mutations could have caused any differences in thermodynamic signatures or in the adsorption process that could be detected using ITC.

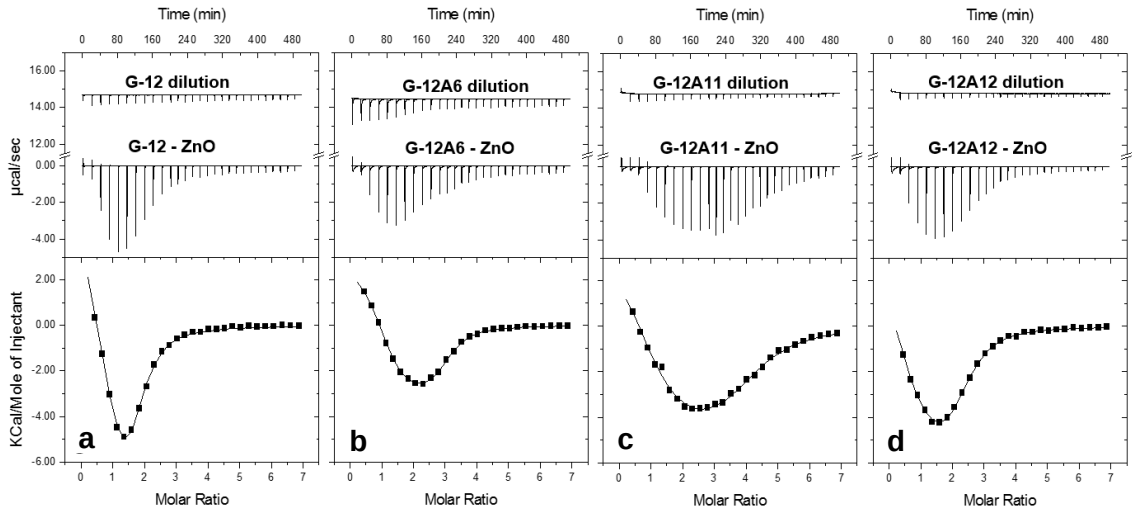

Figure 4.5. ITC isotherms representing heat changes that occurred as a result of titrating different peptides into suspensions of ZnO rods in water. In all experiments, 3.1 mM peptide was added in 28 injections of 10 µl aliquots into a cell containing 0.1 mM ZnO rods (bulk concentration) suspended in 1.4 ml water. Dilution heats were subtracted and integrated heat changes fit using the two sets of independent sites model.

Substitution of single amino acids in the parent sequence with alanine did not completely prevent adsorption of generated mutants to the surface of ZnO. However, peptide sequence dependent qualitative differences in adsorption isotherms could be identified (Figure 4.5). Unlike the other three peptides dilution of G-12A6 peptide into water resulted in a low heat signal which may be attributed to dissociation of peptide molecules that may have been present at higher peptide concentration in the syringe. In all the interactions, two energy changing processes were observed; an endothermic and an exothermic event. The thermodynamic parameters were determined using two sets of independent sites model (Table 4.2).

Table 4.2 Thermodynamic parameters obtained from ITC measurements of interactions between 3.1 mM G-12 peptide and alanine mutant peptides G-12A6, G-12A11 and G-12A12 with 0.1 mM hexagonal ZnO twinned rods (bulk concentration). A constant cell temperature of 298 K was maintained. Entropy change and Gibbs free energy were calculated from $\Delta H - T\Delta S = -RT\ln K_A = \Delta G$.

Peptide and ZnO	*Dp*	K_A (M^{-1})	ΔH (Kcal mol^{-1})	$T\Delta S$ (Kcal mol^{-1})	ΔG (Kcal mol^{-1})
G-12 Rods	+ve	$1.40 \times 10^6 \pm 0.33 \times 10^6$	2.36 ± 0.68	10.73 ± 0.55	-8.37 ± 0.13
	-ve	$9.01 \times 10^4 \pm 0.32 \times 10^4$	-7.55 ± 1.09	-0.79 ± 1.06	-6.76 ± 0.02
G-12A6 Rods	+ve	$2.65 \times 10^5 \pm 0.52 \times 10^5$	5.47 ± 3.12	12.86 ± 3.22	-7.39 ± 0.10
	-ve	$6.79 \times 10^4 \pm 0.62 \times 10^4$	-15.69 ± 8.41	-9.09 ± 5.79	-6.60 ± 0.02
G-12A11 Rods	+ve	$3.86 \times 10^5 \pm 2.14 \times 10^5$ *	4.19 ± 2.07*	11.80 *	-7.61 *
	-ve	$4.51 \times 10^4 \pm 0.47 \times 10^4$	-6.69 ± 1.22	-0.34 ± 1.28	-6.34 ± 0.06
G-12A12 Rods	+ve	$4.47 \times 10^5 \pm 0.76 \times 10^5$	5.74 ± 0.76	13.42 ± 0.86	-7.69 ± 0.10
	-ve	$8.58 \times 10^4 \pm 0.18 \times 10^4$	-6.91 ± 0.78	-0.55 ± 0.25	-6.36 ± 0.53

(+ve) endothermic, (-ve) exothermic, (*) designates parameters determined from one experiment, other parameters are an average of two measurements.

The endothermic process was attributed to peptides conformational changes as well as incorporation or displacement of water molecules supported by positive values of ΔS and ΔH (Cameron *et al*., 2002; Chiad *et al*., 2009; Cliff *et al*., 2004; Leavitt and Freire, 2001; Norde and Lyklema, 1979). The exothermic process was attributed to the occurrence of peptide-surface as well as peptide-peptide interactions driven by non-covalent forces. The concentration of G-12A11 peptide needed to attain saturation was greater than the other three peptides. In G-12A11 peptide, P_{11} of the original G-12 sequence (GLHVMHKVAPPR) was replaced with A_{11}. The amino acid proline is

known to have a restricted backbone conformation because its R-group is cyclised back against the backbone amide position (Williamson, 1994). G-12A11 peptide was the only sequence without a proline-proline dipeptide at position 10 and 11 which may have significantly altered its conformation and packing density at saturation. However, the enthalpy change of the interaction of G-12 peptide and mutants G-12A6, G-12A11 and G-12A12 with ZnO was similar. The only difference observed was a slightly greater affinity of G-12 peptide for the ZnO surface compared to the affinities of the mutant sequences. Negative ΔG values suggest that the interactions were favourable and enthalpy driven.

4.4. Conclusion

The adsorption of peptide onto ZnO surface is a process involving simultaneous interactions *i.e.* peptide-solvent, substrate-solvent, peptide-surface, possible conformation changes between bound and free peptide states and peptide-peptide interactions. Deconvolution of individual events from the global heat change measured in ITC experiments can be difficult, however, the information obtained can significantly contribute to understanding of interaction mechanisms. ΔG values for both the endothermic and exothermic events in the adsorption of G-12 peptide, GT-16 peptide and mutants of G-12 peptide (G-12A6, G-12A11 and G-12A12) to ZnO crystals were estimated to lie in between -6 and -8.5 kcal/mol using ITC. These values are very similar to reported ΔG values for the interaction ZnO with fluorescence tagged EM-12 peptide (-7.91 kcal/mol) which has 67% homology to G-12 peptide (Yokoo *et al*., 2010). The interaction of EM-12 peptide with ZnO rods was also studied using ITC (Appendix 4.6). Like the other examined ZnO-BPs, a biphasic interaction proccesses was observed, an endothermic event with ΔG values of 7.91 ± 0.27 kcal/mol and an exothermic event with ΔG values of 7.38 ± 0.48 kcal/mol. ITC is a faster method that can probe thermodynamic parameters of interaction without the requirement for labelling or carrying out experiments at different concentrations and temperatures to estimate thermodynamic parameters. ITC has shown great potential for use as a standard technique to monitor peptide-inorganic interactions but like any other technique, it has limitations and challenges and should therefore be used together with other complementary techniques that can probe interactions at biotic abiotic interfaces.

Great prospects lie in using information obtained from ITC studies to advance design processes thereby creating novel materials. With continued improvements in instrumentation and methodology and data fitting models, the development of novel applications of ITC is far from being exhausted.

4.5. References

1. Ababou, A., and Ladbury, J.E., 2006. Survey of the year 2004: literature on applications of isothermal titration calorimetry. *Journal of Molecular Recognition*: JMR, 19 (1), 79-89.
2. Almamun Ashrafi, A., Ueta, A., Avramescu, A., Kumano, H., Suemune, I., Young-Woo, O. and Tae-Yeon, S., 2000. Growth and characterization of hypothetical zinc-blende ZnO films on GaAs (001) substrates with ZnS buffer layers. *Applied Physics Letters*, 76 (5), 550-552.
3. Ball, V., and Maechling, C., 2009. Isothermal microcalorimetry to investigate non specific interactions in biophysical chemistry. *International Journal of Molecular Sciences*, 10 (8), 3283-3315.
4. Berg, J.M., and Godwin, H.A., 1997. Lessons from zinc-binding peptides. Annual Review of *Biophysics and Biomolecular Structure*, 26 (1), 357-371.
5. Bouchemal, K., and Mazzaferro, S., 2012. How to conduct and interpret ITC experiments accurately for cyclodextrin–guest interactions. *Drug Discovery Today*, 17 (11), 623-629.
6. Cai, K.F., He, X.R. and Zhang, L.C., 2008. Fabrication, properties and sintering of ZnO nanopowder. *Materials Letters*, 62 (8-9), 1223-1225.
7. Camci-Unal, G., and Pohl, N.L.B., 2010. Thermodynamics of binding interactions between divalent copper and chitin fragments by isothermal titration calorimetry (ITC). *Carbohydrate Polymers*, 81 (1), 8-13.
8. Cameron, K.S., Clark, J.K., Cooper, A., Fielding, L., Palin, R., Rutherford, S.J. and Zhang, M., 2002. Modified ɣ-Cyclodextrins and Their Rocuronium Complexes. *Organic Letters*, 4 (20), 3403-3406.
9. Cedervall, T., Lynch, I., Lindman, S., Berggård, T., Thulin, E., Nilsson, H., Dawson, K.A. and Linse, S., 2007. Understanding the nanoparticle–protein corona using methods to quantify exchange rates and affinities of proteins for nanoparticles. *Proceedings of the National Academy of Sciences*, 104 (7), 2050-2055.
10. Chang, J., and Waclawik, E.R., 2014. Colloidal semiconductor nanocrystals: controlled synthesis and surface chemistry in organic media. *RSC Advances*, 4 (45), 23505-23527.
11. Chiad, K., Stelzig, S.H., Gropeanu, R., Weil, T., Klapper, M. and MuÌˆllen, K., 2009. Isothermal Titration Calorimetry: A Powerful Technique to Quantify Interactions in Polymer Hybrid Systems. *Macromolecules*, 42 (19), 7545-7552.
12. Chiu, C.Y., Li, Y., Ruan, L., Ye, X., Murray, C.B. and Huang, Y., 2011. Platinum nanocrystals selectively shaped using facet-specific peptide sequences. *Nature Chemistry*, 3 (5), 393-399.
13. Chiu, C., Ruan, L. and Huang, Y., 2013. Biomolecular specificity controlled nanomaterial synthesis. Chemical Society Reviews, 42, 2512 - 2527.
14. Cho, N., Cheong, T., Min, J.H., Wu, J.H., Lee, S.J., Kim, D., Yang, J., Kim, S., Kim, Y.K. and Seong, S., 2011. A multifunctional core-shell nanoparticle for dendritic cell-based cancer immunotherapy. *Nature Nanotechnology*, 6 (10), 675-682.
15. Cliff, M.J., Gutierrez, A. and Ladbury, J.E., 2004. A survey of the year 2003 literature on applications of isothermal titration calorimetry. Journal of Molecular Recognition: JMR, 17 (6), 513-523.
16. Cohavi, O., Reichmann, D., Abramovich, R., Tesler, A.B., Bellapadrona, G., Kokh, D.B., Wade, R.C., Vaskevich, A., Rubinstein, I. and Schreiber, G., 2011. A Quantitative, Real-Time Assessment of Binding of Peptides and Proteins to Gold Surfaces. *Chemistry-a European Journal*, 17 (4), 1327-1336.
17. Degen, A., and Kosec, M., 2000. Effect of pH and impurities on the surface charge of zinc oxide in aqueous solution. *Journal of the European Ceramic Society*, 20 (6), 667-673.

18. Diebold, U., Koplitz, L.V. and Dulub, O., 2004. Atomic-scale properties of low-index ZnO surfaces. *Applied Surface Science*, 237 (1), 336-342.

19. Dudev, T., and Lim, C., 2003. Principles governing Mg, Ca, and Zn binding and selectivity in proteins. Chemical Reviews, 103 (3), 773-788.

20. Dulub, O., Boatner, L.A. and Diebold, U., 2002. STM study of the geometric and electronic structure of ZnO (0001)-Zn,(0001)-O,(1010), and (1120) surfaces. *Surface Science*, 519 (3), 201-217

21. Freyer, M.W., and Lewis, E.A., 2008. Isothermal titration calorimetry: experimental design, data analysis, and probing macromolecule/ligand binding and kinetic interactions. *Methods in Cell Biology*, 84, 79-113.

22. Goobes, G., Goobes, R., Shaw, W.J., Gibson, J.M., Long, J.R., Raghunathan, V., Schueler-Furman, O., Popham, J.M., Baker, D. and Campbell, C.T., 2007. The structure, dynamics, and energetics of protein adsorption—lessons learned from adsorption of statherin to hydroxyapatite. *Magnetic Resonance in Chemistry*, 45 (S1), S32-S47.

23. Goobes, R., Goobes, G., Shaw, W.J., Drobny, G.P., Campbell, C.T. and Stayton, P.S., 2007. Thermodynamic roles of basic amino acids in statherin recognition of hydroxyapatite. *Biochemistry*, 46 (16), 4725-4733.

24. Gourishankar, A., Shukla, S., Ganesh, K.N. and Sastry, M., 2004. Isothermal titration calorimetry studies on the binding of DNA bases and PNA base monomers to gold nanoparticles. Journal of the American Chemical Society, 126 (41), 13186-13187.

25. Govender, K., Boyle, D., S., Kenway, P., B. and O'Brien, P., 2004. Understanding the factors that govern the deposition and morphology of thin films of ZnO from aqueous solution. *Journal of Materials Chemistry*, 14, 2575-2591.

26. Hoffmann, F., Cornelius, M., Morell, J. and Fröba, M., 2006. Silica-Based Mesoporous Organic-Inorganic Hybrid Materials. *Angewandte Chemie International Edition*, 45 (20), 3216-3251.

27. Huang, R., Carney, R., Stellacci, F. and Lau, B., 2013. Protein-Nanoparticle Interactions: The effects of Surface Compositional and Structural Heterogeneity is Scale Dependent. *Nanoscale*. 5, 6928-6935.

28. Joshi, H., Shirude, P.S., Bansal, V., Ganesh, K. and Sastry, M., 2004. Isothermal titration calorimetry studies on the binding of amino acids to gold nanoparticles. *The Journal of Physical Chemistry B*, 108 (31), 11535-11540.

29. Karlsen, V., Heggset, E.B. and Sørlie, M., 2010. The use of isothermal titration calorimetry to determine the thermodynamics of metal ion binding to low-cost sorbents. *Thermochimica Acta*, 501 (1-2), 119-121.

30. Ladbury, J.E., and Doyle, M.L., 2005. *Biocalorimetry 2: applications of calorimetry in the biological sciences*. Wiley. com.

31. Leavitt, S., and Freire, E., 2001. Direct measurement of protein binding energetics by isothermal titration calorimetry. *Current Opinion in Structural Biology*, 11 (5), 560-566.

32. Lee, V.A., Craig, R.G., Filisko, F.E. and Zand, R., 2005. Microcalorimetry of the adsorption of lysozyme onto polymeric substrates. *Journal of Colloid and Interface Science*, 288 (1), 6-13.

33. Li, L., Zhai, T., Bando, Y. and Golberg, D., 2012. Recent progress of one-dimensional ZnO nanostructured solar cells. *Nano Energy*, 1 (1), 91-106.

34. Liang, M., Deschaume, O., Patwardhan, S.V. and Perry, C.C., 2011. Direct evidence of ZnO morphology modification via the selective adsorption of ZnO-binding peptides. *Journal of Materials Chemistry*, 21 (1), 80-89.

35. Liang, Y., 2008. Applications of isothermal titration calorimetry in protein science. *Acta Biochimica Et Biophysica Sinica*, 40 (7), 565-576.

36. Lindman, S., Lynch, I., Thulin, E., Nilsson, H., Dawson, K.A. and Linse, S., 2007. Systematic investigation of the thermodynamics of HSA adsorption to N-iso-propylacrylamide/N-tert-

butylacrylamide copolymer nanoparticles. Effects of particle size and hydrophobicity. *Nano Letters*, 7 (4), 914-920.

37. Lynch, I., and Dawson, K.A., 2008. Protein-nanoparticle interactions. *Nano Today*, 3 (1), 40-47.

38. Mahmoudi, M., Lynch, I., Ejtehadi, M.R., Monopoli, M.P., Bombelli, F.B. and Laurent, S., 2011. Protein− nanoparticle interactions: opportunities and challenges. *Chemical Reviews*, 111 (9), 5610-5637.

39. Maret, W., and Li, Y., 2009. Coordination dynamics of zinc in proteins. *Chemical Reviews*, 109 (10), 4682-4707.

40. Mazaheri, M., Zahedi, A.M. and Sadrnezhaad, S.K., 2008. Two-Step Sintering of Nanocrystalline ZnO Compacts: Effect of Temperature on Densification and Grain Growth. *Journal of the American Ceramic Society*, 91 (1), 56-63.

41. MicroCal, L., 1998. *VP-ITC Microcalorimeter User's Manual* [online]. MicroCal, LLC, Northampton, MA. Available at: http://www.uic.edu/orgs/ctrstbio/manuals/vpitc_manual.pdf [Accessed 09/20 2013].

42. MicroCal, L., 2004. *ITC Data Analysis in Origin Tutorial Guide*. Version 7 ed. Northampton, MA, USA.

43. Morkoç, H., and Özgür, Ü., 2008. *Zinc oxide: fundamentals, materials and device technology.* John Wiley & Sons.

44. Muthukumara, M., 2009. Theory of competitive adsorption-nucleation in polypeptide-mediated biomineralization. *The Journal of Chemical Physics*, 130, 161101-161105.

45. Myszka, D., Abdiche, Y., Arisaka, F., Byron, O., Eisenstein, E., Hensley, P., Thomson, J., Lombardo, C., Schwarz, F. and Stafford, W., 2003. The ABRF-MIRG'02 study: assembly state, thermodynamic, and kinetic analysis of an enzyme/inhibitor interaction. *Journal of Biomolecular Techniques*: JBT, 14 (4), 247.

46. Norde, W., and Lyklema, J., 1979. Thermodynamics of protein adsorption. Theory with special reference to the adsorption of human plasma albumin and bovine pancreas ribonuclease at polystyrene surfaces. *Journal of Colloid and Interface Science*, 71 (2), 350-366.

47. Okochi, M., Sugita, T., Furusawa, S., Umetsu, M., Adschiri, T. and Honda, H., 2010. Peptide array-based characterization and design of ZnO-high affinity peptides. *Biotechnology and Bioengineering*, 106 (6), 845-851.

48. Oren, E.E., Tamerler, C. and Sarikaya, M., 2005. Metal recognition of septapeptides via polypod molecular architecture. *Nano Letters*, 5 (3), 415-419.

49. Perry, C.C., Patwardhan, S.V. and Deschaume, O., 2009. From biominerals to biomaterials: the role of biomolecule-mineral interactions. *Biochemical Society Transactions*, 37, 687-691.

50. Puddu, V., and Perry, C.C., 2012. Peptide Adsorption on Silica Nanoparticles: Evidence of Hydrophobic Interactions. *ACS Nano*, 6 (7), 6356-6363.

51. Rasmussen, J.W., Martinez, E., Louka, P. and Wingett, D.G., 2010. Zinc oxide nanoparticles for selective destruction of tumor cells and potential for drug delivery applications. *Expert Opinion on Drug Delivery*, 7 (9), 1063-1077.

52. Rautaray, D., Mandal, S. and Sastry, M., 2005. Synthesis of hydroxyapatite crystals using amino acid-capped gold nanoparticles as a scaffold. *Langmuir*, 21 (11), 5185-5191.

53. Rothenstein, D., Claasen, B., Omiecienski, B., Lammel, P. and Bill, J., 2012. Isolation of ZnO-binding 12-mer peptides and determination of their binding epitopes by NMR spectroscopy. *Journal of the American Chemical Society*, 134 (30), 12547-12556.

54. Ruan, L., Ramezani-Dakhel, H., Chiu, C., Zhu, E., Li, Y., Heinz, H. and Huang, Y., 2013. Tailoring Molecular Specificity toward a Crystal Facet: a Lesson from Biorecognition toward Pt {111}. *Nano Letters*, 13 (2), 840-846.

55. Schmidtchen, F.P., 2012. Isothermal Titration Calorimetry in Supramolecular Chemistry. *Supramolecular Chemistry: From Molecules to Nanomaterials*, 67-103.

56. Thomson, J.A., and Ladbury, J.E., 2004. Isothermal titration calorimetry: a tutorial. *Biocalorimetry*, 2, 37-58.

57. Togashi, T., Yokoo, N., Umetsu, M., Ohara, S., Naka, T., Takami, S., Abe, H., Kumagai, I. and Adschiri, T., 2011. Material-binding peptide application - ZnO crystal structure control by means of a ZnO-binding peptide. *Journal of Bioscience and Bioengineering*, 111 (2), 140-145.

58. Wang, B., Shi, E. and Zhong, W., 1998. Twinning morphologies and mechanisms of ZnO crystallites under hydrothermal conditions. *Crystal Research and Technology*, 33 (6), 937-941.

59. Wang, Z.L., 2004. Zinc oxide nanostructures: growth, properties and applications. Journal of Physics: Condensed Matter, 16 (25), R829.

60. Whyburn, G.P., Li, Y.J. and Huang, Y., 2008. Protein and protein assembly based material structures. *Journal of Materials Chemistry*, 18 (32), 3755-3762.

61. Wikiel, K., Burke, E.M., Perich, J.W., Reynolds, E.C. and Nancollas, G.H., 1994. Hydroxyapatite mineralization and demineralization in the presence of synthetic phosphorylated pentapeptides. *Archives of Oral Biology*, 39 (8), 715-721.

62. Williamson, M.P., 1994. The structure and function of proline-rich regions in proteins. *Biochemical Journal*, 297 (Pt 2), 249.

63. Wöll, C., 2007. The chemistry and physics of zinc oxide surfaces. *Progress in Surface Science*, 82 (2), 55-120

64. Xu, S., and Wang, Z.L., 2011. One-dimensional ZnO nanostructures: Solution growth and functional properties. *Nano Research*, 4 (11), 1013-1098.

65. Yokoo, N., Togashi, T., Umetsu, M., Tsumoto, K., Hattori, T., Nakanishi, T., Ohara, S., Takami, S., Naka, T., Abe, H., Kumagai, I. and Adschiri, T., 2010. Direct and Selective Immobilization of Proteins by Means of an Inorganic Material-Binding Peptide: Discussion on Functionalization in the Elongation to Material-Binding Peptide. *Journal of Physical Chemistry B*, 114 (1), 480-486.

Chapter 5

Study of Interactions between Platinum and Pt Binding Peptides Using QCM-D and ITC

5.1. Introduction

There are several experimental approaches that are more commonly used to probe protein/peptide interactions with solid materials including direct surface and interface characterization techniques (*i.e.* SPR, QCM-D, ellipsometry, XPS, FTIR, CD *etc.*) and indirect techniques like binding and fluorescence assays (Baneyx and Schwartz, 2007; Chiad *et al*., 2009, Chiu *et al*., 2013; Somorjai *et al*., 2009; Zaera, 2012). Some of these techniques can be used to determine kinetics and thermodynamics of peptide surface interactions but ITC is the only technique that can directly measure molar enthalpy of interaction (Ababou and Ladbury, 2006; Chiad *et al*., 2009; Cliff *et al*., 2004). ITC has been presented as a powerful technique that has great potential which can be used to advance our understanding on interactions between peptides and inorganic materials. Conventional approaches of characterizing peptide-inorganic interactions can be used alongside ITC experiments to complement findings and to refine data interpretation which can be challenging especially when there is little or no prior knowledge about the interaction or where definition of the binding sites is difficult like in peptide-surface interactions. Complementary techniques are useful particularly where more than one interaction occurs simultaneously and where interactions occur producing heat changes that are below the detection limit of ITC instruments (Goobes *et al*., 2007; Lindman *et al*., 2007).

In section 1.3.4, two studies were highlighted in which SPR was used to monitor adsorption and desorption kinetics as well as interaction thermodynamics of platinum binding peptides (linear, cyclic constrained and tandem repeat sequences of PTSTGQA and QSVTSTK) on immobilized Pt thin films (Seker *et al*., 2007; Seker *et al*., 2008). ΔG values of the adsorption of the examined platinum binding peptides (Pt-BPs) on Pt thin films were estimated to lie in between -6 and -9 kcal/mol. Some important

characteristics of peptide-solid interactions were identified from the SPR measurements. The authors identified that genetically engineered polypeptides for inorganics (GEPIs) with specific molecular recognition of solid surfaces may have a general characteristic high adsorption and low desorption rate. Therefore solid-binding events may be dominated by the adsorption process (Seker *et al*., 2008). The authors also established that peptide-surface interactions may be complex involving the formation of various ordered dynamic self-assembly processes on the solid including island formation, surface diffusion, peptide-peptide interactions and peptide reorganization as well as reconformation on the solid surface (Seker *et al*., 2008). The adsorption of peptides on solid surfaces may therefore not always follow typical Langmuir adsorption behavior. The authors emphasized that further detailed studies on peptide self-assembly processes are needed for better insight on the molecular mechanisms involved in peptide recognition of solid surfaces (Seker *et al*., 2007; Seker *et al*., 2008).

QCM-D is an established technique that has been used to monitor interactions between biotic and abiotic surfaces (Causa *et al*., 2013: Chen *et al*., 2006; Coppage *et al*., 2013; Date *et al*., 2011; Dolatshahi-Pirouz *et al*., 2008; Ngourn *et al*., 2012; Puddu *et al*., 2013; Sano and Shiba, 2003; Tamerler *et al*., 2006; Tang *et al*., 2013). Chen and co-workers (2006) used QCM-D to study the interaction of phage particles harboring a peptide sequence (HKKPSKS) with specific affinity to both SiO_2 and TiO_2 surfaces. The authors concluded that the interaction of the phages to both metal oxides was mediated by the surface displayed peptide moiety in a pH dependent manner therefore electrostatic interaction largely contributed to observed binding (Chen *et al*., 2006). Recently, QCM-D was used to compare the affinity of a phage identified Pd-binding peptide sequence (TSNAVHPTLRHL) and its mutants (with alanine, histidine and cysteine substitutions at positions 6 and 11) for Pd coated QCM-D Au sensors (Coppage *et al*., 2013). Histidine at position 6 and 11 was thought to anchor the parent peptide to Pd (Pandey *et al*., 2009; Coppage *et al*., 2012). The authors hypothesized that the substitutions would modulate the strength of the peptide's interaction with Pd with alanine being the weakest binder, histidine having intermediate binding strength and cysteine having the strongest interaction. Experiments were conducted at different concentrations to determine binding constants. Doubling of surface coverage was observed as peptide concentration was increased which suggested that peptide

adsorption occurred through both peptide-surface and peptide-peptide interactions (Coppage *et al*., 2013). Third overtone change in frequency measurements were fit using Langmuir isotherms to determine binding constants as described by Tamerler and co-workers, (2006). Langmuir isotherms assume the formation of even monolayers and are not suitable for modeling multilayer formation where peptide-surface and peptide-peptide interactions may differ in strength (Tang *et al*., 2013). Nevertheless, Coppage and colleagues (2013) employed this model for multilayer formation assuming that the parameters obtained were an average of the binding constants of the separate interactions. ΔG values of the parent peptide sequence and examined mutants ranged between -7.65 and -9 kcal/mol. To their surprise, C6A11 (TSNAVCPTLRAL) peptide was the strongest binder and A6C11 (TSNAVAPTLRCL) the weakest. They deduced from their findings that the mutations in C6A11 may have resulted in conformational changes which increased its affinity for the Pd surface. Computational analysis using MD showed that C6A11 was more stable than A6C11 hence a better binder. Their study demonstrated that rational design can be used to improve peptide sequences identified using biocombinatorial techniques for optimization of material design and functionality (Coppage *et al*., 2013). Tang and coworkers (2013) also carried out a similar study investigating the interactions of 12 different phage display identified Au-binding peptide sequences (including TSNAVHPTLRHL peptide which also binds to Pd) with polycrystalline gold QCM sensor surfaces. They carried out QCM-D experiments at different peptide concentrations in order to determine kinetic and thermodynamic parameters of interaction. Peptides were thought to adsorb forming a monolayer on the Au surface as negligible changes in dissipation were measured. The Langmuir adsorption model was used to determine binding constants and ΔG values were estimated to lie in between -7.17 and -9 kcal/mol (Tang *et al*., 2013).

There has been a rise in research interest in improving synthetic processes for Pt towards achieving its potential applications such as its catalytic properties suitable for energy conversion devices like fuel cells (Long *et al*., 2010). For this study, platinum has been selected as a model to study peptide-inorganic interactions for its simpler composition and crystal structure in comparison to the previously studied hexagonal ZnO crystals. Additionally, Pt thin films are stable compared to ZnO thin films and can therefore be used for QCM-D adsorption studies. Interaction studies of Pt with peptides

could therefore be carried out using both QCM-D and ITC. Information generated from QCM-D adsorption studies of peptides on inorganic surfaces can be instrumental in designing ITC experiments of the same counterparts and can additionally contribute to modeling and interpretation of ITC data. In this study, QCM-D and ITC have been used to study interactions between Pt surfaces and three Pt-BPs identified using phage display technique; TLHVSSY (Li *et al*., 2009), TLTTLTN and SSFPQPN (Chiu *et al.*, 2011). In section 1.3.4, literature reports on the mechanisms through which the three Pt-BPs selected uniquely modify the morphology of Pt nanoparticles when incorporated in aqueous synthesis were highlighted (Chiu *et al.*, 2011; Li *et al*., 2009; Li *et al*., 2010; Ruan *et al*., 2011; Ruan *et al*., 2013). The interactions of the three Pt-binding peptides with platinum coated quartz crystal sensors have been monitored in water and in potassium phosphate buffer (PB) using QCM-D and the findings have been used to guide experimentation and support findings of ITC studies probing interactions between Pt nanoparticles and the peptides.

5.2. Materials and Methods

5.2.1. Materials for the Synthesis of Pt Nanoparticles and Pt Binding Peptides

Precursor dihydrogen hexachloroplatinate (IV) hexahydrate ($H_2PtCl_6.6H_2O$), 99.9% (metals basis) with M_r 517.91 was acquired from Alfa Aesar. Silver nitrate ($AgNO_3$), 99+% trace metals basis with M_r of 169.87 and Polyvinylpyrrolidone (PVP; $(C_6H_9NO)_n$) with an average M_r ~55,000 were purchased from Sigma Aldrich. Ethylene glycol ($HOCH_2CH_2OH$), ≥ 99% with M_r of 62.07 was also purchased from Sigma Aldrich to be used as a solvent. Other solvents used; ethanol, acetone and hexane were all obtained from Fisher Scientific. Hydrogen peroxide (H_2O_2), 30%, M_r of 34 and concentrated sulphuric acid (H_2SO_4), 99.9% M_r 98.08, purchased from Fischer Scientific and Sigma Aldrich respectively were used in the piranha reaction to purify Pt nanoparticles. Concentrated nitric acid (HNO_3), 70%, M_r 63.01 and hydrochloric acid (HCl), 36%, M_r 36.46, required for Pt dissolution studies were purchased from Fischer Scientific. Reagents were all used in their purchased form. Materials for the synthesis of

peptides have previously been listed in chapter 3, section 3.2.2.1.

5.2.2. Synthesis and Characterization of Pt Binding Peptides

The selected Pt binding peptides were synthesized using solid phase peptide synthesis technique in the same manner described in detail in section 3.2.2.3 (in the synthesis of ZnO binding peptides) and their purity and molecular weight determined using RP-HPLC and MALDI-TOF mass spectrometry as described in sections 3.2.3.1 and 3.2.3.2 respectively. TLHVSSY and TLTTLTN peptides were successfully synthesized in-house. Synthesis of SSFPQPN peptide was challenging. Premature truncations of the sequence were obtained which could have been caused by steric hindrance of side-chain protecting groups or intra and intermolecular aggregation (Bacsa *et al*., 2008; Garcia Martin and Albericio, 2008). After unsuccessful repeated synthesis, SSFPQPN peptide was purchased from Pepceuticals, Leicester who provided HPLC and mass spectrometric evidence for the composition and purity level of the synthesized peptide which was also confirmed by characterization in-house.

5.2.3. Synthesis and Purification of Pt Nanoparticles

Pt nanoparticles were synthesized using a method described by Song and co-workers, (2005) to obtain cubic (100) phase crystals. Stock solutions required for synthesis were prepared; 0.5 ml $AgNO_3$ (2×10^{-3} M) solution in ethylene glycol (EG), 3 ml PVP (0.375 M) in EG and 1.5 ml $H_2PtCl_6.6H_2O$ (0.0625 M). Thereafter, a volume of 2.5 ml EG solution was refluxed for 5 min to achieve homogeneity of the whole solution. This was followed by addition of 0.5 ml of the $AgNO_3$ (2×10^{-3} M) solution in EG (Ag salt/Pt salt = 1.1 mol %) to the boiling EG. Systematically, 93.8 µl of PVP (0.375 M) and 46.9 µl of H_2PtCl_6. $6H_2O$ (0.0625 M) was added to the boiling EG every 30 sec over a 16 min period (total of 32 times) before allowing the resulting mixture to reflux for an additional 5 min.

The product was then subjected to a cleaning procedure to remove silver by-products and unbound PVP in the solution. The product was centrifuged at 5000 rpm for 15 min after which the supernatant was separated and precipitated by addition of a triple volume of acetone. The resulting precipitate was centrifuged at 3000 rpm for 5 min and the precipitate was collected. A volume of 3 ml ethanol was added to redisperse the

precipitate with sonication then 9 ml hexane was added to the dispersion which was again centrifuged at 3000 rpm for 5 min. The precipitate was washed twice in the same solvent mixture and dispersed in 3 ml ddH_2O before being lyophilized. About 1 mg of the dried Pt nanoparticles was kept for analysis.

As completely pure nanoparticles were required for ITC experiments, the remaining sample was further purified to remove PVP that may have been bound to the surface of Pt nanoparticles using a piranha solution (a 3:1 ratio mixture of concentrated sulfuric acid (H_2SO_4) and hydrogen peroxide (H_2O_2)). Other methods attempted (found to be not so efficient) are described in the results and discussion section. Pt nanoparticles were suspended in 12 ml of piranha solution in an open glass vial and continuously stirred using a magnetic stirrer. The vials were secured to a stand using clamps for safety and left in a fume hood for 24 hrs after which the samples were diluted with 10 volumes of ddH_2O and centrifuged using a Beckman Avanti^{Tm} J-30I ultracentrifuge in acid resistant ultracentrifuge tubes. The pellet was resuspended in ddH_2O and the washing process was repeated severally until the pH of the solution was neutral. Finally, the sample was again washed in a ratio of 1:3 ethanol, hexane mixture to ensure Pt nanoparticles were separated from all organic contaminants present before being resuspended in ddH_2O then dialysed and lyophilized.

5.2.4. Characterization of Pt Nanoparticles and the Surface of Pt QCM-D Sensors

The morphology of synthesized Pt nanoparticles was analysed using a JEOL 2010 transmission electron Microscope (TEM) coupled to an EDX for elemental analysis. Nanoparticles were suspended in ethanol and dispersed by sonication then aliquots containing nanoparticles were dropped on carbon coated copper grids placed on filter papers. The samples were allowed to air dry before being analysed using the TEM operating at 200 kV with technical assistance from Gordon A.

The purity of the Pt nanoparticles was determined by heating about 1 mg from the samples prepared before and after the final treatment with piranha solution using a METTLER TOLEDO TGA/ SDTA 851e instrument heated up to 900 °C as described in section 3.2.3.6 to determine if there was any adsorbed organic contaminant. A Malvern Zetasizer Nano was used to measure the zeta potential of the particles in a capillary cell.

The crystallinity of the treated Pt nanoparticles was determined using XRD as described in section 3.2.3.4. The crystallinity of the purchase Pt sensors for QCM-D studies was also determined using XRD. The surface area of the Pt nanoparticles was determined using the single-point Brunauer-Emmett-Teller (BET) method by Dr. Belton D. using a Quantachrome Monosorb instrument as described in section 4.2.2.

5.2.5. QCM-D Study of Interactions between Pt-BPs and Pt-surface

QCM-D was used to study the adsorption behaviour of Pt-BPs on a Pt-coated sensor surface. The instrument model used was a Q-Sense E4 from Biolin Scientific. Before each experiment, sensor cleaning was carried out using a base piranha protocol from Q-sense where a sensor was immersed for 5 min in a mixture of pure water (filtered, distilled deionised), 25% ammonia and 30% hydrogen peroxide in a volume ratio of 5:1:1 heated to 75 °C. After, the sensor was rinsed with pure water, dried using helium gas flow then rinsed again with filtered ethanol and dried again using helium gas flow. Finally the sensor was UV ozone treated to remove any possible hydrocarbon contaminant. The cleaned sensor was then mounted inside a module that had been thoroughly cleaned using a flow of 2% sodium dodecyl sulphate and rinsed with pure water. Experiments were performed at 23 °C at a flow rate of 0.1 ml/min. Peptide solutions (100 µg/ml) were prepared in water and in phosphate buffer (PB) at different pH in which the peptide was expected to possess a net positive charge, no net charge and a net negative charge. A baseline was established by flowing the buffer or water over the Pt sensor for 10 min then the peptide to be studied was flowed over the surface to allow adsorption to occur. If peptide adsorbed and saturation reached, which was indicated by having no further changes in frequency of sensor oscillation, water or the buffer was again flowed over the adsorbed layer to determine if the adsorbed layer could readily be desorbed and hence the reversibility of the interaction. Where adsorption occurred, experiments were repeated at least three times to determine the weight of the adsorbed mass for rigid adlayers.

5.2.6. ITC Study of Interfacial Interactions between Pt Nanoparticles and Pt-BPs

Thermodynamic binding experiments were carried out using VP-ITC Northampton, MA instrument in a similar way to the method described in chapter 4, section 4.2.3 for ZnO

and ZnO-BPs. Preliminary experiments were carried out to optimize the experiment conditions to attain saturation of the Pt particles by the peptides, to have minimal dilution heats and to attain sufficient measurements of heat change for suitable curve shape to be able to accurately distinguish between bound and unbound peptide for determination of K_A (Cliff *et al*., 2004; Leavitt and Freire, 2001; Thomson and Ladbury, 2004). Different concentrations of peptide (280 µl) were titrated into the ITC sample cell containing Pt nanoparticles in 1.4 ml solution (water or phosphate buffer). The temperature of the reaction was kept constant at 23 °C. Samples prepared were degassed for 7 min using a thermovac before loading in the ITC to ensure there were no air bubbles. Dispersion of Pt nanoparticles in the chosen media (water or buffer) required sonication. To ensure there were no large aggregates, stock solutions containing Pt nanoparticles were filtered using 0.2 µm Minisart® syringe filters. Further dilutions were made from the stock solutions for ITC experiments and the reproducibility of sample preparation was confirmed using a dissolution study whereby Pt nanoparticles were dissolved in aqua regia (a mixture of concentrated nitric acid and concentrated hydrochloric acid, volume ratio 1:3). Thereafter, the concentrated acid mixtures containing dissolved Pt^+ ions were diluted and the amount of Pt^+ present quantified using ICP-OES. Platinum standards for ICP-OES analysis were prepared from platinum atomic adsorption standard solution (1000 ppm) in 10% HCl from Alfa Aesar. ITC dilution experiments of peptides into media (water or phosphate buffer) containing Pt nanoparticle, heat change of titrating water/phosphate buffer into the cell containing the Pt particles in the same media and the dilution of media into itself were also carried out. Normalized heat changes in kcal/mole of injectant were plotted against the molar ratio of the peptide concentration and the bulk concentration of Pt determined using ICP-OES.

5.3. Results and Discussion

5.3.1. QCM-D Study of Interactions between Platinum and Pt Binding Peptides

Morphology modifying Pt-binding peptides identified using phage display technique (sequence and properties shown in Table 5.1) were synthesized, characterized and their adsorption onto a platinum surface monitored using QCM-D. The presence of crystalline platinum, mainly Pt (111) plane was confirmed using XRD (Figure 5.1). The purity and molecular weight of the peptides was determined using RP-HPLC (> 80%) and MALDI-TOF mass spectrometry (Appendix 5.1).

Table 5.1. Properties of Pt binding peptides selected for QCM-D and ITC experiments [a] Isoelectric point (pI) was calculated using peptide property calculator Innovagen.

Pt Binding Peptides	Source	Pt phage display target	[a]pI (pH unit)	Non-polar (%) no charge	Polar no charge	Polar +ve charge
TLHVSSY	Li *et al*., 2009	Nanowires	7.76	LV (29%)	**TSSY**	H
TLTTLTN	Chiu *et al*., 2011	Cubes {100}	6.01	LL (29%)	**TTTT**N	-
SSFPQPN	Chiu *et al*., 2011	Tetrahedrons {111}	6.01	FPP (43%)	SSQN	-

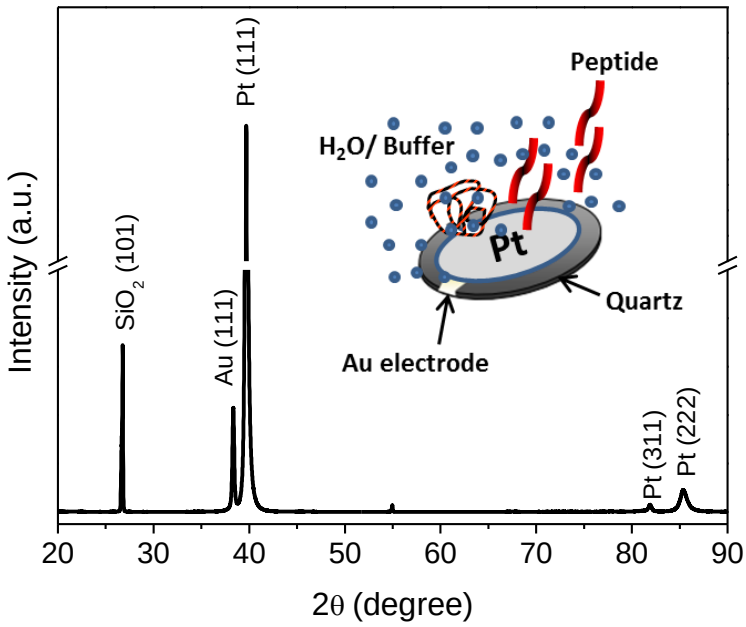

Figure 5.1. XRD diffractogram of a Pt coated QCM-D sensor showing Pt crystal planes that were available to interact with peptides. Inset is a schematic representation of interactions that could take place.

Peptide-inorganic interactions may involve specific chemical (functional groups) and physical recognition between the peptide and the surface. The conformation of a peptide hence the availability of reactive groups for interaction is controlled by its intrinsic conformational constraints or freedom and by the media in which it is dissolved (Sarikaya *et al*., 2004; Seker *et al*., 2007). For example the amino acid proline is known to have a restricted backbone structure (Williamson, 1994) and may impose conformational constraints in SSFPQPN peptide which may affect its interaction mode with Pt surface. Hydroxyl and amide groups are thought to significantly contribute to peptide interactions with metal surfaces like Pt particularly on {111} planes (Li *et al*., 2009; Naik *et al*., 2002; Slocik and Naik, 2010; Whaley *et al*., 2000). All the Pt-BPs used in this study contained hydroxyl groups and SSFPQPN peptide also contained amide groups. In a study by Ruan and co-workers (2013) discussed in section 1.3.4 on the specificity of SSFPQPN peptide for Pt {111} facet, the phenyl ring of phenylalanine (F) was shown to significantly contribute to the interaction of F containing peptide sequences with Pt {111} surface leading to formation of tetrahedrons bound by Pt {111} planes when used in synthesis of Pt nanoparticles. Their computational and experimental work suggested that the specificity of SSFPQPN peptide for Pt {111} surfaces was driven by molecular recognition of physical features of the phenyl ring in F_3 residue and the geometry of the Pt {111} facet (hexagonal epitaxial coordination) and its dissafinity for Pt {100} surface (square pattern). TLTTLTN peptide was shown to have a higher specificity for Pt {100} plane leading to formation of Pt cubes bound by {100} planes (Chiu *et al*., 2011; Ruan *et al*., 2011). Li and colleagues, (2010) demonstrated that TLHVSSY peptide can adsorb to Pt {111} plane although it is thought to have higher affinity for {110} plane.

Herein, adsorption studies of the three selected Pt-BPs on Pt surfaces were carried out in H_2O and in PB. A concentration of 100 µg/ml was prepared for each peptide. In water, at this concentration, the peptide solutions had acidic pH. The net charge of the peptides at different pH was calculated using an online polypeptide charge calculator developed by Prof. Gale Rhodes from University of Southern Maine, USA (Appendix 5.2). Experiments were then carried out at different pH in phosphate buffer (PB) where the peptides were expected to possess a net positive, neutral and negative charge (Table 5.2). In each experiment, H_2O or PB was flowed over the surface to establish a baseline

before the peptide solution dissolved in the same media was allowed to flow over the surface. Changes in frequency and dissipation as a result of peptide adsorption were monitored to saturation following which H_2O/PB was again flowed over the surface with adsorbed peptide to determine if the peptide was tightly adsorbed to the surface or could readily be desorbed. Changes in frequency (Δf) and dissipation (ΔD) were measured at the third overtone for each interaction studied (Figure 5.2). All three peptides adsorbed to the Pt surface when interactions were carried out in water. In PB, the peptides adsorbed to the Pt surface with the exception of high basic pH conditions where the net charge of the peptides was negative which may be attributed to electrostatic repulsion between the peptides and the Pt surface that may have acquired a negative surface charge in solution. In all experiments, the adsorption process was gradual and slow to reach saturation. When saturation was reached, there was no more change in frequency and in interactions carried out in water, it was common to observe a slight decrease in dissipation which can be attributed to rearrangement or packing down of the adsorbed adlayer.

Table 5.2. Pt binding peptides prepared for QCM-D experiments; the peptide concentration of all solutions was 100 µg/ml. Peptides were dissolved in water and in phosphate buffer (PB) to obtain a positive, neutral and negative net charge.

		TLHVSSY			**TLTTLTN**			**SSFPQPN**		
H_2O	**Calculated net charge**		**+1**			**0**			**0**	
	Measured pH		4.02			4.19			4.11	
PB	**Calculated net charge**	**+1**	**0**	**-1**	**+1**	**0**	**-1**	**+1**	**0**	**-1**
	Measured pH	4.01	7.38	8.96	1.98	4.00	8.96	1.91	4.05	8.88

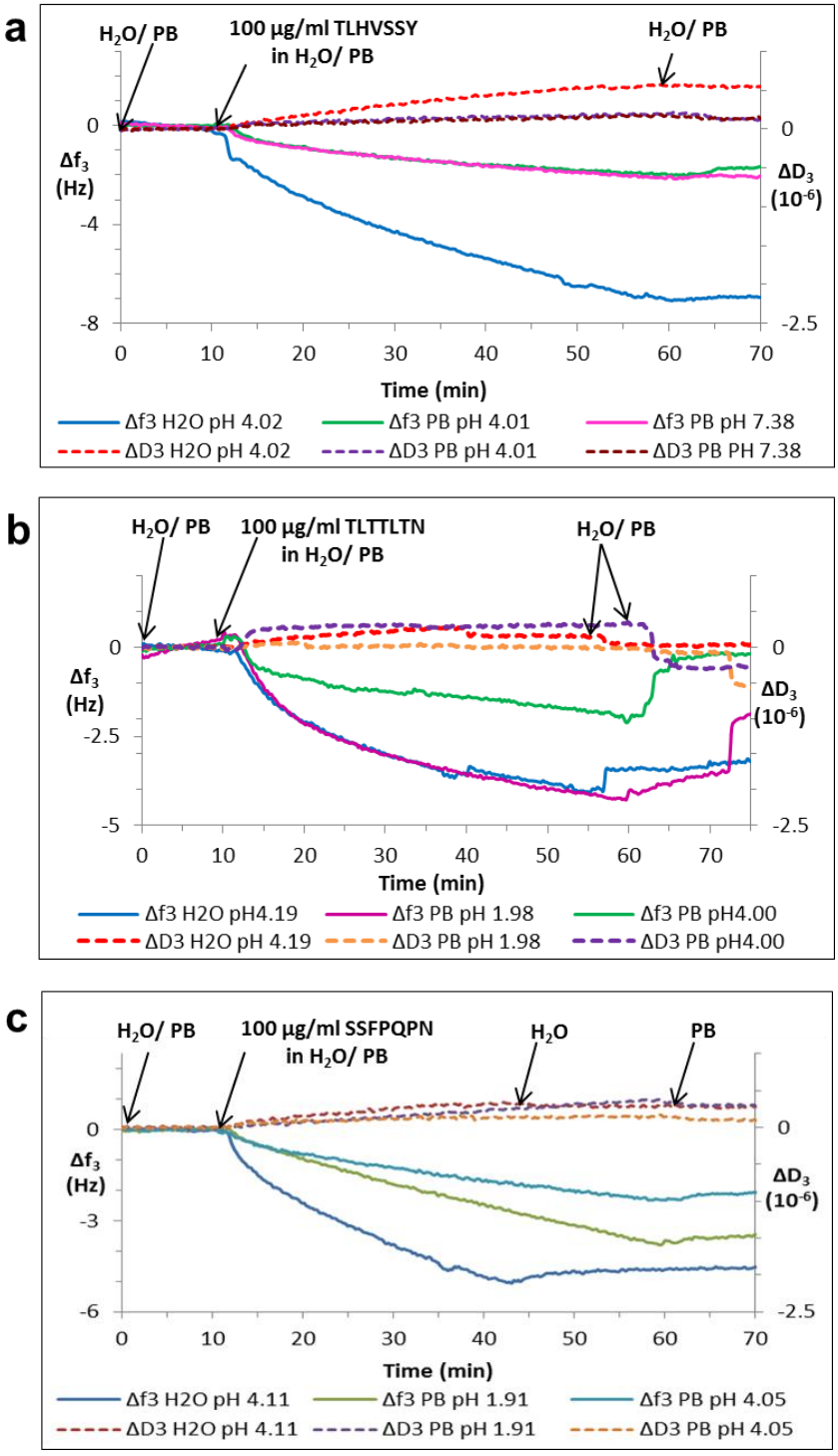

Figure 5.2. QCM-D measured changes in oscillation frequency (Δf) and dissipation (ΔD) at the 3rd overtone for Pt-coated sensor surfaces due to peptide adsorption (a) TLHVSSY peptide, (b) TLTTLTN peptide and (c) SSFPQPN peptide. Water or PB was flowed over the Pt coated sensor to establish a baseline for 10 min followed by 100 µg/ml peptide solution until saturation was reached at which point water/PB was again flowed over the surface with adsorbed peptide to monitor desorption.

Low dissipation shifts (< 10^{-6}) were observed compared to the frequency shifts on peptide adsorption which indicated that rigid films were formed (Causa *et al*., 2013; Dixon, 2008; Dolatshahi-Pirouz *et al*., 2008; Rodahl *et al*., 1997; Tang *et al*., 2013). Therefore, the changes in frequency of the oscillating sensor at the 3rd overtone could directly be correlated to the mass of adsorbed adlayer by applying the Sauerbrey equation (Dixon, 2008; Rodahl *et al*., 1997; Sauerbrey, 1959). The mass of adsorbed adlayer for each peptide and the different conditions studied are shown in figure 5.3. It is important to note that the measured mass coupled to the surface includes added mass due to peptide hydration and entrapment of solvent molecules (Chen *et al*., 2006; Dolatshahi-Pirouz *et al*., 2008; Rodahl *et al*., 1997).

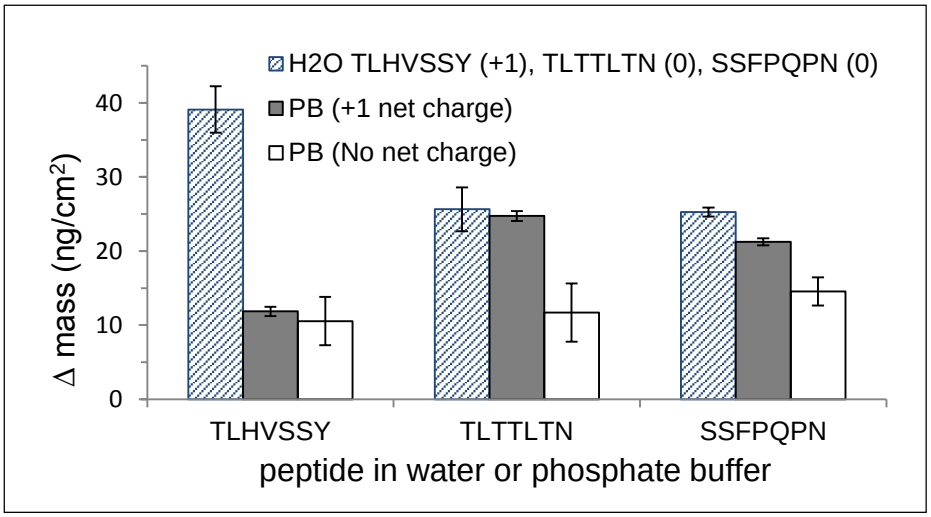

Figure 5.3. Mass of adsorbed adlayer for each peptide interaction with the Pt surface at the different conditions determined using QCM-D. Mass was calculated from changes in frequency (Δf) at the 3rd overtone using the Sauerbrey equation.

The greatest mass adsorbed was from the sample containing TLHVSSY peptide in water at pH 4.02 which can be attributed to electrostatic interactions with H_6 and *via* hydroxyl groups of T_1, S_5, S_6 and Y_7 with the Pt surface (Li *et al*., 2010). In PB at pH 4.01 the mass adsorbed deceased by less than a half of the mass adsorbed when the interaction was carried out in water. There was no significant difference in adsorbed mass of TLHVSSY peptide in PB at pH 4.01 where H_6 and Y_7 were protonated and pH 7.38 where only Y_7 was protonated. This suggests that buffer phosphate ions may have

(through non-specific interactions with the cationic moieties (H_6) of the peptide) competitively interfered with the interaction of the peptide with the Pt surface. A greater change in dissipation measurements was observed for the same concentration of TLHVSSY peptide in H_2O at pH 4.02 than in PB at pH 4.01. The adlayer formed in PB was more rigid than that formed in water which suggests that conformation and organization of the peptide in water may have been different from that in PB which may have subsequently caused differences in the availability of interaction sites and the amount of solvent entrapped in the adsorbed adlayer. Flowing of solvent over the adlayer did not desorb it from the surface therefore the interaction of TLHVSSY peptide with the Pt surface was strong. Li and co-workers stated that the interaction could be reversed by peptide photolysis or pH modulation (Li *et al*., 2009).

The interaction of TLTTLTN peptide with the Pt (111) surface was weak. In some experiments the peptide began to desorb before reaching saturation suggesting that the interaction measured was very weak and reversible. In water, the pH of 100 µg/ml peptide solution was pH 4.19 and the peptide was not charged. Interaction with the Pt surface could have mainly been mediated by hydroxyl groups of T_1, T_3, T_4, T_1 and the amide of N_7. In PB at pH 4.00, much less mass was adsorbed to the surface compared to the interaction with water at the same pH which may be attributed differences in the structuring effect of water on the peptide conformation compared to the structuring effect of the buffer. Decreasing the pH in PB to pH 1.98 increased the amount of adsorbed mass compared to interactions in PB pH 4.00 which may be attributed to protonation of the *N*-terminal amine leading to electrostatic interaction.

Uncharged SSFPQPN peptide was able to interact with the Pt (111) surface in water at pH 4.11 which may have occured through hydroxyl groups of S_1 and S_2, amide groups of Q_5 and N_7 and phenyl of F_3 through physical recognition of Pt (111) surface features as suggested by Ruan and co-workers, (2013). There was less mass adsorbed at the same concentration of the peptide in PB pH 4.05 which may be attributed to differences in peptide conformation or organization. The change in dissipation in PB was less than in water which indicates that the adlayer in PB was more rigid and more solvent could have been entrapped in the structure of the peptide in water. In PB at pH 1.91 the *N*-terminal amine was protonated and electrostatic interactions could have also contributed

to the peptide's interaction with the Pt surface. The interaction of SSFPQPN peptide with the Pt (111) surface is strong and not easily desorbed by flowing water or buffer over the adlayer.

Interactions of the peptides with the Pt surface were dominated by the adsorption process as observed in other studies by Seker and co-workers (2008). For the interaction studies in PB where the three peptides were uncharged, there was no significant difference in mass adsorbed to the Pt (111) surface. However, easy desorption of TLTTLTN peptide from the Pt surface suggested that its interaction was weak in comparison to the interactions with the other two peptides. The amount of peptide adsorbed may therefore not always be directly correlated to the strength/affinity of the interaction. The outcomes of this study correlate with those from Chiu *et al*., (2011) and Ruan *et al*., (2011) showing that SSFPQPN peptide has a higher affinity for Pt (111) plane than TLTTLTN peptide and our findings showed its interaction was stronger.

Overall, the mass adsorbed when interactions were carried out in water was always greater than in PB. Changes in dissipation measured were always lower than 10^{-6} which suggested that the mass contributed by solvent entrapment or peptide hydration was not great. Puddu and co-workers, (2013) demonstrated the importance of considering buffer related effects when used where peptides interact with inorganic materials. When higher peptide concentration was used *i.e.* up to 1 mg/ml in water (Appendix 5.3), the amount of peptide adsorbed greatly increased for all three peptides which suggest that peptide-surface as well as peptide-peptide interactions were taking place leading to the formation of multilayers. At 1 mg/ml the increase in changes in frequency measured was much greater than the changes in dissipation therefore rigid adlayers were formed and with continued adsorption, packing down or reorganisation of the adsorbed adlayer was observed. In some instances dissipation measured was below zero indicating that the sensor may have been mechanically stressed by the added weight. On and off adsorption observed when 1 mg/ml TLTTLTN peptide was flowed continuously over the Pt surface indicated that weak and reversible interaction occurred. It would be interesting to carry out further kinetic studies at different peptide concentrations below 1 mg/ml to determine the average binding constants of the peptide-surface and peptide-peptide interaction using Langmuir isotherms as described by Tamerler and co-workers

(2006) and Coppage and colleagues (2013) from which thermodynamic parameters of interactions can be estimated. Formation of peptide multilayers has been observed in other QCM-D studies of peptide-surface interactions (Coppage *et al*., 2013; Puddu *et al*., 2013). ITC studies can more directly determine thermodynamic parameters of interaction of the three peptides with Pt nanoparticles. Information on the strength and reversibility of the interactions obtained from QCM-D studies was beneficial for experimental design and data interpretation in ITC studies.

5.3.2. Preliminary ITC Study of Interactions between Pt Nanoparticles and Pt-BPs

Synthesize of cubic Pt nanoparticles with the {100} phase crystal structure was carried out using the method described by Song and co-workers (2005) who reported a yield of ~80% cubic {100} Pt nanoparticles which were 9.4 ± 0.6 nm in size. These monodisperse, size and shape controlled metal nanoparticles were thought to be suitable for ITC interaction studies with peptides as a simpler system to study compared to the previously studied hexagonal ZnO crystals with more complex crystal structure and surface chemistry. As the crystals were for use in interaction studies with peptides, it was important to ensure their surface was pure. Synthesized Pt nanoparticles were cleaned using the protocol described by Song and co-workers (2005) to remove contaminants from synthesis mainly silver by-products and unbound-PVP. Removal of bound surface stabilizing polymers like PVP without modifying the nanoparticle structure or causing undesirable aggregation can be challenging (Rioux *et al*., 2006).

The purity of the Pt nanoparticles collected after the first cleaning process described by Song and co-workers (2005) was determined using TGA which can quantify the organic weight component (Figure 5.4a). PVP and polycrystalline Pt nanoparticles purchased from Sigma Aldrich were calcined as controls. The purchased Pt nanoparticles were synthesized without any growth modifying or stabilizing agent thus they were pure but not size or shape controlled. The manufacturer described the nanoparticles to have an average size less than 50 nm and a BET determined surface area of 98.0 m^2/g.

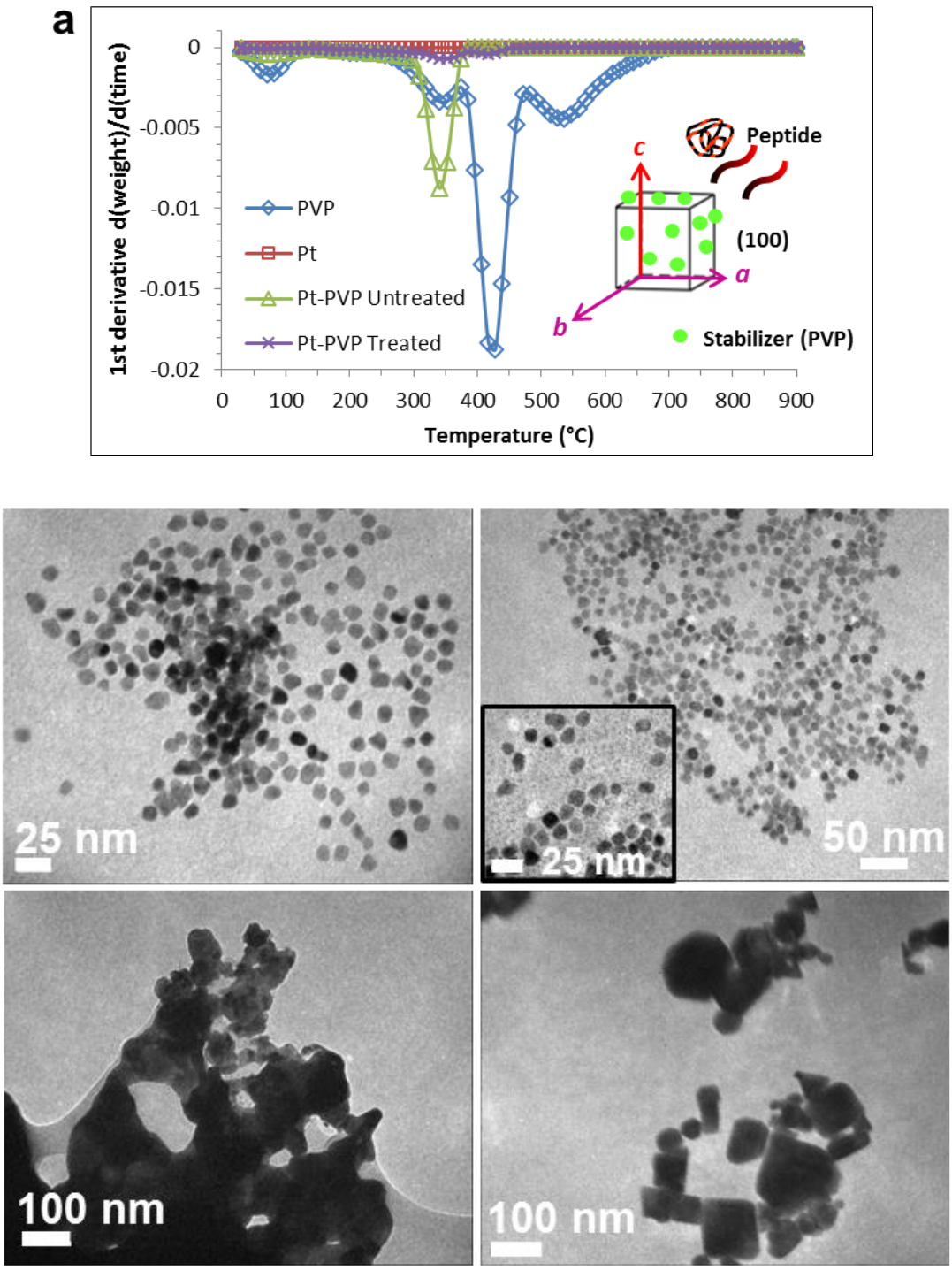

Figure 5.4. (a) 1st derivative TGA graphs [d(weight)/d(time)] showing degradation of the organic weight component in samples heated up to 900 °C. Chemically treated synthesized nanoparticles were pure. Inset is a schematic illustration of PVP bound on Pt nanoparticles highlighting the need for purification before peptide-surface interaction studies. TEM images showing (b) untreated Pt nanoparticles containing PVP, (c) chemically treated pure Pt nanoparticles, (d) aggregated synthesized Pt nanoparticles after calcination up to 450 °C and (e) purchased pure polycrystalline Pt nanoparticles.

TGA analysis showed that there was still a significant amount of bound organic matter on the Pt-surface (~15% weight for 7 ml synthesis volume and for larger batches *i.e.* 35 ml volume more organic matter up to ~50% weight was still present). Calcination of synthesized Pt nanoparticles to about 450 °C was adequate to remove all bound PVP. Decomposition of PVP on its own requires higher temperatures up to about 700 °C. However, when bound to Pt nanoparticles, PVP decomposes at much lower temperatures with the help of platinum which serves as a catalyst (Du *et al*., 2006; Rioux *et al*., 2006).

TEM was used to characterize the morphology of the synthesized crystals to define their shape and size before and after calcination (Figure 5.4). Calcination up to 450 °C removed all bound organic matter but the particles were extensively sintered and aggregated. One way to avoid compromising the structural integrity of the nanoparticles at high temperatures is by encapsulating them in a protecting matrix like silica (Rioux *et al*., 2006). This was however not practical here as nanoparticles free in solution were needed for ITC studies with peptides. Other methods that have been used to remove capping agents like PVP include plasma or UV-ozone cleaning for flat surfaces and use of chemical cleaning methods for nanoparticles (Crespo-Quesada *et al*., 2011; Monzó *et al*., 2012). Most chemical cleaning methods are specific for each capping agent (Monzó *et al*., 2012). For the removal of PVP from Pt nanoparticles, a method using a mixture H_2O_2 and H_2SO_4 has been described and similarly used in this study (Monzó *et al*., 2012). Treated Pt nanoparticles were subjected to TGA analysis and compared to untreated samples containing PVP (Figure 5.4). The method was successful for the removal of bound PVP. The nanoparticles were not aggregated nor their morphology visibly compromised.

The treated synthesized nanoparticles were further characterized, XRD analysis confirmed the formation of crystalline Pt (Figure 5.5a) and EDX analysis confirmed the presence of atomic Pt in the sample (Figure 5.5b). Synthesized Pt nanoparticles were pure and size controlled (10.22 ± 1.39 nm). Complete control over morphology to attain only cubic nanoparticles was challenging (Chiu *et al*., 2011; Rioux *et al*., 2006; Song *et al*., 2005). Cubic nanoparticles were synthesized but also present were some cuboctahedra, and few tetrahedra. As mentioned in chapter 1, Pt crystals have a face-

cantered cubic (*fcc*) symmetry (Figure 5.5c) and their crystal planes possess different surface energies (Tao *et al*., 2008). During growth, to minimize the surface energy of the crystals and the total excess free energy of the system, Pt nanocrystals are commonly bound by low-index crystal planes; three common ones are {111}, {100} and {110} planes (written in order from the plane with the lowest to the plane with the highest surface energy among the three) (Peng and Yang, 2009; Tao *et al*., 2008). Pt tetrahedral are bound by Pt {111} planes and Pt cuboctahedra are bound by a combination of Pt {111} and Pt {100} planes respectively and therefore have lower surface energy than cubic crystals which are bound by Pt {100} planes (Figure 5.5c). This may explain the difficulty in synthesizing purely cubic phase crystals.

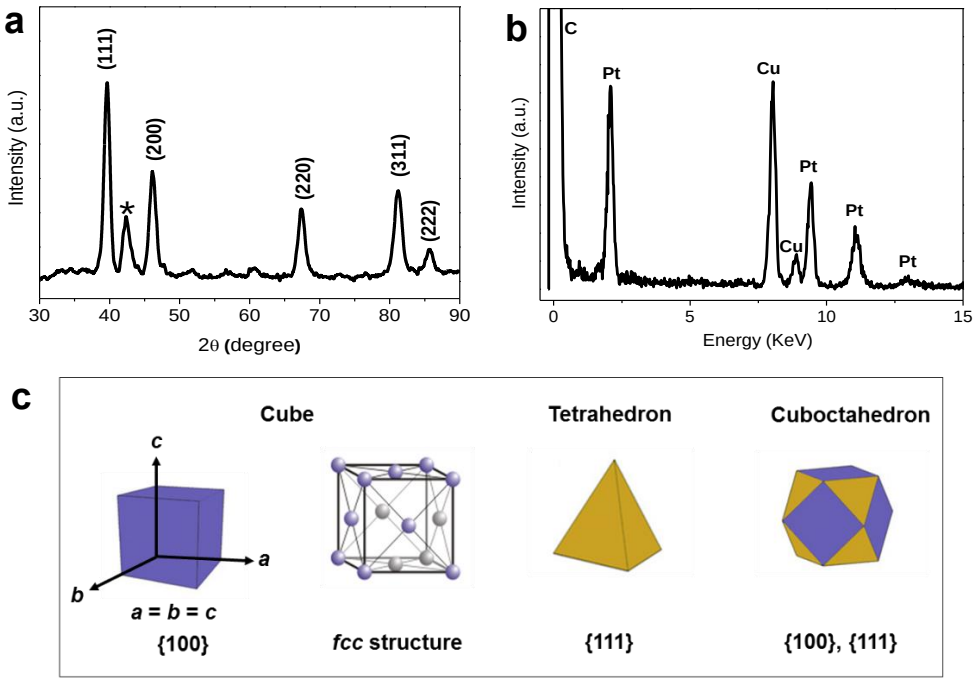

Figure 5.5. (a) XRD diffractogram of pure synthesized Pt nanoparticles showing crystal planes, (*) denotes a peak from the sample holder. (b) EDX elemental analysis showing the presence of atomic Pt in synthesized particles. Peaks of Cu present were from the copper grid on which nanoparticles were prepared for TEM analysis. (c) Models showing crystalline structure and morphologies of Pt adapted from Peng and Yang, 2009 and Generalic, 2014.

Zeta potential measurements of the purified Pt nanoparticles and purchased Pt nanoparticles were carried out in water and determined to be negatively charged at a wide pH range from pH 2 to pH 11 (Appendix 5.4a). The hydrodynamic diameter of synthesized Pt nanoparticles suspended in water determined using DLS analysis was 15.06 ± 2.46 nm and that of the majority of purchased reference sample was 35.07 ± 3.97 nm (Appendix 5.4b). The surface area of the synthesized particles determined using single point BET was 6.7 m^2/g and that of the reference purchased Pt nanoparticles was 8.0 m^2/g (significantly lower than determined by the manufacturer 98.0 m^2/g). This may be attributed to aggregation of dry nanoparticles or sintering during the analysis process which will be investigated with further analysis. Sonication was used to redisperse Pt nanoparticles in solution in preparation for ITC experiments.

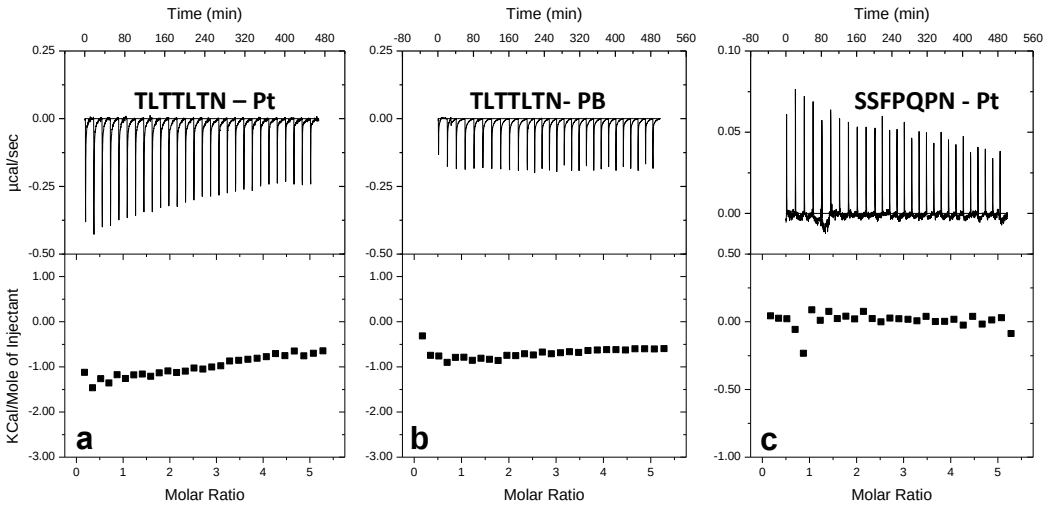

Figure 5.6. ITC isothermal profiles showing heat changes of; (a) titration of 2.8 mM TLTTLTN peptide into a suspension of 0.1 mM Pt nanoparticles in phosphate buffer (PB) pH 4, (b) titration of 2.8 mM TLTTLTN peptide into an ITC cell containing PB pH 4, (c) titration of 2.8 mM SSFPQPN peptide into a suspension of 0.1 mM Pt nanoparticles in PB pH 4. In each experiment 280 µl of peptide was injected into the sample cell in 10 µl aliquots and a constant cell temperature of 296 K was maintained.

ITC studies of the interaction of synthesized Pt nanoparticles with platinum binding peptides were carried out in phosphate buffer under the same conditions as QCM-D studies where adsorption of uncharged peptides was observed (*i.e.* TLTTLTN pH 4.0, SSFPQPN pH 4.0 and TLHVSSY pH 7.4). Interactions of Pt nanoparticles with TLTTLTN and SSFPQPN peptide have been shown in Figure 5.6. For TLTTLTN

peptide, which was shown to have a weak and reversible interaction process in QCM-D experiments, an exothermic heat change was observed but there was very little difference in heat change measured between the interaction of peptide with nanoparticles (Figure 5.6a) and dilution of peptide into buffer (Figure 5.6b). The small difference may suggest that weak interaction took place which is in agreement with findings from QCM-D studies. From the featureless curve shape obtained, it was not possible to accurately determine the concentration of bound and free ligand for determination of thermodynamic parameters.

The interaction of SSFPQPN peptide with the Pt nanoparticles (Figure 5.6c) generated an endothermic heat change and saturation was not reached. The measurable heat change was minimal which may suggest that there was no interaction but as QCM-D studies showed strong adsorption to Pt (111) plane also present in the nanoparticles used and other studies have reported evidence of the interaction of SSFPQPN peptide with platinum (Chiu *et al*., 2011; Ruan *et al*., 2011; Ruan *et al*., 2013), further experimental optimization may be required. The interaction of proteins to particles through entropy driven processes has been reported elsewhere (Lindman *et al*., 2007). The interaction of TLHVSSY peptide with Pt nanoparticles also generated an endothermic heat change in phosphate buffer pH 7.4 (appendix 5.5); however, when an interaction of TLHVSSY peptide with Pt nanoparticles was carried out in water, an exothermic process was measured. The pH of water containing the Pt nanoparticles (pH 7.12) was greater than its pH without Pt nanoparticles (pH 5.88), therefore there would be a mismatch in pH between the interaction experiment and the control experiment. For TLHVSSY peptide, protonation of histidine amino acid may occur with a shift of pH from pH 7.12 in the sample cell at the beginning of the experiment to pH 4.05 at the end of the titration. The possibility of generating heat change of ionisation would need to be considered. However, for SSFPQPN and TLTTLTN peptide, no residues can undergo ionisation at the working pH range if experiments are carried out in water. Further experimentation is required to complete this study but the differences observed in the preliminary study indicate that the peptides may have unique adsorption behaviours.

5.4. Conclusion

The interaction of three Pt-BPs (TLHVSSY, TLTTLTN and SSFPQPN) with Pt thin films and nanoparticles was studied using QCM-D and ITC. The peptides chosen for this study were interesting because of their reported plane specific adsorption behavior and ability to uniquely control the morphology of Pt nanoparticles when used in synthesis (Chiu *et al*., 2011; Li *et al*., 2010; Ruan *et al*., 2011). In QCM-D studies, a gradual adsorption process was observed with each peptide. TLHVSSY and SSFPQPN peptide appeared to adsorb strongly to the Pt (111) surface whereas TLTTLTN peptide had a weak and reversible interaction with the surface. Desorption of TLTTLTN peptide from the Pt surface was more rapid when the interaction was carried out in PB than in H_2O and for all three peptides, the mass adsorbed in water was greater than in PB. These findings suggest that ions from PB may have interfered with the adsorption strength of the peptides to the Pt surface. Non-specific interactions between buffer ions and peptide moieties may have occurred. The conformation and organization of peptide molecules in water may have also differed from that in buffer affecting their modes of interaction with the surface. The amount of peptide adsorbed in QCM-D studies increased with an increase in concentration which suggested that peptide-peptide interactions occurred. Surface coverage is a good indicator of whether monolayers or multilayers are formed but may not always be directly correlated to adsorption strength/affinity of interaction. More detailed studies on peptide-self-assembly processes on inorganic surfaces in different media need to be carried out to better understand their interaction mechanisms.

Information obtained from QCM-D studies was instrumental for the design of ITC studies and in understanding the interaction processes. Preliminary ITC studies indicated that peptide-surface interactions in PB may be weak compared to interactions in water which was in agreement with QCM-D studies. Further optimization and experimentation is needed to progress the study to determine kinetic and thermodynamic parameters of interaction using both QCM-D and ITC. Ultimately we aim to understand differences between the interactions of these three exemplar peptides with Pt at a molecular level. Information obtained may be transferable as guiding principles for the control of organic-inorganic interfacial interactions for material

design. There are clear benefits in using complementary techniques to study adsorption processes.

5.5. References

1. Ababou, A., and Ladbury, J.E., 2006. Survey of the year 2004: literature on applications of isothermal titration calorimetry. *Journal of Molecular Recognition: JMR,* 19 (1), 79-89.
2. Bacsa, B., Horváti, K., Bõsze, S., Andreae, F. and Kappe, C.O., 2008. Solid-phase synthesis of difficult peptide sequences at elevated temperatures: a critical comparison of microwave and conventional heating technologies. *The Journal of Organic Chemistry,* 73 (19), 7532-7542.
3. Baneyx, F., and Schwartz, D.T., 2007. Selection and analysis of solid-binding peptides. *Current Opinion in Biotechnology,* 18 (4), 312-317.
4. Causa, F., Della Moglie, R., Iaccino, E., Mimmi, S., Marasco, D., Scognamiglio, P.L., Battista, E., Palmieri, C., Cosenza, C., Sanguigno, L., Quinto, I., Scala, G. and Netti, P.A., 2013. Evolutionary screening and adsorption behavior of engineered M13 bacteriophage and derived dodecapeptide for selective decoration of gold interfaces. *Journal of Colloid and Interface Science,* 389 (1), 220-229.
5. Chen, H., Su, X., Neoh, K. and Choe, W., 2006. QCM-D analysis of binding mechanism of phage particles displaying a constrained heptapeptide with specific affinity to SiO2 and TiO2. *Analytical Chemistry,* 78 (14), 4872-4879.
6. Chiad, K., Stelzig, S.H., Gropeanu, R., Weil, T., Klapper, M. and MuÌˆllen, K., 2009. Isothermal Titration Calorimetry: A Powerful Technique to Quantify Interactions in Polymer Hybrid Systems. *Macromolecules,* 42 (19), 7545-7552.
7. Chiu, C.Y., Li, Y., Ruan, L., Ye, X., Murray, C.B. and Huang, Y., 2011. Platinum nanocrystals selectively shaped using facet-specific peptide sequences. *Nature Chemistry,* 3 (5), 393-399.
8. Chiu, C., Ruan, L. and Huang, Y., 2013. Biomolecular specificity controlled nanomaterial synthesis. *Chemical Society Reviews,* 42, 2512 - 2527.
9. Cliff, M.J., Gutierrez, A. and Ladbury, J.E., 2004. A survey of the year 2003 literature on applications of isothermal titration calorimetry. *Journal of Molecular Recognition: JMR,* 17 (6), 513-523.
10. Coppage, R., Slocik, J.M., Briggs, B.D., Frenkel, A.I., Naik, R.R. and Knecht, M.R., 2012. Determining Peptide Sequence Effects That Control the Size, Structure, and Function of Nanoparticles. *ACS Nano,* 6 (2), 1625-1636.
11. Coppage, R., Slocik, J.M., Ramezani-Dakhel, H., Bedford, N.M., Heinz, H., Naik, R.R. and Knecht, M.R., 2013. Exploiting Localized Surface Binding Effects to Enhance the Catalytic Reactivity of Peptide-Capped Nanoparticles. *Journal of the American Chemical Society,* 135 (30), 11048-11054.
12. Crespo-Quesada, M., Andanson, J., Yarulin, A., Lim, B., Xia, Y. and Kiwi-Minsker, L., 2011. UV–Ozone Cleaning of Supported Poly (vinylpyrrolidone)-Stabilized Palladium Nanocubes: Effect of Stabilizer Removal on Morphology and Catalytic Behavior. *Langmuir,* 27 (12), 7909-7916.
13. Date, T., Sekine, J., Matsuno, H. and Serizawa, T., 2011. Polymer-Binding Peptides for the Noncovalent Modification of Polymer Surfaces: Effects of Peptide Density on the Subsequent Immobilization of Functional Proteins. *ACS Applied Materials & Interfaces,* 3 (2), 351-359.
14. Dixon MC, 2008. Quartz crystal microbalance with dissipation monitoring: enabling real-time characterization of biological materials and their interactions. *Journal of Biomolecular Techniques: JBT,* 19 (3), 151-8.
15. Dolatshahi-Pirouz, A., Rechendorff, K., Hovgaard, M.B., Foss, M., Chevallier, J. and Besenbacher, F., 2008. Bovine serum albumin adsorption on nano-rough platinum surfaces studied by QCM-D. *Colloids and Surfaces B: Biointerfaces,* 66 (1), 53-59.
16. Du, Y., Yang, P., Mou, Z., Hua, N. and Jiang, L., 2006. Thermal decomposition behaviors of PVP coated on platinum nanoparticles. *Journal of Applied Polymer Science,* 99 (1), 23-26.

17. Garcia Martin, F., and Albericio, F., 2008. Solid supports for the synthesis of peptides. From the first resin used to the most sophisticated in the market. *Chimica Oggi*, 26 (4).

18. Generalic, Eni. "Platinum." *EniG. Periodic Table of the Elements*. KTF-Split, 26 Sep. 2014. Web. 17 Oct. 2014. http://www.periodni.com/pt.html.

19. Goobes, G., Goobes, R., Shaw, W.J., Gibson, J.M., Long, J.R., Raghunathan, V., Schueler-Furman, O., Popham, J.M., Baker, D. and Campbell, C.T., 2007. The structure, dynamics, and energetics of protein adsorption—lessons learned from adsorption of statherin to hydroxyapatite. *Magnetic Resonance in Chemistry*, 45 (S1), S32-S47.

20. Leavitt, S., and Freire, E., 2001. Direct measurement of protein binding energetics by isothermal titration calorimetry. *Current Opinion in Structural Biology*, 11 (5), 560-566.

21. Li, Y., and Huang, Y., 2010. Morphology-Controlled Synthesis of Platinum Nanocrystals with Specific Peptides. *Advanced Materials*, 22 (17), 1921-1925.

22. Li, Y., Whyburn, G.P. and Huang, Y., 2009. Specific Peptide Regulated Synthesis of Ultrasmall Platinum Nanocrystals. *Journal of the American Chemical Society*, 131 (44), 15998-+.

23. Lindman, S., Lynch, I., Thulin, E., Nilsson, H., Dawson, K.A. and Linse, S., 2007. Systematic investigation of the thermodynamics of HSA adsorption to N-iso-propylacrylamide/N-tert-butylacrylamide copolymer nanoparticles. Effects of particle size and hydrophobicity. *Nano Letters*, 7 (4), 914-920.

24. Long N.V., Hayakawa T., Lakshminarayana G., Nogami M., Chien N.D. and Hirata H., 2010. The synthesis and characterization of platinum nanoparticles: A method of controlling the size and morphology. *Nanotechnology Nanotechnology*, 21 (3).

25. Monzó, J., Koper, M. and Rodriguez, P., 2012. Removing Polyvinylpyrrolidone from Catalytic Pt Nanoparticles without Modification of Superficial Order. *Chemphyschem*, 13 (3), 709-715.

26. Naik, R.R., Stringer, S.J., Agarwal, G., Jones, S.E. and Stone, M.O., 2002. Biomimetic synthesis and patterning of silver nanoparticles. *Nature Materials*, 1 (3), 169-172.

27. Ngourn, S.C., Butts, H.A., Petty, A.R., Anderson, J.E. and Gerdon, A.E., 2012. Quartz crystal microbalance analysis of DNA-templated calcium phosphate mineralization. *Langmuir*, 28 (33), 12151-12158.

28. Pandey, R.B., Heinz, H., Feng, J., Farmer, B.L., Slocik, J.M., Drummy, L.F. and Naik, R.R., 2009. Adsorption of peptides (A3, Flg, Pd2, Pd4) on gold and palladium surfaces by a coarse-grained Monte Carlo simulation. *Physical Chemistry Chemical Physics*, 11 (12), 1989-2001.

29. Puddu, V., Slocik, J.M., Naik, R.R. and Perry, C.C., 2013. Titania Binding Peptides as Templates in the Biomimetic Synthesis of Stable Titania Nanosols: Insight into the Role of Buffers in Peptide-Mediated Mineralization. *Langmuir*, 29 (30), 9464-9472.

30. Rioux, R., Song, H., Grass, M., Habas, S., Niesz, K., Hoefelmeyer, J., Yang, P. and Somorjai, G., 2006. Monodisperse platinum nanoparticles of well-defined shape: synthesis, characterization, catalytic properties and future prospects. *Topics in Catalysis*, 39 (3-4), 167-174.

31. Rodahl M, Höök F, Fredriksson C, Keller CA, Krozer A, Brzezinski P, Voinova M and Kasemo B, 1997. Simultaneous frequency and dissipation factor QCM measurements of biomolecular adsorption and cell adhesion. *Faraday Discussions*, (107), 229-46.

32. Ruan, L., Chiu, C., Li, Y. and Huang, Y., 2011. Synthesis of Platinum Single-Twinned Right Bipyramid and {111}-Bipyramid through Targeted Control over Both Nucleation and Growth Using Specific Peptides. *Nano Letters*, 11 (7), 3040-3046.

33. Ruan, L., Ramezani-Dakhel, H., Chiu, C., Zhu, E., Li, Y., Heinz, H. and Huang, Y., 2013. Tailoring Molecular Specificity toward a Crystal Facet: a Lesson from Biorecognition toward Pt {111}. *Nano Letters*, 13 (2), 840-846.

34. Sano, K., and Shiba, K., 2003. A hexapeptide motif that electrostatically binds to the surface of titanium. *Journal of the American Chemical Society*, 125 (47), 14234-14235.

35. Sarikaya, M., Tamerler, C., Schwartz, D.T. and Baneyx, F., 2004. Materials assembly and formation using engineered polypeptides. *Annu. Rev. Mater. Res.*, 34, 373-408.

36. Sauerbrey, G., 1959. Use of quartz vibration for weighing thin films on a microbalance. *J.Physik*, 155, 206-212.

37. Seker, U.O.S., Wilson, B., Sahin, D., Tamerler, C. and Sarikaya, M., 2008. Quantitative affinity of genetically engineered repeating polypeptides to inorganic surfaces. *Biomacromolecules*, 10 (2), 250-257.

38. Seker, U.O.S., Wilson, B., Dincer, S., Kim, I.W., Oren, E.E., Evans, J.S., Tamerler, C. and Sarikaya, M., 2007. Adsorption behavior of linear and cyclic genetically engineered platinum binding peptides. *Langmuir*, 23 (15), 7895-7900.

39. Slocik, J.M., and Naik, R.R., 2010. Probing peptide–nanomaterial interactions. *Chemical Society Reviews*, 39 (9), 3454-3463.

40. Somorjai, G.A., Frei, H. and Park, J.Y., 2009. Advancing the frontiers in nanocatalysis, biointerfaces, and renewable energy conversion by innovations of surface techniques. *Journal of the American Chemical Society*, 131 (46), 16589-16605.

41. Song, H., Kim, F., Connor, S., Somorjai, G.A. and Yang, P.D., 2005. Pt nanocrystals: Shape control and Langmuir-Blodgett monolayer formation. *Journal of Physical Chemistry B*, 109 (1), 188-193.

42. Tamerler, C., Oren, E.E., Duman, M., Venkatasubramanian, E. and Sarikaya, M., 2006. Adsorption kinetics of an engineered gold binding peptide by surface plasmon resonance spectroscopy and a quartz crystal microbalance. *Langmuir*, 22 (18), 7712-7718.

43. Tang, Z., Palafox-Hernandez, J.P., Law, W., E. Hughes, Z., Swihart, M.T., Prasad, P.N., Knecht, M.R. and Walsh, T.R., 2013. Biomolecular Recognition Principles for Bionanocombinatorics: An Integrated Approach to Elucidate Enthalpic and Entropic Factors. *ACS Nano*.

44. Tao, A.R., Habas, S. and Yang, P., 2008. Shape control of colloidal metal nanocrystals. *Small*, 4 (3), 310-325.

45. Thomson, J.A., and Ladbury, J.E., 2004. Isothermal titration calorimetry: a tutorial. *Biocalorimetry*, 2, 37-58.

46. Peng, Z., and Yang, H., 2009. Designer platinum nanoparticles: Control of shape, composition in alloy, nanostructure and electrocatalytic property. *Nano Today*, 4 (2), 143-164.

47. Whaley, S.R., English, D., Hu, E.L., Barbara, P.F. and Belcher, A.M., 2000. Selection of peptides with semiconductor binding specificity for directed nanocrystal assembly. *Nature*, 405 (6787), 665-668.

48. Williamson, M.P., 1994. The structure and function of proline-rich regions in proteins. *Biochemical Journal*, 297 (Pt 2), 249.

49. Zaera, F., 2012. Probing liquid/solid interfaces at the molecular level. *Chemical Reviews*, 112 (5), 2920-2986.

Chapter 6

General Discussion, Conclusions and Insight Towards Further Studies

6.1. Discussion and Conclusions

The research study presented within this thesis was designed to contribute to developing understanding of interactions at abiotic biotic interfaces. The importance of fundamental knowledge on interaction mechanisms has relevant application not just in materials science but also in other fields including biomedical engineering and biotechnology. Herein, interactions of zinc oxide (ZnO) and platinum (Pt) with their specific binding peptides (identified using phage display technique and mutant sequences chosen after computational studies on peptide stability) have been studied using two approaches; (i) peptide induced effects on morphology and growth mechanism of inorganic material (ZnO) have been investigated during solution synthesis from precursors and (ii) interfacial interactions between inorganic materials (ZnO and Pt) and peptides have been monitored using biophysical tools; quartz crystal microbalance with dissipation monitoring (QCM-D) and isothermal titration calorimetry (ITC) to determine their adsorption behaviour and thermodynamics of interaction.

To begin with in chapter 3, the growth of ZnO in the absence and presence of ZnO binding peptides (ZnO-BPs) was investigated. The study was a continuation of previous studies that showed that peptides G-12 (GLHVMHKVAPPR) and GT-16 (GLHVMHKVAPPR-GGGC) adsorbed to and inhibited growth of ZnO rods synthesized in aqueous solution using precursor $Zn(NO_3)_2 \cdot 6H_2O$ and HMTA. Both peptides adsorbed to the $(10\bar{1}0)$ and (0001) planes of ZnO but GT-16 was found to have preferential adsorption to the (0001) plane (Liang *et al.*, 2011). The roles of individual amino acid functionalities, the significance of specific sequence order, sequence length and the exact mechanism through which the specificity of the ZnO-BPs for ZnO was achieved remained largely elusive. To advance the study a combined computational and experimental strategy was employed. Computational alanine scanning mutagenesis

as well as experimental alanine mutations of sequences can enable one to elucidate on the roles of functional groups of amino acids in a peptide sequence (Coppage *et al*., 2012; Massova and Kollman, 1999; Pandey *et al*., 2009; Sano *et al*., 2003; Serizawa *et al*., 2007). Ramasamy R. used computational tools to study the stability of G-12 and its mutants generated by substituting alanine at each position of the sequence. In principle, the peptide conformation with the lowest energy minima is thought to correspond to the inorganic binding configuration (Evans *et al*., 2008, Oren *et al*., 2005). Among all 12 sequences studied after energy minimization using molecular dynamics, G-12 had medial stability, G-12A6 (GLHVMAKVAPPR) and G-12A11 (GLHVMHKVAPAR) were the most stable sequences and G-12A12 (GLHVMHKVAPPA) was the least stable sequence. From the outcomes of the computational study, the original sequence and three mutant sequences G-12A6, G-12A11 G-12A12 were selected for further experimental studies.

ZnO growth was investigated in the absence and presence of G-12 and selected alanine mutants using two different hydrothermal synthesis methods that applied two different precursors; the $Zn(NO_3)_2 \cdot 6H_2O$ and HMTA reaction method described by Tomczak and co-workers (2009) and the $Zn(CH_3COO)_2$ and NH_3 method described by Masuda and colleagues (2007). In both synthesis methods, anisotropic growth of ZnO twinned rods took place when synthesis was carried out at neutral pH without peptide. However, when synthesis was carried out in the presence of peptides, the morphologies of ZnO obtained and the growth habits varied for the same peptide between the two synthesis methods and between different peptides using the same synthesis method. Using the $Zn(NO_3)_2 \cdot 6H_2O$ and HMTA reaction method low aspect ratio ZnO twinned rods were obtained in the presence of 0.3 mM G-12, G-12A11 and G-12A12. In synthesis with 0.3 mM G-12A6, unique microspheres were formed and low aspect ratio ZnO rods also grew as a consequence of a secondary nucleation process. Secondary nucleation may have been induced by the increase of temperature from 20 °C to 65 °C after the 24-hr nucleation period. G-12A6 may have been able to form concentration dependent micelle like structures through peptide-peptide interactions which acted as templates upon which nucleation and isotropic growth of ZnO took place. Aspect ratio reduction of ZnO crystals was caused by peptide adsorption to the growing ZnO crystal planes, a

process which has previously been described as peptide adsorption growth inhibition mechanism (Muthukumara, 2009; Liang *et al*., 2011).

In the $Zn(CH_3COO)_2$ and NH_3 reaction method, ~60% of the Zn^{2+} ions from the precursor was immediately utilized to form an intermediate product LBZA which was then phase transformed to ZnO. However in the presence of G-12 and G-12A6, the intermediate product was stabilized for longer periods inhibiting ZnO growth. This effect was more prominent with G-12 compared to G-12A6 therefore histidine amino acid must have played a significant role in the interaction. At neutral pH, the imidazole side chain group of histidine had a lone pair of electrons on nitrogen which could have coordinated with divalent zinc ions. Most of the peptide sequences that have been identified to interact with ZnO using phage display technique are enriched with histidine residues however it may not singlehandedly drive the interaction process.

The effects of incorporating peptides were modulated by the reaction conditions. In the $Zn(NO_3)_2{\cdot}6H_2O$ and HMTA reaction method, less of the intermediate product was formed *i.e.* only ~10% Zn^{2+} ions from the precursor in solution was utilized to form LBZN during the nucleation period at 20 °C. The peptides may have been able to stabilize the intermediate LBZN in the $Zn(NO_3)_2{\cdot}6H_2O$ and HMTA reaction method (evidenced by the increase in NO_3^- present in samples synthesized with increasing peptide concentration) just as LBZA was stabilized in the $Zn(CH_3COO)_2$ and NH_3 reaction method but suppression of ZnO growth was less effective in the $Zn(NO_3)_2{\cdot}6H_2O$ and HMTA reaction method because less of the intermediate compound was formed and the amount of Zn^{2+} ions in solution was also in excess compared to the depleted amount in the $Zn(CH_3COO)_2$ and NH_3 reaction method. Interestingly, in the $Zn(CH_3COO)_2$ and NH_3 reaction method, the aspect ratio of ZnO crystals synthesized using G-12 and G-12A6 decreased with an increase in peptide concentration even through no adsorbed peptide was detected in the washed precipitates analysed using TGA or FTIR. Although no strongly adsorbed peptide was detected in solid phases, the possible occurrence of reversible interactions of peptides with solid phases in solution cannot be disregarded. Aspect ratio reduction of crystals may have occurred as a consequence of LBZA stabilization causing a lack of ZnO growth units. Questions therefore arise about the stability of the peptide-inorganic particle adducts

(*i.e.* how dynamic or static are adsorbed layers) in solution and what is desirable for material design.

The versatility of peptides as tools that can be used in material design was evident. In suitable environments peptides may be able to, (i) adsorb to inorganic material surfaces inhibiting growth along specific crystals planes modifying material structure, (ii) self-assemble to form structures *i.e.* micelles that may be able to template growth of inorganic materials forming structures that are otherwise not the favourable growth habit of the material, (iii) suppress or inhibit the formation of inorganic materials and stabilize intermediate products that may be desired for different applications. The adsorption of peptides on inorganic surfaces is driven by kinetic and thermodynamic factors and may vary depending on the inherent properties of the peptide, the physico-chemical properties of the inorganic surface and the reaction conditions (concentration of precursors, reaction temperature, and presence of other molecules in the media).

ITC was used to directly probe the thermodynamic changes that occurred during the interaction of ZnO with ZnO-BPs to investigate the possible link between thermodynamic changes (modification of energy barriers at the peptide-inorganic interface) and morphology control. The first part of the study discussed in chapter 4 focused on the interactions of G-12 and GT-16 with two different morphologies of ZnO crystals; ZnO twinned rods and ZnO twinned platelets. These studies were conducted with as synthesized particles as well as calcined particles. The second part of the study used ITC to compare interactions between G-12 and its alanine mutant sequences (G-12A6, G-12A11 and G-12A12) that had been used in solution synthesis of ZnO discussed in chapter 3. The aim was to determine if the mutations could have caused any differences in thermodynamic signatures or in the adsorption process that could be detected using ITC. Under the experimental conditions used, interactions between the studied ZnO-BPs and ZnO produced heat changes that were measurable using ITC. Differences in surface chemistry between calcined and non-calcined (*i.e.* presence of chemisorbed water and trace amounts of LBZN) ZnO particles were manifested in qualitative differences observed in their interaction with G-12 and GT-16. Peptide sequence dependent qualitative differences in adsorption isotherms of different peptides with the same ZnO particles were also identified. Overall a biphasic processes was

observed for the adsorption of the examined ZnO-BPs on ZnO which consisted of an endothermic and an exothermic event. Thermodynamic parameters of interaction; ΔH, ΔS, K_A and ΔG were determined. The endothermic process was attributed to peptide conformational changes as well as incorporation or displacement of water molecules supported by positive values of ΔS and ΔH. The exothermic process was attributed to the occurrence of peptide-surface as well as peptide-peptide interactions driven by non-covalent forces (hydrogen bonding, van der Waals forces or electrostatic interactions).

GT-16 was previously reported to preferentially adsorb to the (0001) plane of ZnO, we had therefore anticipated to observe a difference in its adsorption to ZnO platelets compared to ZnO rods. ZnO platelets had a greater surface area of the (0001) plane compared to ZnO rods. However, the plane selectivity of GT-16 was not clearly identified in ITC studies plausibly because GT-16 was also able to adsorb to the $(10\bar{1}0)$ plane of ZnO. Differences were either not detectable using ITC or the instrument could have been desensitized by simultaneous occurrence of peptide-surface and peptide-peptide interactions forming multilayers. The same may apply to the studies comparing interactions of G-12 and its mutants with ZnO. Peptide sequence dependent qualitative differences in adsorption isotherms and differences in surface coverage could be identified but thermodynamic parameters obtained did not vary drastically. The affinity values of G-12 for ZnO appeared to be slightly greater than those of the other peptides studied. However, for both the endothermic and exothermic events, similar ΔG values (estimated to lie in between -6 and -8.5 kcal/mol) were obtained in interactions of all the examined peptides with ZnO crystals. From the determined thermodynamic parameters, we could deduce that the interactions of the studied peptides with ZnO were favourable based on the high affinity values obtained and negative values of ΔG. The adsorption of peptide onto ZnO surface is a complex process involving simultaneous interactions *i.e.* protein-solvent, substrate-solvent, peptide-surface, possible conformation changes between bound and free peptide states and peptide-peptide interactions. Although information obtained from ITC experiments cannot rigorously define interactions at an atomic scale, it can be a guideline towards understanding the adsorption process and is therefore an invaluable tool.

Greater differences were observed in modification of ZnO growth habits and morphology from solution synthesis studies in the absence and presence of ZnO-BPs (GT-16, G-12 and mutants of G-12) compared to differences observed in adsorption thermodynamics investigated using ITC. In many cases, ITC experiments are an oversimplification of the actual events they need to be correlated to (Cliff *et al*., 2004; Mahmoudi *et al*., 2011). For example in drug development it may only be possible to study interactions of individual proteins with nanoparticles using ITC to obtain information that can be assertively interpreted, however, in the biological milieu we know that there are several proteins of different affinities in coexistence and that cooperative effects must play an important role (Cliff *et al*., 2004; Mahmoudi *et al*., 2011). Here also, more complex thermodynamic changes may have taken place during the synthesis process involving several simultaneous reaction processes (*i.e.* heat change of nucleation and growth of ZnO from precursors though phase transformation of intermediate products like LBZs, heat change of peptide interaction with the ZnO or LBZs and heat change of other parallel reactions like the decomposition of HMTA in solution) all of which contribute the total free energy of the system. Perhaps with continued improvement of instrumentation and methodology, interpretation of more complex ITC experiments involving several interacting components may be feasible.

Use of complementary techniques to study peptide-surface adsorption processes can develop experimental design and facilitate data interpretation. In chapter 5 interactions between Pt (thin films coated on quartz crystal sensors and nanoparticles) and three platinum binding peptides (Pt-BPs) were studied using QCM-D and ITC. ITC can directly measure molar enthalpy of interaction and QCM-D can be used to indirectly determine thermodynamic parameters of interaction from adsorption isotherms of different peptide concentrations. Unlike Pt thin films, ZnO thin film surfaces are chemically unstable therefore QCM-D studies were only carried out with Pt and Pt-BPs. The Pt-BPs used had been identified using phage display technique. These were; TLHVSSY (Li *et al*., 2009), TLTTLTN and SSFPQPN (Chiu *et al.*, 2011). These peptides had been reported to have plane specific adsorption. TLTTLTN peptide preferentially adsorbs to Pt {100} surfaces, SSFPQPN peptide adsorbs to Pt {111} surfaces and TLHVSSY peptide has high affinity for Pt {110} planes although it can

also adsorb to Pt {111} and {100} planes (Chiu *et al*., 2011; Li *et al*., 2010; Ruan *et al*., 2011).

The adsorption process for all three peptides to the Pt (111) coated sensor was gradual. Typical Langmuir shaped adsorption isotherms were obtained. However, because the amount of peptide adsorbed increased with an increase in peptide concentration, more complex adsorption processes involving peptide-peptide interactions could have taken place. The adsorption of TLHVSSY and SSFPQPN peptide to the Pt (111) surface appeared to be strong whereas TLTTLTN peptide had a weak and readily reversible interaction with the surface. The peptides may have interacted with the Pt surface *via* hydroxyl groups, amide groups and through electrostatic interactions when charged. Physical recognition of surface features by peptide moieties could have also occurred (Ruan *et al*., 2013). The presence of phosphate ions in solution appeared to interfere with or disrupt the interaction of the peptides with the Pt surface. The conformation and organization of peptide molecules in water may have differed from that in buffer affecting their modes of interaction with the surface and the overall mass of adsorbed adlayers. Surface coverage was a good indicator of whether monolayers or multilayers were formed but may not always have a direct correlation to adsorption strength/ affinity of interaction. Further experimentation is required to complete this study to determine kinetic and thermodynamic parameters of interaction using QCM-D and ITC. Preliminary studies indicate that the peptides have distinguishable differences in their adsorption properties which if well understood may reveal guiding principles for rational molecular design of peptides that can predictably control inorganic material structure.

6.2. Prospects for Further Studies

Many researchers have come to the realization that although combinatorial techniques like phage display play a great role in identifying peptide sequences that can interact with and in some cases control morphology of inorganic materials these techniques have biases in their selection of material binding peptides. Advancements for peptide design may therefore lie in the development of newer complementary random and rational approaches (Naik *et al.*, 2004; Sarikaya *et al.*, 2003; Vodnik *et al*., 2011;

Whyburn *et al*., 2008). Random rotations of sequences can be made to study the significance of specific sequence alignment, conformation and resulting effects on binding potency during interaction with target substrates. Rational approaches such as bioinformatics and computational modelling continue to be developed especially because they allow one to theoretically investigate the behaviour of complex systems at a molecular level beyond what can be achieved experimentally (Di Felice and Corni, 2011; Leach and Schomburg, 1996; Pandley *et al*., 2009; Raut *et al*., 2005; Sagui and Darden, 1999). Much progress is needed to design better force fields that appropriately describe molecular and atomic level details of peptides adsorbing onto the surface of synthetic materials while describing the material's surface features and the media for more accurate simulations. There are challenges especially in developing accurate simulations of complex surfaces like ZnO. Nevertheless if these challenges are overcome, computational tools may be able to improve and accelerate the rational used to identify inorganic binding peptides and may also progress our understanding of peptide conformation, peptide self-assembly processes and peptide- surface interactions.

Certain characteristics can be identified in peptides that have been studied for particular materials. For studies with Pt, many of the phage display identified Pt-BPs are enriched with neutral residues and residues with hydroxyl groups. Similarly, many identified ZnO-BPs are enriched with histidine residues and tend to have a positive net charge. The thiol residue of cysteine amino acid has also been shown to significantly contribute to the interaction of ZnO-BPs with ZnO and may have even imparted the (0001) plane selectivity characteristic to GT-16 (Liang *et al*., 2011). In this contribution, the role of individual amino acids in G-12 were studied by carrying out alanine mutations of the sequence. From ZnO synthesis studies in the presence of G-12 and mutant sequences, substitution of certain amino acids caused dramatic changes in the properties of the generated peptide which in turn affected the resultant morphologies of ZnO obtained. Reaction conditions also influenced the growth process and the subsequent effect of peptide incorporation. For example, as previously discussed, in one synthesis process, G-12A6 may have self-assembled into structures that could template isotropic growth of ZnO microspheres while in a different system, it appeared to stabilize the intermediate product LBZA. Suppression of ZnO growth by G-12A6 was to a lesser extent than with G-12 which was determined to have higher affinity for ZnO in ITC experiments.

Examined mutations at other positions in the sequence may have had greater effects on the peptides' adsorption conformation and packing density.

From the knowledge obtained, rational mutations can be carried out to introduce amino acids that are expected to improve the interaction of a peptide sequence to a target material. The effects of the mutations on the peptides' conformation can be analysed using computational tools. Other techniques like circular dichroism spectroscopy can be used to study differences between free and bound peptide conformations. ITC can be used as a peptide design screening method that can determine the affinity of sequences for target substrates distinguishing between strong and weak binders. Ultimately, the knowledge gained can be transferred beyond peptide molecular recognition to the design of cheaper and more stable organic molecules with the properties required for inorganic material design. Undoubtedly, interactions at biotic abiotic interfaces are complex and can vary drastically depending on the intrinsic properties of the organic molecule, the physico-chemical features of the surface and the environment in which they are. With continued efforts, much progress continues to be made with the end goal of simplifying selection processes for organic molecules for material design of any inorganic material including synthetic nanoscale constructs/ hybrid functional materials without the need for extensive laborious experimentation of each system. Ultimately, full exploitation of all known elements and the control of materials structure for novel applications may be achieved.

6.3. References

1. Chiu, C.Y., Li, Y., Ruan, L., Ye, X., Murray, C.B. and Huang, Y., 2011. Platinum nanocrystals selectively shaped using facet-specific peptide sequences. *Nature Chemistry,* 3 (5), 393-399.
2. Cliff, M.J., Gutierrez, A. and Ladbury, J.E., 2004. A survey of the year 2003 literature on applications of isothermal titration calorimetry. *Journal of Molecular Recognition: JMR,* 17 (6), 513-523.
3. Coppage, R., Slocik, J.M., Briggs, B.D., Frenkel, A.I., Naik, R.R. and Knecht, M.R., 2012. Determining Peptide Sequence Effects That Control the Size, Structure, and Function of Nanoparticles. *ACS Nano,* 6 (2), 1625-1636.
4. Di Felice, R., and Corni, S., 2011. Simulation of peptide–surface recognition. *The Journal of Physical Chemistry Letters,* 2 (13), 1510-1519.
5. Evans, J.S., Samudrala, R., Walsh, T.R., Oren, E.E. and Tamerler, C., 2008. Molecular design of inorganic-binding polypeptides. *MRS Bulletin,* 33 (05), 514-518.
6. Leach, A.R., and Schomburg, D., 1996. *Molecular modelling: principles and applications.* Longman London.
7. Li, Y., and Huang, Y., 2010. Morphology-Controlled Synthesis of Platinum Nanocrystals with Specific Peptides. *Advanced Materials,* 22 (17), 1921-1925.
8. Li, Y., Whyburn, G.P. and Huang, Y., 2009. Specific Peptide Regulated Synthesis of Ultrasmall Platinum Nanocrystals. *Journal of the American Chemical Society,* 131 (44), 15998.
9. Liang, M., Deschaume, O., Patwardhan, S.V. and Perry, C.C., 2011. Direct evidence of ZnO morphology modification via the selective adsorption of ZnO-binding peptides. *Journal of Materials Chemistry,* 21 (1), 80-89.
10. Mahmoudi, M., Lynch, I., Ejtehadi, M.R., Monopoli, M.P., Bombelli, F.B. and Laurent, S., 2011. Protein− nanoparticle interactions: opportunities and challenges. *Chemical Reviews,* 111 (9), 5610-5637.
11. Massova, I., and Kollman, P.A., 1999. Computational alanine scanning to probe protein-protein interactions: a novel approach to evaluate binding free energies. *Journal of the American Chemical Society,* 121 (36), 8133-8143.
12. Masuda, Y., Kinoshita, N. and Koumoto, K., 2007. Morphology control of ZnO crystalline particles in aqueous solution. *Electrochimica Acta,* 53 (1), 171-174.
13. Muthukumara, M., 2009. Theory of competitive adsorption-nucleation in polypeptide-mediated biomineralization. *The Journal of Chemical Physics,* 130, 161101-161105.
14. Naik, R.R., Jones, S.E., Murray, C.J., McAuliffe, J.C., Vaia, R.A. and Stone, M.O., 2004. Peptide Templates for Nanoparticle Synthesis Derived from Polymerase Chain Reaction-Driven Phage Display. *Advanced Functional Materials,* 14 (1), 25-30.
15. Oren, E.E., Tamerler, C. and Sarikaya, M., 2005. Metal recognition of septapeptides via polypod molecular architecture. *Nano Letters,* 5 (3), 415-419.
16. Pandey, R.B., Heinz, H., Feng, J., Farmer, B.L., Slocik, J.M., Drummy, L.F. and Naik, R.R., 2009. Adsorption of peptides (A3, Flg, Pd2, Pd4) on gold and palladium surfaces by a coarse-grained Monte Carlo simulation. *Physical Chemistry Chemical Physics,* 11 (12), 1989-2001.
17. Raut, V.P., Agashe, M.A., Stuart, S.J. and Latour, R.A., 2005. Molecular dynamics simulations of peptide-surface interactions. *Langmuir,* 21 (4), 1629-1639.
18. Ruan, L., Chiu, C., Li, Y. and Huang, Y., 2011. Synthesis of Platinum Single-Twinned Right Bipyramid and {111}-Bipyramid through Targeted Control over Both Nucleation and Growth Using Specific Peptides. *Nano Letters,* 11 (7), 3040-3046.

19. Ruan, L., Ramezani-Dakhel, H., Chiu, C., Zhu, E., Li, Y., Heinz, H. and Huang, Y., 2013. Tailoring Molecular Specificity toward a Crystal Facet: a Lesson from Biorecognition toward Pt {111}. *Nano Letters*, 13 (2), 840-846.

20. Sagui, C., and Darden, T.A., 1999. Molecular dynamics simulations of biomolecules: long-range electrostatic effects. *Annual Review of Biophysics and Biomolecular Structure,* 28 (1), 155-179.

21. Sano, K., and Shiba, K., 2003. A hexapeptide motif that electrostatically binds to the surface of titanium. *Journal of the American Chemical Society*, 125 (47), 14234-14235.

22. Sarikaya, M., Tamerler, C., Jen, A.K., Schulten, K. and Baneyx, F., 2003. Molecular biomimetics: nanotechnology through biology. *Nature Materials*, 2 (9), 577-585.

23. Serizawa, T., Sawada, T. and Matsuno, H., 2007. Highly specific affinities of short peptides against synthetic polymers. *Langmuir,* 23 (22), 11127-11133.

24. Tomczak, M.M., Gupta, M.K., Drummy, L.F., Rozenzhak, S.M. and Naik, R.R., 2009. Morphological control and assembly of zinc oxide using a biotemplate. *Acta Biomaterialia,* 5 (3), 876-882.

25. Vodnik, M., Zager, U., Strukelj, B. and Lunder, M., 2011. Phage display: selecting straws instead of a needle from a haystack. *Molecules*, 16 (1), 790-817.

26. Whyburn, G.P., Li, Y.J. and Huang, Y., 2008. Protein and protein assembly based material structures. *Journal of Materials Chemistry,* 18 (32), 3755-3762.

Appendices Chapter 3

Appendix 3.1

Graph showing EDX analysis of samples collected at 24 hrs, 25 hrs and 48 hrs of ZnO synthesis using precursor $Zn(NO_3)_2 \cdot 6H_2O$ and HMTA without peptide (control). The presence of atomic zinc and oxygen in the samples was confirmed. Atomic aluminium was detected from the sample holder/stub used and carbon was the conductive material used to coat the samples.

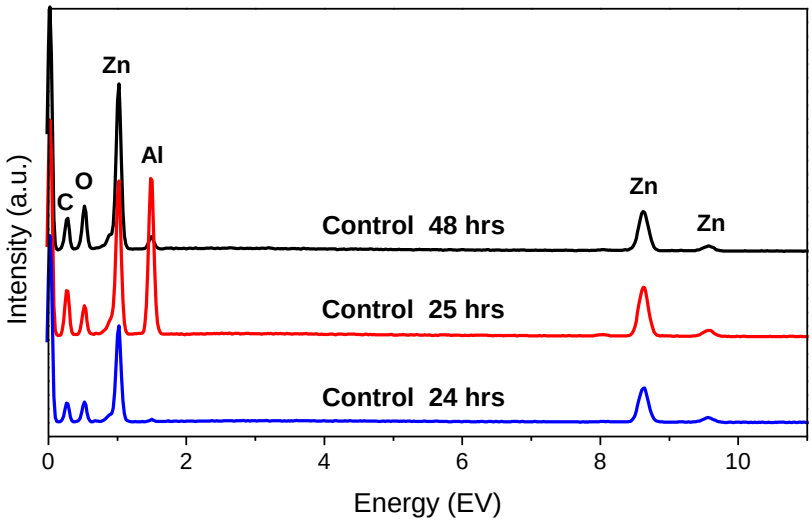

Appendix 3.2

A schematic representation of the layered structure of $Zn_5(OH)_8(NO_3)_2 \cdot 2H_2O$ determined using XRD. The structure has been described by Newman and Jones, (1999) to consist of brucite-like layers which have octahedral sites, one fourth of which are vacant. Tetrahedrally coordinated zinc cations are located on either side of the vacant octahedra. The tetrahedra are formed by a water molecule and three OH groups. Nitrate anions which are not coordinated with the zinc cations lie between the hydroxide layers.

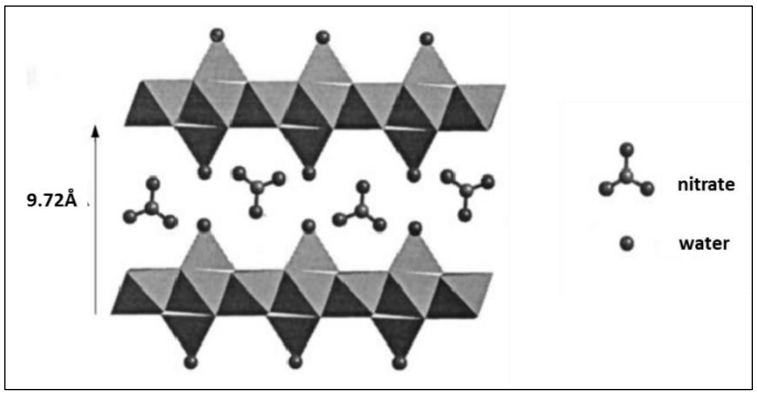

Appendix 3.3

X-ray diffractrogram and SEM micrographs showing the formation of LBZN at 24 hrs and 72 hrs of synthesis using precursor $Zn(NO_3)_2 \cdot 6H_2O$ and HMTA at 20 °C. An increase in reaction temperature was required to overcome the energy barrier for the phase transformation to ZnO.

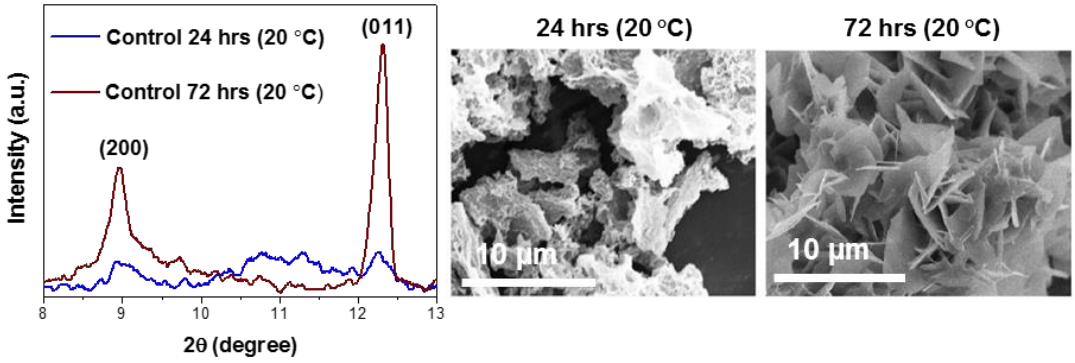

Appendix 3.4

Purity and molecular weight of peptides synthesized using microwave assisted solid phase peptide synthesis protocol. G-12 and GT-16 were ZnO binding peptides that had been identified using phage display technique (Tomczak *et al*., 2009). G-12A6, G-12A11 and G-12A12 are mutants of G-12 peptide with alanine amino acid substituted into certain positions, selected after computational studies on the stability of peptides (Ramasamy R).

Peptide	**HPLC % Purity**	**Calculated M_r (Da)**	**Mass-spectrometry M_r (Da)**
G-12	95.8	1341.6	1341.8
GT-16	94.4	1615.9	1615.8
G-12A6	85.5	1275.6	1275.7
G-12A11	86.5	1315.6	1316.5
G-12A12	82.8	1256.5	1256.7

Appendix 3.5

EDX analysis confirming the presence of atomic zinc and oxygen in rods and microspheres synthesized using the $Zn(NO_3)_2 \cdot 6H_2O$ and HMTA reaction method and incorporating 0.3 mM G-12A6 peptide. Sample analysed was collected at 48 hrs of synthesis.

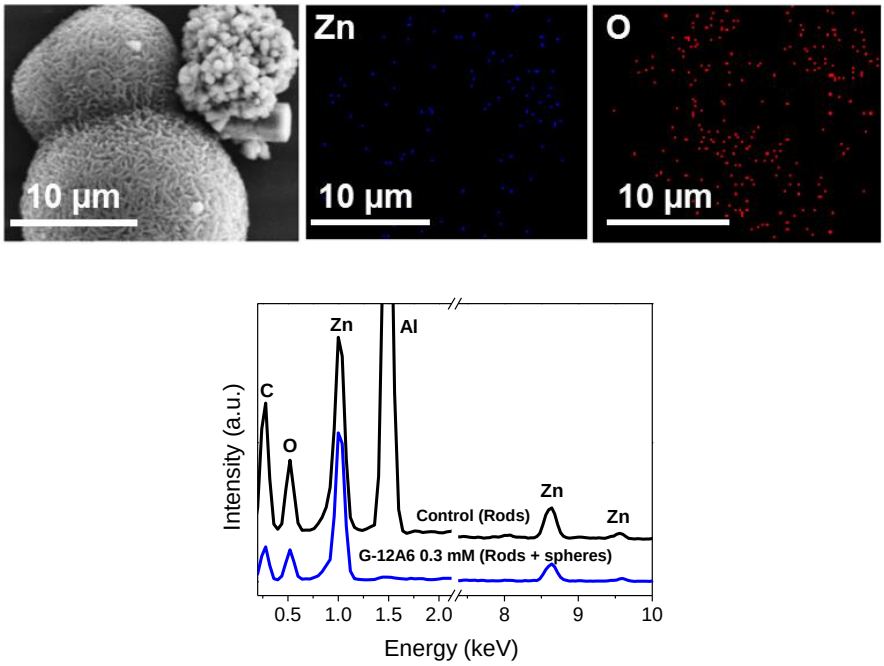

Appendix 3.6

ICP-OES analysis of the percentage of Zn^{2+} ions in supernatants collected at different time points during ZnO synthesis using the $Zn(NO_3)_2 \cdot 6H_2O$ and HMTA method with the different peptides incorporated. The control reaction is synthesis without peptide. Peptides did not alter the kinetics of Zn^{2+} consumption.

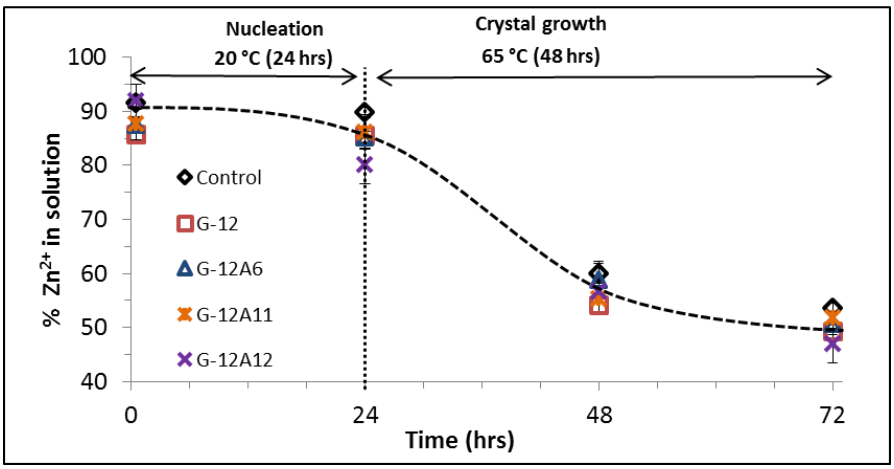

Appendix 3.7

SEM micrographs of ZnO platelets collected at 48 hrs of synthesis using the $Zn(NO_3)_2 \cdot 6H_2O$ and HMTA method with 0.3 mM GT-16 as a growth modifier. The sample consisted of ZnO twinned platelets with a low aspect ratio (L/D = 0.86 ± 0.31). Some of the structures were hexagonal while others were more rounded.

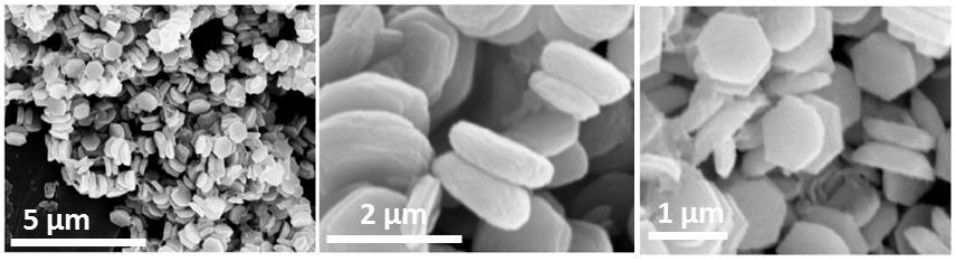

Appendix 3.8

(A) 1st derivative TGA graphs [d(weight)/d(time)] showing weight loss in ZnO crystals collected at 48 hrs of synthesis using the $Zn(NO_3)_2 \cdot 6H_2O$ and HMTA method. Samples were synthesized without peptide (control) and in the presence of peptides. A concentration of 0.3 mM was used for all peptides. The weight loss has been divided into three stages, stage 1, up to 100 °C was weight loss attributed to the loss of physisorbed water, stage 2 to ~250 °C was attributed to loss of chemisorbed water and stage 3 was attributed to loss of organic matter. The weight loss in stage 2 can be more specifically attributed to loss of intercalated water in LBZN or dehydroxylation of zinc hydroxide. The weight loss in stage 2 could be devided into two stages more clearly in some profiles. Organic matter, mainly consisting of peptide strongly adsorbed to the precipitates and nitrate groups decomposed at a temperature of ~650 °C.

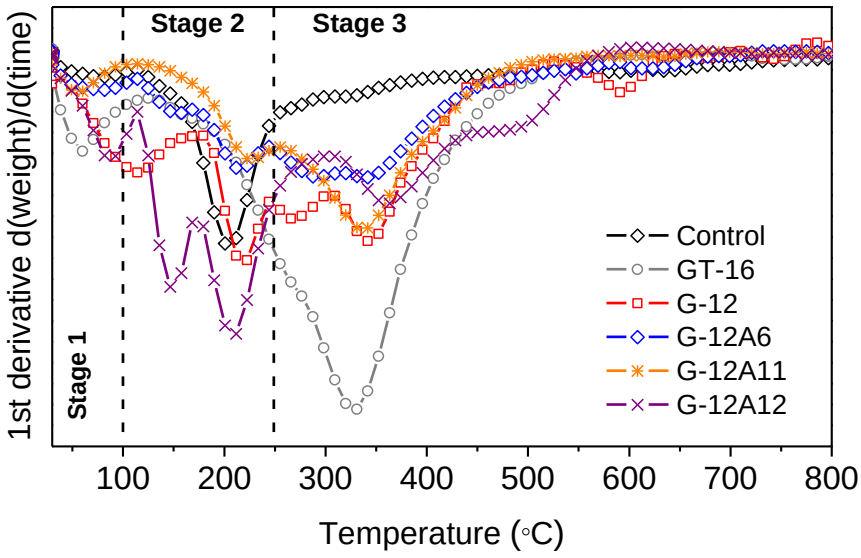

(B) Also shown below is the 1st derivative TGA graphs [d(weight)/d(time)] of the degradation of reagents

used in this study for synthesis of ZnO. Complete degradation of pure peptides occurs at a temperature of ~700 °C. HMTA is completely decomposed at a temperature of ~280 °C. However, in the synthesis we believe that HMTA may have been completely hydrolysed in water. $Zn(NO_3)_2 \cdot 6H_2O$ and $Zn(CH_3COO)_2$ are both decomposed at ~400 °C although in the synthesis they would have already been completely dissociated in water.

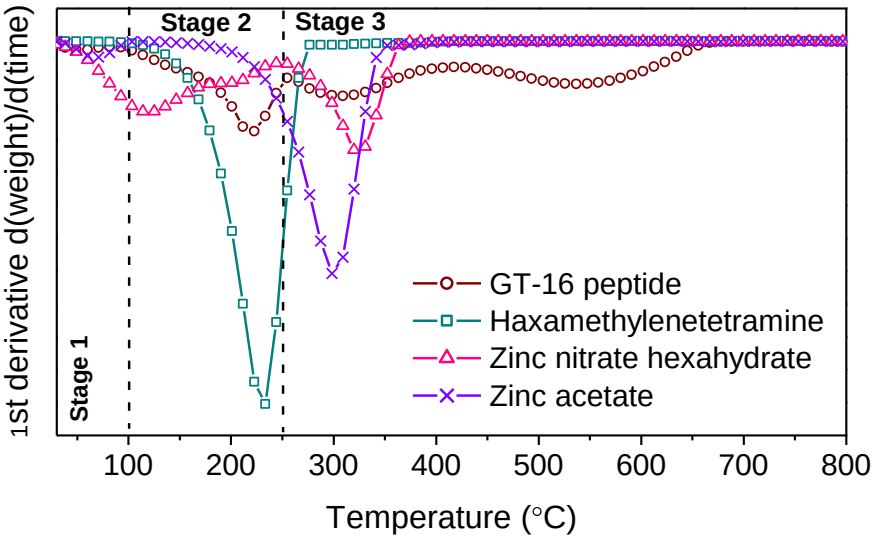

Appendix 3.9

FTIR spectra of precursors $Zn(CH_3COO)_2$ used for ZnO synthesis and precipitates collected during the reaction at the star and at 24 and 48 hrs of synthesis. The absorbance of O-Zn-O at 430 – 550 cm^{-1} is detectable is all the precipitates but becomes dominant with prolonged synthesis time. The amount of zinc acetate present in the precipitates decreased with time.

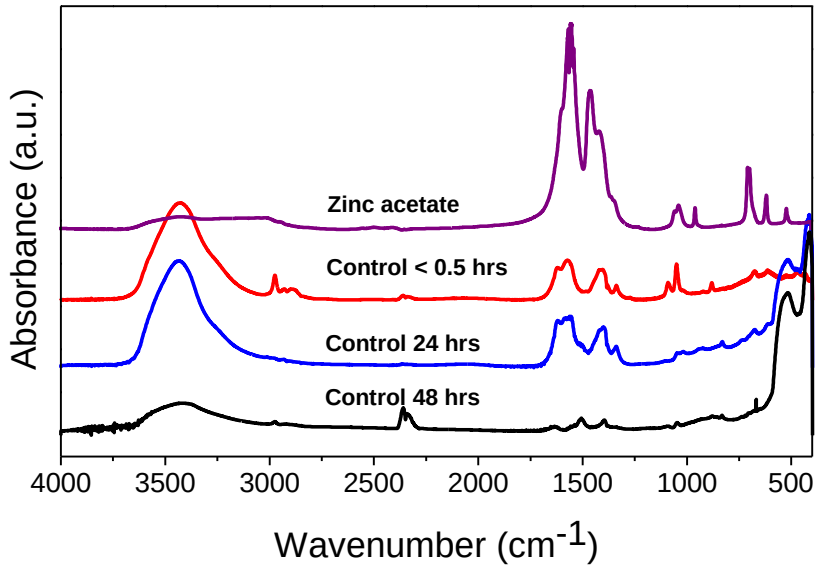

Appendix 3.10

Types of bonding structures/coordination modes of acetate to metals reproduced from Sakohara *et al*., 1998.

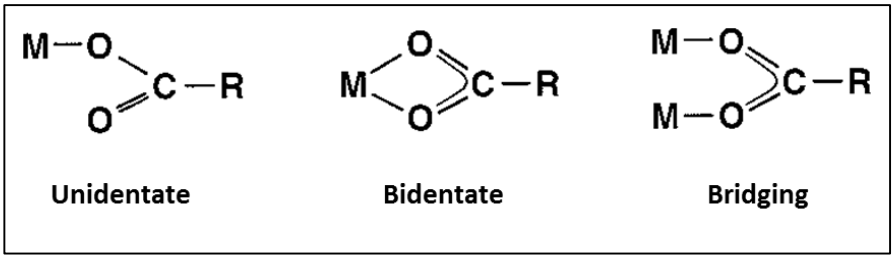

Appendix 3.11

ICP-OES analysis determination of the percentage Zn^{2+} ions in supernatants collected at different time points during ZnO synthesis using precursor $Zn(CH_3COO)_2$ and NH_3. The amount of Zn^{2+} in solution rapidly decreases upon mixing the two reagents as LBZA precipitated from the solution. With time, dissolution of some of the unstable precipitate occurs and Zn^{2+} ions were released back into solution, followed by a second decrease in Zn^{2+} ions in solution as growing stable nuclei develop into ZnO crystals.

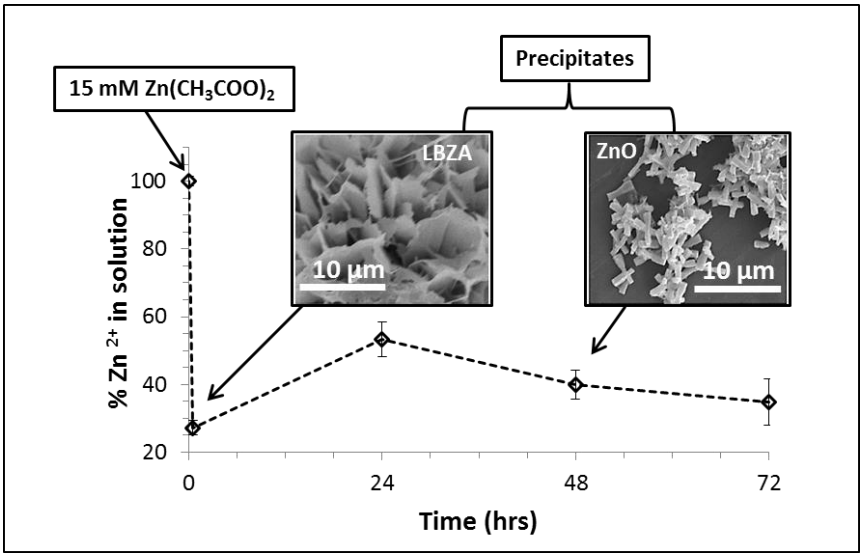

Appendix 3.12

SEM micrographs of precipitates synthesized using the $Zn(NO_3)_2 \cdot 6H_2O$ and HMTA method with three different concentrations of G-12A6 peptide collected at (a-f) 25 hrs (24 h, $t_{20\,°C}$ + 1 h, $t_{65\,°C}$) and (g-l) 48 hrs (24 h, $t_{20\,°C}$ + 24h, $t_{65\,°C}$) of synthesis.

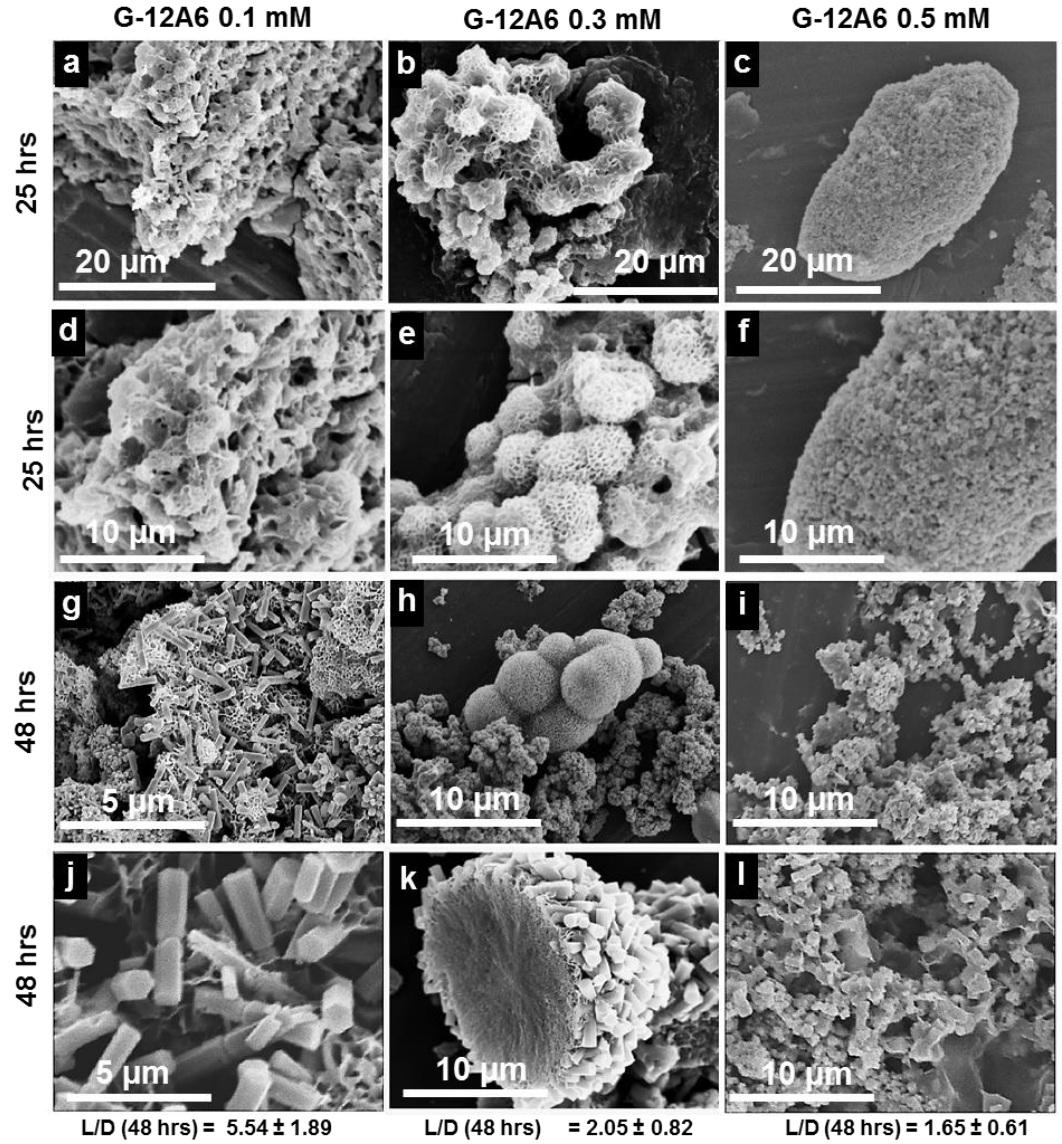

Appendix 3.13

SEM micrographs of precipitates synthesized using the $Zn(CH_3COO)_2$ and NH_3 method with three different concentrations of G-12A6 peptide collected at (a, d, g) 24 hrs, t = 50 °C (b, c, e, f, h, i) 48 hrs, t = 50 °C of synthesis.

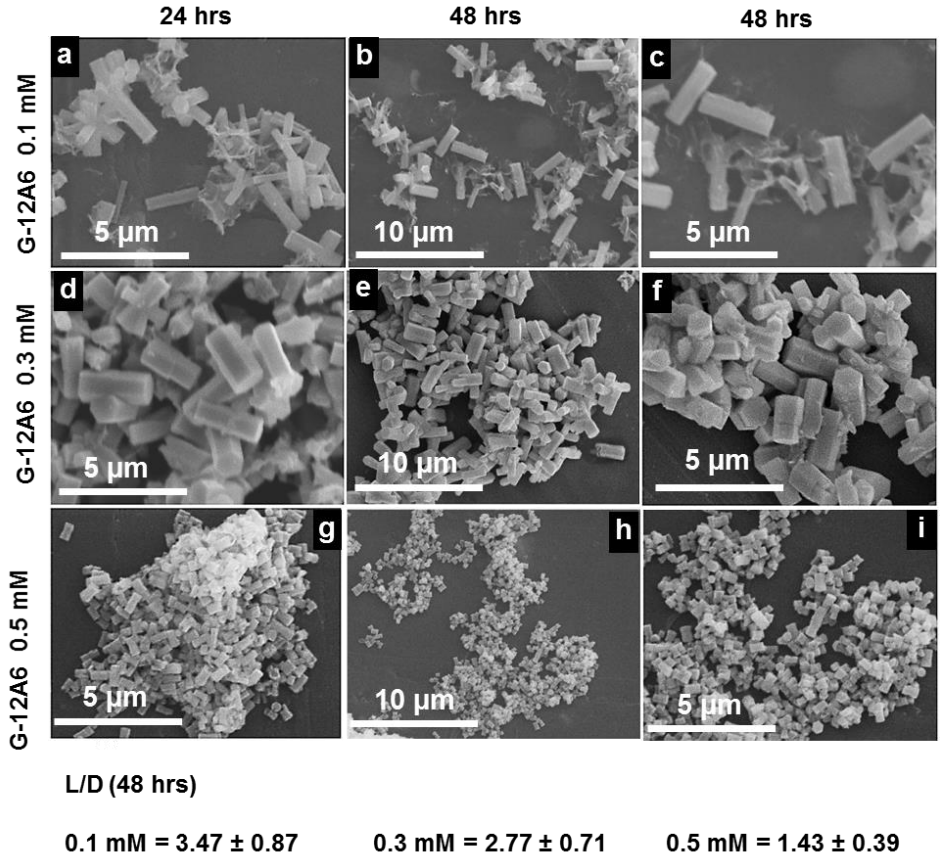

Appendix 3.14

SEM micrographs of precipitates synthesized using the $Zn(NO_3)_2 \cdot 6H_2O$ and HMTA method with three different concentrations of G-12 peptide collected at (a-c) 25 hrs (24 h, $t_{20\,°C}$ + 1 h, $t_{65\,°C}$), (c-i) 48 hrs (24 h, $t_{20\,°C}$ + 24 h, $t_{65\,°C}$) of synthesis.

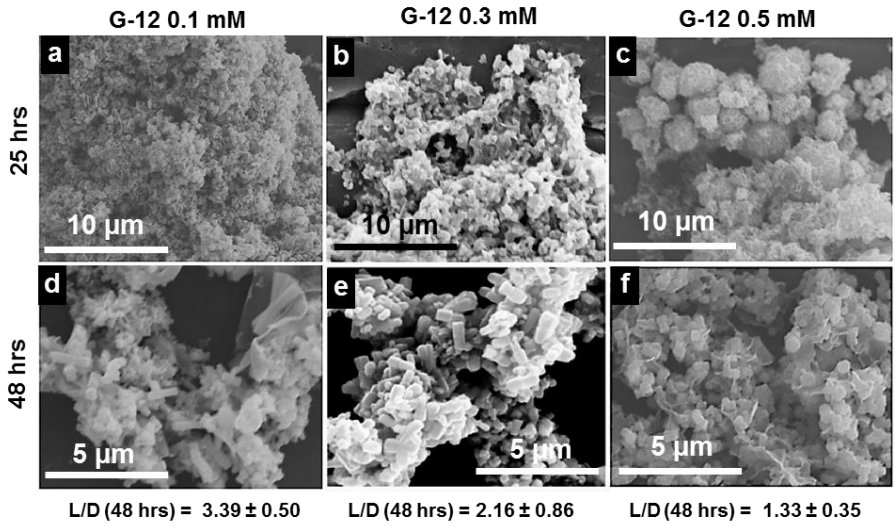

Appendix 3.15

SEM micrographs of precipitates synthesized using the $Zn(CH_3COO)_2$ and NH_3 method with three different concentrations of G-12 peptide collected at (a, d, g) 24 hrs, t = 50 °C (b, c, e, f, h, i) 48 hrs, t = 50 °C of synthesis.

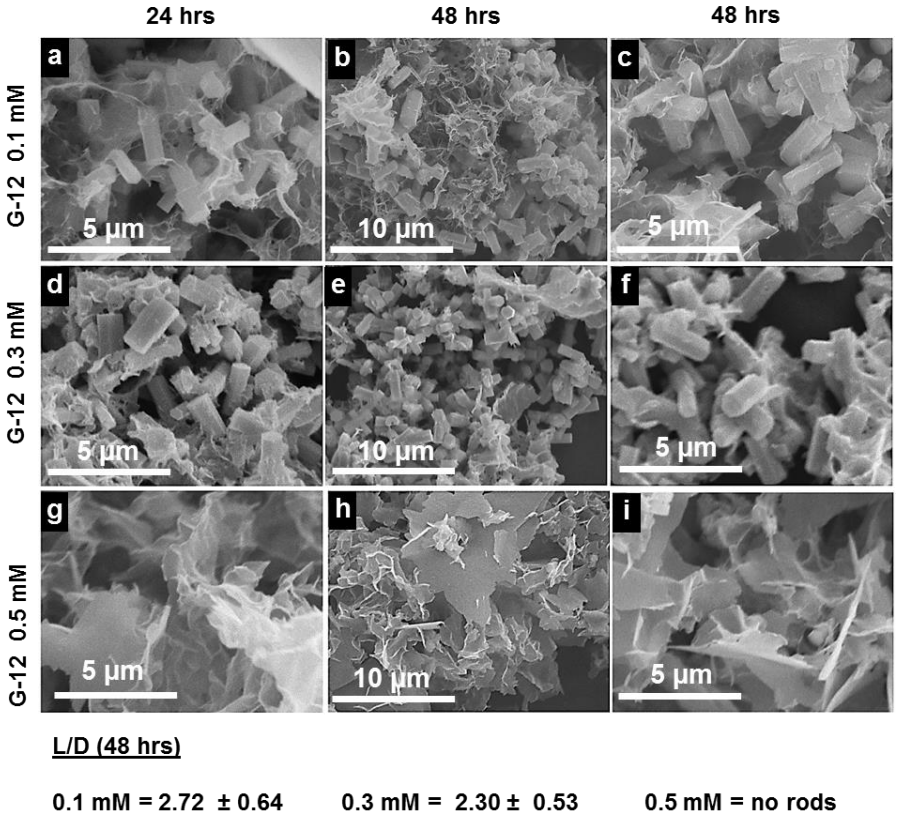

Appendix 3.16

XRD diffractograms comparing the growth of ZnO synthesized in the absence of peptides (control) and in the presence of G-12 and G-12A6 peptides using the $Zn(CH_3COO)_2$ and NH_3 method; (a-c) diffractograms of precipitates collected after at different time points without peptide and with 0.3 mM G-12 and G-12A6, (d) 48-hr precipitates synthesised with different peptide concentrations. (∗) denotes peaks from the polypropylene sample holder.

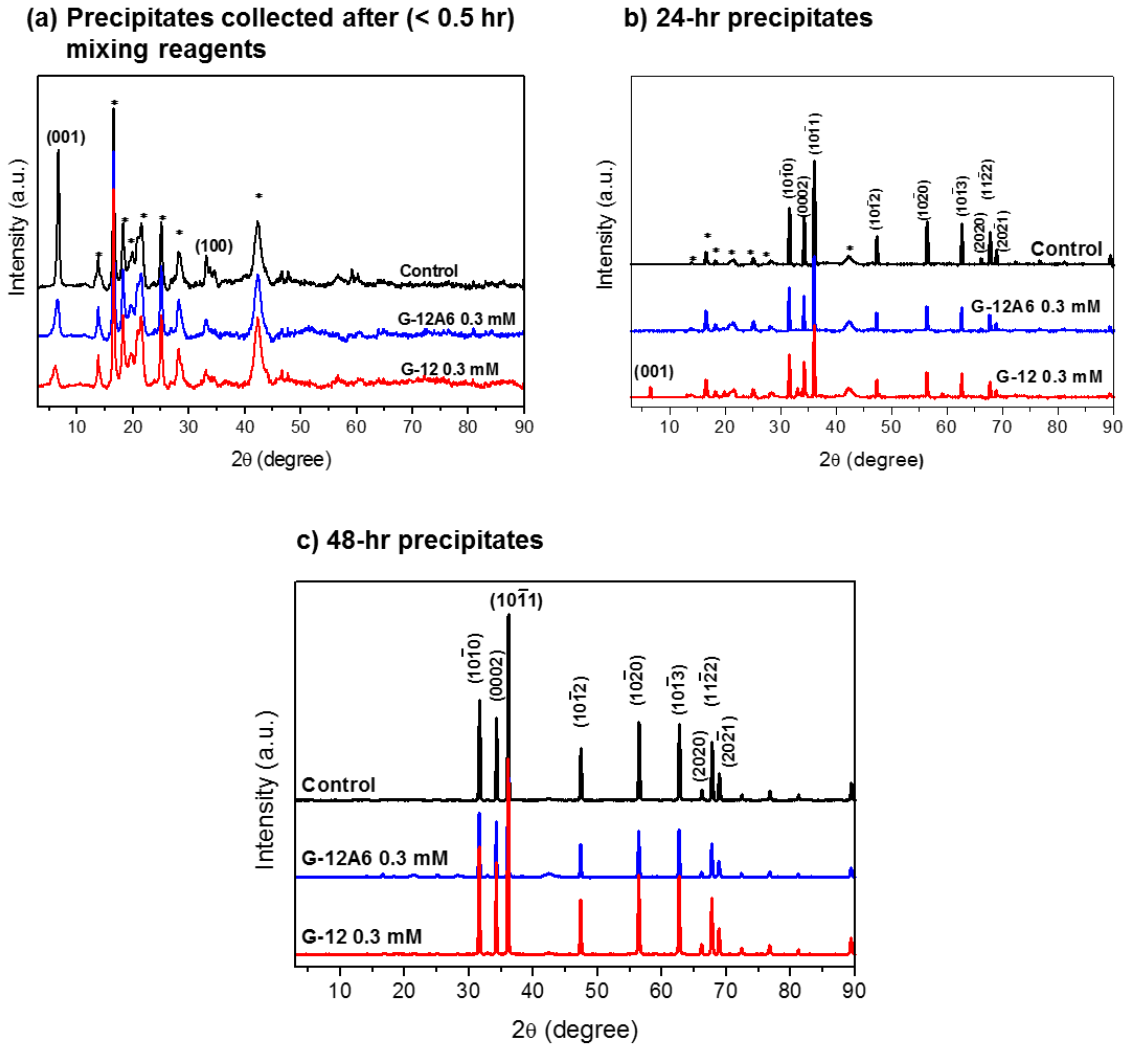

Appendix 3.17

XRD diffractograms showing growth of ZnO synthesized in the absence of peptides (control) and in the presence of G-12 and G-12A6 peptides using the $Zn(NO_3)_2 \cdot 6H_2O$ and HMTA method. Above are diffractograms of precipitates collected at 25 hrs (24 h, $t_{20\,°C}$ + 1 h, $t_{65\,°C}$) and below at 48 hrs (24 h, $t_{20\,°C}$ + 24 h, $t_{65\,°C}$) of synthesis. Wurtzite structured ZnO is the dominant phase in all precipitates collected at 48 hrs of synthesis. (∗) denotes peaks from the polypropylene sample holder.

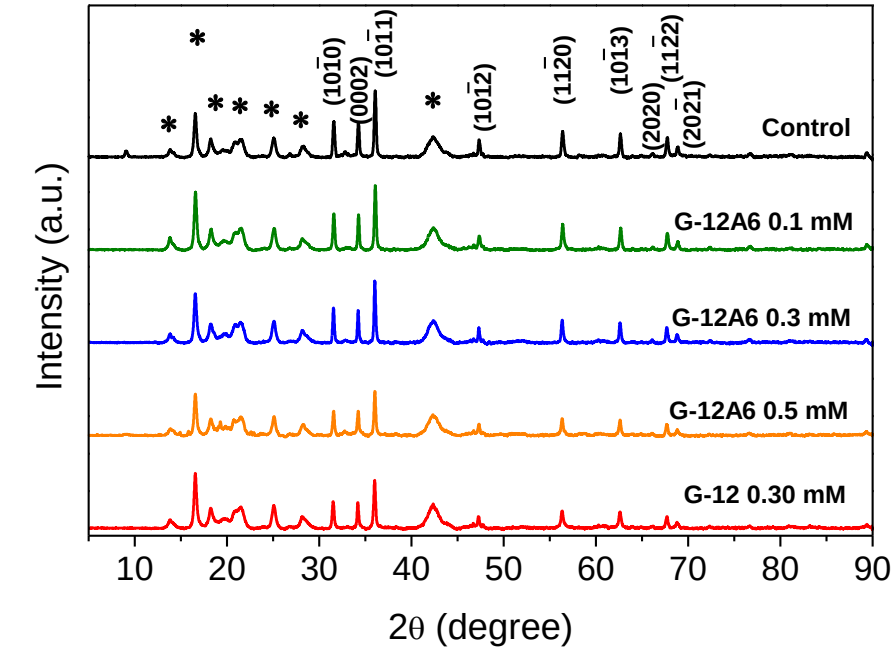

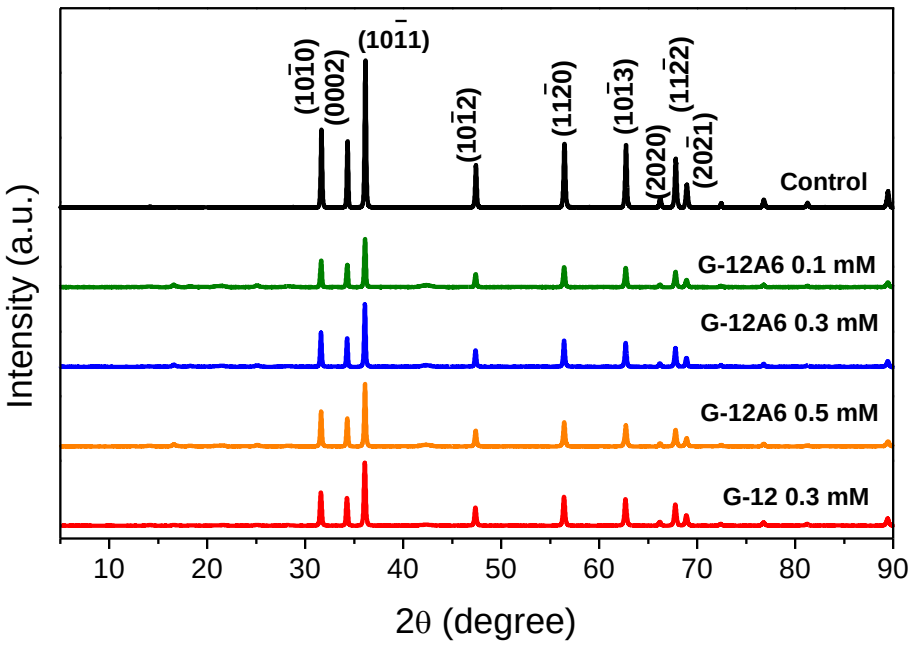

Appendix 3.18

TGA analysis of 48-hr precipitates collected during ZnO synthesis using (a) the $Zn(NO_3)_2 \cdot 6H_2O$ and HMTA synthesis method and (b) the $Zn(CH_3COO)_2$ and NH_3 synthesis method. Peptides G-12 and G-12A6 have also been used in synthesis in both methods at three concentrations, 0.1 mM, 0.3 mM and 0.5 mM. There is a distinctive difference in the organic content between the control reaction (without peptide) and in the reactions with peptides in syntheses using $Zn(NO_3)_2 \cdot 6H_2O$ and HMTA.

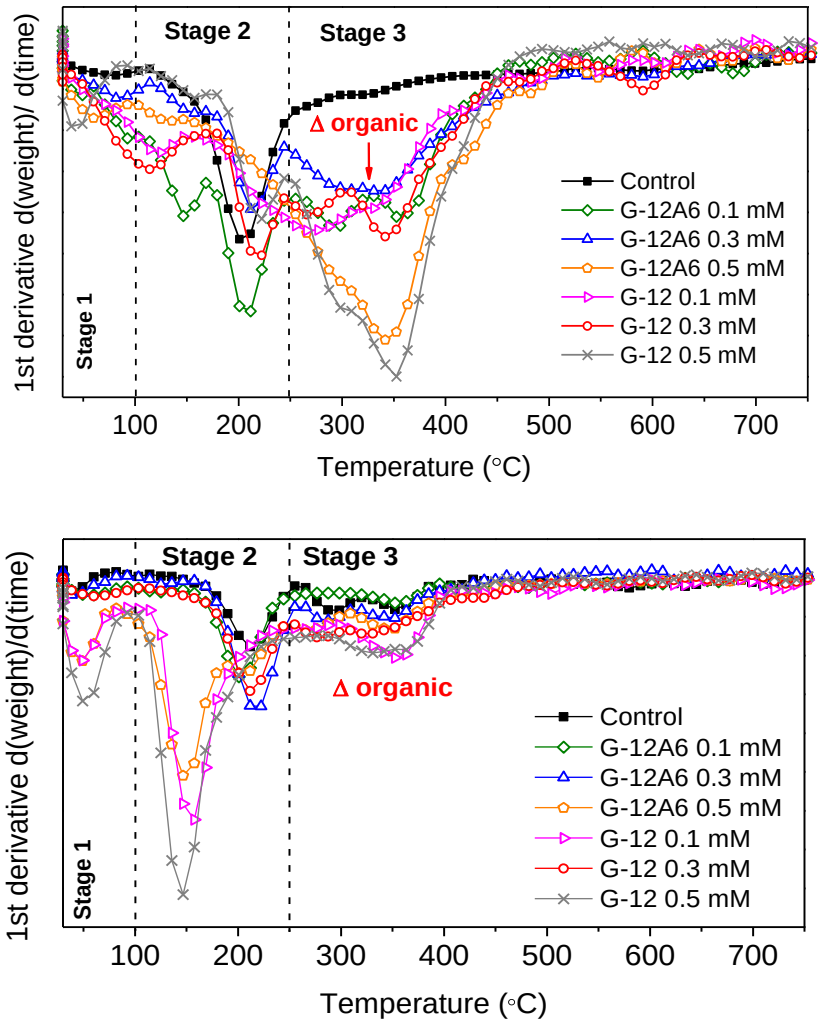

Weight loss observedin stage 1 up to 100 °C could be associated with dehydration of physisorbed water,. Weight loss observed in stage 2 between 100 to ~168 °C could mainly be associated with dehydration of intercalated water, and weight loss from ~168 °C to ~250 °C may be associated with dehydroxylation of layers of zinc hydroxide on surface of ZnO. These regions of weight loss in stage 2 may overlap. Acetate and nitrate groups were decomposed by ~ 400 °C (Appendix 3.8 b) along with any other organic material such as peptides in stage 3.

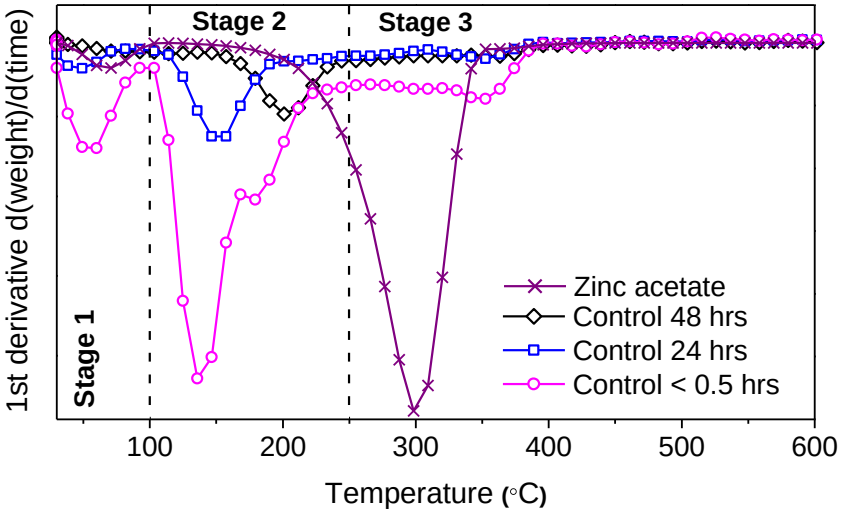

Also shown above is the TGA analysis of precipitates collected at different time points during the synthesis of ZnO using the $Zn(CH_3COO)_2$ and NH_3 reaction method. Total weight loss of precipitates after thermal decomposotion; < 0.5 hr = 32.6 ± 1.4, 24 hrs = 10.8 ± 2.2 and 48 hrs = 32.6 ± 1.4. The control precipitate formed after mixing the reagents was confirmed to be LBZA using XRD. Its profile is similar to LBZA found in 48-hr precipitates synthesized using 0.5 mM G-12 peptide which stabilized the intermediate for a longer period. The control precipitate collected at 48 hrs was confirmed to predominantly consist of ZnO using XRD analysis. The weight loss observed in the control precipitate collected at 48 hrs could be attributed to dehydration of water intercalated within LBZA and/or dehydroxylation of $Zn(OH)_2$.

Appendix 3.19

FTIR analysis of washed precipitates collected at 48 hrs of synthesis using the $Zn(NO_3)_2 \cdot 6H_2O$ and HMTA method. ZnO synthesis was carried out with different concentrations of G-12 peptide (above) and G-12A6 peptide (below). Control is ZnO without peptide. Spectra of peptides only are also shown. Different concentrations of peptide were used for ZnO synthesis. There was an evident adsorption of peptide onto the ZnO precipitates. With increased peptide concentration, the intensity of the shifted amide I band (~1646 cm^{-1}) in ZnO precipitates (430 - 550 cm^{-1}) increased. The intensity of NO_3^- (1384 cm^{-1}) also increased with an increase in peptide concentration.

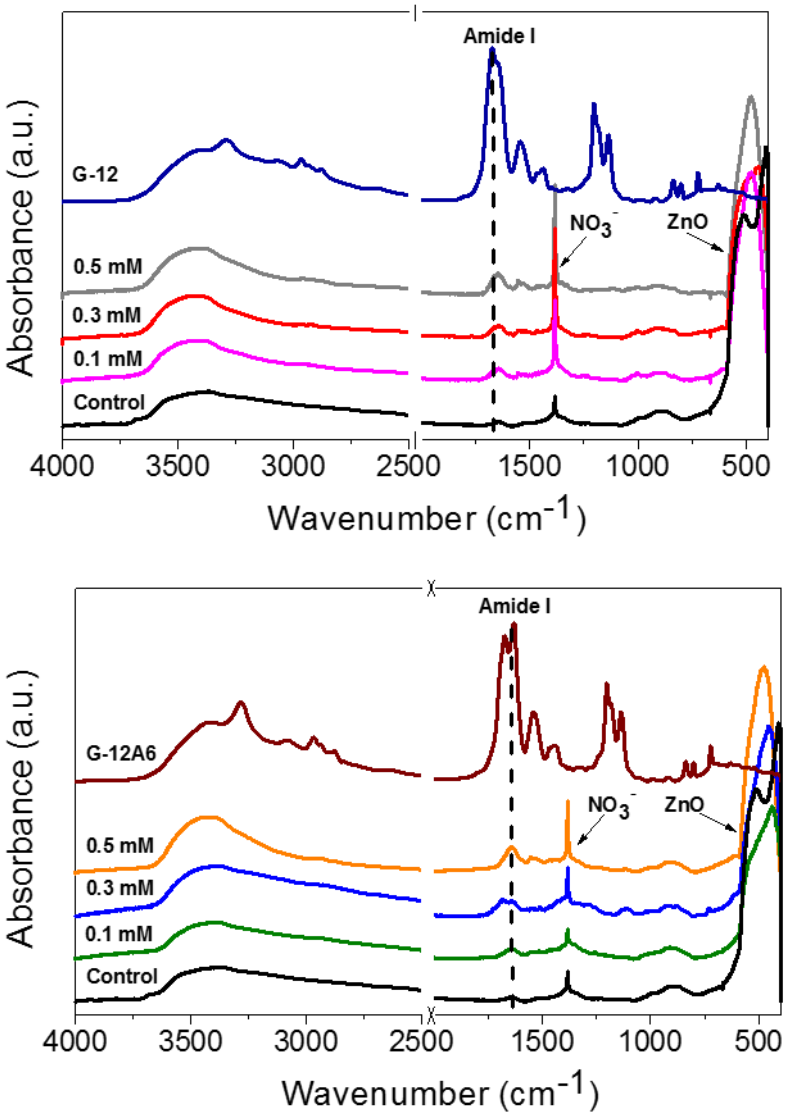

Appendix 3.20

FTIR analysis of washed precipitates collected at 48 hrs of synthesis using the $Zn(CH_3COO)_2$ and NH_3 method. ZnO synthesis was carried out with different concentrations of G-12 peptide (above) and G-12A6 peptide (below). There was no evidence of peptide adsorption onto the ZnO precipitates where peptides were inorporated in the syntheses. The amide I band (1600 - 1700 cm^{-1}) of peptides was not detected in the ZnO precipitates (430 - 550 cm^{-1}). The intensity of acetate anions (1350 - 1600 cm^{-1}) increased with increased peptide concentration.

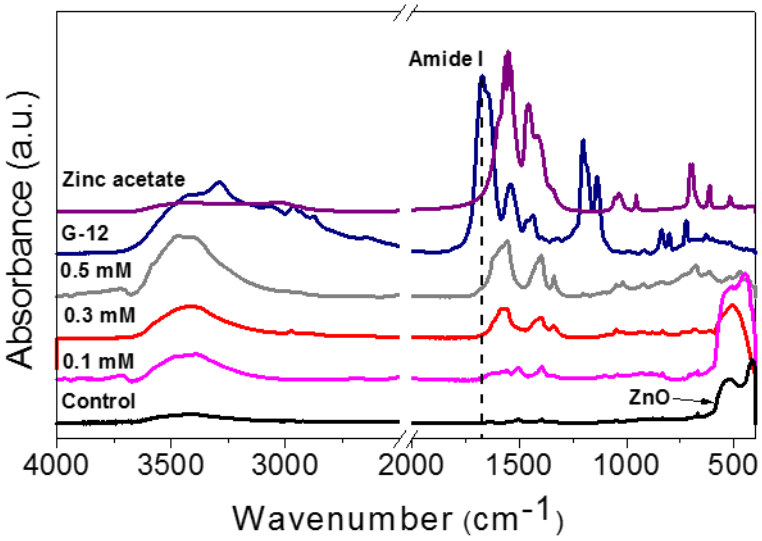

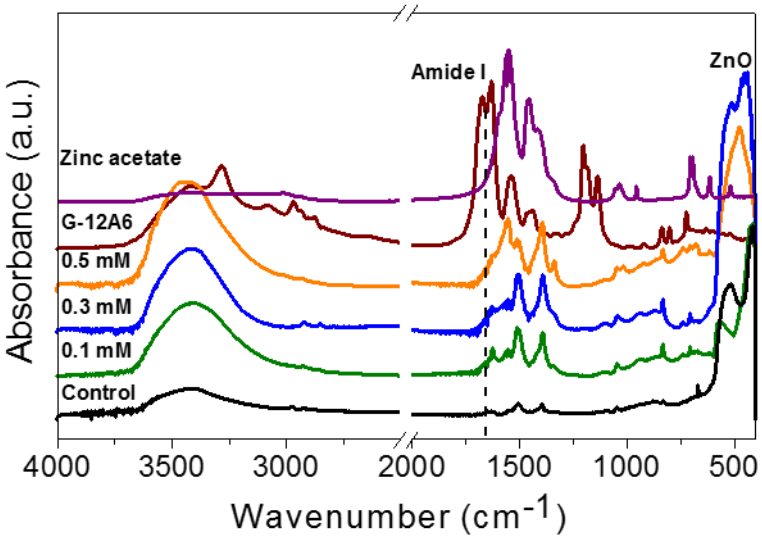

Appendices Chapter 4

Appendix 4.1

XRD diffractograms confirming that ZnO rods and platelets were not phase transformed by calcination up to 900 °C which was carried out to remove organic contaminants.

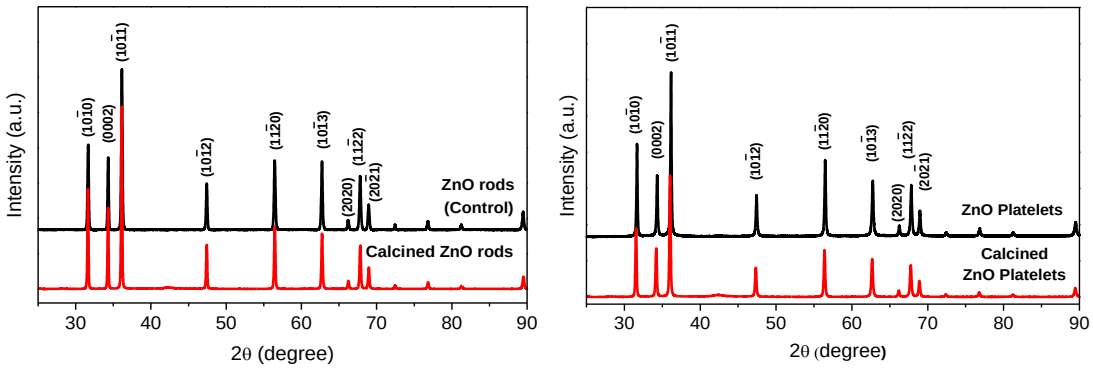

Appendix 4.2

Isothermal profiles showing titrations of; (a) 1.25 mM GT-16 peptide into an ITC cell containing a suspension of 0.2 mM ZnO rods (bulk concentration) in water, heats measured were predominantly endothermic and saturation of the exothermic event was not reached (b) 3.1 mM GT-16 into an ITC cell containing a suspension of 0.1 mM ZnO rods (bulk concentration), saturation was reached and both endothermic and exothermic heats were measured. In each experiment, 280 µl of peptide was injected in 10 µl aliquots and the cell temperature was maintained at 298 K.

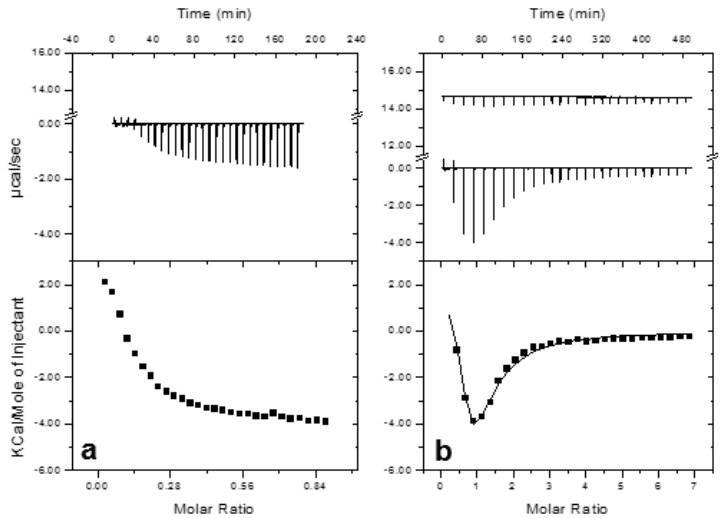

Appendix 4.3

Isothermal profiles showing titrations of 3.1 mM G-12 into a suspension of 0.1 mM ZnO platelets (bulk concentration). In each experiment, 280 µl of peptide was injected in 10 µl aliquots and the cell temperature was maintained at 298 K. The shapes of the isothermal profiles in (a) and (b) appear to be very similar showing reproducibility of the experiment. The profile of the third repeat (c) looks more dissimilar to the first two but the values of thermodynamic parameters obtained after fitting data using two sets of independent sites model give more similar values for (b) and (c).

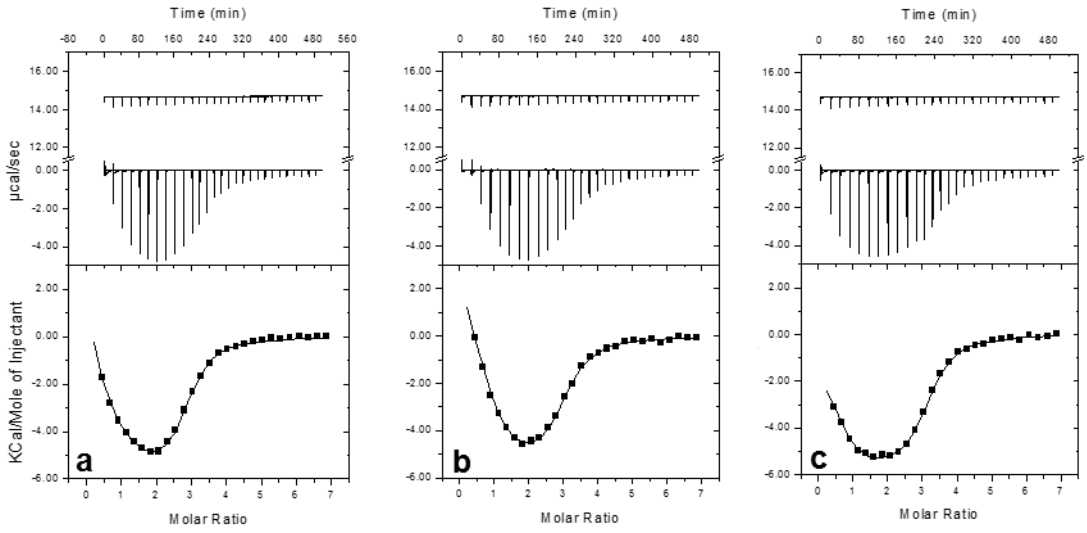

Data: A110120ZnODG_NDH
Model: TwoSites
Chi^2 = 4154

N1	0.122	±0.331 Sites
K1	5.50E5	±1.11E5 M^{-1}
ΔH1	5.878E4	±1.91E5 cal/mol
ΔS1	223 cal/mol/deg	
N2	2.65	±0.319 Sites
K2	1.85E5	±4.56E4 M^{-1}
ΔH2	-7334	±635 cal/mol
ΔS2	-0.496 cal/mol/deg	

Data: A110126G12Zn_NDH
Model: TwoSites
Chi^2 = 4436

N1	0.618	±0.0755 Sites
K1	9.94E5	±2.98E5 M^{-1}
ΔH1	5819	±2.40E3 cal/mol
ΔS1	47.0 cal/mol/deg	
N2	2.31	±0.0633 Sites
K2	1.30E5	±1.10E4 M^{-1}
ΔH2	-6295	±354 cal/mol
ΔS2	2.29 cal/mol/deg	

Data: A110127G12Zn_NDH
Model: TwoSites
Chi^2 = 4503

N1	0.597	±0.0904 Sites
K1	2.15E6	±9.05E5 M^{-1}
ΔH1	-967.9	±1.20E3 cal/mol
ΔS1	25.7 cal/mol/deg	
N2	2.50	±0.0830 Sites
K2	1.60E5	±1.40E4 M^{-1}
ΔH2	-6064	±161 cal/mol
ΔS2	3.47 cal/mol/deg	

G-12 and ZnO	*Dp*	K_A (M^{-1})	ΔH (Kcal mol^{-1})	$T\Delta S$ (Kcal mol^{-1})	ΔG (Kcal mol^{-1})
Experiment a	+ve	$5.50 \times 10^5 \pm 1.11 \times 10^5$	58.78 ± 191 *	66.45 *	-7.67
	- ve	$1.85 \times 10^5 \pm 4.56 \times 10^4$	-7.33 ± 0.64	-0.15	-7.19
Experiment b	+ve	$9.94 \times 10^5 \pm 2.98 \times 10^5$	5.82 ± 2.4	14.01	-8.19
	-ve	$1.30 \times 10^5 \pm 1.10 \times 10^4$	-6.30 ± 0.35	0.68	-6.98
Experiment c	+ve	$2.15 \times 10^6 \pm 9.05 \times 10^5$	-0.97± 1.2 *	7.66	-8.63
	-ve	$1.60 \times 10^5 \pm 1.40 \times 10^4$	-6.06 ± 0.16	1.03	-7.10

(+ve) endothermic, (-ve) exothermic, (*) unreasonable data for the rapidly completed endothermic process

Appendix 4.4

Net charge of ZnO binding peptides used in ITC experiments calculated using an online calculator by Gale Rhodes, University of Southern Maine. The peptides have a net positive charge at the working pH of ITC experiments. Measured zeta potential of GT-16 peptide in Tris buffer shows that calculated net charge gives reasonable estimates of the acid base behaviour of peptides.

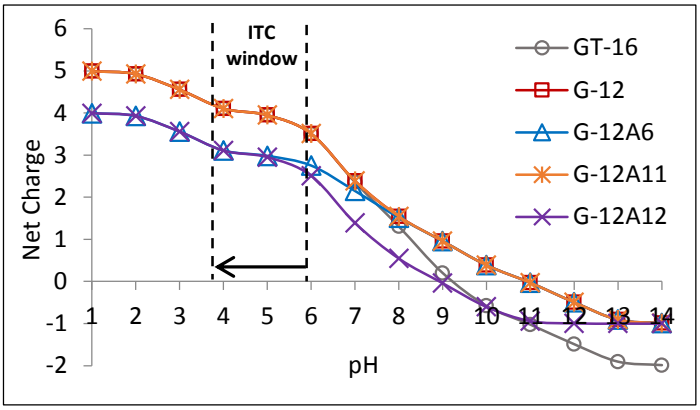

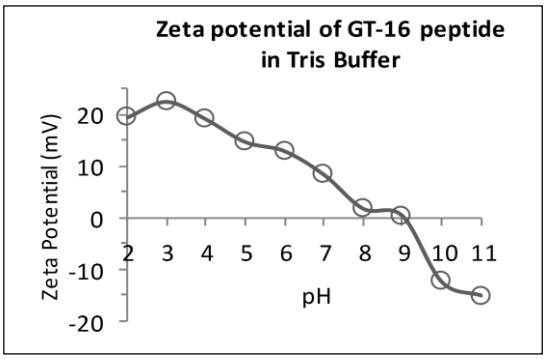

Appendix 4.5

DLS size measurements of ZnO binding peptides, 1 mg/ml in water. DLS data in volume percentage (%) distribution shows that there were aggregates of different sizes in solution but the number % distribution shows that the average hydrodynamic radius of the majority was ~60 nm in size.

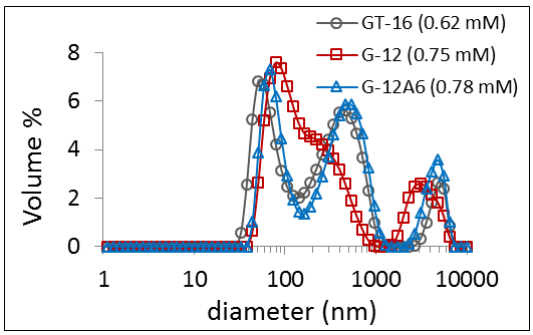

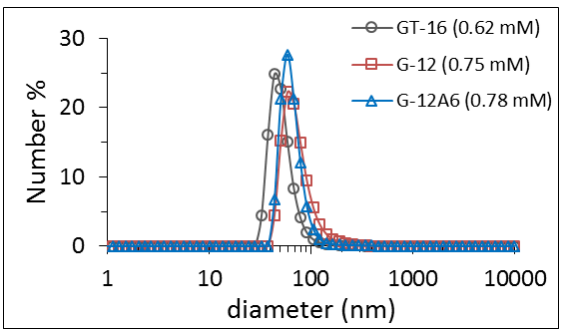

Appendix 4.6

Isothermal profile showing titrations of 3.1 mM EM-12 peptide into a suspension of 0.1 mM ZnO rods (bulk concentration). A total volume of 280 µl of peptide was injected in 10 µl aliquots into an ITC sample cell containing ZnO particles at 298 K.

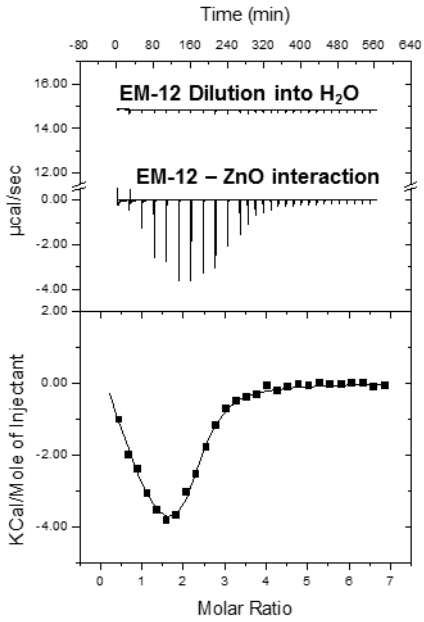

EM-12 and ZnO	***Dp***	***K_A* (M^{-1})**	**ΔH (Kcal mol^{-1})**	**$T\Delta S$ (Kcal mol^{-1})**	**ΔG (Kcal mol^{-1})**
Experiment a	+ve	$8.60 \times 10^5 \pm 4.98 \times 10^5$	0.27 ± 1.33	7.84	-8.10
	- ve	$1.08 \times 10^5 \pm 1.50 \times 10^4$	-6.83 ± 0.68	0.03	-6.87
Experiment b	+ve	$4.73 \times 10^5 \pm 4.31 \times 10^5$	5.15 ± 1.10	12.87	-7.72
	- ve	$1.45 \times 10^5 \pm 4.33 \times 10^4$	-7.24 ± 3.25	-0.20	-7.04

(+ve) endothermic, (-ve) exothermic

Appendices Chapter 5

Appendix 5.1

Characterization of Pt-binding peptides identified using phage display technique by Li *et al.*, 2009 and Chiu *et al.*, 2011 using RP-HPLC and MALDI-TOF mass-spectrometry.

Peptide sequence	**HPLC % Purity**	**Calculated M_r (Da)**	**Mass-spectrometry M_r (Da)**
TLHVSSY	81.2	805.9	806.3
TLTTLTN	83.0	762.3	763.4
SSFPQPN	85.0	775.8	776.3

Appendix 5.2

Peptide charge of Pt-binding peptides determined using polypeptide charge calculator - Gale Rhodes, University of Southern Maine, Portland, USA.

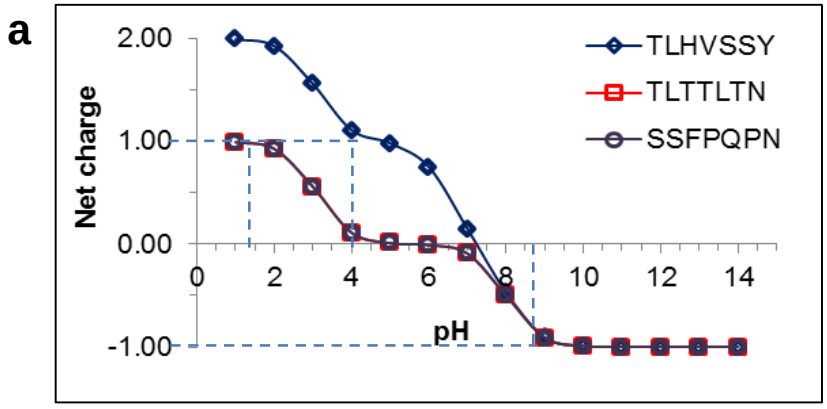

Hydrodynamic diameter of Pt binding peptides 1mg/ml in H_2O determined using DLS. Peptides appear to be monodisperse in solution.

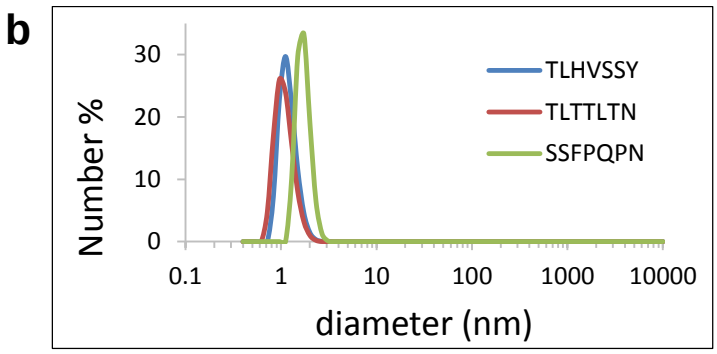

Appendix 5.3

Preliminary studies to determine the kinetic constants for the adsorption of Pt-binding peptides on Pt surface using QCM-D. Different concentrations of peptides have been used. The mass of peptide adsorbed increased with an increase in peptide concentration which indicated that peptide-surface and peptide-peptide interactions were taking place. When 1 mg/ml peptide was used, packing down or rearrangement of the adsorbed layer took place evidenced by a decrease in dissipation which in some instances went below zero indicating that the sensor could have been experiencing mechanical stress due to the mass adsorbed. Peptide TLTTLTN had on and off adsorption indicating it had weak and reversible interaction.

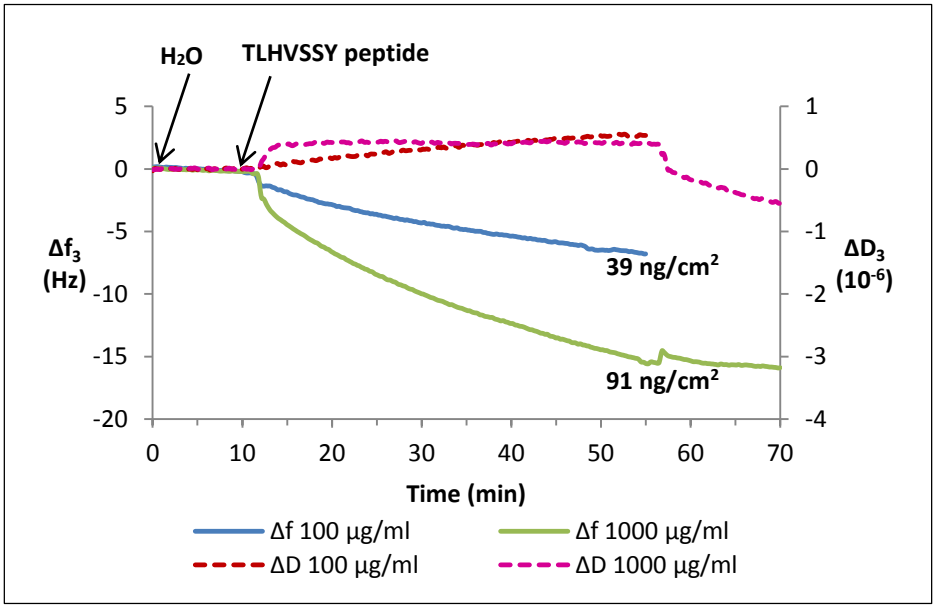

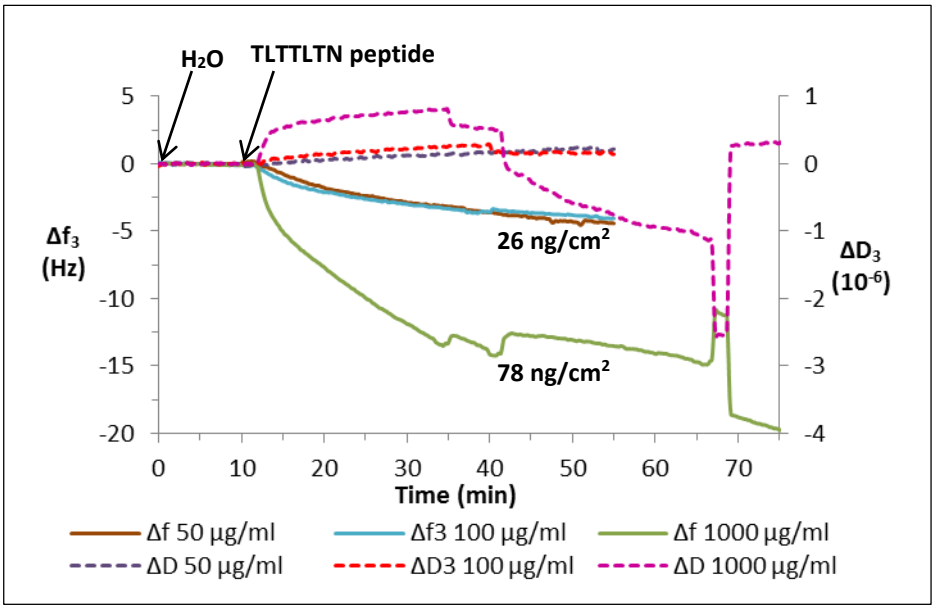

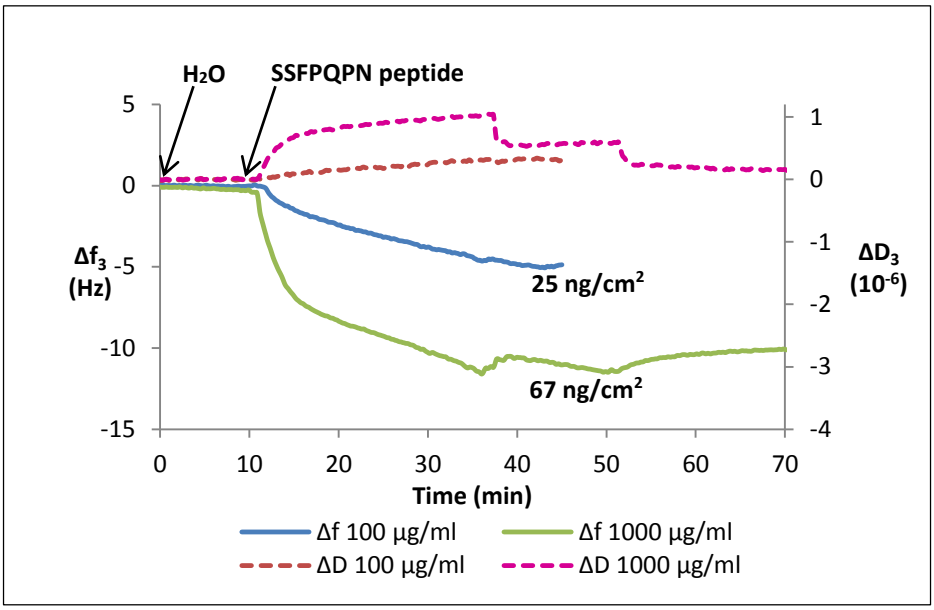

Appendix 5.4

Zeta potential measurements of pure Pt nanoparticles (purchased and in-house synthesized) determined in water at different pH. Particles possess a negative surface charge.

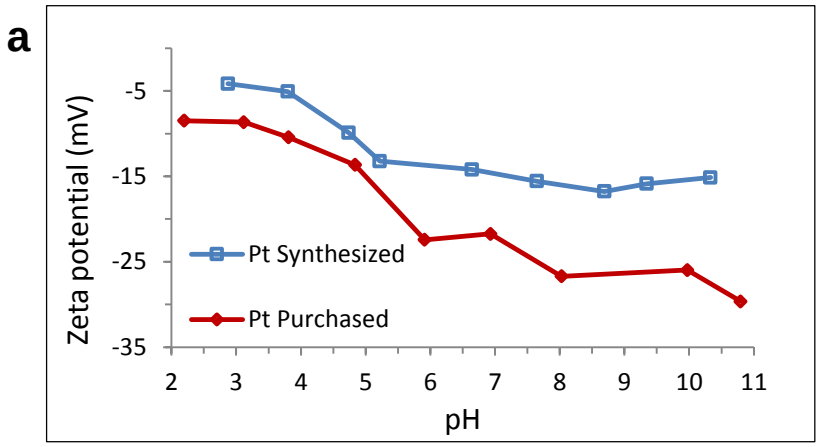

DLS measurements of purchased and in-house synthesized Pt nanoparticles in water. Hydrodynamic diameter of synthesized Pt nanoparticles is 15.06 ± 2.46 nm and that of purchased particles is 35.07 ± 3.97 nm.

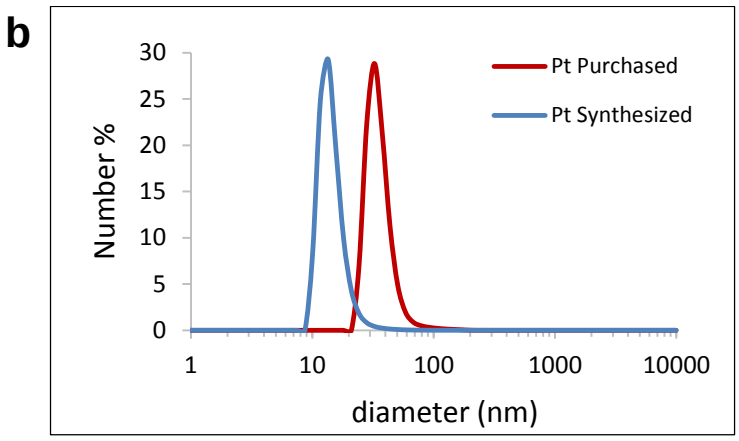

Appendix 5.5

Preliminary ITC studies showing titration of (a) TLHVSSY peptide into a suspension of Pt nanoparticles in phosphate buffer pH 7.4, (b) TLHVSSY peptide into a suspension of Pt nanoparticles in water. Greater heat change was observed when interaction was carried out in water compared to buffer. For experiments to be carried out in water, effects of the pH mismatch between the interaction experiment and the control experiment (peptide dilution into water) need to be considered.

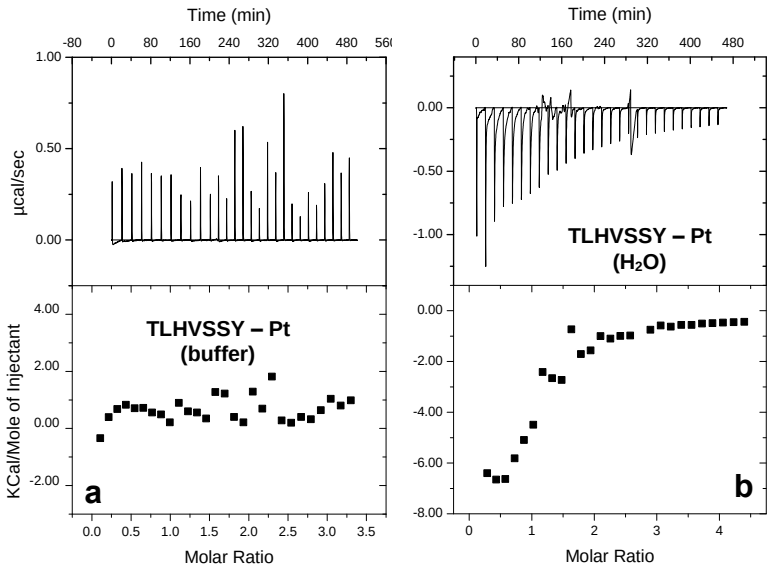

Glossary

ΔG	Change in Gibbs free energy
ΔH	Change in enthalpy
ΔH_{obs}	Global observed heat change also termed apparent heat change (ΔH_{app})
ΔS	Change in entropy
1D	One dimensional
AFM	Atomic force microscopy
AI	Adsorption binding isotherms
AMBER	Assisted Model Building and Energy Refinement
AMOEBA	Atomic Multipole Optimized Energetics for Biomolecular Applications
ATR	Attenuated total reflectance
Au	Gold
AUC	Analytical ultracentrifugation
BET	Brunauer-Emmett-Teller
CD	Circular dichroism spectroscopy
CHARMM	Chemistry at Harvard Molecular Mechanics
CSD	Cell-surface display
ddH_2O	distilled deionised water
DLS	Dynamics light scattering
DNA	Deoxyribonucleic acid
Dp	Differential power
EDX	Energy dispersive X-ray analysis
EG	Ethylene glycol
EM -12	ZnO binding peptide with sequence EAHVMHKVAPRP
FITC	Fluorescein isothiocyanate
FTIR	Fourier transform infrared spectroscopy
G-12	ZnO binding peptide with sequence GLHVMHKVAPPR
G-12A11	Mutant sequence of G-12 with alanine at position 11 GLHVMHKVAP<u>A</u>R
G-12A12	Mutant sequence of G-12 with alanine at position six GLHVMHKVAPP<u>A</u>
G-12A6	Mutant sequence of G-12 with alanine at position 6 GLHVM<u>A</u>KVAPPR
GEPIs	Genetically engineered polypeptides for inorganics
GFP	Green fluorescent protein
GROMACS	Variant of GROMOS
GROMOS	Groningen Molecular Simulation
GT-16	ZnO binding peptide with sequence GLHVMHKVAPPR - GGGC
HAP	Hydroxyapatite
HMTA	Hexamethylenetetramine
HSA	Human serum albumin

ICP-OES	Inductively coupled plasma-optical emission spectroscopy
INTERFACE FF	Interface force field
ITC	Isothermal titration calorimetry
K_A	Association constant (for adsorption or binding)
KBr	Potassium bromide
K_D	Dissociation constant (for desorption)
L/D	Length/ diameter
LBZs	Layered basic zinc salt *i.e.* layered basic zinc acetate (LBZA) and LBZN (N: nitrate)
MALDI-TOF MS	Matrix-Assisted Laser Desorption Ionization Time-of-Flight mass spectrometry
MC	Monte Carlo
MD	Molecular Dynamics
M_r	Molecular weight
n	Stoichiometry
NAMD	Not (just) Another Molecular Dynamics program
NH_3	Ammonia
NMR	Nuclear magnetic resonance
OPLS	Optimized Potential for Liquid Simulations
OWLS	Optical waveguide lightmode spectroscopy
PB	Potassium phosphate buffer
PCFF-SILICA	Polymer Consistent Force Field for Silica
Pd	Palladium
PD	Phage display
PNA	Peptide nucleic acid
PNEA	Poly(*N*-ethylacrylamide
Pt	Platinum
Pt-BPs	Platinum binding peptides
PVP	Polyvinylpyrrolidone
QCM-D	Quartz crystal microbalance with dissipation monitoring
RD	Ribosome display
RNA	Ribonucleic acid
RP-HPLC	Reverse phase high performance liquid chromatography
SDAs	Structure directing agents
SDS	Sodium dodecylsulfate
SEM	Scanning electron microscopy
SERS	Surface enhanced Raman spectroscopy
SFG	Sum-frequency generation
SiO_2	Silicon dioxide (Silica)
SPPS	Solid phase peptide synthesis
SPR	Surface plasmon resonance spectroscopy

TEM	Transmission electron microscopy
TGA	Thermogravimetric analysis
TiO_2	Titanium dioxide
TMV	Tobacco mosaic virus
UV-Vis	Ultraviolet visible
XPS	X-ray photoelectron spectroscopy
XRD	X-ray diffraction
$Zn(CH_3COO)_2$	Zinc acetate
$Zn(NO_3)_2 \cdot 6H_2O$	Zinc nitrate hexahydrate
ZnO	Zinc oxide
ZnO-BPs	ZnO binding peptides

Amino Acids Structures and Abbreviations

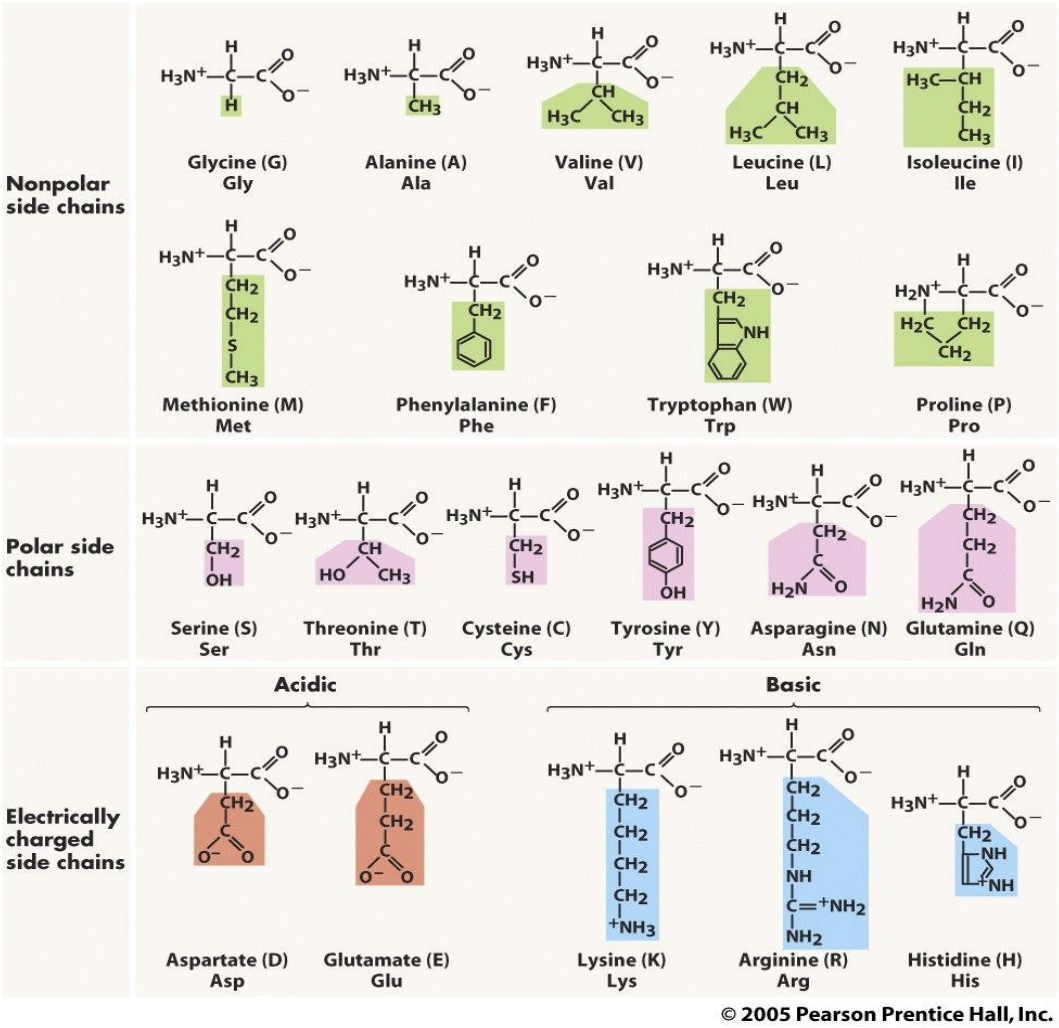

Freeman, S., and Hamilton, H., 2005. *Biological science.* Upper Saddle River, N.J.: Pearson Prentice Hall.

Communications

Oral and Poster Presentations

Oral presentation - Hybrid Materials Conference, Strasbourg, France (6 - 10th March, 2011). Towards an understanding of peptide mineral interactions: a predictive approach. Marion J. Limo and Carole C. Perry.

Oral and poster presentation - NTU annual research conference (10 - 11th May, 2011). The use of isothermal titration calorimetry to understand the thermodynamics of peptide mineral interactions: a predictive approach. Marion J. Limo and Carole C. Perry.

Poster presentation - SET for Britain, House of Commons, London (12th March, 2012). The novel application of isothermal titration calorimetry (ITC) to understand the thermodynamics of peptide - mineral interactions. Marion Limo, David J. Belton and Carole C. Perry.

Poster presentation - RSC Nanopeptide Conference, The University of Manchester (12 - 14th, November, 2012). Peptide template morphology modification and the application of isothermal titration calorimentry (ITC) towards an understanding of peptide - mineral interactions. Marion J. Limo, David J. Belton and Carole C. Perry. Awarded the young researcher poster prize from the peptide and protein speciality grouping of the RSC at this meeting.

Oral presentation - NTU Chemistry and Forensic Science Seminar Series (5th June, 2013). Peptide directed morphology modification and the application of biophysical tools towards an understanding of peptide - inorganic interactions. Marion J. Limo, David J. Belton, Valeria Puddu and Carole C. Perry.

Publication Under Review

Book Title: Bio-Inspired Nanotechnology: From Surface Analysis to Applications

Book Publisher: Springer

Chapter Title: Experimental Characterization of Peptide-Surface Interactions

Marion J. Limo and Yang Wei (equal contributors to the writing of this chapter)

Carole C. Perry and Robert A. Latour (joint corresponding authors)